Capture post-combustion du dioxyde de carbone en couplant des contacteurs membranaires et liquides ioniques : étude expérimentale, modélisation et simulation

Qazi Sohaib

THÈSE POUR OBTENIR LE GRADE DE DOCTEUR DE L'UNIVERSITÉ DE MONTPELLIER

En Génie des procédés

École doctorale GAIA

Unité de recherche : Institut Européen des Membranes (UMR 5635)

CAPTURE POST-COMBUSTION DU DIOXYDE DE CARBONE EN COUPLANT DES CONTACTEURS MEMBRANAIRES ET LIQUIDES IONIQUES : ETUDE EXPÉRIMENTALE, MODÉLISATION ET SIMULATION

Présentée par Qazi SOHAIB

Le 06 Octobre 2020

Sous la direction de : Jose SANCHEZ MARCANO
et Stéphanie DRUON-BOCQUET

Devant le jury composé de

Mme. Violaine ATHES, Professeur, AgroParisTech	Rapporteur
M. Christophe CASTEL, Professeur, Université de Lorraine	Rapporteur
M. Ihsanullah IHSANULLAH, Assistant Professor, KFUPM, Arabie Saoudite	Examinateur
M. Denis BOUYER, Professeur, Université de Montpellier	Président du jury
M. Jose SANCHEZ MARCANO, Directeur de Recherche, Institut Européen des Membranes	Directeur de thèse
Mme. Stéphanie DRUON BOCQUET, Maitre de Conférences, ENSCM	Co-encadrant de thèse

UNIVERSITÉ DE MONTPELLIER

Acknowledgments

Writing this part of the manuscript gives me more happiness, as it reminds me about the achievement of my final goal and accomplishment of a long journey, a journey of deep learning, transfer of knowledge and self-development. This thesis represents my contribution in more than two decades of work at Institut Européen des Membranes (IEM), specifically in the laboratories of the department of Génie des Procédés Membranaires (GPM). It's been an amazing experience, working at IEM, with provided unique opportunities to take advantage of. Throughout these years, I have learned a lot from professional as well as personnel perspective. Living in a culturally rich country such as France, with diverse nationalities, religions and cultures, allowed me to gain enormous personnel growth and to polish various aspects of my life. Considering all things, this thesis is the outcome of many individual and collective experiences at IEM, along with the remarkable individuals working at the laboratory, to whom I am very grateful and always wish to acknowledge.

First and foremost, I wish to thank my thesis director, **Prof. Jose Sanchez-Marcano**, directeur de Recherche at IEM. He has been very supportive, flexible and kindhearted, since the beginning of my work. I admire him for being very thoughtful and kind to me all the time. He is among the few very well-organized people that I know. He helped me cross this rough road, by his mentorship, continuous guidance and encouragement. Similarly, I would like to thank my co director **Dr. Stephanie Druon-bocquet,** who was always available for a productive discussion and valuable advice. She helped me a lot, especially during corrections of my articles and thesis. Jose and Stephanie, it's been an honor for me working with you for the past few years. Also, I would like to acknowledge **Higher Education Commission, Pakistan** and **Campus France** for the PhD scholarship and other academic and living support during these years.

I would like to express my gratitude to **Prof. Angel Irabien** for giving me an opportunity to work in collaboration at Department of Chemical and Biomolecular Engineering Universidad de Cantabria (UC), in Santander, Spain. Thank you for your kindness and guidance throughout my stay at UC. **Dr. Lucía Gómez-Coma** and **Dr. Jonathan Albo** of UC, thank you very much for providing me a very friendly environment and guiding me throughout my experimentations. I really appreciate your efforts in providing me experimental data for the modelling and reviewing my articles. Many thanks to my dearest colleague and friend **Jose Manuel Vadillo**, for giving me a very fruitful company and helping me during my

experiments. I am grateful to all other colleagues at UC, **Guillermo Diaz-Sainz, Sergio Castro-Gonzalez** and others, for welcoming me to the research group and for their cooperation.

I would like to express my deepest gratitude to the members of the jury, who have kindly accepted to be part of thesis defense; **Prof. Denis Bouyer, Prof. Violaine Athès, Prof. Christophe Castel** and **Dr. Ihsanullah.**

I would like to thank all those people from IEM, that were somehow involved in my thesis. **Dr. Thierry Thami, Dr. Christophe Charmette, Dr. Yves-Marie Legrand** and **Jim Cartier,** thank you very much for your cooperation. I have had the wonderful opportunity to meet excellent human beings, sharing with me some unforgettable moments during these three years. My colleagues, **Sher Ahmad**, **Marine Harguindeguy**, **Ahmed Jarboui**, **Ana Luisa, Maya Abdhalah** and **Wassim Sebai,** thank you all for sharing countless precious moments with me during these years. I have been fortunate to work among very kind people of the laboratory, for which I would thank all those people that I met including my other colleagues and staff.

To my family, father and mother, everything that I have now and every milestone that I have achieved in my life, is because of you. They sacrificed their lives for providing every possible means to make me happy and successful in my life. Thank you very much for believing in me, for your love and unconditional support.

I would like to dedicate this paragraph to the most beautiful and amazing person that I have ever met. My dear Fatima, thank you for always being by my side. I have never met a person with such a good heart and as caring as you. You have given me peace of mind and have encouraged and supported me to overcome all those hurdles that I faced during these years. Together, we made it possible.

Abstract

Post-combustion CO_2 capture in a hollow fiber membrane contactor (HFMC), using imidazolium-based room temperature ionic liquids (RTILs) and amino acid ionic liquids (AAILs) as absorbents, was studied through an experimental and modeling approach. Equilibrium solubility of CO_2 in RTILs was measured by isochoric pressure drop. Pore wetting was analyzed by measuring surface tension of the RTILs, contact angle and liquid entry pressure (LEP). The experimental work of CO_2 capture from a gas mixture was carried out with a laboratory scale unit using a single HFMC for absorption or two coupled HFMCs one for absorption and a second for desorption working simultaneously. Furthermore, robust and rigorous dynamic modeling approaches were developed for isothermal (with RTILs) and non-isothermal (with AAILs) absorption. Both isothermal and non-isothermal models were validated with experimental data and were used to simulate a large range of operating conditions. Initial high values of CO_2 absorption rate and experimental mass transfer coefficients decreased with operation time and reached a nearly constant value at pseudo-steady-state. Before reaching pseudo-steady-state, the separation efficiency of coupled process was higher when compared with the absorption with a single module.

Keywords: Post-Combustion CO_2 Capture, Membrane Contactor, Ionic Liquid, CO_2 Solubility, Modeling and Simulation.

Résumé

Des contacteurs membranaires à fibres creuses (HFMC) ont été utilisés pour la capture du CO_2 des courants gazeux. Pour ce faire, des liquides ioniques à température ambiante (RTIL) et des liquides ioniques d'acides aminés (AAIL) à base d'imidazolium ont été utilisés comme absorbants, avec une double approche expérimentale et de modélisation. La solubilité du CO_2 à l'équilibre dans les RTIL a été mesurée par la chute de pression isochronique. Le mouillage des pores a été analysé avec la mesure de la tension superficielle des RTIL, l'angle de contact et la pression d'intrusion (LEP). Le travail expérimental de capture du CO_2 à partir d'un mélange gazeux a été réalisé avec une unité à l'échelle de laboratoire en utilisant soit un HFMC pour l'absorption simple soit deux HFMC couplés, travaillant simultanément un en absorption et le second en désorption. En outre, une approche de modélisation en régime dynamique robuste et rigoureuse a été développée pour l'absorption isotherme (avec des RTIL) et non isotherme (avec des AAIL), les modèles développés ont étés validés avec les résultats expérimentaux et utilisés pour simuler un large éventail des conditions opératoires. Le flux d'absorption du CO_2 et les coefficients de transfert de masse expérimentaux, initialement très élevés, décroisent avec le temps atteignant une valeur presque constante arrivant à un état pseudo-stationnaire. Avant d'atteindre l'état pseudo-stationnaire, le rendement de séparation du procédé couplé s'est montré plus efficace que l'absorption avec un module unique.

Mots-clés: Capture de CO_2 Post-combustion, Contacteur à Membrane, Liquide Ionique, Solubilité au CO_2, Modélisation et Simulation.

Nomenclature

Latin symbols

A	Area (m^2)
C	Concentration ($mol\ m^{-3}$)
a	Gas dependent constant $(Jcm^{-3})^{-1}$
b	Gas dependent constant $(Jcm^{-3})^{-1}$
C_p	Specific heat ($J\ mol^{-1}\ K^{-1}$)
d	Diameter (m)
D	Diffusivity ($cm^2\ s^{-1}$)
E	Enhancement factor (-)
f	Fugacity (Pa)
S	Solubility of CO_2 ($mol\ m^{-3}\ Pa^{-1}$)
h_i	Ion specific constant ($m^3\ Kmol^{-1}$)
h_g	Gas specific constant ($m^3\ Kmol^{-1}$)
H	Henry's law constant (Bar)
H_d	Dimensionless Henry's law constant (-)
H_a	Hatta number (-)
ΔH_{abs}	Enthalpy ($J\ mol^{-1}$)
j	Molar flux ($mol.\ m^{-2}.\ s^{-1}$)
K_2	2nd order rate constant ($L\ mol^{-1}\ s^{-1}$)
K	Overall mass transfer coefficient ($m\ s^{-1}$)
k	Local mass transfer coefficient ($m\ s^{-1}$)
K_r	Kinetic constant (s^{-1})
L	Length of membrane(m)
M	Molar weight ($kg\ mol^{-1}$)
N	Number of fibers (-)
ñ	Number of moles (mol)
P	Pressure (Pa)
Q	Volumetric flowrate ($m^3\ s^{-1}$)
R	Module inner radius (m)

$\acute{R}$	Perfect gas constant ($J\ mol^{-1}\ K^{-1}$)
$\check{R}$	Mass transfer resistance ($s\ m^{-1}$)
r	Radius (m)
$\acute{r}_i$	Reaction rate ($mol\ m^{-3}\ s^{-1}$)
R_e	Reynolds number (-)
S_c	Schmidt number (-)
S_h	Sherwood number (-)
t	Time(s)
T	Temperature (K)
U	Interstitial velocity ($m\ s^{-1}$)
v	Molar volume ($cm^3\ mol^{-1}$)
V	Volume (m^3)
x^*	Mole fraction of CO_2 in IL (-)
y^*	Mole fraction of CO_2 in gas (-)

Subscripts

A	Membrane absorber
C	Contactor
CO_2	Carbon dioxide
exp	Experimental
g	Gas
h	Hydraulic
i	Inner
in	Inlet
IL	Ionic Liquid
Kn	Knudsen
l	Liquid
lm	Log mean
m	membrane
out	Outlet
o	Outer
ov	Overall
p	Pore

r	Radial coordinate
ř	Reservoir
S	Membrane stripper
s	Steady-state
z	Axial coordinate

Greek symbols

α	CO_2 loading ($mol\ mol^{-1}$)
β	Contact angle (deg)
ρ	Density ($g\ cm^{-3}$)
ε	Membrane porosity (-)
τ	Membrane tortuosity (-)
$\mathcal{T}$	Residence time (s)
δ	Membrane thickness (m)
Π	Surface pressure (Pa)
$\emptyset$	Packing fraction of contactor (-)
ϕ	Fugacity coefficient (-)
φ_v	CO_2 concentration in the gas (Vol %)
Υ	Surface tension ($mN\ m^{-1}$)
μ	Viscosity (cP)
λ	Thermal conductivity ($W\ m^{-1}\ K^{-1}$)

Abbreviations and Acronyms

[apmim][BF_4]	1-(3-aminopropyl)-3-methyl-imidazolium tetrafluoroborate
[bmim][BF_4]	1-butyl-3-methyl-imidazolium tetrafluoroborate
[Bmim][DCA]	1-Butyl-3-methylimidazolium dicyanamide
[bmim][Gly]	1-butyl-3-methylimidazolium glycinate
[Bmim][TCM]	1-Butyl-3-methlyimidazolium tricyanomethanide
[emim][Ac]	1-ethyl-3-methylimidazolium acetate
[emim][DCA]	1-ethyl-3-methylimidazolium dicyanamide
[emim][$EtSO_4$]	1-ethyl-3-methylimidazolium ethyl sulfate
[emim][Gly]	1-ethyl-3-methylimidazolium glycinate
[emim][$MeSO_4$]	1-ethyl-3-methylimidazolium methyl sulfate
[hmim][Gly]	1-hexyl-3-methylimidazolium glycinate

[MEA][Gly]	Monoethanolamine glycinate
[N_{1111}][Gly]	Tetramethylammonium glycinate
AAILs	Amino acid ILs
AMP	2-amino-2-methyl-1-propanol
CC	CO_2 capture
CCS	Carbon capture and storage
CCUS	Carbon capture, utilization and storage
HFMCs	Hollow fiber membrane contactors
ILs	Ionic liquids
LEP	Liquid entry pressure
MDEA	Methyl-diethanolamine
MEA	Mono-ethanolamine
PCC	Post-combustion capture
PE	Polyethylene
PP	Polypropylene
PTFE	Polytetrafluoroethylene
PVDF	Polyvinylidene fluoride
RTILs	Room temperature ionic liquids
TSILs	Task Specific ionic liquids

Contents

Synthèse des travaux en français

Contexte

Au niveau mondial, une grande partie de la recherche actuelle s'est focalisée sur l'étude des causes et des solutions à l'augmentation anthropique des émissions de dioxyde de carbone (CO_2) qui contribuent de manière importante au réchauffement de la planète et au changement climatique. Les activités humaines ont provoqué une augmentation de 100 ppm (+36 %) de la concentration atmosphérique de CO_2 au cours des 250 dernières années (Barker, 2007 ; Jie et al., 2013). Cependant, ces dernières décennies, les émissions de CO_2 se sont précipitées augmentant de 6 % chaque année (Chabanon et al., 2013 ; Dai et al., 2016b, 2016c) en raison de la dépendance du monde vis-à-vis des combustibles fossiles et de l'accélération de la croissance économique mondiale. La capture du CO_2 (CC) est l'une des options les plus prometteuses pour minimiser l'influence de l'utilisation des combustibles fossiles sur le changement climatique (Yang et al., 2008). En général, trois stratégies différentes de CC sont étudiées pour atténuer les émissions de ce gaz : l'oxy-combustion, la précombustion et les procédés de séparation postcombustion. La capture du CO_2 de gaz de postcombustion (PCC) est le moyen le plus efficace et le plus réalisable d'atténuer les émissions de CO_2 car ce procédé de séparation peut être appliqué à tous les procédés de combustion et peut être adapté aux centrales électriques et aux installations industrielles existantes (Chabanon et al., 2013 ; Zhao et al., 2016).

Il existe diverses technologies utilisées pour le piégeage du CO_2, notamment des méthodes industrielles d'absorption classiques comme les tours à garnissage, les tours de pulvérisation etc. (Fazaeli et al., 2015). Concernant les procédés membranaires, la séparation membranaire en phase gaz a été très étudiée, mais c'est surtout les contacteurs membranaires gaz-liquide à fibres creuses (HFMC) qui semblent être la technologie la plus prometteuse de par son caractère hybride combinant à la fois une très grande surface de contact et l'absorption, permettant ainsi d'obtenir des transferts de masse gaz/liquide optimisés. En outre, les HFMCs offrent une surface inter-faciale 30 fois plus importante que les autres absorbeurs conventionnels à colonne, évitant en même temps la formation des mousses et permettant un contrôle indépendant des débits de fluides. Par ailleurs, leur modularité permet aussi une certaine facilité lors du changement d'échelle. Un inconvénient majeur des HFMCs est la résistance supplémentaire au transfert de masse due à la membrane, en particulier lorsque le

mouillage est présent, c'est-à-dire lorsque les pores des fibres sont partiellement ou totalement remplis de liquide (Azari et al., 2016 ; Gabelman et Hwang, 1999 ; Muhammad et al., 2017 ; Zhao et al., 2016). En effet, si le phénomène de mouillage est présent, le transfert est fait par diffusion dans la phase liquide stagnante à l'intérieur des pores, en conséquence la résistance au transfert de masse augmente ce qui peut entraîner une forte diminution des performances d'absorption (Mosadegh-Sedghi et al., 2014 ; Rangwala, 1996). Le mouillage des pores de la membrane peut être évité en maintenant la pression en dessous de la pression d'entrée du liquide (LEP), également appelée pression de percée. Selon l'équation de Laplace-Young, la LEP peut être augmentée en améliorant le cosinus de l'angle de contact, en utilisant des absorbants à haute tension de surface et/ou en utilisant des fibres avec des pores de très petite taille. Li et Chen, (2005) et Mosadegh-Sedghi et autres (2014) ont suggéré les paramètres mentionnés ci-dessus pour contrôler le mouillage des pores en utilisant des membranes hydrophobes, en employant des absorbants non corrosifs et compatibles avec les membranes et en maintenant la pression transmembranaire à un niveau inférieur à celui de la LEP. Les membranes poreuses utilisées dans les contacteurs membranaires sont généralement constituées de matériaux hydrophobes tels que le polypropylène (PP), le polyéthylène (PE), le polytétrafluoroéthylène (PTFE) et le polyfluorure de vinylidène (PVDF). Ces membranes seraient surtout utilisées pour le piégeage du CO_2 avec des solutions hydrophiles, en raison de leur grande hydrophobie et de leur bonne stabilité (Chabanon et al., 2015 ; Dai et al., 2016a). Le choix des absorbants pour la CC dans les contacteurs à membrane est très critique en raison des divers problèmes causés par les absorbants classiques (Constantinou et al., 2014 ; Dindore et al., 2004). Les solvants à base d'amines ont été principalement utilisés jusqu'à présent, en raison de leur grande capacité de régénération. Cependant, l'utilisation de ces solvants est menacée par leur grande volatilité, leur perte importante de solvant, leur dégradation à haute température et leur taux de corrosion élevé, qui peuvent être critiques pour la stabilité des membranes (Iliuta et al., 2015 ; Wang et al., 2013a). Pour surmonter ces inconvénients, de nombreux autres types de solvants ont été proposés pour l'absorption du CO_2 dans les contacteurs à membrane, tels que les solutions d'ammoniac et de carbonate, les liquides ioniques (IL), etc.

Les ILs sont des sels organiques avec une pression de vapeur négligeable et une grande stabilité thermique, par ailleurs, certains permettent une solubilité du CO_2 élevée, (Li et al., 2016). Selon Ramdin (2012) ces propriétés conduisent à une perte de solvant presque nulle et à une consommation d'énergie relativement faible pendant l'étape de régénération du solvant

(Ramdin et al., 2012). Un autre avantage des ILs est leur faible toxicité et leur corrosivité relativement faible, qui sont presque deux fois inférieures à celles des amines couramment utilisées (Papatryfon et al., 2014). Les ILs sont classés en deux catégories, les ILs à température ambiante (RTILs) et les liquides ioniques spécifiques (TSILs). Les RTILs sont considérés comme se comportant comme des solvants physiques typiques du CO_2 et d'autres gaz. La solubilité des gaz dans les RTILs est largement représentée par la constante de Henry (Dai et al., 2016b ; Lei et al., 2014). Les ILs à base d'imidazolium ont été largement utilisés pour la capture du CO_2. Des études ont rapporté un effet moindre des cations de chaîne alkyle sur la solubilité du CO_2 par rapport aux anions qui ont une forte influence sur la solubilité de ce gaz (Chen et al., 2006 ; Zhang et al., 2012). La solubilité et la constante de Henry du CO_2 dans divers RTILs ont été largement étudiées et rapportées dans la littérature (Blath et al., 2012, 2011 ; Mejía et al., 2013 ; Ramdin et al., 2012 ; Soriano et al., 2009 ; Yim et al., 2018 ; Yokozeki et al., 2008). Au cours des dernières années, de nombreux chercheurs ont appliqué les ILs en combinaison avec des contacteurs membranaires pour la séparation des gaz. Par exemple, Dai et Deng, (2016) ont utilisé l'IL 1-Butyl-3-méthlyimidazolium tricyanométhanide ([Bmim] [TCM]) pour l'absorption du CO_2 en utilisant une membrane de microfiltration en verre. Dans une autre étude, l'auteur a utilisé le même IL pour étudier et comparer la compatibilité de six membranes polymères différentes pour l'absorption du CO_2 (Dai et al., 2016a). Lu et al. (2013), (2014), (2015) et (2017) ont mis au point une unité d'absorption membranaire et de régénération sous vide pour l'absorption et la régénération du CO_2 avec du tétrafluoroborate de 1-butyl-3-méthyl-imidazolium ([bmim] [BF_4]), tétrafluoroborate de 1-(3-aminopropyl)-3-méthyl-imidazolium ([apmim] [BF_4]), glycinate de monoéthanolamine ([MEA] [GLY]) et un mélange de 2-amino-2-méthyl-1-propanol (AMP) avec [bmim] [BF_4] et ([apmim] [BF_4]). Gómez-Coma et al. (2014) et Albo et al. (2010) ont utilisé le sulfate de 1-éthyl-3-méthylimidazolium ([emim] [$EtSO_4$]) dans leurs études sur l'absorption du CO_2 dans un contacteur à membrane. Chau et al. (2016) et (2014) ont utilisé le 1-Butyl-3-méthylimidazolium dicyanamide ([Bmim] [DCA]) pour le procédé d'absorption par membrane à pression alternée pour absorber le CO_2 du gaz de synthèse à basse température.

Ce travail vise à développer une approche expérimentale et de modélisation pour l'absorption du CO_2 dans un contacteur à membrane à fibres creuses avec quatre ILs différents à base d'imidazolium à température ambiante, et quatre ILs d'acides aminés spécifiques (AAIL). Les ILs à base d'imidazolium considérés pour ce travail sont le sulfate de méthyle 1-éthyl-3-

méthylimidazolium ([emim] [$MeSO_4$]), le dicyanamide 1-éthyl-3-méthylimidazolium ([emim] [DCA]), le sulfate de 1-éthyl-3-méthylimidazolium éthylique ([emim] [$EtSO_4$]) et l'acétate de 1-éthyl-3-méthylimidazolium ([emim] [Ac]) alors que les AAIL considérés étaient le glycinate de tétraméthylammonium ([N1111] [Gly]), Glycinate de 1-éthyl-3-méthylimidazolium ([emim] [Gly]), le glycinate de 1-butyl-3-méthylimidazolium ([bmim] [Gly]) et le glycinate de 1-hexyl-3-méthylimidazolium ([hmim] [Gly]). Les structures moléculaires des cations et des anions des ILs susmentionnés sont présentées dans la figure 1.1 ci-dessous.

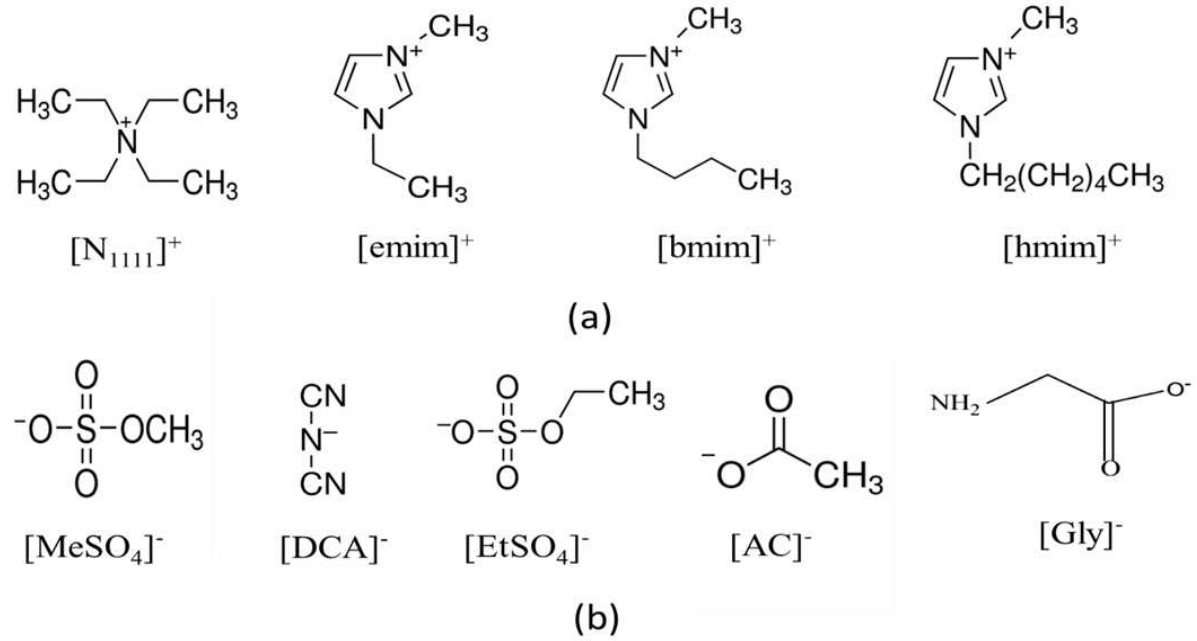

Figure 1 Structures moléculaires des (a) cations et (b) anions des liquides ioniques sélectionnés.

Deux séries différentes des procédés de capture du CO_2 ont été réalisées expérimentalement : une absorption simple avec un seul HFMC et une absorption/désorption couplée réalisée avec deux modules membranaires. Le dispositif d'absorption à un seul module n'absorbe le CO_2 qu'en boucle fermée jusqu'à ce qu'il atteigne un état pseudo-stationnaire, suivi d'une étape d'extraction et de régénération séparée. Le dispositif d'absorption/désorption couplée permet d'absorber le CO_2 d'une mélange gazeux dans un premier HFMC, puis de le désorber par balayage d'azote dans un deuxième HFMC en un seul cycle de recirculation du IL. Cette configuration permet des étapes simultanées d'absorption et de désorption dans un seul cycle. Le mélange de gaz d'alimentation et le gaz de balayage ont été alimentés à l'intérieur des fibres de chaque HFMC et à contre-courant par rapport au IL qui était alimenté à l'extérieur

des fibres. Des contacteurs à membrane contenant des fibres mésoporeuses en polypropylène ont été sélectionnés pour l'absorption. La solubilité du CO_2, l'équilibre du transfert de masse et les constantes de la loi d'Henry ont été mesurés en utilisant le principe de la chute de pression iso-chorique. Les fibres et ILs ont été caractérisés par diverses techniques, notamment la mesure de l'angle de contact, la tension superficielle, la microscopie électronique à balayage (MEB) avant et après l'absorption et l'analyse thermogravimétrique (TGA).

La modélisation et la simulation sont des outils indispensables pour minimiser le nombre d'expériences afin d'étudier un large spectre des conditions opératoires, faciliter la mise à l'échelle et réduire le coût d'optimisation lors de la conception d'un procédé. La modélisation 2-D des transferts dans les fibres permet de calculer les transferts de masse axiaux et radiaux. En outre, si la modélisation est correctement réalisée et validée par des résultats expérimentaux, un large spectre de situations d'absorption réelles ou simulées peuvent être étudiées, permettant d'évaluer le rôle de l'absorbant, de la membrane et de l'hydrodynamique séparément, comme cela a été suggéré dans la revue de Zhao et al. (2016). De nombreux chercheurs se sont concentrés sur la modélisation et la simulation de l'absorption du CO_2 dans les HFMC avec des absorbants classiques. Cependant, il existe peu de littérature disponible sur la modélisation et la simulation de l'absorption du CO_2 dans les HFMC avec des ILs (Azari et al., 2016 ; Dai et al., 2016c). Cette thèse comporte une forte composante de modélisation avec des approches de modélisation dynamique en régime permanent et pseudo-stationnaire. Ces modèles ont été mis en œuvre pour étudier le procédé d'absorption/désorption du CO_2 des courants gazeux à travers la simulation et pour effectuer des analyses paramétriques et de sensibilité ainsi qu'une optimisation. Une approche de modélisation isotherme a été développée pour les RTILs à base d'imidazolium tandis que pour les AAILs, un modèle non-isotherme a été construit.

Problématique

Cette thèse a été réalisée en tenant compte des problèmes suivants :

- Le développement des technologies de capture du CO_2 est nécessaire pour contrôler la croissance rapide du niveau de ce gaz dans l'atmosphère.

- Des améliorations dans la conception et l'intensification des procédés avec des HFMCs sont essentielles dans les opérations de capture du CO_2 de gaz de postcombustion.
- Jusqu'à présent, la plupart des absorbants utilisés pour la capture du CO_2 sont corrosifs, volatils et sensibles à la dégradation. D'autres absorbants respectueux de l'environnement, tels que les ILs, qui peuvent minimiser les problèmes mentionnés ci-dessus, doivent être explorés.
- La connaissance actuelle des cinétiques de réaction et d'absorption du CO_2 dans les ILs est très incomplète mais nécessaire pour développer l'absorption du CO_2 dans les HFMCs.
- La plupart des études précédentes sur la capture du CO_2 de gaz de postcombustion dans les contacteurs à membrane sont basées sur des études au niveau de laboratoire et à petite échelle.
- Dans la littérature il existe un nombre très limité d'études développant une approche de modélisation détaillée qui peut faciliter le changement d'échelle des procédés.
- Il y a un manque d'analyses paramétriques et de sensibilité complètes ainsi que d'études d'optimisation des procédés de capture du CO_2 avec des ILs et HFMCs.
- L'approche de modélisation non isotherme a été très rarement signalée car la plupart des études de modélisation publiées sont basées sur une modélisation isotherme, alors que le procédé est non isotherme dans le cas des absorbants réactifs.

Objectifs de la recherche

Ces travaux ont porté sur l'étude de la faisabilité de la capture du CO_2 contenu dans un gaz de postcombustion en couplant l'absorption avec des ILs et la technologie d'extraction membranaire avec des HFMCs. Pour ce faire, une étude expérimentale a été réalisée et différents modèles mathématiques permettant la simulation des procédés en question ont été développés. Afin d'atteindre les objectifs globaux mentionnés ci-dessus, les études suivantes ont été accomplies au cours de ces travaux :

- Étude de la solubilité, de l'équilibre gaz/liquide, de la cinétique de réaction et d'absorption du CO_2 dans des RTILs et des AAILs sélectionnés.

- Étude de la faisabilité du couplage des ILs avec les HFMCs pour la capture du CO_2 des courants gazeux avec absorption avec un seul HFMC ou 'absorption/désorption couplées avec deux HFMCs.
- Identification et caractérisation des ILs, absorbants plus respectueux de l'environnement, plus rentables et plus efficaces sur le plan énergétique pour la capture du CO_2.
- Développement d'approches de modélisation dynamique robustes et rigoureuses pour les l'absorption isotherme et non isotherme du CO_2 dans les HFMC avec ILs.
- Utilisation de modèles développés pour des recherches qui ne sont pas possibles et/ou faisables par des expérimentations telles que l'optimisation du procédé, l'analyse paramétrique, l'analyse de sensibilité et l'analyse du niveau de mouillage de la membrane.
- Reproduction des données expérimentales de capture du CO_2 après combustion par le biais de modèles et de simulations développées en vue d'une intensification, d'amélioration et d'une éventuelle mise à l'échelle.

Schéma de la thèse

La thèse présentée ici est basée sur la faisabilité de la capture du CO_2 de gaz de postcombustion en couplant les RTILs et les AAILs avec les HFMC, par l'expérimentation, la modélisation et la simulation. Elle est structurée en 7 chapitres, comme suit ;

Le chapitre 1 présente le contexte général, les problèmes et les objectifs du travail.

Le chapitre 2 présente le contexte général des travaux. Les émissions de CO_2 et leurs impacts globaux et environnementaux sont décrits. Des détails sur les méthodes, les technologies et le stockage du dioxyde carbone sont également présentés. Les HFMCs, leurs avantages et inconvénients pour la séparation gaz/liquide et leur mise en œuvre pour la capture du CO_2 de gaz de postcombustion sont présentés en détail. La sélection d'absorbants liquides appropriés pour la capture du CO_2 est décrite. Une attention particulière est accordée aux ILs et à leur capacité à capturer le CO_2.

Le chapitre 3 présente des détails sur les matériels et les méthodes. Les ILs et HFMCs, leurs propriétés et les techniques de caractérisation sont présentés. L'approche expérimentale mise en œuvre pour les mesures de solubilité du CO_2 à l'équilibre et l'absorption/désorption du CO_2 dans les HFMCs couplés aux ILs est décrite en détail.

Le chapitre 4 présente l'approche théorique et le développement de modèles pour la capture du CO_2 d'un courant gazeux dans les HFMC. Toutes les équations utilisées pour décrire les différents phénomènes sont présentées en détail ici : équations et corrélations empiriques pour la cinétique de transfert de masse, équations pour le transport de masse et de quantité de mouvement du modèle isotherme et pour le transport de masse, de quantité de mouvement et d'énergie du modèle non isotherme, équations pour la prédiction et le calcul de la solubilité, des équilibres de phase et des coefficients de diffusion. Les conditions aux limites et la résolution numérique des modèles sont également abordées.

Le chapitre 5 présente l'étude expérimentale d'absorption du CO_2 d'un courant gazeux simulant des gaz de postcombustion avec un système d'absorption à un seul module et un système d'absorption/désorption couplé à deux modules. Les propriétés et la caractérisation des ILs et des membranes sont d'abord décrites. La performance de la capture du CO_2 avec un système d'absorption à un seul module est discutée en détail, sur la base des résultats des efficacités d'élimination du CO_2, et de la cinétique de transfert de masse mesurée. Les efficacités d'élimination du CO_2, les charges de CO_2 des ILs, les coefficients de transfert de masse et les facteurs d'amélioration sont comparés pour le système d'absorption à un seul module et le système d'absorption/désorption couplé.

Le chapitre 6 présente des simulations du modèle développé dans des conditions isothermes. Une comparaison entre les simulations et les données expérimentales est présentée pour la validation du modèle. Les simulations de la distribution axiale et radiale de la concentration de CO_2, l'effet des conditions opératoires et l'analyse paramétrique sont présentés en détail. Les résultats sont décrits pour les modes pseudo-stationnaire et stationnaire. Une analyse détaillée du mouillage partiel et complet des pores de la membrane est également présentée.

Le chapitre 7 présente des simulations du modèle développé dans des conditions non isothermes. Une comparaison entre les simulations et les données expérimentales est présentée pour la validation du modèle. Les profils de la concentration en CO_2, de la concentration du IL dans des mélanges eau-IL, de la température et de la constante de vitesse de réaction, le long du contacteur, sont discutés en détail. Les performances des différents ILs utilisés dans les HFMC pour la capture du CO_2 sont présentées et comparées. Les variations du flux limite et de la vitesse de réaction sur la longueur du contacteur sont également présentées.

Enfin, la thèse se termine par la conclusion générale des investigations et les perspectives de travaux futurs.

Principaux résultats

Les résultats concernant la solubilité du CO_2 dans les ILs montrent que celle-ci est affectée négativement par la température. En effet, une augmentation de la constante de la loi de Henry a été observée avec l'augmentation de la température. Par exemple, la constante de la loi de Henry pour l'IL [emim] [DCA] passe de 74,3 à 86,6 bar, lorsque la température augmente de 298 à 313 K. La solubilité du CO_2 mesurée expérimentalement pour les quatre RTIL peut être classée comme suit : [emim] [Ac] > [emim] [$EtSO_4$] > [emim] [$MeSO_4$] > [emim] [DCA]. À 298 K. Les diffusivités du CO_2 dans les RTIL calculées à l'aide des corrélations est de 1,15 10^{-5} cm^2 s^{-1}, 3,9 10^{-6} cm^2 s^{-1}, 3,38 10^{-6} cm^2 s^{-1} et 2,64 10^{-6} cm^2 s^{-1} pour [emim] [DCA], [emim] [$MeSO_4$], [emim] [$EtSO_4$] et [emim] [Ac] respectivement. Cet ordre qui correspond exactement à la variation de la viscosité des RTILs montre que ce paramètre est fondamental dans la diffusivité du CO_2 dans ces liquides.

La solubilité et la diffusivité sont les paramètres les plus importants pour l'absorption du CO_2 dans le procédé étudié. Cependant, ces deux paramètres agissent de façon antagoniste et l'effet global de ces deux paramètres ne peut être observé qu'à partir de la performance globale d'absorption.

Lors de l'analyse de stabilité thermique des ILs par la TGA, il est observé que le [emim] [$MeSO_4$] ne présente que 4 % de perte pour des expériences réalisées entre la température ambiante et jusqu'à 200 ^oC, [emim] [DCA] présente 4 % de perte de poids jusqu'à 270 ^oC, [emim] [$EtSO_4$] ne présente que 4 % de perte de poids jusqu'à 300 ^oC et [emim] [Ac] ne perd

que 2 % de poids jusqu'à 200 ^{o}C. En conclusion, tous les RTILs peuvent être considérés comme thermiquement stables pour les expériences actuelles dans la plage de température de 288-323 K.

Les expériences de vieillissement des fibres en PP en présence de IL n'ont montré aucune influence des ILs sur les membranes. En effet, aucun effet notable sur la surface et la structure poreuse des membranes en PP n'a été observé, après 20 jours d'immersion des fibres dans les RTILs. Par ailleurs, les angles de contact mesurés entre des RTILs et les fibres qui étaient de l'ordre de 72°-85° pour des fibres neuves n'ont guère été affectés. En effet ils n'ont montré qu'une légère chute de 1° à 2° après 40 jours d'immersion des fibres dans les RTILs.

Concernant le procédé d'absorption du CO_2 avec un seul module, il a été observé que le CO_2 est absorbé initialement à un taux très élevé, ralentissant progressivement en raison de l'accumulation graduelle de CO_2 due à la diminution du gradient. Par exemple, pendant les dix premières minutes, [emim] [$MeSO_4$] absorbe 56 % de la capacité totale d'absorption du CO_2, pendant que le reste du CO_2 est absorbé les 70 dernières minutes du procédé. Cependant, pour les plus faibles débits de gaz utilisés l'efficacité initiale reste proche de 100 %. Par exemple, l'[emim] [$EtSO_4$] montre une efficacité de 98% même après 20 minutes de recirculation à un débit de gaz de 50 ml min^{-1}. Comme il a été décrit ci-dessus, le taux d'absorption du CO_2 et donc la performance de séparation diminue avec le temps jusqu'à atteindre un état pseudo-stationnaire. À l'état pseudo-stationnaire, le taux d'absorption devient très lent et est presque constant. L'absorption avec les RTILs a été plus affectée par le débit du gaz d'alimentation que par la température du procédé. Pour les ILs [emim] [$MeSO_4$] et [emim] [DCA], il a été observé une diminution de l'efficacité d'élimination du CO_2 du mélange d'alimentation de 43 % et 58 %, respectivement, lorsque le débit de gaz d'alimentation est augmenté de 20 ml min^{-1} à 50 ml min^{-1}. Des effets similaires ont été observés pour deux autres ILs. Néanmoins, une augmentation du débit de gaz (bien qu'elle diminue l'efficacité côté gaz) et une diminution de la température du procédé pourraient augmenter les performances globales car elles améliorent le coefficient de transfert de masse global et le flux de CO_2. L'amélioration du transfert de masse diminue avec l'augmentation de la charge en CO_2 dans les ILs. Dans le cas de [emim] [$EtSO_4$], le facteur d'amélioration initial (à $100\alpha_t = 0$ mol mol^{-1}) étant initialement de 18.7 décroit jusqu'à 0.47 lorsque l'état pseudo-stationnaire est atteint (à $100\alpha_t = 2.11$ mol mol^{-1}).

Le procédé couplé d'absorption/désorption avec deux HFMCs permet de maintenir un taux d'absorption de CO_2 très élevé et à long terme par rapport à l'absorption avec un seul module. En effet, l'absorption et la désorption dans un seul cycle permet à l'absorbant de maintenir une très faible charge de CO_2 et un très fort gradient qui se traduit par une grande performance à long terme. Les ILs [emim] [$MeSO_4$] et [emim] [DCA] ont pu maintenir 82 % et 66 % d'efficacité en conditions pseudo-stationnaires à un débit de gaz d'alimentation de 10 ml min^{-1}. Si nous comparons les deux procédés de capture étudiés, l'absorption/désorption couplée permet de maintenir une efficacité allant jusqu'à 90 % ; pendant que l'absorption avec un seul module résulte dans une diminution de l'efficacité et pouvant descendre jusqu'à 10 % à l'état pseudo-stationnaire. En effet, l'absorption/désorption couplée a permis de maintenir une charge maximale de CO_2 inférieure de 2 à 6 fois et une amélioration du transfert de masse supérieure de 4 à 5 fois à l'état pseudo-stationnaire, par rapport à l'absorption avec un seul module. Le désorbeur à membrane a pu atteindre une efficacité de près de 90 % en un seul passage après absorption dans l'absorbeur à membrane, ce qui confirme la nature même de l'absorption physique, la facilité de régénération, la nature des économies d'énergie et la faisabilité des RTILs dans la configuration actuelle à deux modules.

Les simulations obtenues avec le modèle isotherme, qui a été développé pour l'absorption du CO_2 en régime permanent et pseudo-stationnaire dans les RTILs, sont en accord avec les résultats expérimentaux obtenus à la fois avec le procédé d'absorption à module unique et de d'absorption/désorption couplée. Le modèle a ainsi pu prédire les résultats expérimentaux dans une fourchette de 2 à 5 % d'écart type, tout en tenant compte des erreurs expérimentales.

Les modèles ainsi validés ont permis d'étudier l'influence des paramètres structuraux et opératoires sur l'efficacité du procédé de capture du CO_2. Une analyse détaillée du mouillage partiel et complet de la membrane a confirmé l'importance de ce paramètre dans le transfert de masse à travers la membrane. Le flux de CO_2 est diminué de moitié avec une membrane partiellement mouillée seulement à 5 %, pendant qu'une membrane complètement mouillée fait chuter le flux de CO_2 à presque zéro. Les autres paramètres qui pourraient influencer la séparation du CO_2, y compris la porosité de la membrane, la tortuosité de la membrane, le diamètre et la longueur des fibres ont été analysés. Une augmentation de la porosité de 0,1 à 0,5 a permis d'augmenter l'efficacité de la séparation de 53 %. Tout en maintenant une valeur constante de la porosité (0,5), une diminution d'environ 20 % de l'efficacité de séparation a été observée en faisant passer la valeur de la tortuosité de 1 à 7.

Lorsque le diamètre intérieur des fibres est augmenté de 0,1 mm à 1 mm, l'efficacité de la séparation est réduite de 33 %. Les simulations ont prévu une augmentation de 35 % de la concentration de CO_2 à la sortie côté gaz, tout en faisant varier le débit de gaz de 10 ml min^{-1} à 130 ml min^{-1}. Quand le débit du IL est augmenté de 5 ml min^{-1} à 65 ml min^{-1}, la concentration de CO_2 à la sortie côté gaz diminue de 12 %. Cependant, bien que l'augmentation du débit de gaz réduise l'efficacité de la séparation du CO_2 côté gaz, le transfert de masse et le flux de CO_2 augmentent avec l'augmentation des débits de gaz et de liquide. Une analyse de sensibilité en régime pseudo-stationnaire a confirmé que le procédé est très sensible aux variations du débit de gaz plutôt que du débit de liquide. Pour l'absorption/désorption couplée, le débit de gaz de balayage, le débit d'IL et la porosité de la membrane ont été optimisés afin obtenir une concentration nulle de CO_2 à la sortie du désorbeur de la membrane. La concentration cible de CO_2 pourrait être atteinte pour une membrane avec une porosité de 60 %, en maintenant un débit de liquide de 48 ml min^{-1} et un débit de gaz de balayage de 200 ml min^{-1}. Pour la même membrane poreuse, si le débit de gaz de balayage tombe à 50 ml min^{-1}, le débit de liquide doit être maintenu à 18 ml min^{-1} pour atteindre l'objectif. La sensibilité des paramètres optimisés pourrait être classée comme suit : débit d'IL > débit de gaz de balayage > porosité de la membrane.

Le modèle non isotherme, qui a été développé pour l'absorption en régime permanent du CO_2 dans les AAILs qui sont réactifs, a permis de faire des simulations des données expérimentales de la littérature, ce qui a donné suffisamment de précision pour valider le modèle et réaliser des simulations. Les simulations réalisées avec les AAILs ont fait état de variations de température importantes sur la longueur du contacteur en raison de la réaction entre le soluté et l'absorbant, car la chaleur d'absorption s'accumule sur la longueur du contacteur. L'augmentation de la température se situe entre 10 et 25 K, selon la réactivité de l'AAIL. Le gradient de température est très élevé dans la section après la moitié de la longueur de la fibre (z/L=0,5-z/L=1). D'autres paramètres dépendant de la température ont été influencés par cette variation, notamment la diffusivité et la solubilité du CO_2, et la vitesse de réaction. En comparant les performances de séparation des AAILs, [hmim] [Gly] pourrait être considéré comme le meilleur parmi tous ceux testés ici, avec la plus haute efficacité de séparation arrivant jusqu'à 85 %. En analysant l'effet de la concentration des solutions aqueuses d'AAIL, une augmentation de l'efficacité de 23 % a été observée en faisant passer la concentration de $[N_{1111}][Gly]$ de 0,3 à 2,0 mol L^{-1}.

Des résultats similaires ont été observés pour d'autres AAILs. Pour le $[N_{1111}][Gly]$, une augmentation de la température de 298 K à 323 K n'augmente l'efficacité que de 5 %. Bien que l'effet de la température du procédé sur la performance de séparation du CO_2, le flux limite et la vitesse de réaction aient été suffisamment significatifs, la plus forte influence a cependant été enregistrée avec la variation de la concentration des AAILs. La prépondérance de la chimisorption a pu être observée avec un transfert de masse très efficace près de l'interface gaz/liquide. Cependant, même si la diffusion des produits de la réaction pourrait affecter le procédé global, elle a été négligée, car la réaction ne se produit qu'au-dessus et/ou à proximité de l'interface gaz/liquide.

Conclusions et perspectives

La capture du CO_2 de gaz de postcombustion en couplant l'absorption avec des ILs et des HFMCs a déjà bien été bien étudiée auparavant, cependant cette étude a permis d'améliorer d'une part la compréhension du procédé et d'autre part d'établir des modèles de connaissance qui permettent d'optimiser la capture de ce gaz avec ces systèmes en simulant une série des paramètres opératoires ainsi que les caractéristiques des ILs et des fibres. Toutefois, certains aspects doivent être abordés pour rendre ce procédé plus attractif et surtout applicable au niveau pilote industriel.

Le choix des absorbants appropriés à utiliser avec les HFMCs est très critique en raison des divers problèmes rencontrés avec les absorbants conventionnels. Bien que la faisabilité de la capture du CO_2 avec les ILs ait été prouvée et que ces composés se soient montrés parmi les meilleurs absorbants du CO_2, il reste cependant quelques problèmes importants à résoudre, notamment les viscosités élevées des ILs ainsi que leur coût de fabrication. Ces deux problèmes peuvent être résolus en les mélangeant avec un certain pourcentage d'eau et/ou en adaptant les structures des anions et/ou des cations des ILs, tout en gardant à l'esprit la solubilité du CO_2, qui est par ailleurs le paramètre le plus important. De nombreux chercheurs travaillent déjà à l'exploration et à la résolution de ces questions afin de rendre les ILs plus adaptés industriellement pour la capture du CO_2 des gaz de postcombustion avec les HFMCs. Les deux types d'ILs étudiés dans ce travail, à savoir les RTILs et les AAILs, ont un impact différent sur le procédé d'absorption. Les RTILs peuvent fournir une capacité modérée d'absorption du CO_2 mais peuvent être régénérés très facilement. Ainsi, les RTILs peuvent être très efficaces sur le plan énergétique et très rentable (sous réserve de diminution du prix

de fabrication à échelle industrielle), ce qui les rend très attractifs pour les opérations d'absorption de CO_2 continue à long terme. Les AAILs peuvent fournir une capacité d'absorption très élevée, mais la régénération n'est pas très facile en raison de leur nature réactive pouvant être coûteuse. Pour les contacteurs à membrane hydrophobe, les ILs à haute tension superficielle doivent être sélectionnés pour éviter le mouillage des pores. De plus, certains ILs peuvent interagir avec les polymères composant les fibres et donc ne sont pas utilisables pour des opérations à long terme. Par conséquent, une sélection expérimentale minutieuse du couple IL-membrane est fondamentale.

Bien que l'absorption à HFMC unique ait été largement étudiée et utilisée pour l'absorption du CO_2 de courants gazeux, l'absorption/désorption couplée est bien plus efficace et intéressante du point de vue de l'application. L'absorption/désorption couplée avec les RTILs (avec l'avantage d'une régénération très facile) pourrait être très appropriée pour le captage continu du CO_2 de gaz de postcombustion à l'échelle commerciale. Néanmoins, il faudrait étudier plus en profondeur le changement d'échelle et optimiser le procédé afin de s'approcher de 100% d'efficacité. L'étude d'optimisation a été réalisée dans le cadre de ces travaux pour trois paramètres, ils pourront certainement être étendus à d'autres paramètres. D'autres modifications et améliorations du procédé sont essentielles pour le rendre plus attractif, en particulier des modifications des moyens de désorption dans le désorbeur à membrane. Des techniques de désorption plus efficaces pourraient être mises en œuvre, telles que la désorption sous vide, éventuellement avec une légère augmentation de la température. Un procédé couplé pourrait également être mis en œuvre pour les AAILs ou TSILs, mais avec une étape de désorption simultanée plus efficace. Aucune analyse économique spécifique n'a été effectuée dans le cadre de ce travail. Il est en outre recommandé pour les travaux futurs d'aborder l'économie du procédé couplé, tout en considérant le cadre du procédé optimisé.

Les modèles 2-D isothermes et non isothermes développés dans ce travail peuvent être utilisés pour différents absorbants. Cependant, bien que les modèles prédisent correctement les données expérimentales, pour améliorer la capacité prédictive du modèle, une estimation très précise des différents paramètres et des propriétés physico-chimiques est nécessaire. Par exemple, lors de l'analyse du mouillage, les ratios de mouillage considérés étaient basés sur des modèles relativement simples et non réels, la quantité réelle et l'emplacement du mouillage peuvent être beaucoup plus complexes compte tenu de l'origine industrielle des fibres. De même, la diffusion des gaz à travers différents domaines a été calculée à l'aide de

corrélations empiriques. Bien que les corrélations empiriques utilisées ici aient été vérifiées et comparées aux données expérimentales dans diverses études de la littérature, il pourrait toutefois y avoir une différence entre les valeurs réelles et les valeurs calculées, en particulier pour les ILs qui n'ont pas été étudiés auparavant. L'absorption/désorption couplée pourrait être une option très réalisable à l'échelle industrielle. Il est donc recommandé d'utiliser les prédictions du modèle en utilisant des paramètres et des conditions de fonctionnement à grande échelle provenant de l'environnement industriel. Cela pourrait être réalisé en même temps que l'optimisation du procédé et l'analyse des coûts pour la boucle continue d'absorption/désorption couplée. Ces études peuvent être réalisées en améliorant le modèle existant ou à l'aide d'un simulateur de procédés.

Chapter 1. Introduction

1.1 Background

Anthropogenic increase in emission of carbon dioxide (CO_2), which is a major contributor to global warming and climate change, has driven world's attention towards CO_2 capture and storage. Due to the world's dependency on fossil fuels, CO_2 emission is increasing by 6 % every year (Chabanon et al., 2013; Dai et al., 2016b, 2016c). Human activities have caused an increase of 100 ppm (36%) in atmospheric CO_2 concentration over the past 250 years (Barker, 2007; Jie et al., 2013). CO_2 capture (CC) is one of the most promising options to minimize the influence of fossil fuel utilization on climate change (Yang et al., 2008). Generally, three different CC strategies are being studied to mitigate CO_2 emissions: oxyfuel-combustion, pre-combustion and post-combustion separation processes. Post-combustion capture (PCC) is the most effective and feasible way for CO_2 mitigation because this separation process can be applied to all combustion processes and can be retrofitted to existing power and industrial plants (Chabanon et al., 2013; Zhao et al., 2016).

There are various technologies used for CO_2 capture including membranes, packed towers, spray towers, absorption columns and other conventional industrial methods (Fazaeli et al., 2015). HFMCs are a hybrid technology that combines both membrane and absorption and can achieve dispersion free gas/liquid and liquid/liquid mass transfers. HFMCs are more advantageous than other conventional columns due to their larger and constant interfacial area per volume unit, absence of flooding, foaming and entrainment, independent control of flowrates, easy scale up and modularity. A HFMC provides 30 times more interfacial area compared to other conventional absorbers. A major drawback in HFMC is the additional mass transfer resistance due to the membrane especially in wetting mode (Azari et al., 2016; Gabelman and Hwang, 1999; Muhammad et al., 2017; Zhao et al., 2016). Indeed, in the wetting zone of membrane contactors the mass transfer resistance enhances due to the membrane itself or membrane pore wetting which can significantly result on a sharp drop in absorption performance (Mosadegh-Sedghi et al., 2014; Rangwala, 1996). Membrane pore wetting can be prevented by maintaining the pressure below liquid entry pressure (LEP) also called breakthrough pressure. According to Laplace-Young equation, LEP can be increased

by enhancing cosine of the contact angle, using absorbents of high surface tension and small membrane pores. Li and Chen, (2005) and Mosadegh-Sedghi et al. (2014) suggested the above mentioned parameters to control pore wetting by using hydrophobic membranes, employing non-corrosive and membrane compatible absorbents and maintaining transmembrane pressure lower than LEP. The porous membranes used in membrane contactors are usually made of hydrophobic material such as polypropylene (PP), polyethylene (PE), polytetrafluoroethylene (PTFE) and polyvinylidenefluoride (PVDF). These membranes are mostly reported to be used for CO_2 capture due to their high hydrophobicity and good stability (Chabanon et al., 2015; Dai et al., 2016a). Selection of absorbents for CC in membrane contactors is very critical because of the various problems caused by conventional absorbents (Constantinou et al., 2014; Dindore et al., 2004). Amine based solvents have been mostly used so far, because of their large regeneration capacities. However, use of these solvents is threatened by their high volatility, large amount of solvent loss, degradation at high temperature and high corrosion rate which can be critical for the membranes stability (Iliuta et al., 2015; Wang et al., 2013a). To overcome these drawbacks many other types of solvents have been suggested for CO_2 absorption in membrane contactors such as ammonia and carbonate solutions, ionic liquids (ILs) etc.

ILs are organic salts having extraordinarily high CO_2 solubility, negligible vapor pressure and high thermal stability (Li et al., 2016). These properties lead to almost zero solvent loss and lower energy consumption during regeneration (Ramdin et al., 2012). Another advantage of ILs is their low toxicity and relatively low corrosiveness, which are almost two magnitudes lower than those of commonly used amines (Papatryfon et al., 2014). ILs are classified in two categories, room temperature ILs (RTILs) and task specific ionic liquids (TSILs). RTILs are considered to behave as typical physical solvents for CO_2 and other gases. Gas solubility in RTILS is widely represented by Henry's law constant (Dai et al., 2016b; Lei et al., 2014). Imidazolium based ILs are widely reported to be used for CO_2 capture. Studies have reported less effect of alkyl chain cations on CO_2 solubility compared to anions which has strong influence on the solubility of CO_2 (Chen et al., 2006; Zhang et al., 2012). Solubility and Henry's Law constant of CO_2 in various RTILs have been extensively studied and reported in the literature (Blath et al., 2012, 2011; Mejía et al., 2013; Ramdin et al., 2012; Soriano et al., 2009; Yim et al., 2018; Yokozeki et al., 2008). In the past few years, many researchers have applied ILs in combination with membrane contactors for gas separation. For example Dai and Deng, (2016) used IL 1-Butyl-3-methlyimidazolium tricyanomethanide ([Bmim][TCM])

for CO_2 absorption using a microfiltration glass membrane. In another study the author used the same IL [Bmim][TCM] to study and compare the compatibility of six different polymeric membranes for CO_2 absorption (Dai et al., 2016a). Lu et al. (2013), (2014), (2015) and (2017), developed membrane absorption and vacuum regeneration unit for absorption and regeneration/stripping of CO_2 with ILs 1-butyl-3-methyl-imidazolium tetrafluoroborate ([bmim][BF_4]), 1-(3-aminopropyl)-3-methyl-imidazolium tetrafluoroborate ([apmim][BF_4]), monoethanolamine glycinate ([MEA][Gly]) and mixture of 2-amino-2-methyl-1-propanol (AMP) with [bmim][BF_4] and ([apmim][BF_4]. Gómez-Coma et al. (2014) and Albo et al. (2010) used 1-ethyl-3-methylimidazolium ethyl sulfate ([emim][$EtSO_4$]) in their studies for CO_2 absorption in a membrane contactor. Chau et al. (2016) and (2014) used 1-Butyl-3-methylimidazolium dicyanamide ([Bmim][DCA]) for pressure swing membrane absorption process to absorb CO_2 from low temperature shifted syngas.

This work aims to develop an experimental and modeling approach for CO_2 absorption in a hollow fiber membrane contactor with four different room temperature imidazolium based ILs, and four task specific amino acid ILs. The imidazolium based ILs considered for this work were 1-ethyl-3-methylimidazolium methyl sulfate ([emim][$MeSO_4$]), 1-ethyl-3-methylimidazolium dicyanamide ([emim][DCA]), 1-ethyl-3-methylimidazolium ethyl sulfate ([emim][$EtSO_4$]) and 1-ethyl-3-methylimidazolium acetate ([emim][Ac]) while the AAILs considered were tetramethylammonium glycinate ([N_{1111}][Gly]), 1-ethyl-3-methylimidazolium glycinate ([emim][Gly]), 1-butyl-3-methylimidazolium glycinate ([bmim][Gly]) and 1-hexyl-3-methylimidazolium glycinate ([hmim][Gly]). Molecular structures of the cations and anions of the above mentioned ILs are presented in the Figure 1.1 below.

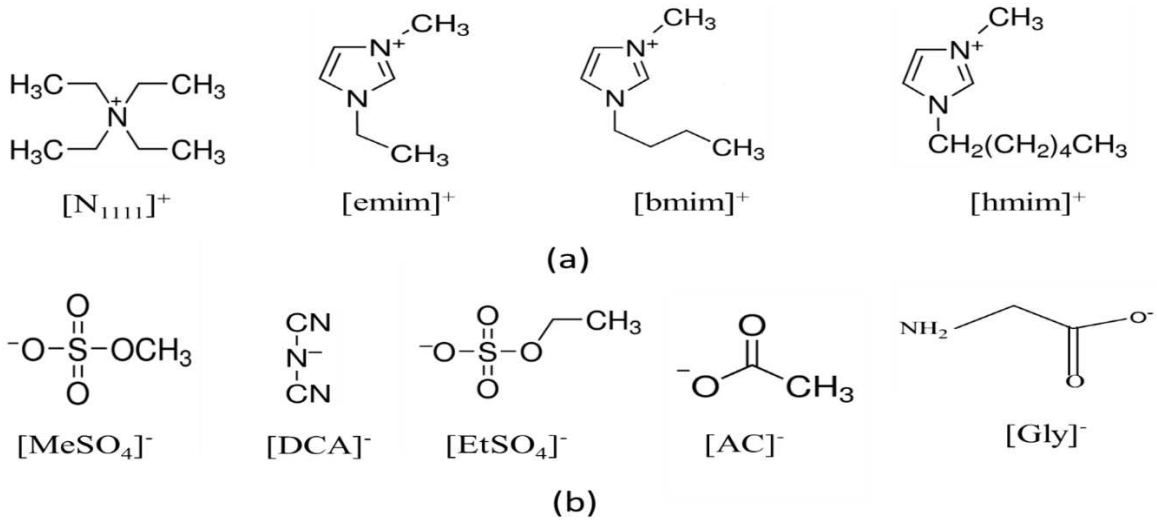

Figure 1.1 Molecular structures of the (a) cations and (b) anions of the selected ionic liquids.

Two different sets of CO_2 absorption experiments were carried out experimentally: a single module absorption and a coupled absorption/desorption. The single module absorption setup only absorbs CO_2 in a closed loop until reaching pseudo-steady-state followed by a separate stripping and regeneration step. The coupled absorption/desorption setup allows to absorb CO_2 in a HFMC absorber followed by the desorption in a HFMC stripper within a single cycle of IL recirculation. This setup allows simultaneous absorption and desorption steps in a single cycle. Feed gas mixture and pure N_2 (sweep gas) were allowed to flow in an open loop counter-currently through the lumen side of the membrane absorber and membrane stripper, respectively. Mesoporous polypropylene membrane contactors were selected for the absorption. CO_2 solubility, mass transfer equilibrium and Henry's law constants were measured using the isochoric pressure drop principle. ILs and HFMC fibers were characterized through various techniques including contact angle measurement, surface tension measurement, scanning electron microscopy (SEM) before and after absorption and thermo gravimetric analysis (TGA).

Modeling and simulation are potential tools for easy scale up and reduction of optimization cost of an available design. 2-D model is an approach allowing calculating both axial and radial mass transfers. Moreover, if the model is correctly built and validated with experimental results it can be applicable to real or simulated absorption situations. The modeling also allows to evaluate the role of absorbent, membrane and hydrodynamics separately as it has been suggested in the review of Zhao et al., (2016). Many researchers have focused on modeling and simulation of CO_2 capture in HFMCs with conventional absorbents. However, there is a limited literature available on modeling and simulation of CO_2 absorption in HFMCs with ILs (Azari et al., 2016; Dai et al., 2016c). In the modeling part of this thesis, steady-state and pseudo-steady-state dynamic modeling approaches were implemented to replicate the experimental findings by simulations and to perform parametric and sensitivity analysis as well as process optimization. Isothermal modeling approach was considered for imidazolium based RTILs while for amino acid based TSILs non-isothermal modeling approach was implemented.

1.2 Problem statement

The thesis addresses the following problems.

- Development of carbon capture technologies is required to control the rapid growth of carbon level in the atmosphere
- Design and process improvements are needed in membrane contactor based post-combustion CO_2 capture operations for process intensification
- Until now, most of used absorbents for carbon capture are corrosive, volatile and degradation sensitive. Other environmentally friendly absorbents, such as ionic liquids, which can minimize the above-mentioned problems must be explored.
- There is a lack of reaction and absorption kinetics of CO_2 dissolution in ionic liquids for developing CO_2 absorption in membrane contactors.
- Most of the previous studies for post-combustion CO_2 capture in membrane contactors are based on lab scale.
- A very limited number of investigations are available in the existing literature developing a detailed modeling approach which can facilitate the scale-up process.
- There is a lack of complete parametric and sensitivity analysis as well as optimization studies.
- Non-isothermal modeling approach has been very rarely reported as most of the reported modeling studies are based on isothermal modeling, while the process is non-isothermal in case of reactive absorbents.

1.3 Research objectives

This work addressed the feasibility of post-combustion CO_2 capture by coupling RTILs and TSILs with HFMCs, through experimentation, modeling and simulation. In a broader perspective, for design and absorption process improvement and intensification of the coupled (HFMC and IL) membrane gas absorption setup was experimentally studied and replicated by developing a dynamic mathematical model and simulations. In order to achieve the above-mentioned targets, the following objectives were accomplished during this work:

- Investigation of solubility, gas/liquid equilibrium, reaction and absorption kinetics of CO_2 in selected RTILs and TSILs.

- Study of the feasibility of coupling ILs with HFMCs for post-combustion CO_2 capture
- Development of single module and dual module coupled absorption/desorption membrane gas separation units.
- Comparative analysis and identification of more environmentally friendly, cost effective and energy efficient absorbents for CO_2 capture
- Development of robust and rigorous dynamic modeling approaches for isothermal and non-isothermal CO_2 absorptions in HFMCs with ILs.
- Utilization of developed models for investigations which are not possible and/or not feasible through experimentations such as optimization of the process, parametric analysis, sensitivity analysis and analysis of the level of membrane wetting.
- Replication of the experimental post-combustion CO_2 capture data through developed models and simulations for further intensification, improvements and possible scale-up

1.4 Thesis outline

The thesis presented here is based on the feasibility of post-combustion CO_2 capture by coupling RTILs and TSILs with HFMCs, through experimentation, modeling and simulation. It is structured in 7 chapters, as follows;

Chapter 1 presents the overall background, problems and objectives of the work.

Chapter 2 presents the general context of the work. Carbon dioxide emissions and its global and environmental impacts are described. Details about carbon capture methods, technologies and storages are also presented. HFMCs, their advantages and disadvantages for gas/liquid separation and implementation for post-combustion carbon capture are presented in detail. Selection of proper liquid absorbents for carbon dioxide capture is described. Particular emphasis is given to ILs and their ability to capture carbon dioxide.

Chapter 3 presents details about materials and methods. ILs and HFMC selection, properties and characterization techniques are presented. Experimental approach implemented for

equilibrium, carbon dioxide solubility measurements and carbon dioxide absorption/desorption in HFMCs coupled with ILs are described in detail.

Chapter 4 presents the theoretical approach and development of models for the HFMC based post-combustion carbon dioxide capture. All equations used to describe the different phenomena are presented in detail here: equations and empirical correlations for mass transfer kinetics, equations for mass and momentum transport of isothermal model and for mass, momentum and energy transport of the non-isothermal model, equations for the prediction and calculation of solubility, phase equilibria and diffusion coefficients. Boundary conditions and numerical resolution of the models are also discussed.

Chapter 5 presents the experimental post-combustion carbon dioxide capture with single module absorption system and coupled absorption/desorption system. ILs and membrane properties and characterization are described first. Carbon dioxide capture performance of the single module absorption system is discussed in detail, based on results of carbon dioxide removal efficiencies, and measured mass transfer kinetics. Carbon dioxide removal efficiencies, carbon dioxide loadings of the ILs, mass transfer coefficients and enhancement factors are compared for the single module absorption system and coupled absorption/desorption system.

Chapter 6 presents simulations of the model developed under isothermal conditions. A comparison between simulations and experimental data is presented for the validation of the model. Simulations of the axial and radial concentration distribution of carbon dioxide, effect of operational conditions and parametric analysis are presented in detail. Results are described for both pseudo-steady-state and steady-state modes. A detailed analysis of partial and full wetting of the membrane pores is also presented.

Chapter 7 presents simulations of the model developed under non-isothermal conditions. A comparison between simulations and experimental data is presented for the validation of the model. Profiles of carbon dioxide concentration, IL concentration, temperature and reaction rate constant, along contactor length, are discussed in detail. Carbon dioxide capture

performance of different AAILs used in HFMCs are presented and compared. Variations in the boundary flux and reaction rate along contactor length are also presented.

Finally, the dissertation ends with the general conclusion of investigations and outlook for future work.

Chapter 2. Context; State of the Art

2.1 Carbon dioxide emissions, capture and storage

2.1.1 Carbon dioxide emissions; global and environmental concerns

Global warming and climate change are serious challenges for the world. United Nations Framework Convention on Climate Change (UNFCCC) has determined the objective for the stabilization of atmospheric concentration of greenhouse gases to be at a level where the climate system will be safe from the dangerous anthropogenic interventions (Sands, 1992). Figure 2.1 below shows the contribution of different gases to the total global greenhouse gas emissions. CO_2 is the major contributor of greenhouse gas emissions which accounts for nearly three quarter of the total. The global mean annual atmospheric CO_2 concentration is shown in Figure 2.2.

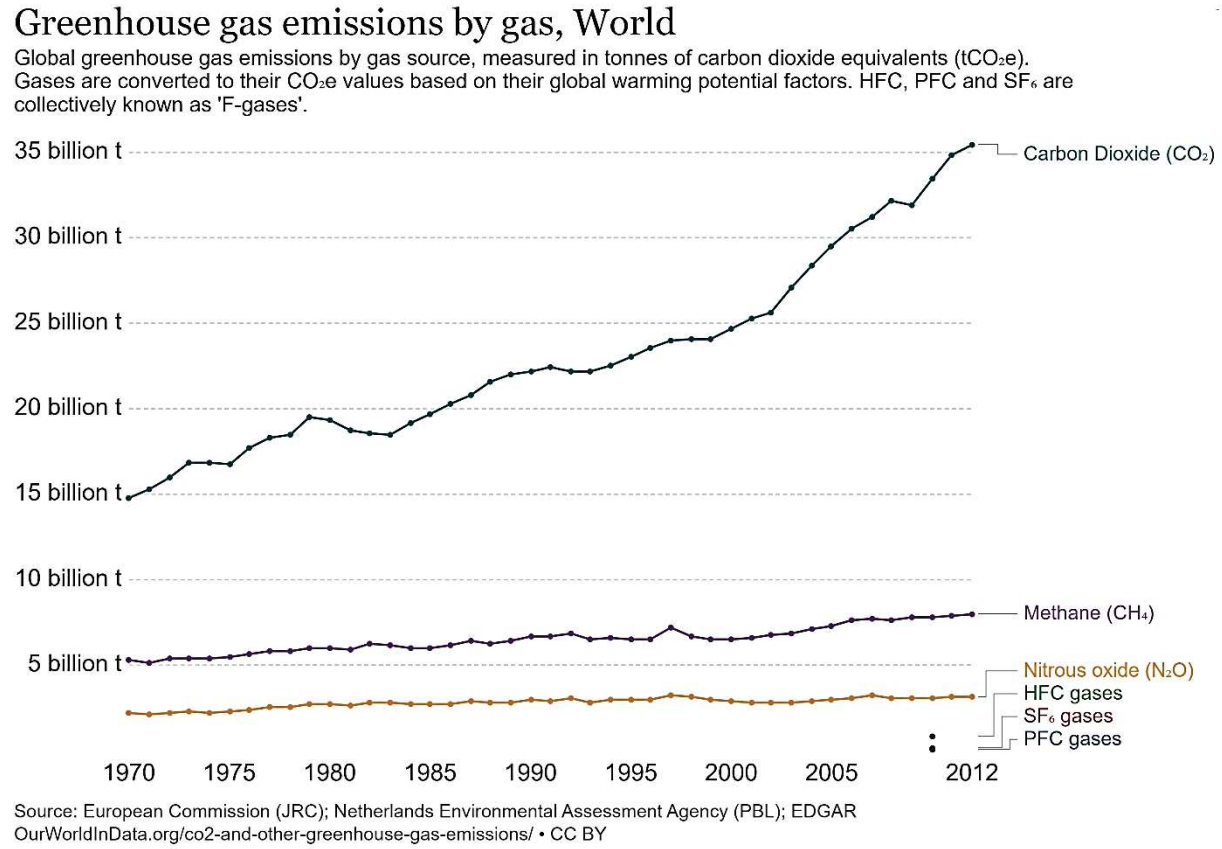

Figure 2.1 Contribution of gases to global greenhouse gas emissions, (Adapted from Ritchie and Roser, 2020).

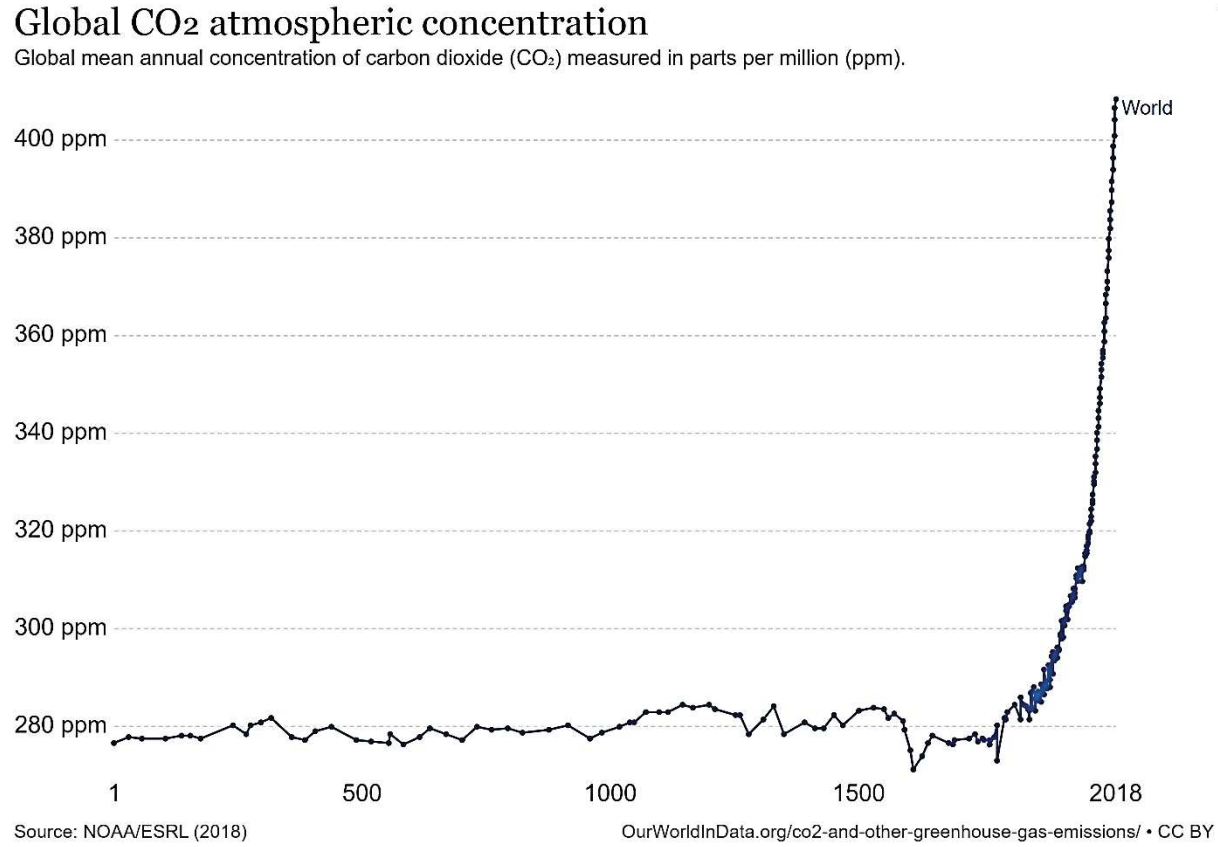

Figure 2.2 Global mean annual atmospheric CO_2 concentration (Adapted from Ritchie and Roser, 2020)

Since pre-industrial times, anthropogenic emissions of greenhouse gases have increased global temperature by 1°C (Ma, 1998). Potential impacts of climate change include ecological changes, physical impacts and health impacts. Global climate change can cause extreme weather conditions such as flooding, storms, heat and cold waves, rise in the sea level, alteration in crop growth and disruption in water system (Intergovernmental Panel on Climate Change, 2014). To control this climate change, UN members in the Paris agreement have set an average limiting target of 2 °C above pre-industrial temperatures (Ritchie and Roser, 2020).

Power and energy sectors are major contributors of the CO_2 emissions as presented in Figure 2.3. Energy sector emissions include emissions from manufacturing and energy industries, construction, electricity and heat generation, oil and gas, power plants and public heat. Other sectors that contribute to the CO_2 emissions include transport, agriculture, land use and waste.

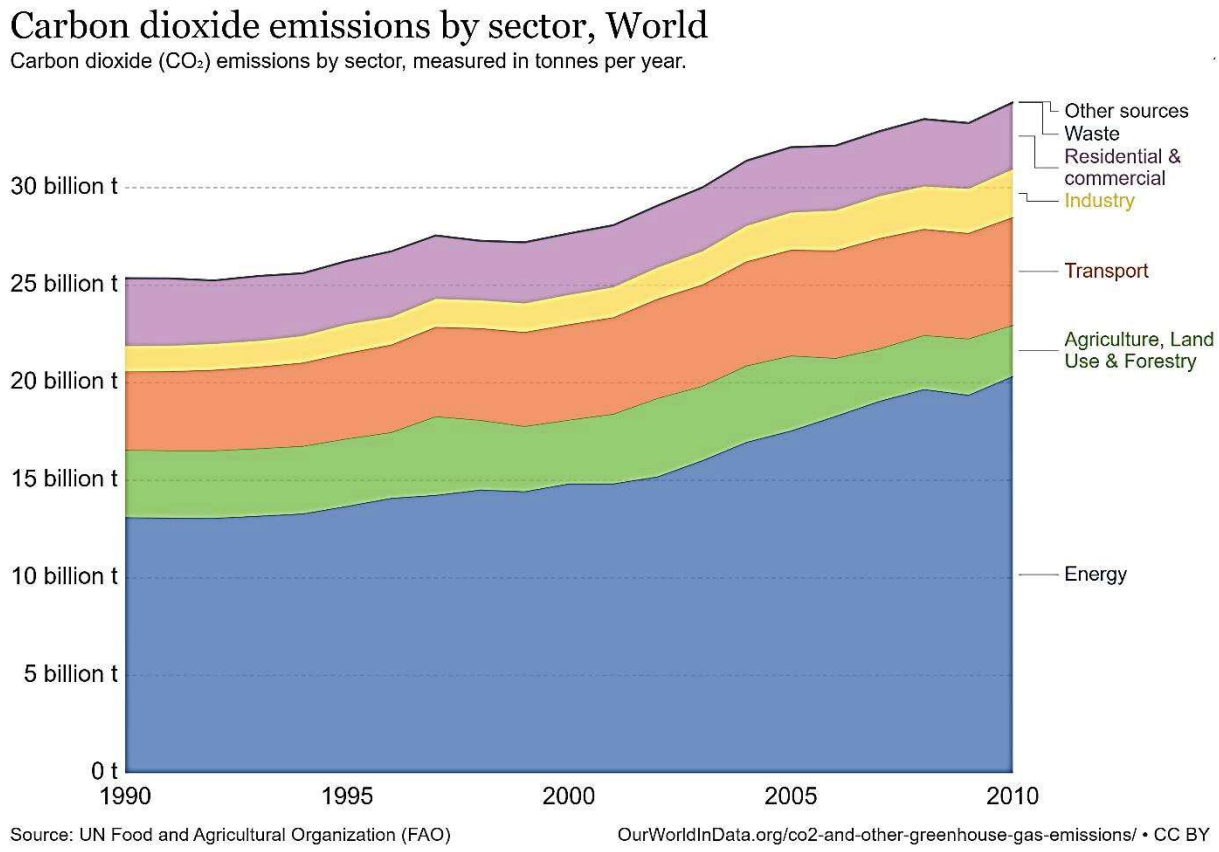

Figure 2.3 Various sectors contributing to global CO_2 emissions (Adapted from Ritchie and Roser, 2020)

According to the world energy outlook 2019, United Nations Sustainable Development Goals (SDGs) related to energy, can be achieved by following the Sustainable Development Scenario (SDS), including reduction in the impact of air pollution (SDG 3.9), universal energy access achievement (SDG 7) and control of climate change (SDG 13). The scenario is designed to meet the above-mentioned goals and the Paris agreement in a more realistic and cost-effective way. Fundamental changes are needed in the ways of energy production and consumption to achieve the Sustainable Development Scenario. Uptake of low-carbon technologies, namely energy efficiency, renewables, carbon capture, utilization and storage (CCUS) and nuclear must be significantly accelerated in all sectors of economy as presented in Figure 2.4. CCUS must be widely implemented in order to put the world on track and achieve the objectives of Paris agreement. For this purpose, an annual average of 1.5 Gt CO_2 must be captured between 2019 and 2050. By 2050, SDS divides the CCUS equally between power sector and industry. Major industries include cement, steel, oil and gas and refineries (International Energy Agency (IEA), 2019).

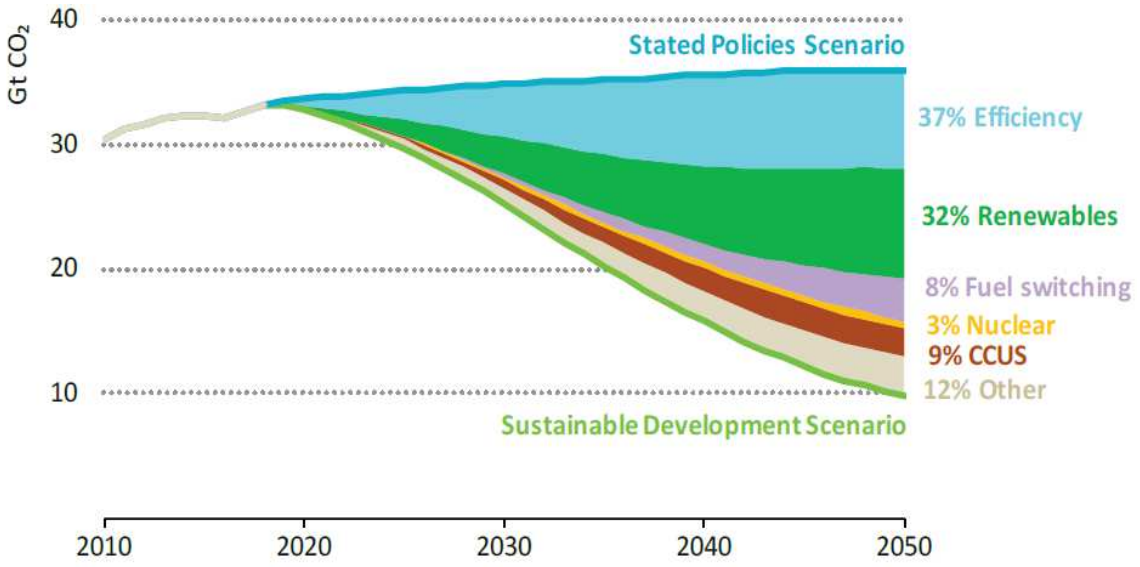

Figure 2.4 Reductions in the emissions of CO_2 by measure in the SDS relative to the Stated Policies Scenario (Adapted from International Energy Agency (IEA), 2020).

2.1.2 Carbon dioxide capture and storage

Carbon capture and storage (CCS) is considered as one of the viable options for mitigation of climate change and achieving the above-mentioned targets of Paris agreement and to initiate the decrease of global temperature of 2 °C in order to reach the level of pre-industrial era (International Energy Agency (IEA), 2013). In this process, CO_2 is captured and separated from concentrated industrial and power gaseous sources. The captured CO_2 is compressed and then transported to a final storage. In 2014, Canada introduced the first commercial scale CCS unit which was incorporated to a power plant. It has the capacity of 40 Mt/year CC and 120 MW. However, large scale implementation of CCS is still under development due to technical and economic barriers. A major economical barrier is the large capital investment for an unprofitable activity. Technical barriers include uncertain CO_2 leakage rates and limited geological storage capacity in some countries leading to increased transportation and injection costs (Khoo et al., 2011; Styring et al., 2011).

The CC technologies are generally classified as oxy-fuel conversion, pre-conversion and post-conversion (Dai et al., 2016b; Singh et al., 2011; UNIDO; IEA, 2011). These technologies are also named as oxy-fuel combustion, pre-combustion and post-combustion. All three technologies are explained in the preceding sections and presented in Figure 2.5 below.

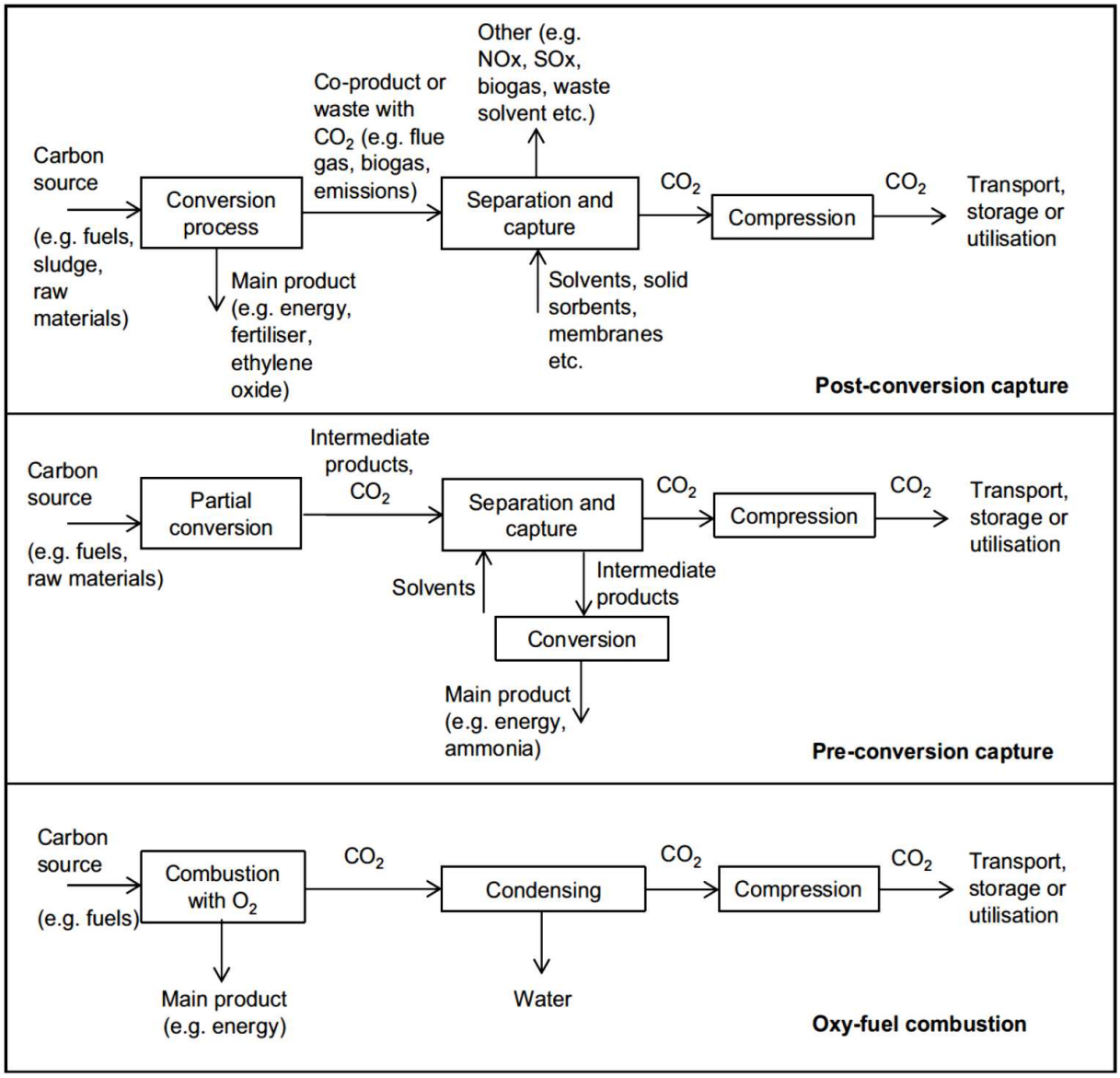

Figure 2.5 Carbon capture technologies (Adapted from Cuéllar-Franca and Azapagic, 2015)

2.1.2.1 Oxy-fuel conversion

Oxy-fuel conversion or oxy-fuel combustion is only applicable to processes involving combustion. These processes include fossil fuel plants power generation, iron/steel industries and cement industries. In oxy-fuel conversion fuel is burned in the presence of pure oxygen to produce high CO_2 concentrated flue gas which is free from nitrogen and nitrogen oxides like NO and NO_2. Major disadvantages of this technology include use of expensive oxygen and environmental impacts (Cuéllar-Franca and Azapagic, 2015).

2.1.2.2 Pre-conversion capture

In pre-conversion or pre-combustion capture CO_2 is captured after its generation as an undesired co-product during reaction of a conversion process. For example CO_2 is co-produced in the steam reforming step of ammonia production and must be removed (Farla et al., 1995; IPCC, 2005). Similarly, CO_2 must be separated from H_2 during an integrated gasification combined cycle (IGCC) of power plant. Usually physical solvents such as Rectisol® and Selexol® are used for such process (Odeh and Cockerill, 2008; Pehnt and Henkel, 2009; Singh et al., 2011). This technology is more energy efficient with physical solvents rather than chemical solvents for which the cost of regeneration is usually very high which makes the process unfeasible.

2.1.2.3 Post-conversion capture

In Post-conversion capture (PCC), CO_2 is captured from waste gas streams after the conversion of carbon source to CO_2. For example CO_2 capture after the combustion of fossil fuels or after the digestion of sludge from wastewater (Aresta, 2003; IPCC, 2005). Table 2.1 presented below shows different techniques of post-conversion capture including chemical and physical absorption by solvents, adsorption by solid sorbents, membrane separations, cryogenic separations and pressure/vacuum swing adsorption.

Table 2.1 Post-conversion capture and applications (Cuéllar-Franca and Azapagic, 2015; Krishnamurthy et al., 2014; Kuramochi et al., 2012; Maring and Webley, 2013; Markewitz et al., 2012; Sung and Suh, 2014)

Technology	Method	Applications
Absorption; chemical absorbents	Amine-based absorbents, e.g. monoethanolamine (MEA), diethanolamine (DEA), and hindered amine (KS-1), Alkaline absorbents, e.g. NaOH and $Ca(OH)_2$, Ionic Liquids	Power plants, iron and steel industry, cement industry, oil refineries
Adsorption; solid sorbents	Amine-based solid sorbents, Alkali earth metal based solid sorbents, e.g. $CaCO_3$, Alkali metal carbonate solid sorbents, e.g. Na_2CO_3 and K_2CO_3	No application reported
Membrane separation	Porous organic frameworks – polymers, Polymeric membranes, e.g. polymeric gas permeation membranes, Inorganic membranes, e.g. zeolites, Hybrid membranes	Power plants, natural gas sweetening

Cryogenic separation	Cryogenic separation	Power plants
Pressure/vacuum swing adsorption	Activated carbon, Zeolites	Power plants, iron and steel industry

Among all of these techniques, liquid absorbents based PCC is known as the most applied technology for CO_2 reduction due to its high efficiency of CO_2 separation from flue gas, which is usually higher than 80 % (Feron, 2010; Figueroa et al., 2008). In a typical PCC based on liquid absorbents (Figure 2.6), power plant flue gas is pretreated before entering into the absorption unit usually to remove undesirable particles, SO_x and NO_x (Neftel et al., 1985). CO_2 from the flue gas is absorbed in the absorption unit which forms a CO_2 rich absorbent. The CO_2 rich absorbent is preheated in a heat exchanger and then sent to desorption unit. CO_2 is thermally desorbed in the stripping unit (desorber) where the thermal energy is provided by the reboiler.

Major challenges to PCC include low pressure of flue gas, low concentration of CO_2 in the treated flue gas and size difference of the gas molecules in the gas mixture (D'Alessandro et al., 2010).

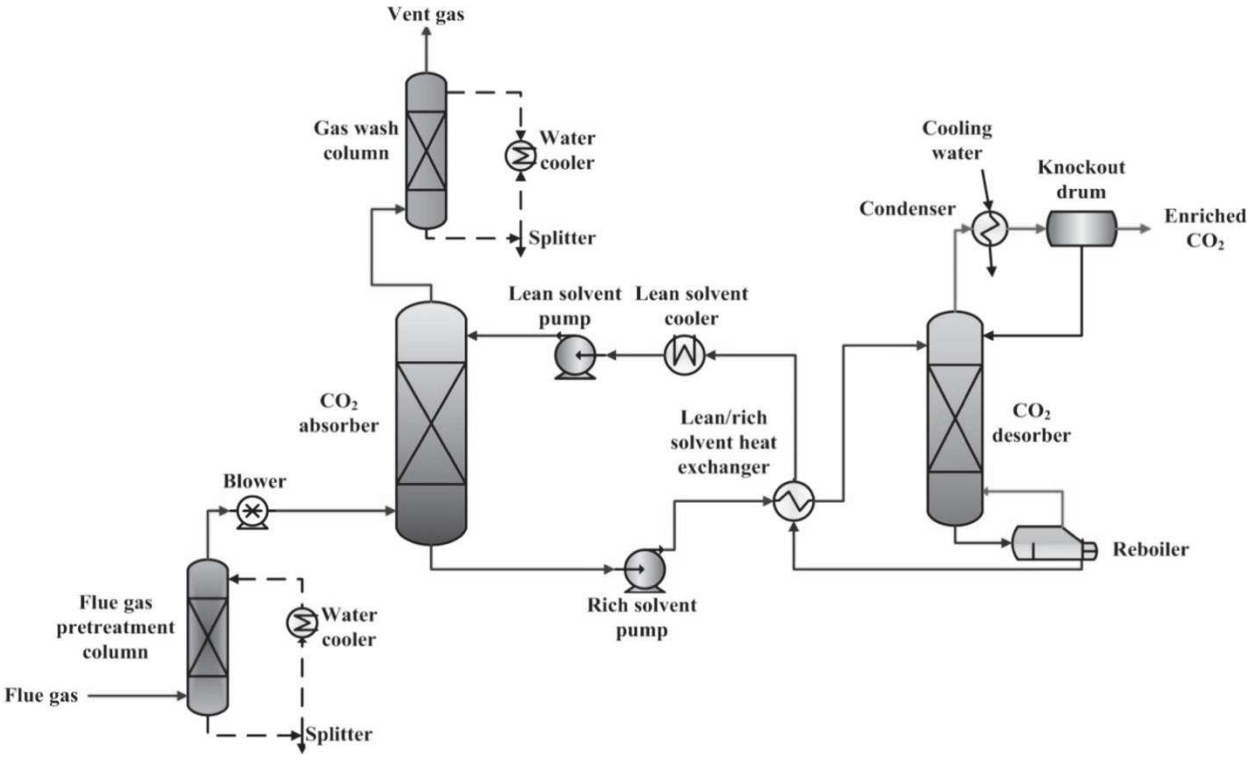

Figure 2.6 Typical process of liquid absorbent based PCC (Adapted from Zhao et al., 2016)

Currently used industrial gas/liquid contactors for CO_2 absorption can be divided in two categories (Perry, 2007):

- Stage-wise gas–liquid contactors: In this type of contactor gas/liquid equilibrium is almost achieved with each stage of the contactor for example in plate columns and rotating disc contactors.
- Differential gas–liquid contactors: In this type of contactor, mass transfer happens with in the entire contactor without reaching gas/liquid equilibrium at any point of the contactor for example in spray towers, bubble columns and packed columns.

Gas/liquid interfacial area and liquid hold up are the most important parameters for a contactor. Usually high interfacial area and low liquid holdup are optimal for gas/liquid mass transfer in contactors. The above-mentioned absorbers face some crucial problems including high energy consumption, flooding, foaming, solvent loss due to degradation and entrainments, equipment corrosion and large footprint. During the last decade, HFMC technology is being studied as an alternative to overcome these problems (Dindore et al., 2005; Gabelman and Hwang, 1999).

2.2 Hollow fiber membrane contactors

At industrial level, tower columns and mixed settlers are currently used for liquid/liquid and gas /liquid mass transfer contacting processes. For optimal operations of such extraction processes an improved interfacial area is mandatory in order to boost the mass transfer. To achieve this in packed columns selection of proper packing material and uniform distribution of fluids are necessary. Although these traditional liquid/liquid and gas/liquid extractors have been used for decades, a major disadvantage is the dispersion of the two contacting fluids. This dispersion can cause problems such as flooding, foaming, unloading and emulsions. HFMCs are non-dispersive contacting systems in which the membrane does not provide selectivity by itself and rather works as a barrier between the fluids and increases the mass transfer area. HFMCs can alternatively be used to overcome the disadvantages of traditional extractors described above with the advantage of providing better controlled and higher interfacial area. Just like other traditional contacting systems, diffusional mass transfer in HFMCs occurs at the fluids interface (Gabelman and Hwang, 1999). Usually the membrane

in HFMCs works as a porous barrier and does not provide selectivity, unlike in other membrane separations. For most of the membrane operations the driving force is a pressure gradient however the driving force for separation in HFMCs is a concentration gradient (Kiani et al., 1984; Qi and Cussler, 1985a; Seibert et al., 1993).

2.2.1 Membrane module characteristics

A HFMC consists of two main parts, fibers and shell. A bundle containing a known number of fibers is geometrically arranged inside the shell. A typical HFMC from Liqui-Cel^{TM} is presented in Figure 2.7 below. A sealing ring is used to support these bundles. One of the two contacting fluids passes through the lumen side (inside the fibers) while the other one flows through the shell side around the fibers. The shape of a HFMC is analogous to the shell and tube heat exchanger. The flow configurations can be oriented in different directions for example co-current and counter-current in parallel flow HFMCs and cross flow in cross flow HFMCs. A laboratory scale HFMCs contains a small number of fibers (10s to 100s) which can stand by itself, however an industrial scale HFMC consists of thousands of fibers for which a grid is installed during sealing to support the structure (Chabanon et al., 2015).

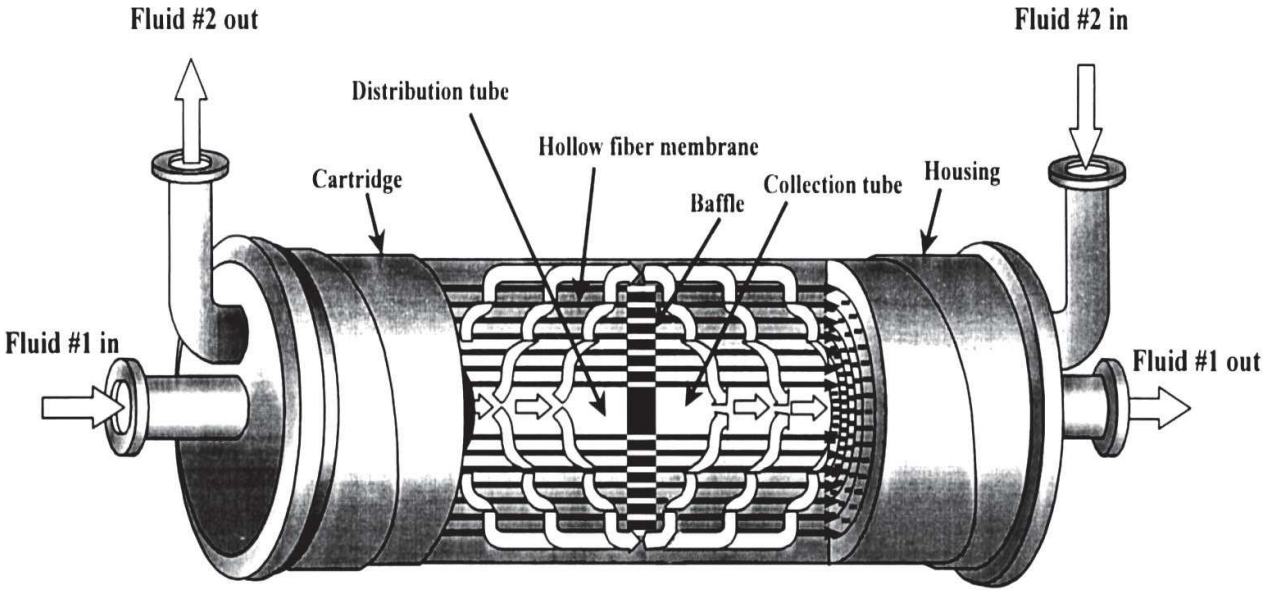

Figure 2.7 Hollow fiber membrane contactor module (Adapted from Gabelman and Hwang, 1999).

2.2.2 Advantages and disadvantages

Main advantages of the HFMCs over other traditional extractors are presented below (Gabelman and Hwang, 1999; Zhao et al., 2016):

- Very high, known and constant interfacial area which makes the performance prediction very easy. Also, the intensification potential is very high due to high per unit volume interfacial area.
- Independent flowrates of the contacting fluids. This property is very useful in providing contact surface area in high and low flowrates.
- Absence of flooding, foaming and entrainment.
- Due to non-dispersive nature there is no emulsion formation.
- Modularity which provides very high predictability and straightforward scale up. A predictable increase in capacity can be easily achieved by linear scaling.

However, HFMCs present also some drawbacks (Gabelman and Hwang, 1999; Zhao et al., 2016):

- The mass transfer through the membrane porosity produces an extra mass transfer resistance.
- Membrane fouling and then a dramatic decrease of mass transfer can occur in some cases involving solids in suspension.
- Finite life of the membranes

2.2.3 Post-combustion carbon capture with hollow fiber membrane contactors

HFMCs have been extensively studied for CO_2 absorption in the past. Qi and Cussler, (1985a) and (1985b) were the first to use HFMCs for CO_2 capture. HFMCs can capture CO_2 as well as other gases including H_2S, SO_2 and volatile organic compounds. Some of the published works on experimental and modeling of post-combustion CO_2 capture are presented in the Table 2.2 below.

Table 2.2 Experimental and modeling post-combustion capture investigations in HFMCs

Membrane material	CO_2 concentration	Absorbent [Molarity]	Mode of study	Main remarks	Ref

PP, PTFE	6.9-14 % CO_2/Air	MEA, AMP [1-3M]	Experimental	Operation of counter-current flow configuration was 20 % more efficient that co-current. PTFE membrane retained the initial performance, while a decline in performance was observed for PP membrane.	(de Montigny et al., 2006)
PP, PTFE	15 % CO_2/N_2	MEA [5M]	Experimental	A drop of 18 % in the mass transfer rate for PTFE membrane after exposure of 25 days to MEA. Although PTFE fibers are expensive, they showed a high resistance toward wetting.	(Chabanon et al., 2011)
PP	14 % $CO_2/N_2/O_2$	MEA [1M]	Experimental	Fresh and/or non-wetted HFMC was able to show higher performance than that of chemical absorption system	(Yan et al., 2008)
PP, PVDF	1-15 % CO_2/N_2	PZ, MDEA, AMP [1 M]	Experimental	Gas flowrate and absorbents concentration positively affected the absorption flux. Wetting ratio of the PP membranes decreased with plasma treatment	(Lin et al., 2009)
PP	[NA] CO_2/N_2	[bmim][BF_4], [apmim][BF_4] [1-5 M]	Experimental	The absorption process was favored by low water content of [apmim][BF_4] and high-water content of [bmim][BF_4]. Performance and CO_2 loading capacity of [apmim][BF_4] was very high compared to [bmim][BF_4]. Regeneration was very easy for [bmim][BF_4].	(Lu et al., 2014)
PVDF	[NA] CO_2/N_2	PZ, AMP [1 M]	Modeling	An increase in gas flowrate, liquid flowrate and absorbent concentration favored the CO_2 absorption process. The model well replicated the experimental data.	(Razavi et al., 2013)
PTFE	15 % CO_2/N_2	MEA [3 M]	Modeling	CO_2 concentration was predicted with high accuracy using Wilson plot method. An acceptable membrane wetting ratio of 40 % was reported.	(Khaisri et al., 2010)
PP	15 % CO_2/N_2	NH_3 [NA]	Modeling	Corresponding NH_3 slip was reduced to 4.3 %. Although dense layer over membranes reduced the NH_3 slip, however it also reduces the CO_2 absorption capacity.	(Villeneuve et al., 2018)

2.3 Liquid absorbents for CO_2 capture

Many of the absorbents suitable for conventional absorption process can in principle be also appropriate for membrane contactor operations. However, considering the physical and chemical properties of absorbents, the suitability can vary accordingly. An ideal absorbent for CO_2 absorption should have the following properties (Dindore et al., 2004; Kohl and Nielsen, 1997; Zhao et al., 2016).

- High absorption capacity/CO_2 loading of the absorbent
- Fast absorption and reaction rate
- Low heat of dissolution or heat of reaction
- Long term compatibility with the membrane material
- High surface tension and low viscosity
- Chemical, oxidative and thermal stability
- Low vapor pressure or volatility
- Easy and cost-effective regeneration
- Commercial availability at low cost

Absorbents with high CO_2 absorption capacity can effectively reduce the operational cost by reducing the volume of absorbent and required surface area. High reactivity and high absorption rate of absorbent can result in the reduction of the mass transfer resistance of the membrane. Thermal stability is fundamental for operations at high temperature to avoid thermal degradation of the absorbent. Absorbents with low vapor pressure or volatility can minimize the solvent loss and are very effective for heat and vacuum regeneration operations. Liquid absorbents should be long term compatible with the membrane material to avoid physical and chemical damage to the membrane material. On one hand, an interaction can result on the modification of membrane wetting and then a dramatic decrease of mass transfer. On the other hand, in case of swelling of the membrane or chemical structural damages the membrane morphology can be modified and then will affect the absorption process. High surface tension is a very important property of an absorbent, especially for porous membranes. This will provide a high liquid entry pressure and will avoid membrane pores wetting. Low viscous absorbents can induce a thin boundary layer resulting in a low mass transfer resistance and in a low pressure drop across the membrane length. None of the absorbents can completely satisfy the above-mentioned requirements, yet they have been used and studied based on their properties and applications.

Various absorbents have been studied and proposed for post-combustion CO_2 absorption process. Amines are the most widely used absorbents until now, due to their high reactivity and absorption capacity for CO_2. Commonly used amines for post-combustion CO_2 capture in HFMCs include mono-ethanolamine (MEA), methyl-diethanolamine (MDEA) and 2-amino-2-methyl-1-propanol (AMP) (Kothandaraman, 2010; Riemer and Ormerod, 1995). However, amine-based operations are facing several drawbacks including high corrosion rate of equipments, high volatility, large amount of solvent loss, degradation of amines due to the presence of other unwanted gases in the flue gas mixture and very high energy consumption during absorbent regeneration (Yu et al., 2012). Moreover, during long-term runs amines interact with membrane materials resulting on wetting and/or swelling (Ahmad et al., 2019; Lv et al., 2010; Mosadegh-Sedghi et al., 2014, 2012). Extensive studies have been performed previously to find an alternative replacement for amines having low volatility and low vapor pressure, better thermal stability, low regeneration cost and low corrosion rate. A new class of absorbents namely ionic liquids(ILs) have been proposed as a potential replacement to overcome the above-mentioned drawbacks (Anthony et al., 2002a; Kothandaraman, 2010; Riemer and Ormerod, 1995; Rochelle, 2009).

2.3.1 Ionic liquids for CO_2 capture

An IL is a salt, which consists exclusively of organic cations and inorganic or organic anions, with a melting point lower than 100 ^oC (Ramdin et al., 2012). Low volatility, negligible vapor pressure, thermal stability, high CO_2 solubility, less toxicity and low corrosion rates are the main features of ILs (Dai and Deng, 2016; Ghandi, 2014; Papatryfon et al., 2014; Yan et al., 2019). Generalized properties of ILs are presented in Table 2.3 below.

Table 2.3 Properties of ionic liquids (Adapted from Aghaie et al., 2018; Johnson, 2007).

Property	Value
Salt ions	Large cations and anions
Melting point	< 100 °C
Boiling point	> 200 °C
Thermal stability	High
Viscosity	< 100 cP, workable
Dielectric constant	< 30
Polarity	Moderate

Specific conductivity	< 10 mS/cm, good
Vapor pressure	Negligible
Solvency	Strong
Catalytical character	Excellent (for organic reactions)

ILs have been divided into two categories, room temperature ILs and task specific ILs or functionalized ILs. RTILs are conventional ILs that provide typical physical solvent behavior for the gas solubility following Henry's Law. Most of the RTILs have very high CO_2 solubility compared to other gases such as N_2, O_2, H_2 and CH_4 (Dai et al., 2016b; Lei et al., 2014). TSILs provide very high CO_2 solubility which can reach up to three times of the corresponding alkyl chain RTILs. These ILs can absorb CO_2 by both chemical and physical sorption, for which the CO_2 loading increases with an increase in pressure. However, TSILs can absorb CO_2 at low partial pressures due to chemical reaction (Shiflett and Yokozeki, 2009). Some of the TSILs developed for CO_2 capture include protic ILs (Wang et al., 2010), amino acid-based ILs (Ohno and Fukumoto, 2007) and amine-based ILs (Ren et al., 2012; Wang et al., 2012). Some commonly used anions and cations of ILs are presented in Figure 2.8 below.

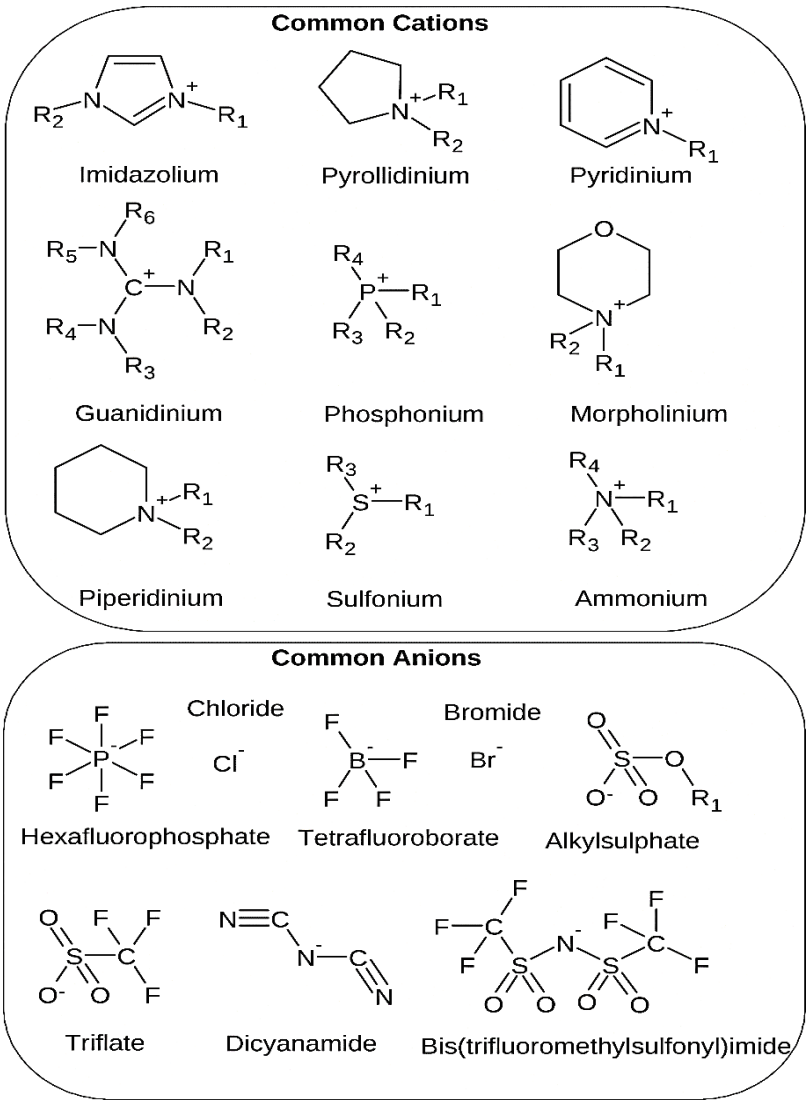

Figure 2.8 Different cations and anions commonly used in ionic liquids (Adapted from Ramdin et al., 2012).

Recently many researchers have considered the combination of ILs with membrane contactors for CO_2 Capture. Luis et al. (2009) and Albo et al. (2010) used IL 1-ethyl-3-methylimidazolium ethylsulfate in a cross-flow membrane contactor to develop a zero solvent emission process concept. Gómez-Coma et al. (2014) and Albo and Irabien, (2012) used the same IL for non-dispersive absorption of CO_2 in parallel and cross flow membrane contactors. In their studies, the effect of different process parameters, overall mass transfer coefficients and first order rate constant were systematically evaluated. Gómez-Coma et al. (2017) also studied the effect of addition of water to IL 1-ethyl-3-methylimidazolium acetate on CO_2 capture efficiency in polyvinylidene fluoride (PVDF) membrane contactor. An optimum IL-water mixture of 70-30 % was recommended for 5 times higher overall mass

transfer coefficient than that of pure IL. Lu et al. (2014) developed a membrane absorption and desorption unit based on the ILs 1-butyl-3-methyl-imidazolium tetrafluoroborate ([bmim][BF_4]) (as physical absorbent) and 1-(3-aminopropyl)-3-methyl-imidazolium tetrafluoroborate ([apmim][BF_4]) (as chemical absorbent). Aqueous [apmim][BF_4] was able to give high CO_2 loading capacity even at atmospheric pressure. Aqueous [bmim][BF_4] was very easily regenerated at low cost compared to aqueous ([apmim][BF_4]. The author also investigated the membrane contactor absorption/desorption system for aqueous mixtures of ILs [bmim][BF_4] and [apmim][BF_4] with alkanolamine of 2-amino-2-methyl-1-propanol (AMP) (Lu et al., 2015). Results showed an enhanced transmembrane flux and loading capacity for ILs and AMP mixtures.

2.3.2 CO_2 solubility in ionic liquids

Both anion and cation have effects on the CO_2 solubility, however anion is believed to have higher impact on the solubility than cation. This phenomenon has been verified by various experimental findings and simulations (Aki et al., 2004; Anthony et al., 2005; Cadena et al., 2004). The solubility can not only be explained by CO_2-anion interactions. Other works have claimed a considerable role of free volume mechanism on the CO_2 solubility. In a free volume mechanism, the liquid absorbent captures the CO_2 molecule in the available free spaces, while the volume of liquid does not change even after absorbing large amount of CO_2 (Aki et al., 2004; Blanchard et al., 2001; Cadena et al., 2004; Kazarian et al., 2000). An experimental study (Figure 2.9 a) was conducted to investigate the effect of anion on the CO_2 solubility considering [bmim] cation at 333 K temperature. CO_2 solubilities were increased in the order of [NO_3] < [SCN] < [$MeSO_4$] < [BF_4] < [DCA] < [PF_6] < [Tf_2N] < [Methide] < [$C_7F_{15}CO_2$]. ILs which contain fluor groups have been reported to have higher solubilities than the one without fluor groups. Studies were conducted (Figure 2.9b) to observe the effects of anion fluorination with [bmim] cation at 333 K temperature. The solubilities were increased in the order of [BF_4] < [TfO] < [TfA] < [PF_6] < [Tf_2N] < [methide] < [$C_7F_{15}CO_2$] < [eFAP] < [bFAP]. Although the cation is believed to have a small effect on the solubility, yet it might be considered as it is known to have a secondary role in solubility. To observe the effect of cation different cations including imidazolium, pyridinium, pyrrolidinium, cholinium, ammonium, and phosphonium were considered with [Tf_2N] anion (Figure 2.9 c). Fluorination of the cation showed considerable effect on the solubility; however, it has been

observed to have less significant effect compared to anion. An increase in the alkyl chain length of the cation can also increase the solubility. For this purpose, different alkyl chain lengths of imidazolium cations were paired with [Tf_2N] anion (Figure 2.9 d). The results clearly verified the phenomena as the order of increase in solubility was [omim] > [hmim] > [pmim] > [bmim] > [emim].

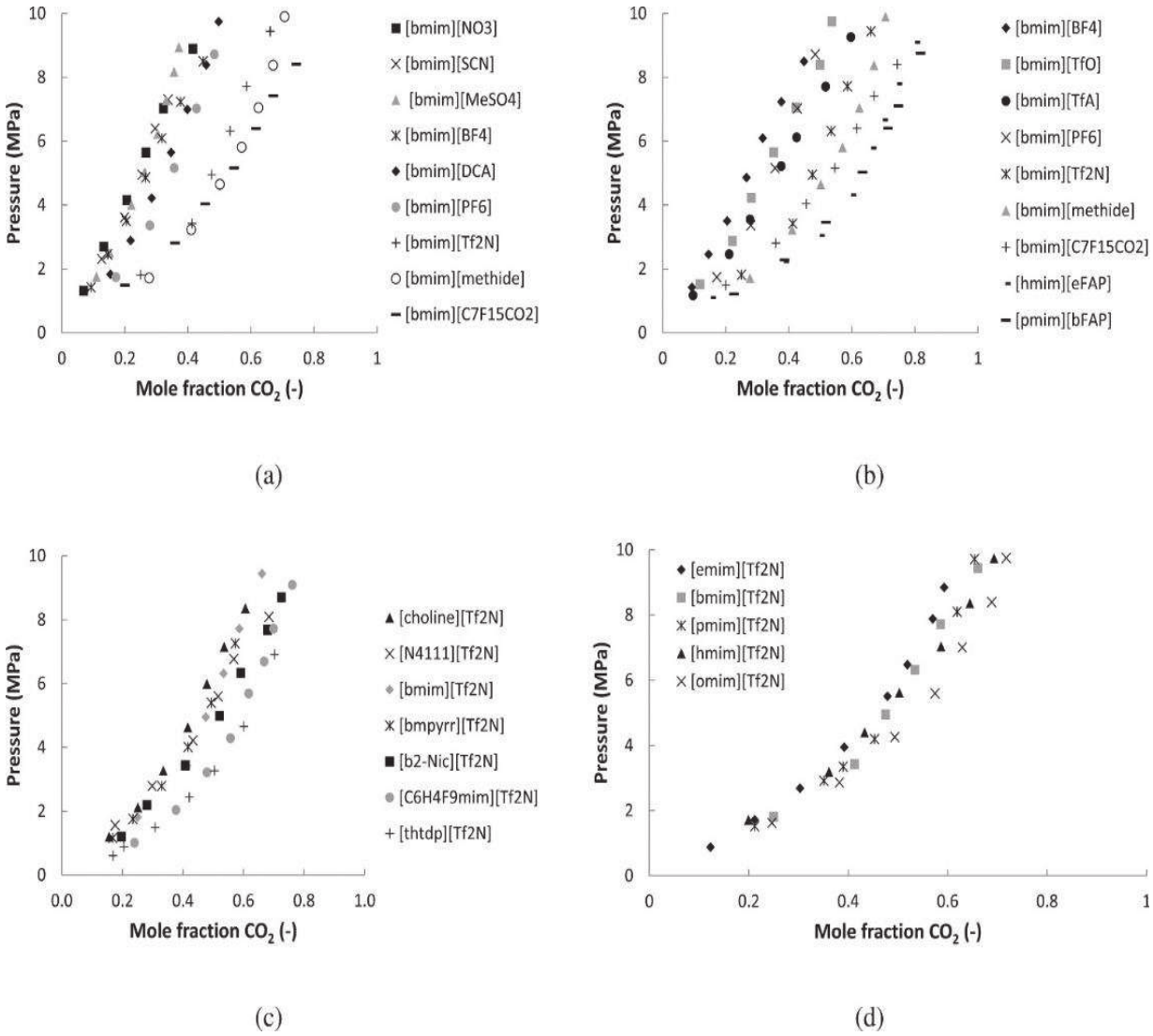

Figure 2.9 (a) Effect of IL anion on the solubility of CO_2, (b) Effect of fluorination of IL anion on the solubility of CO_2, (c) Effect of IL cation on the solubility of CO_2, (d) Effect of cation alkyl chain length on the solubility of CO_2; (Adapted from Ramdin et al., 2012)

Chapter 3. Experimental

The experimental part of this work was carried out in collaboration between the Institut Européen des Membranes (IEM), in Montpellier, France and the Department of Chemical and Biomolecular Engineering Universidad de Cantabria (UC), in Santander, Spain. ILs and membranes characterization and CO_2 solubility experiments were carried out at IEM, whereas CO_2 absorption and desorption experiments in a HFMC in a pilot unit were carried out at UC.

3.1 Ionic liquids and other materials selection

Four different imidazolium based RTILs, 1-ethyl-3-methylimidazolium methyl sulfate ([emim][$MeSO_4$]), 1-ethyl-3-methylimidazolium dicyanamide ([emim][DCA]), 1-ethyl-3-methylimidazolium ethyl sulfate ([emim][$EtSO_4$]) and 1-ethyl-3-methylimidazolium acetate ([emim][Ac]) were selected for CO_2 absorption and desorption experiments. To our knowledge it is the first time that ILs [emim][$MeSO_4$] and [emim][DCA] have been tested for CO_2 absorption in a membrane contactor. ILs [emim][$MeSO_4$] (Mejía et al., 2013; Santos and Baldelli, 2009; Yim et al., 2018), [emim][DCA] (Almeida et al., 2012; Huang and Peng, 2017; Quijada-Maldonado et al., 2012), [emim][$EtSO_4$] (Carvalho et al., 2014; Fröba et al., 2008; Jalili et al., 2010; Quijada-Maldonado et al., 2012; Soriano et al., 2009) and [emim][Ac] (Almeida et al., 2012; Quijada-Maldonado et al., 2012; Yim et al., 2018; Yokozeki et al., 2008) have been reported as excellent absorbents with high solubility for CO_2 and moderate surface tensions which makes them very feasible to be used for CO_2 absorption operation with hydrophobic membranes.

Table 3.1 Ionic Liquids basic information.

S.No	IL	Molecular Formula	M.W. (g.mol^{-1})	Purity[a]	Supplier
1	[emim][$MeSO_4$]	$C_7H_{14}N_2O_4S$	222.26	> 95 %	Sigma Aldrich

2	[emim][DCA]	$C_8H_{11}N_5$	177.21	> 95 %	Sigma Aldrich
3	[emim][$EtSO_4$]	$C_8H_{16}N_2O_4S$	236.29	> 95 %	Sigma Aldrich
4	[emim][Ac]	$C_8H_{14}N_2O_2$	170.21	> 95 %	Sigma Aldrich

[a]As received from supplier

To make CO_2/N_2 mixture for absorption experiments, carbon dioxide of 99.7 % ±0.01 vol% purity and nitrogen of 99.9 % ±0.001 vol% purity were purchased from Air Liquide, Spain.

3.2 Material characterization

3.2.1 Surface tension

Surface tension was measured with a Langmuir device (KSV NIMA Langmuir-Blodgett) using a Wilhelmy plate made of platinum partially immersed in the IL. The apparatus determines the surface pressure using the Wilhelmy plate method. Usually in this method the force (gravity, surface tension and buoyancy) on the suspended plate due to surface tension is measured while the plate is partially immersed in the subphase (Figure 3.1). Surface tension is measured from this force using plate dimensions. The relationship is given below.

$$\Pi = \Upsilon - \Upsilon_\circ \qquad (3.1)$$

Where Π is surface pressure, while Υ and $\Upsilon_\circ$ are surface tensions in the absence and presence of monolayer.

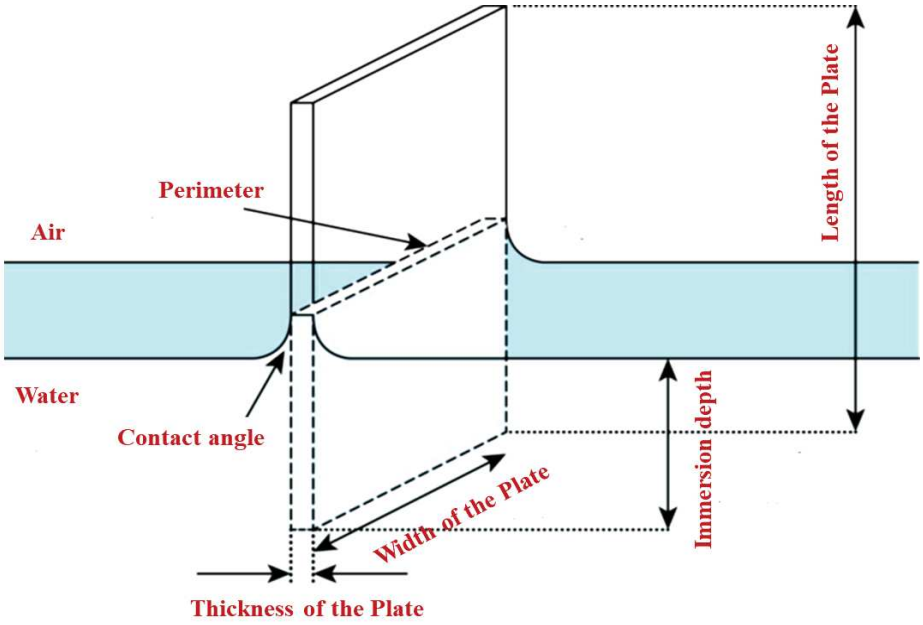

Figure 3.1 Partial immersion of Wilhelmy Plate (Adapted from Biolin Scientific, 2020).

3.2.2 Contact angle

The contact angle of the ILs on membrane surface was measured by a contact angle meter (DIGIDROP-Modular contact angle technology, GBX). The instrument can measure contact angle with ±0.1° of accuracy with maximum frame recording speed of 50/60 images/s. The associated software automatically controls the droplet volumes and its deposition on the surface. The software provides various polynomial and manual techniques to measure the average contact angle.

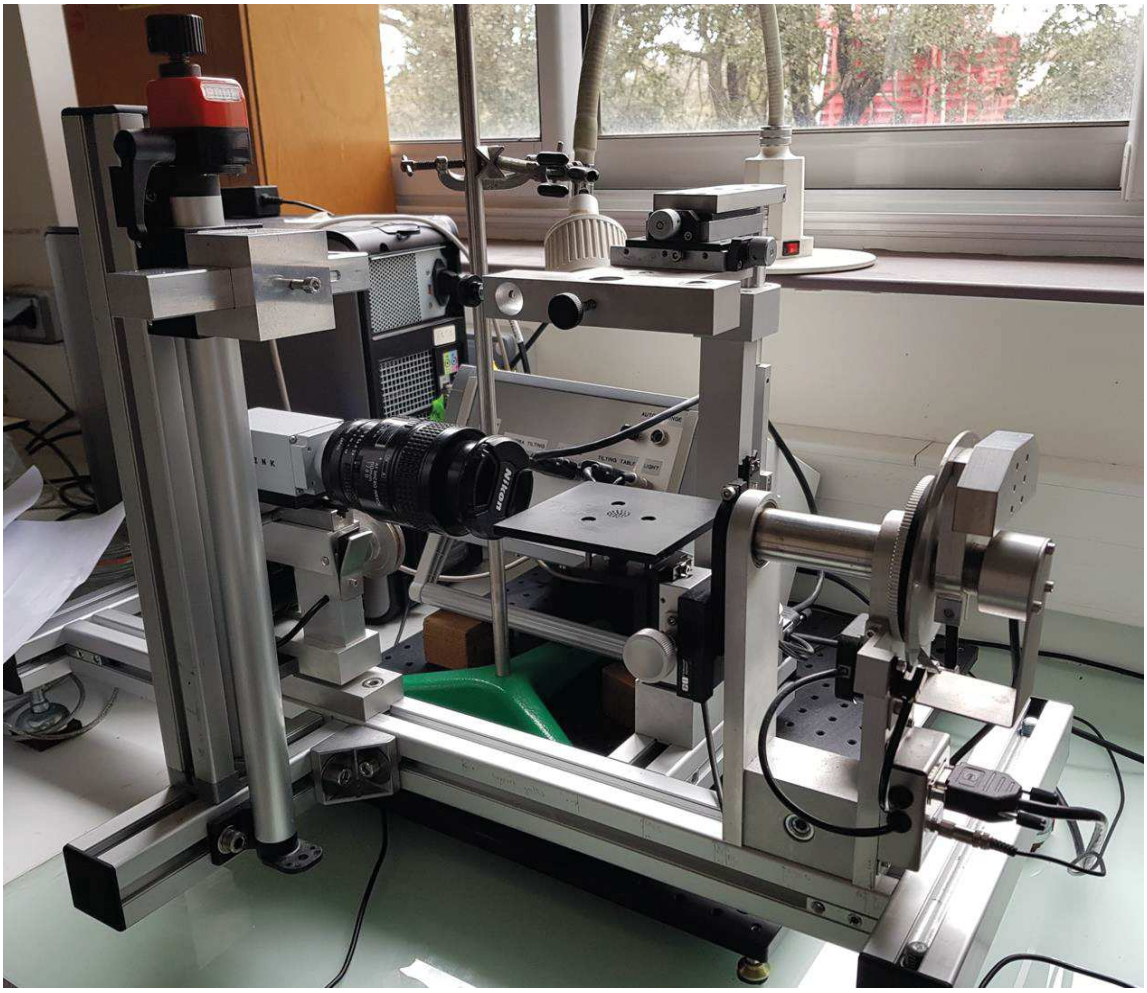

Figure 3.2 DIGIDROP Contact angle measuring instrument

3.2.3 Membrane Morphology

The possible morphological changes of hollow fibers surface and porous structure due to long term contact with ILs were investigated with scanning electron microscope (Hitachi S-4800 FE-SEM). Prior to SEM analysis, samples were sputter coated with platinum for 5 minutes to ensure better conductivity. Samples were observed at an acceleration voltage of 2kv.

3.2.4 Thermal stability

Thermal stability of the ILs used in the present study was analyzed by a thermogravimetric and differential thermal analyzer (Shimadzu, DTG-60). Samples of IL were analyzed with a heating rate of 5 $^{o}C.min^{-1}$ in the presence of N_2 flowing at 50 $ml.min^{-1}$.

3.3 Equilibrium CO_2 solubility measurements

Equilibrium solubility of CO_2 in the four different imidazolium based ILs, [emim][$MeSO_4$], [emim][DCA], [emim][$EtSO_4$] and [emim][Ac] was measured with the help of isochoric pressure drop principle using an IEM-built apparatus presented in Figure 3.3. Equilibrium solubility values of CO_2 were measured at different temperatures and pressures.

To maintain a controlled and constant temperature the apparatus was kept inside a temperature controlling chamber (Sartorius Certomat HK). The apparatus can record two readings at the same time. Top of each equilibrium cell is sealed with a copper gasket. Both equilibrium cells are connected to a secondary reservoir used for the gas injection. The primary reservoir is made of stainless steel and provides gas to each secondary reservoir. Pressure values of the equilibrium cells and primary reservoir are monitored by highly precise (0.01%) pressure sensors (PA33X). These pressure sensors are connected to a computer for automatic data collection.

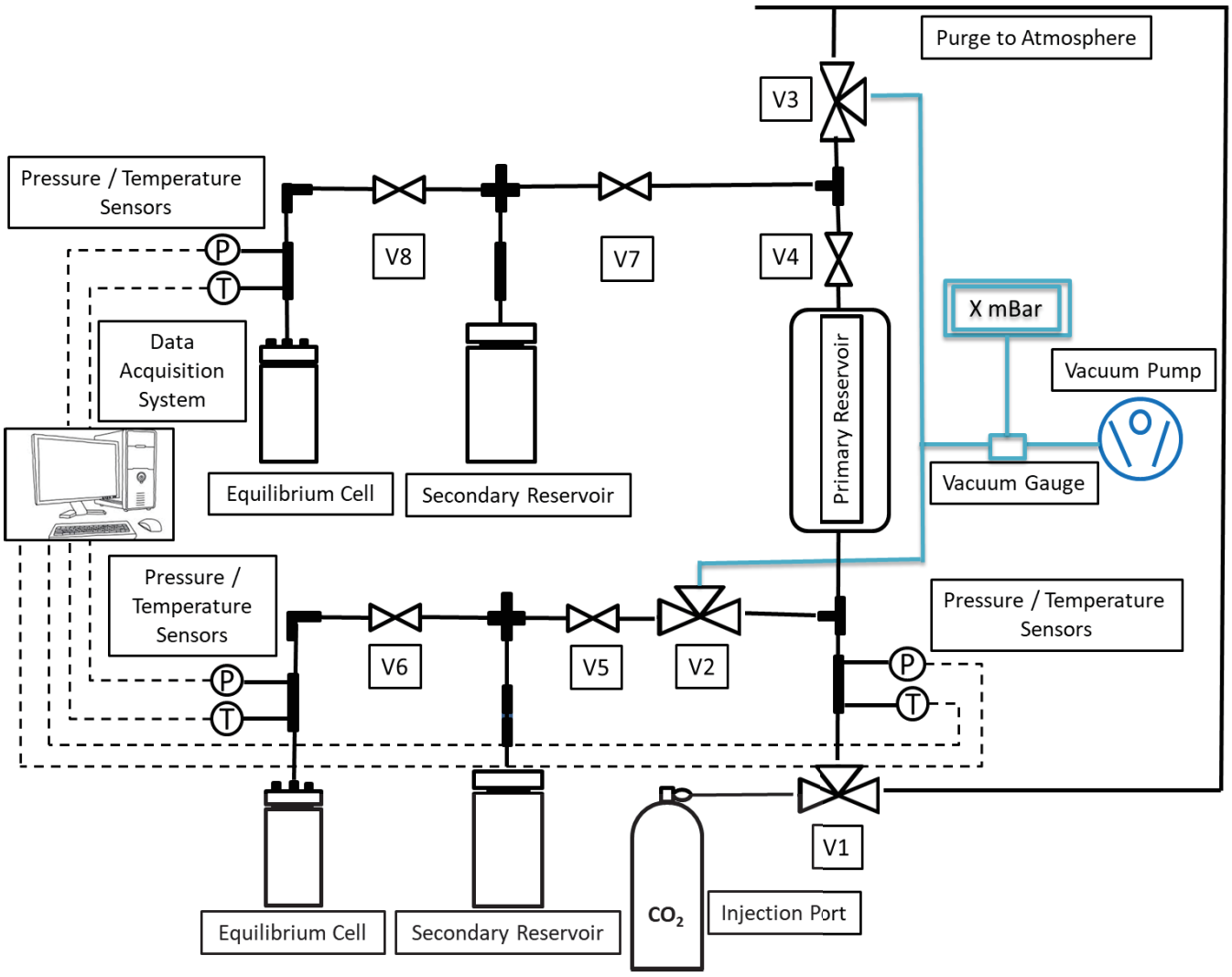

Figure 3.3 Schematic representation of the IEM-built gas solubility apparatus.

Prior to the experiments, the system was checked for the possible leakage by filling it with helium gas (He) and using Alcatel ASM series Leak detectors. Volume of each part of the system was measured using He gas while implementing ideal gas law. For equilibrium solubility measurement IL of known volume (5 ml) was added to the equilibrium cell and sealed using copper gasket. The system was then put on the degassing and/or desorption mode by applying a vacuum pressure of 5 x 10^{-5} mbar for 10 hrs. After degassing, the gas was filed in the primary reservoir from where it was transferred to the secondary reservoir. Experiments were stated after allowing the gas to extend in the system for 30 minutes. Once the experiment is started, the gradual pressure drop can be observed from the computer. The amount of gas absorbed is calculated by the ideal gas law:

$$\tilde{n}_g = \frac{\Delta P\, V}{\acute{R}\, T} \tag{3.2}$$

Where $\tilde{n}_g$ is the amount (molar) of gas absorbed at equilibrium, $\Delta P\ (Bar)$ represents the pressure difference of the beginning and equilibrium states of equilibrium cell, $V\ (L)$ represents volume of the gas which is found by subtracting IL volume from volume of the empty cell, *T (K)* is the equilibrium temperature, and $\acute{R}$ *(L Bar mol^{-1} K^{-1})* is the ideal gas constant. The molar amount of absorbed gas can be found as under.

$$x_g = \frac{\tilde{n}_g}{\tilde{n}_g + \tilde{n}_{IL}} \tag{3.3}$$

Where $\tilde{n}_{IL}$ represents the number of moles of IL used.

Henry's Law constant $H\ (Bar)$ can be calculated from the recorded equilibrium pressure P_{eq} and the corresponding molar fraction of the gas x_g.

$$H = \frac{P_{eq}}{x_g} \tag{3.4}$$

3.4 Hollow fiber membrane contactor selection

A Polypropylene HFMC (1 x 5.5 MiniModule^{TM}) potted with polyurethane was selected for experiments as presented in Figure 3.4. The HFMC was in parallel flow and hydrophobic by nature. It was supplied by Liqui-Cel ^{TM}, USA. The module consists of mesoporous polypropylene hollow fibers with 40 % porosity and mean pore diameter of 0.04 μm. The detailed specifications of the membrane contactor are presented in Table 3.2.

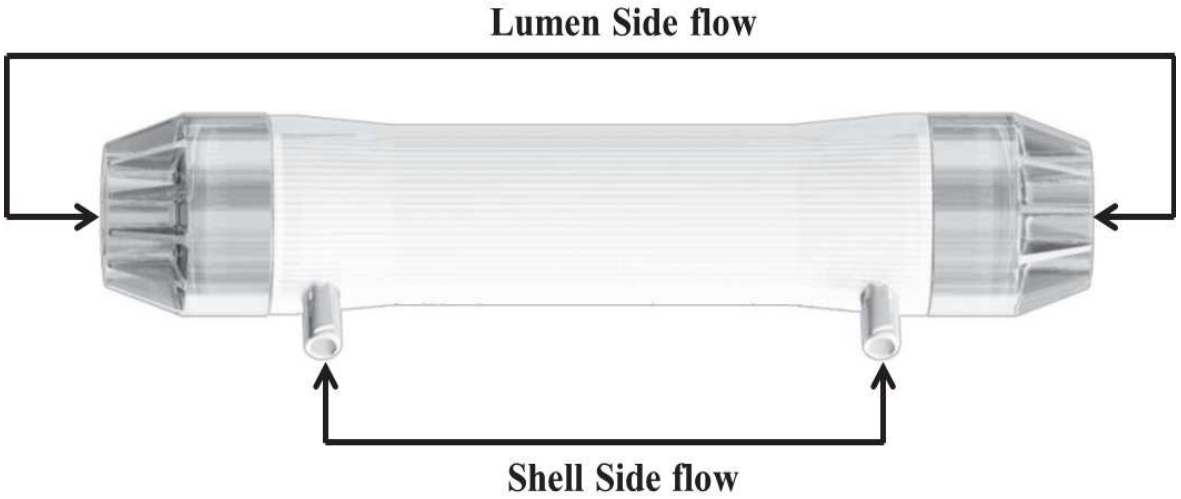

Figure 3.4 Polypropylene hollow fiber membrane contactor module (1 x 5.5 MiniModule^{TM}) (Adapted from "3M^{TM} Liqui-Cel^{TM} EXF 1X5.5 Series Membrane Contactor," 2020).

Table 3.2 Specifications of the membrane module

Parameter	Value	unit
Membrane material	Polypropylene	-
Inner diameter of the tube (d_i)	$2.2\ 10^{-4}$	m
Outer diameter of the tube (d_o)	$3.0\ 10^{-4}$	m
Membrane thickness (δ)	$0.4\ 10^{-4}$	m
Length of the contactor (L)	0.115	m
Number of fibers (N)	2300	-
Membrane pore diameter(d_p)	0.04	µm
Effective inner membrane area (A)	0.18	m^2
Lumen side volume (V_g)	$1.6\ 10^{-5}$	m^3
Shell side volume (V_l)	$2.5\ 10^{-5}$	m^3
Porosity (ε)	40	%
Packing factor ($\emptyset$)	0.39	-
Tortuosity (τ)[a]	6.4	-

[a] $\tau = \frac{(2-\varepsilon)^2}{\varepsilon}$ (Iversen et al., 1997)

3.5 Experimental approach of CO_2 absorption/desorption in HFMCs

A HFMC setup suitable for post-combustion CO_2 capture with ILs was developed here. As illustrated in Figure 3.5, the setup can operate in two modes; single module absorption and coupled absorption/desorption. In the single module absorption system ILs were recirculated (in a closed loop) from the reservoir to the shell side of the membrane absorber (membrane stripper disconnected). In the coupled absorption/desorption system, ILs were recirculated (in a closed loop) at the same time through the shell side of both membrane absorber and membrane stripper.

A digital gear pump (Cole-Parmer Gear Pump System, Benchtop Digital Drive, 0.017 mL/rev, 220 VAC, Spain) was used to maintain a constant flowrate and avoid fluctuations. The feed gas mixture containing CO_2 (15 % Vol.) and N_2 (rest to balance) was introduced through the lumen side of the membrane absorber. The gas mixture was kept in open loop conditions with constant CO_2 concentration 15 % by Vol. Pure N_2 could pass from the lumen side of membrane stripper used as sweep gas. Gas mass flowmeters (Alicat scientific, MC–gas mass flow controller, Spain) were used to measure and control the inflow and outflow of

gases for both membrane absorber and membrane stripper. CO_2 concentration at the inlet and outlet of the membrane absorber and at the outlet of membrane stripper was analyzed by a CO_2 analyzer (Geotech, G110 0-100%, UK). Liquid side pressure was always kept higher than the pressure of the gas side to avoid penetration of the gas into the liquid side. Although liquid side pressure was kept higher, however the transmembrane pressure was always controlled and kept below LEP to avoid wetting of the membrane. Wetting of the mesopores of membrane was not considered as fresh hydrophobic membranes were used with high surface tension ILs and experiments were carried out under controlled transmembrane pressure (< LEP). Operating conditions are presented in Table 3.3. Experimental setup was kept inside an oven to maintain isothermal conditions throughout the experiments. Gas flowmeters and gear measuring pumps were calibrated before experiments. ILs and gas streams were kept in countercurrent arrangements in both membrane absorber and stripper.

In single module absorption IL recirculates through the shell side of the membrane absorber, absorbing CO_2 from the gas mixture. The CO_2 accumulates on the liquid side until reaching pseudo-steady-state. The evolution of CO_2 concentration at the gas side outlet was continuously monitored with a CO_2 analyzer. After reaching pseudo-steady-state, the CO_2 desorption/stripping was initiated in the same module which was used as a stripper using N_2 as sweep gas. IL was kept recirculating in the closed loop and the CO_2 desorbing from IL on the interface diffused inside the pores of the membrane filled with N_2, whose concentration was continuously analyzed at the gas side outlet.

In coupled absorption/desorption, simultaneous absorption and desorption were carried out in a single step. IL liquid during recirculation first passes into the membrane absorber absorbing CO_2 and then enters the membrane stripper having N_2 as sweep gas to desorb CO_2 in the same step. CO_2 concentration at the gas side outlet of membrane absorber and stripper was continuously monitored with a CO_2 analyzer. During recirculation CO_2 was absorbed in the absorption module a part of which desorbs after entering the stripper module. The experiment was carried out until a constant CO_2 concentration was achieved at the gas side outlet (reaching pseudo-steady-state). All the experiments were reproduced three times. The data presented in the manuscript represents the average values for the set of three experiments.

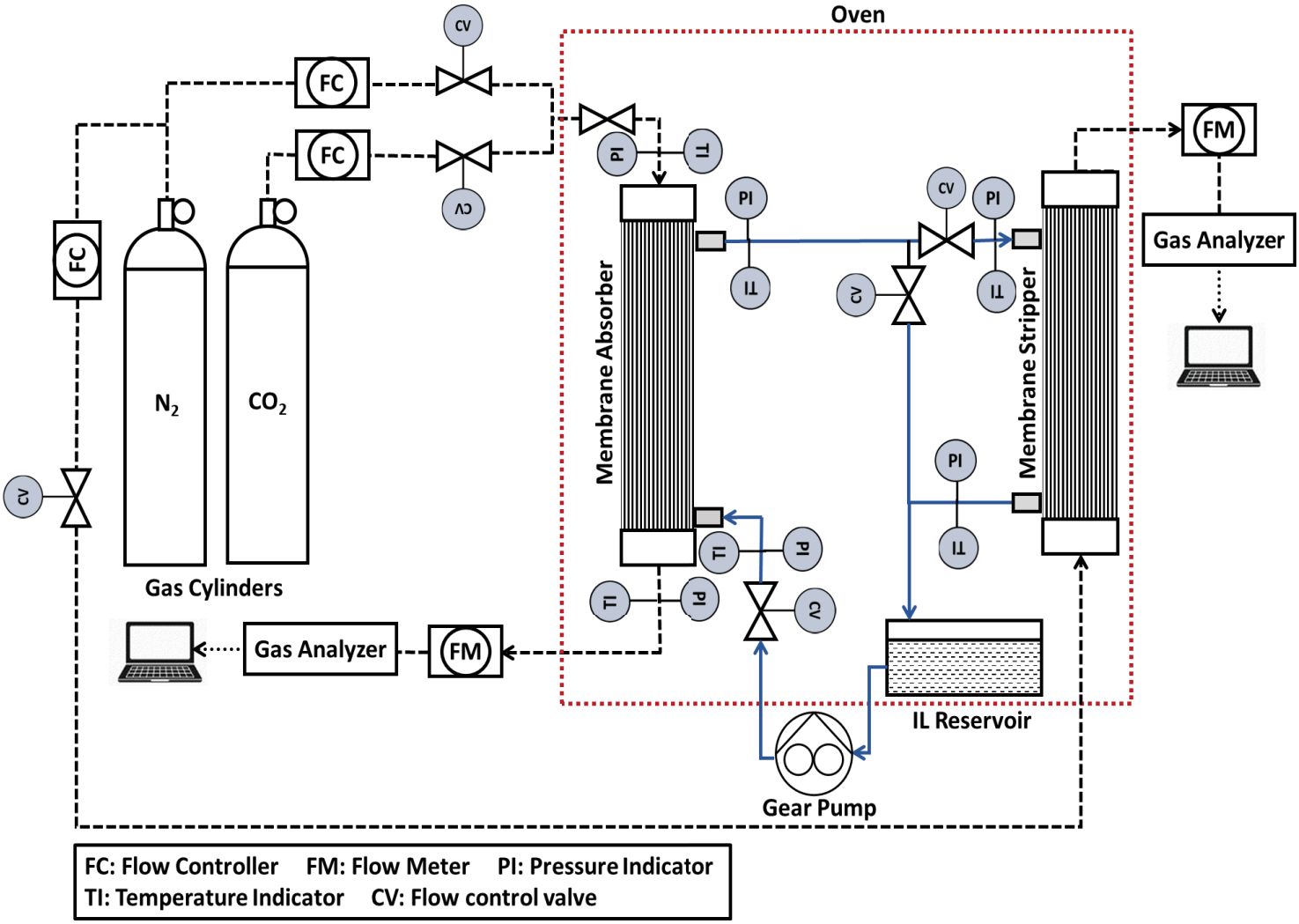

Figure 3.5 Schematic representation of the experimental setup; Gas flow (dashed lines), Liquid flow (solid lines)

Table 3.3 Operating conditions

Parameter/Property Description	Value	Unit
CO_2 concentration in the gas (φ_v)	15	Vol %
Initial CO_2 loading of Absorbent (α)	0	mol mol^{-1}
Temperature, T	288-323	K
Sweeping gas flowrate, Q_{N_2}	100-200	ml min^{-1}
Feed gas flowrate, $Q_{g,}$	10-200	ml min^{-1}
Liquid flowrate, Q_{IL}	60	ml min^{-1}
Gas inlet pressure, $P_{g,in}$	1.03	Bar
Liquid inlet pressure, $P_{l,in}$	2.40	Bar

Chapter 4. Theoretical Approach and Modeling

The theoretical approach and modeling are implemented based on the measurements of mass transfer kinetics and two-dimensional axial radial mass, momentum and energy transport. Mass transfer kinetics are measured based on the basic resistance in series model which considers boundary layers at the different interfaces in the HFMC and resistance in the membrane. The two-dimensional model is implemented under isothermal and non-isothermal conditions. Isothermal conditions were adopted for room temperature ILs which behave as physical absorbents. The experimental arrangements for isothermal modeling are adopted from Chapter 3, section 3.5 where the IL is recirculated continuously in a closed loop and gas mixture flows counter currently in open loop. This kind of arrangement leads to pseudo-steady-state conditions, which is explained in detail in the mentioned section. Both pseudo-steady-state and steady-state analysis are performed. For AAILs, which are known as highly reactive ILs, a non-isothermal modeling approach is adopted. The experimental arrangements for non-isothermal modeling are adopted from the work of Lu et al. (2017) for validation. Both ILs and gas mixtures were considered in open loop conditions, which develop steady-state. Here below the model development is described in detail.

4.1 Mass transfer kinetics

The overall gas mass transfer in membrane contactor is composed of three main resistances i.e. resistance in the gas phase, membrane and liquid phase. Resistance in series approach combines these individual resistances:

$$\check{R}_{ov} = \check{R}_{ov} = \check{R}_g + \check{R}_m + \check{R}_l \tag{4.1}$$

A hollow fiber membrane contactor is used with gas on the lumen side and liquid on the shell side. The gas liquid interface is located on the outer boundary of the tubes assuming no wetting conditions. Considering an enhancement factor (E) for chemical reaction on the shell side, the equation can be written as below(Ortiz et al., 2010) :

$$\frac{1}{K_{ov}} = \frac{d_o}{k_g d_i} + \frac{d_o}{k_m d_{lm}} + \frac{1}{k_l H_d E} \tag{4.2}$$

In the above equation, $k_g(m\,s^{-1})$, $k_m(m\,s^{-1})$ and $k_l(m\,s^{-1})$ are individual mass transfer coefficients of gas, membrane and liquid phase while d_o, d_i and d_{lm} are the outer, inner and log mean diameters of the membrane fiber. H_d in the above equation represents dimensionless Henry's law constant. This parameter is very important as it represents CO_2 solubility in ILs and is mostly used for RTILs (Lei et al., 2014; Wang et al., 2011).

As reported previously, contributions of the gas and membrane phase can be neglected, by considering non-wetting conditions and gas filled membrane pores (Ortiz et al., 2010). Equation 2 can then be rewritten as below:

$$\frac{1}{K_{ov}} = \frac{1}{k_l H_d E} \tag{4.3}$$

Several empirical correlations have been proposed by different authors for shell side liquid mass transfer coefficient in parallel flow membrane contactors, depending upon the operating conditions of the liquid flowing and characteristics of the membrane contactor. The correlation developed by Li et al. has been used in this study as it closely meets the conditions of current absorption process (Shen et al., 2010):

$$Sh_s = \left(\frac{k_l d_h}{D_l}\right) = (0.52 - 0.64\emptyset){R_e}^{(0.36+0.3\emptyset)}{S_c}^{0.33};\ 0 < R_e < 100;\ 0.30 < \emptyset < 0.70 \tag{4.4}$$

While d_h, D_l, $\emptyset$, R_e and S_c are hydraulic diameter, CO_2 diffusivity in liquid phase, packing fraction of membrane contactor, Reynolds number and Schmidt number, respectively. These parameters are calculated as under:

$$d_h = \frac{{d_{c-i}}^2 - N{d_o}^2}{d_{c-i} + N d_o} \tag{4.5}$$

While d_{c-i}, d_o and N represent contactor inner diameter, fiber outer diameter and number of fibers, respectively.

CO_2 diffusivity in liquid phase was predicted by the correlation developed by Morgan et al. (2005):

$$D_l = 2.66\,.\,10^{-3}\,\frac{1}{\mu_{IL}^{0.66} v_{CO_2}^{1.04}} \tag{4.6}$$

Where $\mu_{IL}(cP)$ and $v_{CO_2}(cm^3.mol^{-1})$ are viscosity of IL and molar volume of CO_2. The correlation developed by Morgan et al. is very well known for CO_2 diffusivities in imidazolium cation based ILs with different anions and has been confirmed experimentally by many authors (Moganty and Baltus, 2010; Zubeir et al., 2015).

Reynolds number is calculated as follows:

$$R_e = \frac{4\rho_{IL}Q}{\pi\mu_{IL}(d_{c-i}+Nd_0)} \tag{4.7}$$

The CO_2 mass transfer flux can be calculated from the following equation:

$$j_{CO_2-g} = \frac{1}{A}\left(\frac{d\tilde{n}}{dt}\right) = \frac{Q_{g-in}\,C_{g-in} - Q_{g-out}C_{g-out}}{A} = K_{exp}\,\Delta C_{g-lm} \tag{4.8}$$

Where ñ represents moles of CO_2, Q_{g-in} and Q_{g-out} are gas side inlet and outlet flowrates ($m^3.s^{-1}$), respectively, C_{g-in} and C_{g-out} are gas side inlet and outlet concentrations ($mol.m^{-3}$) of CO_2, respectively, while K_{exp} denotes the experimental overall mass transfer coefficient ($m\,s^{-1}$). K_{exp} can be calculated from mass transfer flux and concentration gradient. ΔC_{g-lm} in the above equation represents logarithmic mean of the driving force which can be calculated using the equation below:

$$\Delta C_{g-lm} = \frac{\left(C_{g-in}-C^*_{g-in}\right)-\left(C_{g-out}-C^*_{g-out}\right)}{\ln\left(\frac{C_{g-in}-C^*_{g-in}}{C_{g-out}-C^*_{g-out}}\right)} \tag{4.9}$$

Where C^*_{g-in} and C^*_{g-out} represents equilibrium concentration of the gas phase with corresponding CO_2 concentration in the liquid phase C^*_l. Equilibrium concentration of gas phase C^*_g can be found using equation ($C^*_g = H_d\,C^*_l$) based on Henry's Law constant. The enhancement factor E determines the absorption rate of CO_2 in absorbents and quantifies how and up to what extent the absorption is enhanced by the chemical reaction (Dindore and Versteeg, 2005; Lu et al., 2005). Experimental overall mass transfer coefficient, K_{exp} calculated from equation 4.8 can be used instead of K_{ov} in equation 4.3 to predict the enhancement factor for CO_2 absorption in ILs. Equation 4.3 after rearranging can be written as:

$$E = \frac{K_{exp}}{k_l H_d} \tag{4.10}$$

Considering first order interfacial chemical reaction, mass transfer rate for gas absorption in membrane contactor can be described as:

$$-\acute{r}_i = \left(-\frac{dC_{CO_2}}{dt}\right)_g = \frac{1}{V_g}\left(-\frac{d\tilde{n}}{dt}\right) = K_r\,\Delta C_{g-lm} \tag{4.11}$$

V_g in the above equation represents gas side volume. The equation represents the mechanism of first order chemical reaction of CO_2 with IL. Combining equation 4.8 and 4.11 can give us the following new equation:

$$j_{CO_2-g}\, A = \acute{r}_i\, V_g \tag{4.12}$$

By combining equation 4.11 and 4.12 we can get the following equation:

$$j_{CO_2-g} = \acute{r}_i \left(\frac{V_g}{A}\right) = K_r \left(\frac{V_g}{A}\right) \Delta C_{g-lm} \tag{4.13}$$

The final equation for the surface reaction rate (K_r) of CO_2 with IL is expressed as:

$$K_r = K_{exp} \left(\frac{A}{V_g}\right) \tag{4.14}$$

The kinetic constant K_r (s^{-1}) represents first order gas liquid reaction, which will be used to quantify the chemical absorption potential of ILs and its variation with increase of CO_2 concentration in ILs as it is directly proportional to experimental overall mass transfer coefficient.

4.2 Modeling

4.2.1 Isothermal modeling approach

Isothermal modeling approach was implemented for ILs [emim][$MeSO_4$], [emim][DCA], [emim][$EtSO_4$] and [emim][Ac] which are known to involve physical absorption for CO_2. Thus, the absorption process is assumed to be isothermal. A comprehensive 2-D model is presented here for CO_2 mass transport in a hollow fiber membrane contactor for both steady-state and pseudo-steady-state modes. The process is explained in Figure 4.1. The dotted lines show steady-state mode in which both gas and IL are passed from the membrane contactor in a non-closed loop. In the pseudo steady-state mode IL is recirculated from a reservoir which is represented by solid lines while gas flows in a non-closed loop. Fresh CO_2/N_2 gaseous mixture is introduced into the inner side of hollow fibers. While IL flows in the shell side either in a closed loop or non-closed loop. For pseudo-steady-state mode, a dynamic model is linked with the mass transport model for the recirculated IL in the tank.

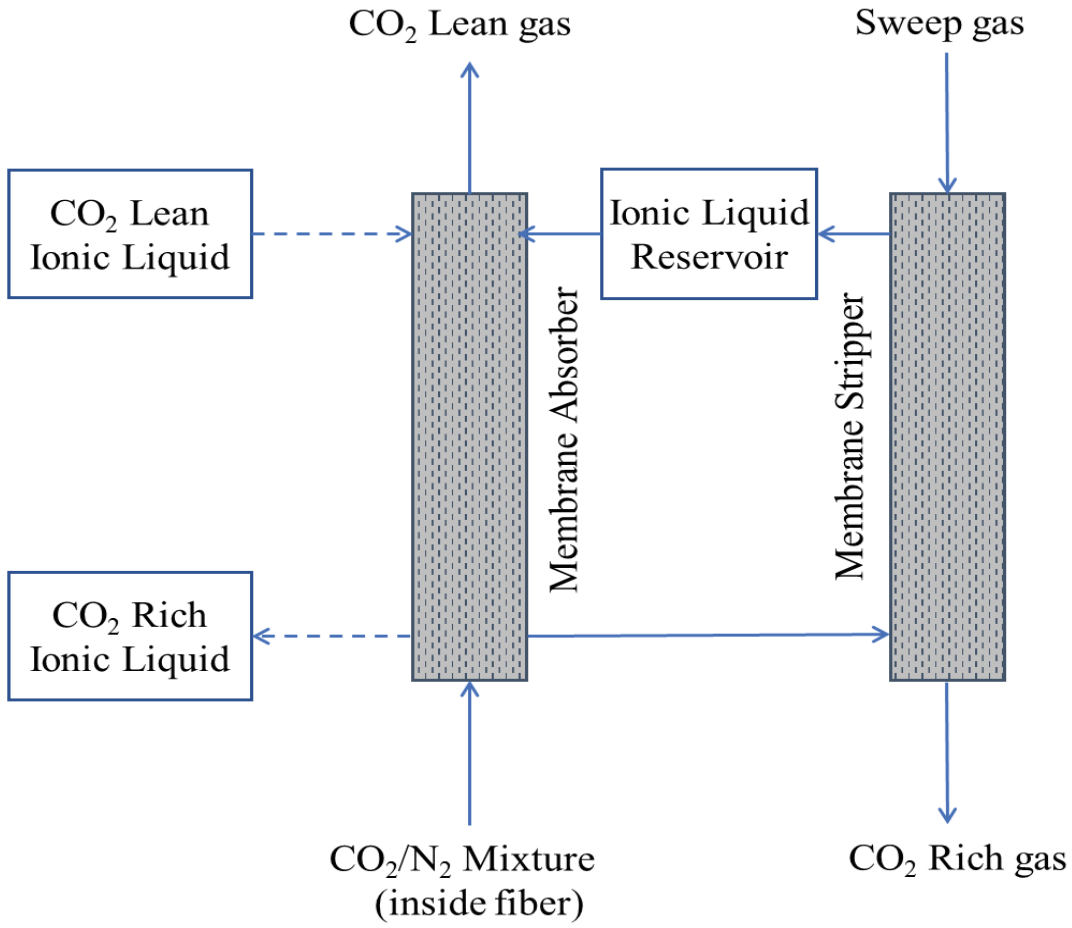

Figure 4.1 Schematic representation of the setup assumed to be modeled.

A polypropylene membrane contactor module with the same properties as Liquicel™ membrane contactors (USA) with mesoporous, thin walled, opaque, polypropylene hollow-fibers was considered for the separation of CO_2 from CO_2/N_2 mixture using ILs. Characteristics of the module and operating conditions are presented in Table 3.2 and 3.3, respectively. In order to reach reasonable computing times, we considered for the model establishment a single hollow fiber with arbitrary shell predicted by Happel's model (Happel, 1959). A portion of the fiber along with the arbitrary shell (Figure 4.2) was modeled. Continuity equations were solved for the three domains of the flow cell namely, tube, membrane and shell.

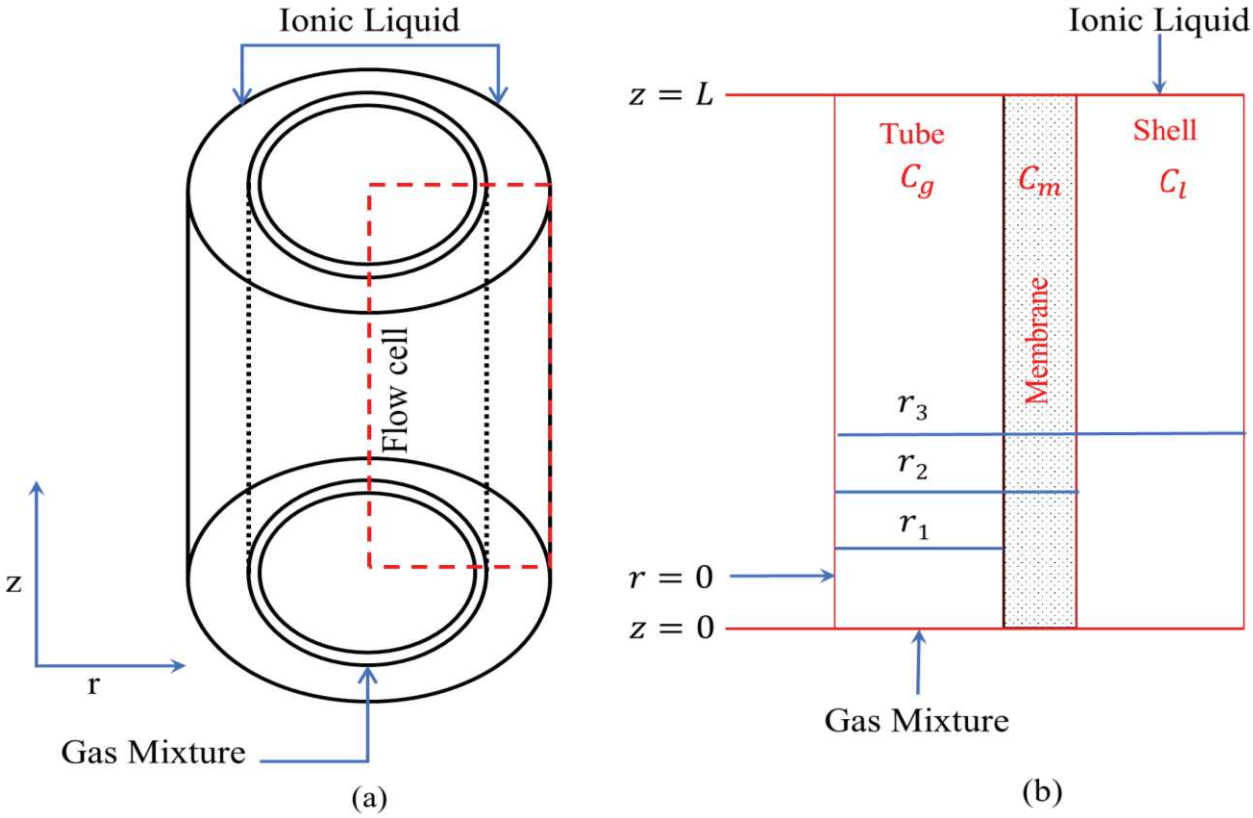

Figure 4.2 Schematic diagram of single hollow fiber and section used for model development.

The mass transport model of the flow cell (Figure 4.2) is based on the following assumptions:

a) Pseudo-steady-state (unless mentioned for steady-state).

b) Countercurrent mode for gas and IL flow in membrane contactor.

c) Laminar flow with fully developed velocity profile in the shell and tube.

d) Ideal gas behavior.

e) Application of Henry's law on gas-liquid interface for CO_2 with neglected solubility of N_2.

f) The membrane is not selective and not wetted by the IL (unless otherwise specified, non-wetting conditions).

g) Membrane mass transfer using Fick's diffusion through porous media and neglecting convective contributions.

h) Contributions of advection and diffusion to mass balance solved by considering local concentrations.

i) The reservoir where the IL is recycled is considered as a perfectly stirred tank.

j) There is no heat transfer during absorption and desorption processes, making the global process isothermal.

4.2.1.1 Mass transport equations

The continuity equation for each section is expressed as:

$$\frac{\partial C_i}{\partial t} = -\nabla . C_i U - \nabla . j_i + \acute{r}_i \quad (4.15)$$

Where the concentration of the species is $C_i (mol.m^{-3})$, $U\ (ms^{-1})$ is the velocity, $j_i\ (mol.m^{-2}.s^{-1})$ is the molar flux, $\acute{r}_i\ (mol.m^{-3}.s^{-1})$ is the reaction rate and $t\ (s)$ is the time. The steady-state form of the equation is presented below:

$$0 = -\nabla . C_i U - \nabla . j_i + \acute{r}_i \quad (4.16)$$

Terms on the right-hand side of the equation represent convection, diffusion and reaction. Fick's law of diffusion is applicable for the diffusion in membrane contactor (Bird et al., 2002).

4.2.1.1.1 Transport in gas

Based on the above assumptions, CO_2 transport in the gas can be expressed as below (Subscripts A and S represent equations for membrane absorber and membrane stripper):

<u>For pseudo-steady-state:</u>

$$U_{z,g-A}\frac{\partial C_{g-A}}{\partial z} = \frac{\partial C_{g-A}}{\partial t} + D_{g-A}\left[\frac{\partial^2 C_{g-A}}{\partial r^2} + \frac{1}{r}\frac{\partial C_{g-A}}{\partial r} + \frac{\partial^2 C_{g-A}}{\partial z^2}\right]; U_{z,g-S}\frac{\partial C_{g-S}}{\partial z} = \frac{\partial C_{g-S}}{\partial t} + D_{g-S}\left[\frac{\partial^2 C_{g-S}}{\partial r^2} + \frac{1}{r}\frac{\partial C_{g-S}}{\partial r} + \frac{\partial^2 C_{g-S}}{\partial z^2}\right] \quad (4.17)$$

<u>For steady-state:</u>

$$U_{z,g-A}\frac{\partial C_{g-A}}{\partial z} = D_{g-A}\left[\frac{\partial^2 C_{g-A}}{\partial r^2} + \frac{1}{r}\frac{\partial C_{g-A}}{\partial r} + \frac{\partial^2 C_{g-A}}{\partial z^2}\right]; \quad U_{z,g-S}\frac{\partial C_{g-S}}{\partial z} = D_{g-S}\left[\frac{\partial^2 C_{g-S}}{\partial r^2} + \frac{1}{r}\frac{\partial C_{g-S}}{\partial r} + \frac{\partial^2 C_{g-S}}{\partial z^2}\right] \quad (4.18)$$

Where D_{g-A}/D_{g-S} $(m^2.s^{-1})$, C_{g-A}/C_{g-S} $(mol.m^{-3})$ and $U_{z,g-A}/U_{z,g-S}$ $(m.s^{-1})$ denote the gas side CO_2 diffusivity, CO_2 concentration and gas velocity, respectively.

4.2.1.1.2 Transport in liquid

Based on the above assumptions CO_2 transport in the liquid phase can be expressed as below:

For pseudo-steady-state:

$$U_{z,l-A}\frac{\partial C_{l-A}}{\partial z} = \frac{\partial C_{l-A}}{\partial t} + D_{l-A}\left[\frac{\partial^2 C_{l-A}}{\partial r^2} + \frac{1}{r}\frac{\partial C_{l-A}}{\partial r} + \frac{\partial^2 C_{l-A}}{\partial z^2}\right]; U_{z,l-S}\frac{\partial C_{l-S}}{\partial z} = \frac{\partial C_{l-S}}{\partial t} + D_{l-S}\left[\frac{\partial^2 C_{l-S}}{\partial r^2} + \frac{1}{r}\frac{\partial C_{l-A}}{\partial r} + \frac{\partial^2 C_{l-A}}{\partial z^2}\right] \quad (4.19)$$

For steady-state:

$$U_{z,l-A}\frac{\partial C_{l-A}}{\partial z} = D_{l-A}\left[\frac{\partial^2 C_{l-A}}{\partial r^2} + \frac{1}{r}\frac{\partial C_{l-A}}{\partial r} + \frac{\partial^2 C_{l-A}}{\partial z^2}\right]; \qquad U_{z,l-S}\frac{\partial C_{l-S}}{\partial z} = D_{l-S}\left[\frac{\partial^2 C_{l-S}}{\partial r^2} + \frac{1}{r}\frac{\partial C_{l-A}}{\partial r} + \frac{\partial^2 C_{l-A}}{\partial z^2}\right] \quad (4.20)$$

Where D_{l-A}/D_{l-S} $(m^2.s^{-1})$, C_{l-A}/C_{l-S} $(mol.m^{-3})$ and $U_{z,l-A}/U_{z,l-S}$ $(m.s^{-1})$ denote the liquid side CO_2 diffusivity, CO_2 concentration and gas velocity, respectively.

4.2.1.1.3 Transport in membrane

Although the model considers non-wetting conditions for the prediction of the experimental data, however, a detailed analysis of the non-wetting, partial wetting and full wetting conditions was performed. Wetting can be avoided during short term operations and using fresh hydrophobic membranes, however, it is more likely to occur during long term operations and due to reuse of membranes and liquid absorbents. Therefore, a wetting analysis was performed for which the schematic diagram of membrane thickness is shown in Figure 4.3. Boundary conditions for all three modes are listed in Table 4.1. Whatever wetting mode considered equilibrium between CO_2 concentrations in the gas and liquid phase has been assumed, following Henry's law. The difference between all three modes is the location of the gas-liquid interface. For no wetting conditions, the gas-liquid interface is at the pore's exit, on the shell side ($r = r_2$). For fully wetted conditions, the interface is at the pores

entrance, on the tube side ($r = r_1$). For partially wetted conditions, the interface is inside the membrane's pores ($r = r_w$) between r_1 and r_2.

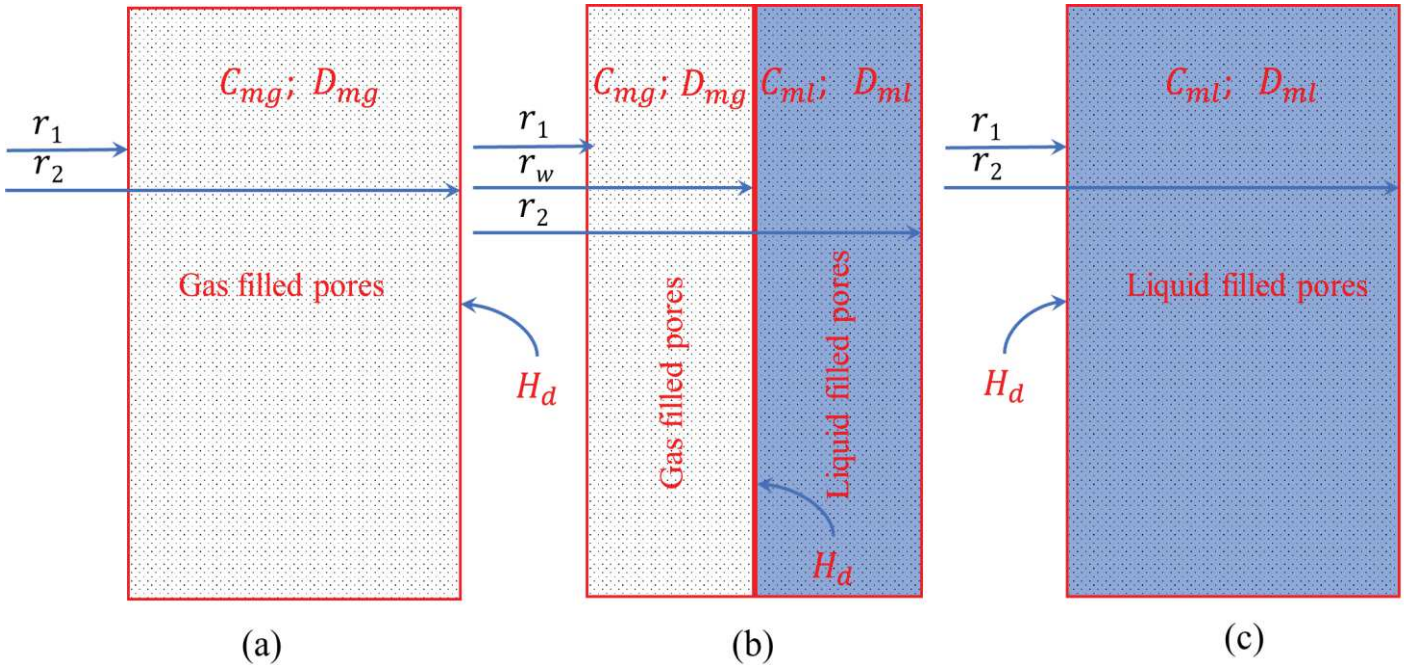

Figure 4.3 Schematic diagram of membrane thickness under (a) Non-wetted (b) Partially wetted and (c) Fully wetted conditions.

For gas filled membrane pores, corresponding to no-wetting conditions the equations can be written as:

For pseudo-steady-state:

$$0 = \frac{\partial C_{mg-A}}{\partial t} + D_{mg-A}\left[\frac{\partial^2 C_{mg-A}}{\partial r^2} + \frac{1}{r}\frac{\partial C_{mg-A}}{\partial r} + \frac{\partial^2 C_{mg-A}}{\partial z^2}\right]; \qquad 0 = \frac{\partial C_{mg-S}}{\partial t} + D_{mg-S}\left[\frac{\partial^2 C_{mg-S}}{\partial r^2} + \frac{1}{r}\frac{\partial C_{mg-S}}{\partial r} + \frac{\partial^2 C_{mg-S}}{\partial z^2}\right] \tag{4.21}$$

For steady-state:

$$0 = D_{mg-A}\left[\frac{\partial^2 C_{mg-A}}{\partial r^2} + \frac{1}{r}\frac{\partial C_{mg-A}}{\partial r} + \frac{\partial^2 C_{mg-A}}{\partial z^2}\right]; \qquad 0 = D_{mg-S}\left[\frac{\partial^2 C_{mg-S}}{\partial r^2} + \frac{1}{r}\frac{\partial C_{mg-S}}{\partial r} + \frac{\partial^2 C_{mg-S}}{\partial z^2}\right] \tag{4.22}$$

Where $D_{mg-A}/D_{mg-S}\ (m^2.s^{-1})$ and $C_{mg-A}/C_{mg-S}\ (mol.m^{-3})$ denotes the gas filled membrane CO_2 diffusivity and CO_2 concentration.

For gas filled portion of the partially wetted membrane equations can be rearranged as:

For pseudo-steady-state:

Equation 4.21 can be used.

For steady-state:

Equation 4.22 can be used.

For liquid filled portion of the partially wetted membrane equations can be rearranged as;

For pseudo-steady-state:

$$0 = \frac{\partial C_{ml-A}}{\partial t} + D_{ml-A}\left[\frac{\partial^2 C_{ml-A}}{\partial r^2} + \frac{1}{r}\frac{\partial C_{ml-A}}{\partial r} + \frac{\partial^2 C_{ml-A}}{\partial z^2}\right]; 0 = \frac{\partial C_{ml-S}}{\partial t} + D_{ml-S}\left[\frac{\partial^2 C_{ml-S}}{\partial r^2} + \frac{1}{r}\frac{\partial C_{ml-S}}{\partial r} + \frac{\partial^2 C_{ml-S}}{\partial z^2}\right] \quad (4.23)$$

For steady-state:

$$0 = D_{ml-A}\left[\frac{\partial^2 C_{ml-A}}{\partial r^2} + \frac{1}{r}\frac{\partial C_{ml-A}}{\partial r} + \frac{\partial^2 C_{ml-A}}{\partial z^2}\right]; 0 = D_{ml-S}\left[\frac{\partial^2 C_{ml-S}}{\partial r^2} + \frac{1}{r}\frac{\partial C_{ml-S}}{\partial r} + \frac{\partial^2 C_{ml-S}}{\partial z^2}\right] \quad (4.24)$$

Where D_{ml-A}/D_{ml-S} $(m^2.s^{-1})$ and C_{ml-A}/C_{ml-S} $(mol.m^{-3})$ denotes the liquid filled membrane CO_2 diffusivity and CO_2 concentration.

For fully wetted membrane equations can be rearranged as:

For pseudo-steady-state:

Equation 4.23 can be used.

For steady-state:

Equation 4.24 can be used.

4.2.1.2 Momentum equations

A fully developed velocity profile of the gas on lumen side was predicted by Hagen-Poiseuille equation with no slip conditions presented below:

$$U_{z,g-A} = 2u_{g-A}\left[1 - \left(\frac{r}{r_1}\right)^2\right]; U_{z,g-S} = 2u_{g-S}\left[1 - \left(\frac{r}{r_1}\right)^2\right] \quad (4.25)$$

Where u_{g-A}/u_{g-S} $(m.s^{-1})$ in the equations represents gas average velocity in the tube.

Velocity profile inside the shell is expressed by Happel's free surface model (Happel, 1959):

$$U_{z,l-A} = 2u_{l-A}\left[1-(\frac{r_2}{r_3})^2\right]\frac{(r/r_3)^2-(r_2/r_3)^2+2\ln(r_2/r)}{3+(r_2/r_3)^4-4(r_2/r_3)^2+4\ln(r_2/r_3)};\quad U_{z,l-S} = 2u_{l-S}\left[1-(\frac{r_2}{r_3})^2\right]\frac{(r/r_3)^2-(r_2/r_3)^2+2\ln(r_2/r)}{3+(r_2/r_3)^4-4(r_2/r_3)^2+4ln(r_2/r_3)} \quad (4.26)$$

Where $u_{l-A}/u_{l-S}\ (m.s^{-1})$, r_2 and r_3 are average velocity of absorbent in the shell, outer radius of fiber and radius of free surface. The relationship between r_2 and r_3 is expressed as:

$$r_3 = \left(\frac{1}{1-\Theta}\right)^{1/2} r_2 \quad (4.27)$$

Where Θ is the volume fraction of the void space, which can be calculated from the following equation:

$$1-\Theta = \frac{Nr_2^2}{R^2} \quad (4.28)$$

Where N is the number of fibers and R is the module inner radius.

4.2.1.3 Differential mass balance in the reservoir

The model adopts a setup in which the absorbent is recirculated into a tank, until a pseudo-steady-state is achieved for the absorbent in the tank. A differential transient equation has been developed across the tank to measure the continuous evolution of CO_2 in the absorbent. The absorbent passing from the contactor leaves the contactor at time t entering the reservoir and exits the tank at $t+\Delta t$ with different concentration.

$$V_{IL}\frac{dC_{\check{r}(t)}}{dt} = Q_{IL}\left(C_{\check{r},in}(t) - C_{\check{r},out}(t)\right) \quad (4.29)$$

Where $C_{\check{r}}$ in equation 4.29 represents the concentration of CO_2 in the IL reservoir, while $V_{IL}\ (m^3)$ and $Q_{IL}(m^3.s^{-1})$ are total volume and volumetric flowrate of ionic liquid, respectively. Final form of the equation can be as:

$$C_{\check{r},out}(t+\Delta t) = \frac{\Delta t}{\mathcal{T}_{IL}}C_{\check{r},in}(t) + C_{\check{r}}(t)\left[1+\frac{\Delta t}{\mathcal{T}_{IL}}\right] \quad (4.30)$$

The term $C_{\check{r},out}(t+\Delta t)$ in the above equation represents the outlet concentration of the reservoir at time $t+\Delta t$. Concentration $C_{\check{r},in}(t)$ was found using the following boundary integral equation:

$$C_{\check{r},in}(t) = \frac{\int\int_{r=r_2}^{r=r_3} C_l(r) r dr d\theta}{\int\int_{r=r_2}^{r=r_3} r dr d\theta} \quad (4.31)$$

$\mathcal{T}_{IL}$ is the residence time of ionic liquid in the tank which is found from the following equation:

$$\mathcal{T}_{IL} = \frac{V_{IL}}{Q_{IL}} \quad (4.32)$$

4.2.1.4 Solubility, phase equilibria and diffusion coefficients

CO_2 solubility in ILs is mostly represented by Henry's law constant. Moreover, generally the models consider Henry's law for the gas liquid interface. Indeed, the calculations of this constant are of high importance for the modeling of CO_2 absorption on ILs. The magnitude of the Henry's constant indicates whether the absorption is chemical or physical. A small value of Henry's constant (usually less than 30 Bar) denotes chemical absorption of CO_2 in ILs (Wang et al., 2011; Yokozeki et al., 2008) and high gas solubility (Anthony et al., 2002b; Lei et al., 2014). Henry's Law constants were calculated from these experimental PTx data using the following equation (Blath et al., 2012; Sander, 2015; Yokozeki et al., 2008; Zubeir et al., 2015) :

$$H(T,P) = \lim_{x\to 0} \frac{f(T,P,x_{CO_2})}{x_{CO_2}} = \lim_{x\to 0} \frac{\phi(T_{eq},P_{eq})\, P_{eq}}{x_{CO_2}} \quad (4.33)$$

Where $H(Bar)$ is the Henry's constant, f is the fugacity of CO_2, x_{CO_2} is the mole fraction of CO_2 dissolved in IL, ϕ is the fugacity coefficient, T_{eq} is the equilibrium temperature and $P_{eq}$is the equilibrium pressure. As the solubility varies with temperature, Equation 4.33 allowed calculating Henry's constant at various temperatures. The constant found from Equation 4.33 was used in the following equation to calculate dimensionless Henry's constant (Sander, 2015):

$$H_d = \frac{\rho_{IL}\, \acute{R}_g\, T}{M_{IL}\, H} \quad (4.34)$$

Where $\rho_{IL}(kg.m^{-3})$ is the density of IL, $\acute{R}_g$ $(J.K^{-1}.mol^{-1})$ is the gas constant, M_{IL} $(kg.mol^{-1})$ is the molar weight of IL, T (K) is the temperature and $H(Bar)$ Henry's law constant for CO_2 in the four ILs.

Densities had strong dependency on temperature which in turn affected the Henry's Law constant and solubility of CO_2. Temperature dependency of the density for the four ILs [emim][$MeSO_4$], [emim][DCA], [emim][$EtSO_4$] and [emim][Ac], are presented in equations 4.39, 4.40, 4.41 and 4.42, respectively (Costa et al., 2011; Gómez et al., 2006; Jalili et al., 2010; Nazet et al., 2015; Schmidt et al., 2012). Equations below correspond to density in $kg.m^{-3}$ and temperature in K:

$$ln\,\rho(T)_{[MeSO_4]^-} = 7.33100 - 6.17220\,10^{-4}\,T + 1.3862\,10^{-4}\,T^2 \quad (4.35)$$

$$\rho(T)_{[DCA]^-} = \frac{1346}{1+7.19\,10^{-2}\,T} \quad (4.36)$$

$$\rho(T)_{[EtSO_4]^-} = 1451.5928 - 0.757562\,T + 0.00013391\,T^2 \quad (4.37)$$

$$\rho(T)_{[Ac]^-} = 1280.8 + 0.608\,T \quad (4.38)$$

The diffusion coefficient in the gas phase can be estimated by the following equation (Fuller et al., 1966):

$$D_g = \frac{0.01013.T^{1.75}\left(\frac{1}{M_{CO_2}}+\frac{1}{M_{N_2}}\right)^{0,5}}{P\left[\left(\sum \bar{\upsilon}_{CO_2}\right)^{\frac{1}{3}}+\left(\sum \bar{\upsilon}_{N_2}\right)^{\frac{1}{3}}\right]^2} \quad (4.39)$$

In the above equation $T(K)$, $P\ (Pa)$, $M\ (g.mol^{-1})$ and $\bar{\upsilon}$ are temperature, pressure, molar weight and atomic diffusion volumes, respectively. Equation 4.39 has been used in different studies to predict gas side diffusivity in membrane contactor operations (Albo et al., 2011; Dai et al., 2016c; Saidi, 2017).

Diffusivity of CO_2 and N_2 inside the membrane (D_m) which is mesoporous but near the limit of macropores (4.0 10^{-8} m) was considered as combined effects of gas diffusivity, D_g and Knudsen diffusivity D_{Kn}:

$$\frac{1}{D_m} = \frac{1}{D_g} + \frac{1}{\mathrm{D_{Kn}}} \quad (4.40)$$

If the membrane pore diameter is larger than 1 10^{-5} m bulk diffusion, D_g (Equation 4.39) is dominant; if it is less than 1 10^{-7} m, Knudsen diffusion is dominant. In case of pore diameter between above two values, both types of diffusion can exist. Knudsen diffusion coefficient can be found as below:

$$D_{Kn} = \frac{1}{2} d_p \sqrt{\frac{8\acute{R}T}{\pi M}} \quad (4.41)$$

If the membrane is considered completely gas filled, the only mass transfer resistance inside the membrane is given by the gas diffusion through the membrane structure, then effective diffusion coefficient can be applied:

$$D_m = D_{eff} = \frac{\varepsilon D_g}{\tau} \quad (4.42)$$

Gas diffusion coefficient in the ionic liquids can be described by the Equation 4.6 which was developed by Morgan et al. (2005). An increase in temperature effectively reduces viscosity of IL which causes an increase in diffusivity of CO_2 in IL at relatively high temperatures. Equation 4.6 had been verified in various studies by comparing the diffusivities from correlation with experimental diffusivities (Moganty and Baltus, 2010; Zubeir et al., 2015). Temperature dependency of the viscosity for the four ILs are presented below (Costa et al., 2011; Gómez et al., 2006; Jalili et al., 2010; Nazet et al., 2015; Quijada-Maldonado et al., 2012; Schmidt et al., 2012) :

$$ln\,\mu(T)_{[MeSO_4]^-} = ln\,\rho M - 18.25 + (\frac{1266.1}{T}) \quad (4.43)$$

$$ln\,\mu(T)_{[DCA]^-} = -1.719 + \frac{682.4}{T-143.7} \quad (4.44)$$

$$ln\,\mu(T)_{[EtSO_4]^-} = -1.6558 + (\frac{792.98}{T-171.15}) \quad (4.45)$$

$$ln\,\mu(T)_{[Ac]^-} = -1.657 + (\frac{673.7}{T-196.1}) \quad (4.46)$$

4.2.1.5 Meshing, boundary conditions and numerical resolution

Selecting an appropriate mesh for the finite element analysis is very critical. A rigorous absorption model with enough discretization (particularly in radial direction) of the liquid (due to high resistance for mass transfer) and membrane phase (due to high resistance for mass transfer and existence of interface) is required. A refined mapped mesh was applied across the three domains of the current symmetrical geometry. More refined mesh was selected inside the mesoporous membrane. The meshed geometry is presented in Figure 4.4.

The rectangular meshing elements are in accordance with the two directional (r, z) mass transport. Details about mesh are presented below;

- Meshed domains: 3
- Mesh vertices: 968121
- Quads: 960000
- Edge elements: 32240
- Vertex elements: 8
- Element quality: 1

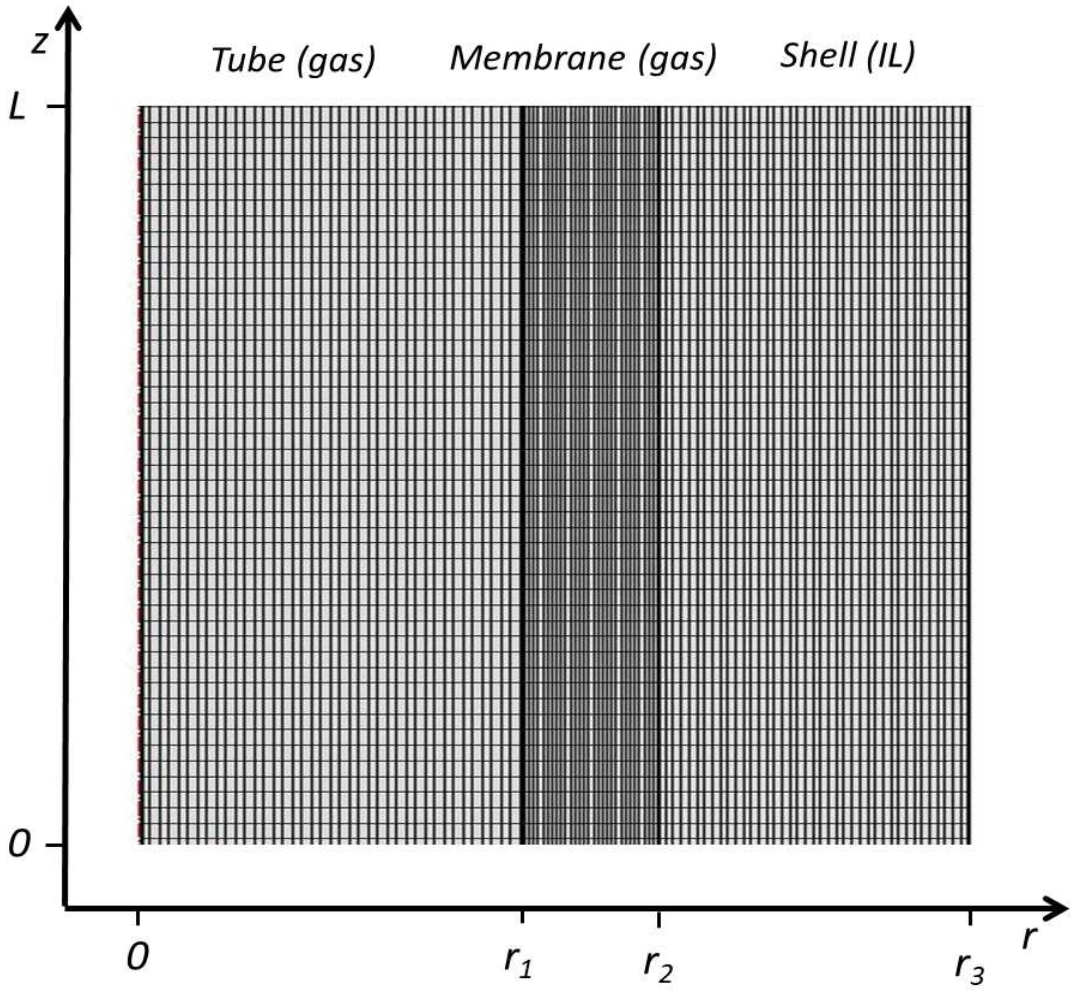

Figure 4.4 Schematic representation of the meshed domains

Boundary Conditions for the set of equations (mass and momentum transport in membrane absorber and membrane stripper) presented in preceding section are listed in Table 4.1 below.

Table 4.1 Boundary Conditions for the model

Boundary	Tube Side Absorption/Stripping	Porous Membrane Absorption/Stripping	Shell Side Absorption/Stripping
$z = 0$	$C_{g-A} = C_{g-A,in}/\ C_{g-S} = C_{g-S,in}$	$-D_{mg-A}\frac{\partial C_{mg-A}}{\partial z} = 0/-D_{mg-S}\frac{\partial C_{mg-S}}{\partial z} = 0$	$-D_{l-A}\frac{\partial C_{l-A}}{\partial z} = 0/$ $-D_{l-S}\frac{\partial C_{l-S}}{\partial z} = 0$
$z = L$	$-D_{g-A}\frac{\partial C_{g-A}}{\partial z} = 0/$ $-D_{g-S}\frac{\partial C_{g-S}}{\partial z} = 0$	$-D_{mg-A}\frac{\partial C_{mg-A}}{\partial z} = 0/-D_{mg-S}\frac{\partial C_{mg-S}}{\partial z} = 0$	$C_{l-A} = C_{\check{r},out}(t + \Delta t)/$ $C_{l-S} = C_{l-A,out}$
$r = 0$	$\frac{\partial C_{g-A}}{\partial r} = 0/$ $\frac{\partial C_{g-S}}{\partial r} = 0$	-	-
$r = r_3$	-	-	$\frac{\partial C_{l-A}}{\partial r} = 0/\frac{\partial C_{l-S}}{\partial r} = 0$
		No Wetting	
$r = r_1$	$C_{g-A} = C_{mg-A}/$ $C_{g-S} = C_{mg-S}$	$C_{mg-A} = C_{g-A}/C_{mg-S} = C_{g-S}$	-
$r = r_2$	-	$C_{mg-A} = \frac{C_{l-A}}{H_d}/C_{mg-S} = H_d\, C_{l-S}$	$C_{l-A} = H_d\, C_{m-A}/$ $C_{l-S} = \frac{C_{mg-S}}{H_d}$
		Full Wetting	
$r = r_1$	$C_{g-A} = \frac{C_{ml-A}}{H_d}/C_{g-S} = H_d\, C_{ml-S}$	$C_{g-A} = \frac{C_{ml-A}}{H_d}/C_{g-S} = H_d\, C_{ml-S}$	-
$r = r_2$	-	$C_{ml-A} = C_{l-A}/C_{ml-S} = C_{l-S}$	$C_{l-A} = C_{ml-A}/C_{l-S} = C_{ml-S}$
		Partial Wetting	
		Gas filled portion	**Liquid filled portion**	
$z = 0$	$C_{g-A} = C_{g-A,in}/\ C_{g-S} = C_{g-S,in}$	$-D_{mg-A}\frac{\partial C_{mg-A}}{\partial z} = 0/-D_{mg-S}\frac{\partial C_{mg-S}}{\partial z} = 0$	$-D_{ml-A}\frac{\partial C_{ml-A}}{\partial z} = 0/-D_{ml-S}\frac{\partial C_{ml-S}}{\partial z} = 0$	$-D_{l-A}\frac{\partial C_{l-A}}{\partial z} = 0/$ $-D_{l-S}\frac{\partial C_{l-S}}{\partial z} = 0$
$z = L$	$-D_{g-A}\frac{\partial C_{g-A}}{\partial z} = 0/-D_{g-S}\frac{\partial C_{g-S}}{\partial z} = 0$	$-D_{mg-A}\frac{\partial C_{mg-A}}{\partial z} = 0/-D_{mg-S}\frac{\partial C_{mg-S}}{\partial z} = 0$	$-D_{ml-A}\frac{\partial C_{ml-A}}{\partial z} = 0/-D_{ml-S}\frac{\partial C_{ml-S}}{\partial z} = 0$	$C_{l-A} = C_{\check{r},out}(t + \Delta t)/$ $C_{l-S} = C_{l-A,out}$
$r = 0$	$\frac{\partial C_{g-A}}{\partial r} = 0/\frac{\partial C_{g-S}}{\partial r} = 0$	-	-	-
$r = r_1$	$C_{g-A} = C_{mg-A}/C_{g-S} = C_{mg-S}$	$C_{mg-A} = C_{g-A}/C_{mg-S} = C_{g-S}$	-	-

$r = r_w$	-	$C_{mg-A} = \frac{C_{ml-A}}{H_d} / C_{mg-S} = H_d\, C_{ml-S}$	$C_{ml-A} = H_d\, C_{mg-A} / C_{ml-S} = \frac{C_{mg-S}}{H_d}$	-
$r = r_2$	-	-	$C_{ml-A} = C_{l-A} /$ $C_{ml-S} = C_{l-S}$	$C_{l-A} = C_{ml-A} /$ $C_{l-S} = C_{ml-S}$
$r = r_3$	-	-	-	$\frac{\partial C_{l-A}}{\partial r} = 0 / \frac{\partial C_{l-S}}{\partial r} = 0$

Equations presented in the preceding sections were solved using COMSOL Multiphysics® (version 5.3a, 2018) and MATLAB R2017a using LiveLink™ for MATLAB®. Finite element method was implemented here. This method considers piecewise polynomial interpolation over the domains and numerically resolves equations at each of the nodes. Fully coupled solver settings were applied for BDF time stepping and strict steps were implemented for the solver. To avoid a high number of elements in the axial direction and reduce the large difference between r and z directions, the 2D equation system was scaled down axially. An axial scale factor was applied on the axial coordinate, fiber length, diffusion coefficients and interstitial velocities.

4.2.2 Non-isothermal modeling approach

Non-isothermal modeling approach was implemented for absorption of CO_2 in aqueous solutions of four amino-based TSILs namely, tetramethylammonium glycinate [N_{1111}][Gly], 1-ethyl-3-methylimidazolium glycinate [emim][Gly], 1-butyl-3-methylimidazolium glycinate [bmim][Gly] and 1-hexyl-3-methylimidazolium glycinate [hmim][Gly] using HFMCs. The IL concentration of the solutions was varied from 0.3 to 2 mol L^{-1}. In fact, for very reactive absorbents as considered for the current study, the process of absorption of CO_2 is non-isothermal as the energy of dissolution reaction is released and accumulated along the membrane contactor length. The current model considers a new approach for the non-isothermal behavior of the chemisorption of CO_2 in the amino acid based reactive ILs used as absorbents in the membrane contactor. A membrane contactor gas absorption setup suitable for post-combustion CO_2 capture is adopted to be modeled here. The simplified form of the setup is presented in Figure 4.5. A mesoporous hydrophobic membrane contactor (poly-propylene fibers) of parallel configuration was selected for the study whose characteristics, process parameters and operating conditions are presented in Table 4.2. Dry gas mixture

(CO_2+N_2) and absorbents were considered flowing counter currently on the shell side and lumen side of the membrane contactor, respectively. For industrial operations, the reported CO_2 concentration is about 8-15 % (Jing et al., 2012). Thus 15 % CO_2 concentration is considered throughout the model. The absorption species (CO_2) transfer from the shell side (by convection and diffusion) to the pores of the membrane (only diffusion in the pores) and then absorbs (chemisorption followed by physisorption) in the absorbent on the lumen side of the membrane contactor.

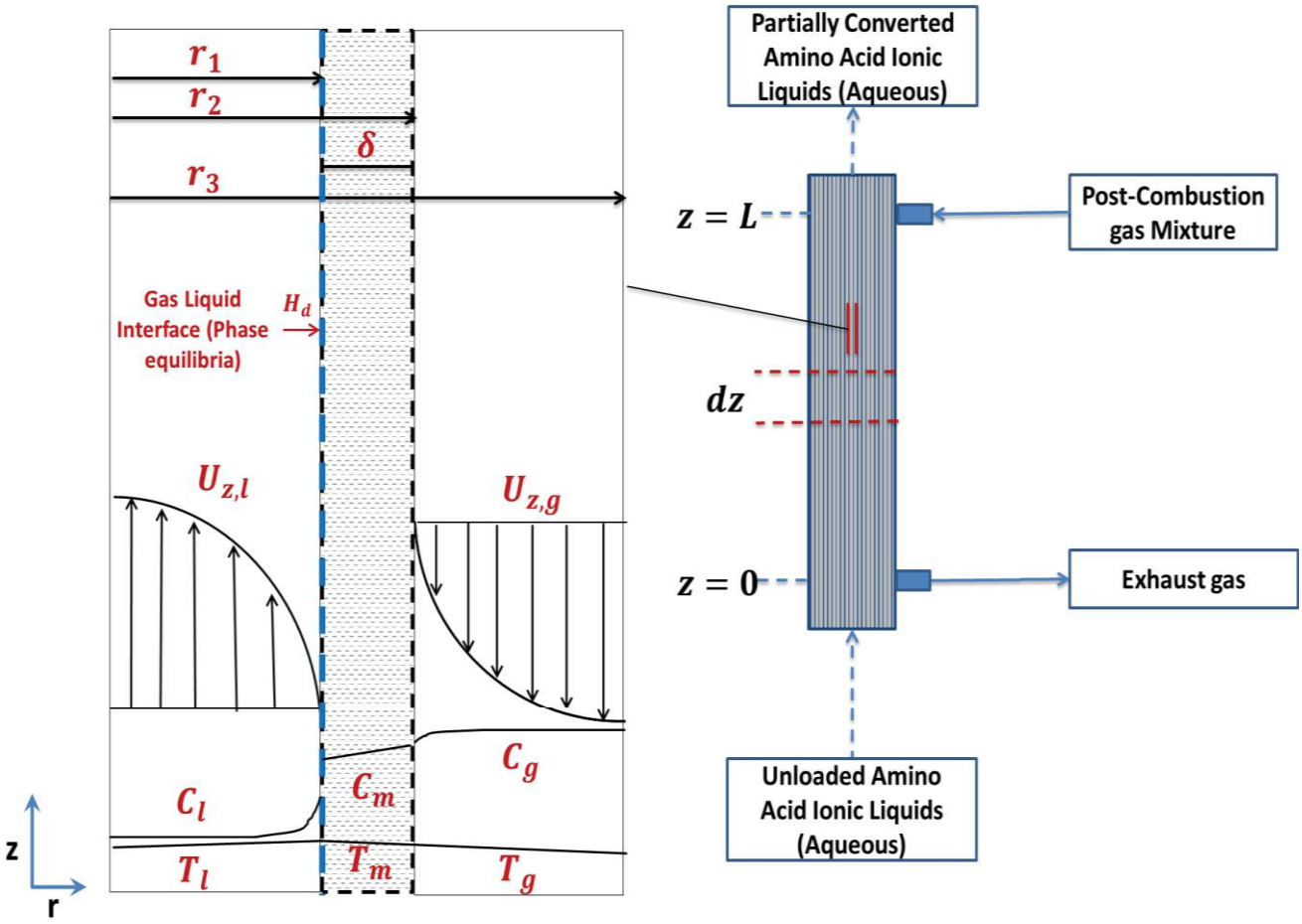

Figure 4.5 Schematic representation of the membrane contactor PCCC setup and the section used for model development.

Table 4.2 Characteristics of HFMC and operating conditions considered for simulations.

Parameter	Value	Unit
HFMC (Hydrophobic, Parallel flow)		

Fiber inner radius (r_1)	2.0×10^{-4}	m
Fiber outer radius (r_2)	2.5×10^{-4}	m
Fiber thickness (δ)	0.5×10^{-4}	m
Fiber length (L)	0.150	m
Number of fibers (N)	140	-
Porosity (ε)	60	%
Packing factor ($\emptyset$)	0.30	-
Shell side (gas)		
CO_2 molar fraction	15	%
Flowrate (Q_g)	60	ml min^{-1}
Inlet temperature (T)	298-323	K
Shell side Pressure (P)	2.20	Bar
Lumen side (liquid)		
Absorbent Concentration (C_{IL})	0.3-2	mol L^{-1}
Inlet CO_2 loading of Absorbent (α)	0	mol mol^{-1}
Flowrate (Q_{IL})	20	ml min^{-1}
Inlet temperature (T)	298-323	K
Lumen side Pressure (P)	3.10	Bar

A two dimensional (2D) convective and diffusive mass and heat transport model was developed for the ILs based membrane contactor CO_2 capture process. The model was based on the non-isothermal absorption process across the membrane contactor. CO_2 is the only specie that can cross the gas liquid interface. The following assumptions were made to solve the model:

Hydrodynamics:

k) Steady-state conditions.

l) Countercurrent arrangements for gas and IL flow in membrane contactor.

m) Gas and liquid flows under laminar conditions with fully developed velocity profile with no radial components.

Thermodynamics:

a) Application of Henry's law for gas liquid equilibrium on interface.

b) Membrane works as a non-selective barrier.

c) Neglected solubility of N_2.

d) Ideal gas behavior.

Kinetics, mass transfer and heat transfer

a) Reversible reaction kinetics.

b) Application of Fick's diffusion through porous media for membrane mass transfer, neglecting convective contributions.

c) Contributions of advection and diffusion to mass balance solved by considering local concentrations and contributions of convection, conduction and heat of reaction to energy balance solved by local temperatures.

d) Gas mixture is dry (no water vapor).

e) Neglecting the presence of water evaporation and condensation.

4.2.2.1 Mass transport equations

The mass and energy transport equations for the three domains are presented in the following sections.

4.2.2.1.1 Transport in gas

Based on the above assumption mass and energy transport equations for gas can be written as:

$$D_g \left[\frac{\partial^2 C_g}{\partial r^2} + \frac{1}{r}\frac{\partial C_g}{\partial r} + \frac{\partial^2 C_g}{\partial z^2}\right] = U_{z,g}\frac{\partial C_g}{\partial z} \quad (4.47)$$

$$\lambda_g \left[\frac{\partial^2 T_g}{\partial r^2} + \frac{1}{r}\frac{\partial T_g}{\partial r} + \frac{\partial^2 T_g}{\partial z^2}\right] = U_{z,g} C_{p,g}\rho_g \frac{\partial T_g}{\partial z} \quad (4.48)$$

Where λ_g $(W\ m^{-1}\ K^{-1})$, T_g (K) and $C_{p,g}$ $(J\ mol^{-1}\ K^{-1})$ represents thermal conductivity of the gas, temperature of the gas and specific heat.

4.2.2.1.2 Transport in liquid

Based on the above assumption mass and energy transport equations for liquid can be written as:

$$D_l\left[\frac{\partial^2 C_l}{\partial r^2}+\frac{1}{r}\frac{\partial C_l}{\partial r}+\frac{\partial^2 C_l}{\partial z^2}\right]+\acute{r}_i = U_{z,l}\frac{\partial C_l}{\partial z} \tag{4.49}$$

$$\lambda_l\left[\frac{\partial^2 T_l}{\partial r^2}+\frac{1}{r}\frac{\partial T_l}{\partial r}+\frac{\partial^2 T_l}{\partial z^2}\right]+\acute{r}_i\Delta H_{abs} = U_{z,l}C_{p,l}\rho_l\frac{\partial T_l}{\partial z} \tag{4.50}$$

Where λ_l $(W\ m^{-1}\ K^{-1})$, T_l (K), $C_{p,l}$ $(J\ mol^{-1}\ K^{-1})$, $\acute{r}_i$ $(mol\ m^{-3}\ s^{-1})$ and ΔH_{abs} $(\mathrm{J\ mol^{-1}})$ represents thermal conductivity of the liquid, temperature of the liquid, specific heat, reaction rate and enthalpy of absorption reaction.

4.2.2.1.3 Transport in membrane

Mass and energy transport equations for membrane (gas filled pores) can be written as:

$$D_m\left[\frac{\partial^2 C_m}{\partial r^2}+\frac{1}{r}\frac{\partial C_m}{\partial r}+\frac{\partial^2 C_m}{\partial z^2}\right]=0 \tag{4.51}$$

$$\lambda_{m,e}\left[\frac{\partial^2 T_m}{\partial r^2}+\frac{1}{r}\frac{\partial T_m}{\partial r}+\frac{\partial^2 T_m}{\partial z^2}\right]=0\ ;\quad \lambda_{m,e}=\varepsilon\lambda_g+(1-\varepsilon)\lambda_m \tag{4.52}$$

Where $\lambda_{m,e}$ $(W\ m^{-1}\ K^{-1})$ and T_m (K) represents effective thermal conductivity of the membrane and temperature of the gas filled inside membrane.

4.2.2.2 Momentum equations

A fully developed velocity profile of the gas on lumen side was predicted by Hagen-Poiseuille equation with no slip conditions presented below:

$$U_{z,g}=2u_g\left[1-\left(\frac{r}{r_1}\right)^2\right] \tag{4.53}$$

Where $u_g(m.s^{-1})$ in the equation represents gas average velocity in the tube.

Velocity profile inside the shell is expressed by Happel's free surface model (Happel, 1959).

$$U_{z,l} = 2u_l \left[1 - (\frac{r_2}{r_3})^2\right] \frac{(r/r_3)^2 - (r_2/r_3)^2 + 2\ln(r_2/r)}{3 + (r_2/r_3)^4 - 4(r_2/r_3)^2 + 4\ln(r_2/r_3)} \quad (4.54)$$

Where $u_l(m\,s^{-1})$, r_2 and r_3 are average velocity of absorbent in the shell, outer radius of fiber and radius of free surface. The term r_3 can be calculated using Equations 4.31 and 4.32 presented in preceding section.

4.2.2.3 Reaction and absorption kinetics

The four ILs selected for the current study, [N_{1111}][Gly], [emim][Gly], [bmim][Gly] and [hmim][Gly] have the same glycine ([Gly]) anion and different cations. The mechanism is similar for the above-mentioned amino acid-based ILs. Glycine based aqueous alkaline salts show similar reactivity for CO_2 as of primary alkanolamines (Jing et al., 2012; Kumar et al., 2003; Wu et al., 2015). The zwitterion mechanism proposed by Caplow, (1968) for primary alkanol amines is considered as a reaction mechanism for amino acid-based ILs here. CO_2 reacts with the amino acid-based ILs via the formation of zwitterion due to the deprotonation by a base present in the aqueous solution (Jing et al., 2012) :

$$H_2N - CH_2 - COO^-R^+ + CO_2 \rightleftharpoons_{K_1}^{K_2} {}^-OOC^+H_2N - CH_2 - COO^-R^+ \quad (4.55)$$

$$^-OOC^+H_2N - CH_2 - COO^-R^+ + B_i \rightarrow^{K_{B_i}} {}^- OOCHN - CH_2 - COO^-R^+ + B_iH^+ \quad (4.56)$$

B_i is the base present in the solution to deprotonate zwitterions. Liquid phase equilibrium reactions considered are the following:

$$^-OOCHN - CH_2 - COO^-R^+ + H_2O \rightleftharpoons H_2N - CH_2 - COO^-R^+ + HCO_3^- \quad (4.57)$$

$$H_3N - CH_2 - COO^-R^+ \rightleftharpoons H_2N - CH_2 - COO^-R^+ + H^+ \quad (4.58)$$

$$CO_2 + H_2O \rightleftharpoons H^+ + HCO_3^- \quad (4.59)$$

$$HCO_3^- \rightleftharpoons H^+ + CO_3^- \quad (4.60)$$

$$H_2O \rightleftharpoons H^+ + OH^- \quad (4.61)$$

The criterion to determine whether the reaction completely occurs in the bulk or in the liquid film is based on the Hatta number. Hatta number can be defined as under:

$$H_a = \frac{\sqrt{D_iK_o}}{k_l} \quad (4.62)$$

Where K_o and k_l represent the overall reaction rate constant (s^{-1}) and liquid film mass transfer coefficient (m s^{-1}). To confirm the fast pseudo-first-order regime, the Hatta number must follow the criterion of $2 < H_a \ll E_\infty$ (Danckwerts, 1970; Jing et al., 2012). E_∞ represents infinite enhancement factor. When this criterion is fulfilled, the reaction of CO_2 and amino acid based ILs can be considered as in the fast pseudo first order regime which means that change in the concentration of the absorbent is negligible and reaction is of the first order for CO_2 (Kierzkowska-Pawlak, 2012). ILs $[N_{1111}][Gly]$ (Jing et al., 2012), [emim][Gly] (Wu et al., 2015), [bmim][Gly] (Wu et al., 2016) and [hmim][Gly] (Guo et al., 2013) fulfill the criteria of fast pseudo-first-order reaction regime for a range of concentrations. Enhancement factors, Hatta numbers, and second-order rate constants are presented in Table 4.3. The second-order reaction rate was temperature-dependent and increased with an increase in temperature. The kinetic data for all four ILs (at 1M Concentration) were calculated from the Arrhenius plot and are presented in Table 4.3.

Table 4.3 Enhancement factor (E), Hatta number (H_a) and rate constant (K_2) for the ILs

IL concentration (mole L^{-1})	**E 303 K**	**H_a 303 K**	**K_2 (L mol^{-1} s^{-1}) 303 K**	**K_2 (L mol^{-1} s^{-1})**	**Ref.**
$[N_{1111}][Gly]$					
0.3	14.56	14.56	242.16	-	(Jing et al., 2012)
0.7	34.39	34.39	719.34	-	(Jing et al., 2012)
1.0	41.33	41.33	736.93	$4.6930\ 10^5$ exp (-1856/T)	(Jing et al., 2012)
2.0	62.68	62.68	1297.13	-	(Jing et al., 2012)
$[C_2mim][Gly]$					
0.5	23.67	23.67	296.29	-	(Wu et al., 2015)
1.0	51.58	51.58	662.95	$6.041\ 10^6$ exp (-2801/T)	(Wu et al., 2015)
1.5	87.57	87.57	1213.52	-	(Wu et al., 2015)
2.0	107.15	107.15	1280.78	-	(Wu et al., 2015)
$[C_4mim][Gly]$					
0.5	28.31	28.31	417.52	-	(Wu et al., 2016)
1.0	52.65	52.65	675.51	$1.3460\ 10^{10}$ exp (-5038/T)	(Wu et al., 2016)
1.5	102.27	102.27	1539.38	-	(Wu et al., 2016)
2.0	139.49	139.49	1955.60	-	(Wu et al., 2016)
$[C_6mim][Gly]$					
0.5	36.02	36.02	759.22	-	(Guo et al., 2013)
0.8	48.86	48.86	1091.81	-	(Guo et al., 2013)

1.0	57.50	57.50	1402.38	3.04 10^7 exp (-3050/T)	(Guo et al., 2013)
1.2	66.75	66.75	1855.99	-	(Guo et al., 2013)

4.2.2.4 Solubility, phase equilibria, and diffusion coefficients

The interfacial phase equilibrium for the absorption species can be defined as follows:

$$C_l = H_d\, C_g \tag{4.63}$$

Where H_d is the dimensionless distribution coefficient for the absorption species which can be calculated as below:

$$H_d = \acute{R}TS \tag{4.64}$$

where $S(mol\, m^{-3}Pa^{-1})$ represents the solubility of the absorption species. The solubility of CO_2 in IL $[N_{1111}][Gly]$ was estimated by Jing et al. (2012) using the Schumpe model (Schumpe, 1993; Weisenberger and Schumpe, 1996) presented below:

$$\log\left(\frac{S_w}{S_i}\right) = \sum(h_i + h_g)C_i \tag{4.65}$$

Where h_i and h_g represent ion and gas specific constants, respectively and C_i is ion concentration. The solubility of CO_2 in water was calculated as under (Versteeg and van Swaaij, 1988):

$$S_w = 3.54\ 10^{-7} \exp\left(\frac{2044}{T}\right) \tag{4.66}$$

The solubility of [emim][Gly], [bmim][Gly] and [hmim][Gly] was calculated according to the regular solution theory. For ILs the Henry law constant $H(Pa)$ decreases with an increase in solubility. The regular solution theory is presented below:

$$\ln H = a + \frac{b(\delta_1 - \delta_2)^2}{T} \tag{4.67}$$

Where $\delta\ (Jcm^{-3})^{\frac{1}{2}}$ represents the solubility parameter, while $a\ (Jcm^{-3})^{-1}$ and $b(Jcm^{-3})^{-1}$ are constants depending on the gas (Barton, 1991; Camper et al., 2005).

The solubility of CO_2, $S(mol\, m^{-3}Pa^{-1})$ in aqueous solutions of [emim][Gly], [bmim][Gly] and [hmim][Gly] was found from the Henry law using the parameter H (Sander, 2015).:

$$S = \frac{10\,\rho}{M\,H} \tag{4.68}$$

Diffusivity of CO_2 and N_2 in the gas phase can be found using the correlation (Equation 4.39) developed by Fuller et al. (1966). While Diffusivity of CO_2 and N_2 in the membrane can be calculated using Equations 4.39-4.42 presented in the preceding sections.

The aqueous solutions of $[N_{1111}][Gly]$, [emim][Gly], [bmim][Gly] and [hmim][Gly] are electrolyte solutions. Equations developed by Barret (Barrett, 1966) and Danckwerts (Danckwerts, 1970) were used to calculate the diffusivities of CO_2 in these solutions:

$$(D_l\,{\mu_l}^{0.8})_T = (D_w\,{\mu_w}^{0.8})_T \tag{4.69}$$

$$\log D_w = -8.1764 + \frac{712.5}{T} - \frac{2.591\,10^5}{T^2} \tag{4.70}$$

4.2.2.5 Meshing, boundary conditions and numerical resolution

Meshing and proper discretization of the geometry are very important for the finite element analysis. The current absorption process is mostly controlled by the liquid side resistance. Therefore, a rigorous absorption model with enough discretization is needed. Moreover, interfacial chemical reactions were considered in the current absorption process, as it can also be confirmed from the analysis in Section 4.2.2.3 and the high values of Hatta number presented in Table 4.3. Refined mapped (rectangular shaped) meshing was implemented across the symmetrical geometry with more refining along with the interface and inside the membrane. The meshed surface along with the labeled boundary conditions (BCs) is presented in Figure 4.4. Boundary conditions for both mass and energy transport equations are presented in Table 4.4.

Table 4.4 Boundary conditions for non-isothermal model.

Boundary	**Tube Side**		**Porous Membrane**		**Shell Side**	
	Mass	**Energy**	**Mass**	**Energy**	**Mass**	**Energy**
$\boldsymbol{z = 0}$	$C_l = C_{l-in}$	$T_l = T_{l-in}$	$-D_m\frac{\partial C_m}{\partial z} = 0$	$\frac{\partial T_m}{\partial z} = 0$	$-D_g\frac{\partial C_g}{\partial z} = 0$	$-\lambda_g\frac{\partial T_g}{\partial z} = 0$
$\boldsymbol{z = L}$	$-D_l\frac{\partial C_l}{\partial z} = 0$	$-\lambda_l\frac{\partial T_l}{\partial z} = 0$	$-D_m\frac{\partial C_m}{\partial z} = 0$	$\frac{\partial T_m}{\partial z} = 0$	$C_g = C_{g-in}$	$T_g = T_{g-in}$

$\boldsymbol{r = 0}$	$\frac{\partial C_{i,l}}{\partial r} = 0$	$\frac{\partial T_l}{\partial r} = 0$	-	-	-	-
$\boldsymbol{r = r_1}$	$C_l = H_d C_m$	$T_l = T_m$	$C_m = \frac{C_l}{H_d}$	$T_m = T_l$	-	-
$\boldsymbol{r = r_2}$	-	-	$C_m = C_g$	$T_m = T_g$	$C_g = C_m$	$T_g = T_m$
$\boldsymbol{r = r_3}$	-	-	-	-	$\frac{\partial C_{i,g}}{\partial r} = 0$	$\frac{\partial T_g}{\partial r} = 0$

The set of 2D model equations presented in the preceding sections are boundary value problems of the partial differential equation system. The model was developed and solved using COMSOL Multiphysics® which uses the finite element method. The solved model was post-processed in MATLAB® and Microsoft Excel.

Chapter 5. Post-combustion CO_2 Capture

This chapter presents the characterization of ILs, membranes and the experimental outcomes of the post-combustion carbon dioxide capture with ILs in HFMC. The materials, characterization techniques and methodology of the experiments are described in Chapter 3. The following publications from the authors correspond to this Chapter.

- Sohaib, Q., Vadillo, J.M., Gómez-Coma, L., Albo, J., Druon-Bocquet, S., Irabien, A., Sanchez-Marcano, J., 2020. Post-Combustion CO_2 Capture by Coupling [emim] Cation Based Ionic Liquids with a Membrane Contactor; Pseudo-Steady-State Approach. *Int J Greenh Gas Control*
- Sohaib, Q., Vadillo, J.M., Gómez-Coma, L., Albo, J., Druon-Bocquet, S., Irabien, A., Sanchez-Marcano, J., 2020. CO_2 Capture with Room Temperature Ionic Liquids; Coupled Absorption/Desorption and Single Module Absorption in Membrane Contactor. *Chem. Eng. Sci.*

ILs and membrane properties and characterization

5.1.1 IL properties and characterization

There are various fundamental properties that need to be considered for an absorbent to be used in membrane contactors; they include viscosity, surface tension, CO_2 diffusivity, CO_2 solubility and thermal stability of the absorbent. Some of these properties have been experimentally measured in this work, others have been calculated or obtained from literature. Table 5.1 below reports the values of these properties for [emim][Ac], [emim][$MeSO_4$], [emim][$EtSO_4$] and [emim] [DCA].

CO_2 solubility and Henry's law constant (H (Bar)), are important parameters to characterize the capacity of ILs for CO_2 absorption. A low value of the Henry's law constant indicates very high gas solubility (Anthony et al., 2002a; Lei et al., 2014). The magnitude of this constant also indicates the physical and chemical nature of the absorption. Smaller values of Henry's law constant (H <30 Bar) denote the chemical absorption nature of the absorbent for CO_2 (Wang et al., 2011; Yokozeki et al., 2008). Table 5.1 shows equilibrium concentration of CO_2 in IL at specified pressure and temperature and Henry's law constants. As can be seen

from the Table, the solubility is negatively affected with increase in temperature which is also confirmed by Lei et al. (2014) and Okoturo and VanderNoot, (2004). According to the values reported in the table, in terms of CO_2 solubility the four ILs are ranked as: [emim][Ac] > [emim][$EtSO_4$] > [emim][$MeSO_4$] > [emim] [DCA].

Viscosity is another important parameter, which affects the flow of absorbent in membrane contactors and affects the diffusivity of CO_2 in the absorbent. A higher viscosity not only reduces the overall mass transfer coefficient but also increases the liquid side pressure drop in membrane contactors, especially when operating at room temperature (Zhao et al., 2016). Among the ILs considered for this study, [emim][DCA] has the lowest values of viscosity (4-6 times lower than other three ILs), as shown in table 5.1. Viscosities of ILs [emim] [DCA], [emim] [$MeSO_4$], [emim][$EtSO_4$] and [emim][Ac] at 298 K are reported to be 15.1 mPa s, 78.1 mPa s, 97 mPa s and 141.1 mPa s, respectively. An increase in temperature decreases viscosity which is a favorable feature for enhanced diffusivity. Temperature dependency of viscosity for the four ILs [emim][Ac], [emim][$EtSO_4$], [emim][$MeSO_4$] and [emim][DCA] have been studied by Nazet et al. (2015), Schmidt et al. (2012), Costa et al. (2011), Quijada-Maldonado et al. (2012), and Vataščin and Dohnal, (2017) respectively. It can be observed from Table 5.1 that increase in temperature has effectively decreased the viscosity of ILs and increased the diffusivity of CO_2 in ILs. CO_2 diffusivities in ILs were calculated using the correlation (Equation 4.6) developed by Morgan et al. (2005). This correlation confirms the inverse effect of the viscosity on CO_2 diffusivity. Other correlations developed for CO_2 diffusivity in ILs also confirm the strong dependency of CO_2 diffusivity on viscosity and their inverse relation (Moganty and Baltus, 2010; Moya et al., 2014; Ying and Baltus, 2007; Zubeir et al., 2015). Diffusivities of the ILs [emim] [DCA], [emim] [$MeSO_4$], [emim][$EtSO_4$] and [emim][Ac] at 298 K are reported to be 1.15 10^{-5} cm^2 s^{-1}, 3.9 10^{-6} cm^2 s^{-1}, 3.38 10^{-6} cm^2 s^{-1} and 2.64 10^{-6} cm^2 s^{-1}, respectively. Diffusivity of [emim][DCA] is one magnitude higher than diffusivities of other three ILs due to far lower viscosity compared to other ILs. In terms of viscosity and diffusivity these ILs can be ranked as [emim][DCA] > [emim][$MeSO_4$] > [emim][$EtSO_4$] > [emim][Ac].

Surface tension is a fundamental parameter for absorbents to be used with porous membrane contactors as it can describe the pore wetting resistance of membrane for absorbents and affects the LEP which is a critical parameter to prevent pore wetting of membrane (Zhao et al., 2016). Values of surface tension for all four ILs were measured by the method described in section 2.2 and reported in Table 5.1. The contact angle for water was also measured and

reported as reference. Values of surface tension show a gradual decrease with increase in temperature. IL [emim][$MeSO_4$] shows the highest surface tension of 52.6 mN m^{-1} at 288 K, among other ILs studied here.

The above described findings confirmed that temperature has two opposite effects on the absorption of CO_2 in room temperature ILs. Increase in temperature significantly reduces the viscosity of ILs, thus enhancing CO_2 diffusivity while CO_2 solubility in ILs decreases as Henry's law constant increases. Thus, thermal stability of liquid absorbents is an important parameter which can be fundamental when treating hot flue gases or during stripping process at relatively high temperature. Thermal stability of ILs was tested using TGA analysis. Samples were heated from 18 ^oC to 450 ^oC. The results in Figure 5.1 confirm the higher thermal stability of the ILs. IL [emim][$MeSO_4$] presents only 4% of loss until 200 ^oC and reaches to 90 % until 450 ^oC. IL [emim][DCA] shows 4 % weight loss until 270 ^oC and undergoes only 60 % loss when reaching 450 ^oC. IL [emim][$EtSO_4$] shows only 4 % weight loss until 300 ^oC, after this temperature it starts degrading and losses 80 % until 400 ^oC. IL [emim][Ac] loses only 2 % weight until 200 ^oC, after this temperature it starts degrading and reaches almost 100 % loss near 280 ^oC. All the initial minor losses from 2-4 % can be attributed as losses of water from the samples. In conclusion, all four studied ILs can be applied at temperatures below 200°C.

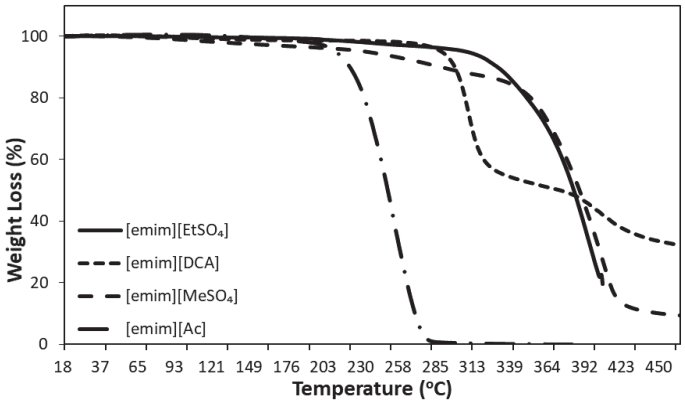

Figure 5.1 TGA analysis of ILs

Table 5.1 Properties of ILs and parameters for CO_2 absorption

IL	T(K)	x*/P (Bar)	Ref.	H_{px} (Bar)	Ref.	ρ (g cm^{-3})	Ref.	μ (mPa s)	Ref.	D_{CO_2} (cm^2 s^{-1}) 10^6	Ref.	ϒ (mN m^{-1})	Ref.
[emim][$MeSO_4$]	288	-	-	-	-	1.289	(Costa et al., 2011)	128.6	(Costa et al., 2011)	2.81	This Work	52.6	This Work
	298	0.033/2.7	This Work	81.8	This Work	1.286	(Costa et al., 2011)	78.1	(Costa et al., 2011)	3.90	This Work	51.2	This Work
	313	0.031/2.7	This Work	87.1	This Work	1.275	(Costa et al., 2011)	42.9	(Costa et al., 2011)	5.80	This Work	50.5	This Work
[emim][DCA]	288	-	-	-	-	1.114	(Klomfar et al., 2011)	19.5	(Larriba et al., 2013)	9.76	This Work	46.4	This Work
	298	0.035/2.6	This Work	74.3	This Work	1.108	(Klomfar et al., 2011)	15.1	(Larriba et al., 2013)	11.56	This Work	45.4	This Work
	313	0.032/2.6	This Work	86.6	This Work	1.098	(Klomfar et al., 2011)	10.2	(Larriba et al., 2013)	14.97	This Work	45.0	This Work
[emim][$EtSO_4$]	288	-	-	-	-	1.241	(Gómez et al., 2006)	152.0	(Gómez et al., 2006)	2.51	This Work	46.8	This Work
	298	0.059/2.7	This Work	45.7	This Work	1.237	(Gómez et al., 2006)	97.0	(Gómez et al., 2006)	3.38	This Work	46.3	This Work
	313	0.049/2.7	This Work	55.1	This Work	1.227	(Gómez et al., 2006)	50.9	(Gómez et al., 2006)	5.18	This Work	45.2	This Work
[emim][Ac]	288	-	-	-	-	1.105	(Nazet et al., 2015)	288.0	(Nazet et al., 2015)	1.65	This Work	47.3	This Work
	298	0.26/2.6	This Work	10.0	This Work	1.099	(Nazet et al., 2015)	141.1	(Nazet et al., 2015)	2.64	This Work	46.8	This Work
	313	0.23/2.6	This Work	11.3	This Work	1.087	(Nazet et al., 2015)	78.2	(Nazet et al., 2015)	3.90	This Work	45.9	This Work

5.1.2 Membrane properties and characterization

Selection of membrane is also very important for membrane contactor gas liquid absorption process. In this study, a mesoporous hydrophobic polypropylene membrane is used. PP material is resistant to dissolution in solvents and is suitable for low temperature applications (Mansourizadeh and Ismail, 2009).

Surface morphology of membrane was characterized by SEM analysis to investigate effect of long-term contact between ILs and the membrane. The surface of the porous membrane was analyzed before and after immersion for 20 days in ILs. Wang et al. (2005) has reported significant changes in surface morphologies and degradation due to various solvents. In the present work however, no evident changes can be observed for all ILs. Figure 5.2 shows SEM of the surface (at x 1.00 k magnification) and porous structure (at x 50.0 k magnification) of membrane before and after immersion in [emim][$MeSO_4$]. Similar effects were confirmed for the other three ILs. These SEM confirm that there are no noticeable effects of ILs on surface and porous structure of PP membrane.

Contact angle measurements were carried out to confirm the absence of pore wetting and of degradation due to solvent as suggested by SEM observations above. The contact angle represents the polarity difference between the membrane surface and the fluid (Gabelman and Hwang, 1999). It is important to notice that contact angle measurements are precise for flat and dense materials. However, in this case we have fibers which are cylindrical and porous. Indeed, contact angle measurements are given only as an indication of possible modifications of the hydrophobicity before and after 40 days of immersion of fiber in ILs and water and not as quantitative results. Table 5.2 shows contact angles of four ILs before and after immersion experiments. Visuals of the measurements are presented in Figure 5.3 below. PP fibers were cleaned properly before measurements, and each angle was measured 15 times. PP fiber showed higher contact angle of 101.9^O with water. Contact angles measured for IL [emim][$MeSO_4$] and [emim][DCA] were higher than that of [emim][$EtSO_4$] and [emim][Ac]. Before immersion the angles measure for [emim][$MeSO_4$], [emim], [emim][$EtSO_4$] and [emim][Ac] were 84.2^O, 82.9^O, 71.1^O and 72.9^O, respectively. There is only 1^O-2^O drop in contact angles measured after 40 days of immersion of fiber in ILs. Finally, it can be concluded from negligible variations in the contact angles that there was no physical or chemical interaction between ILs and membrane material.

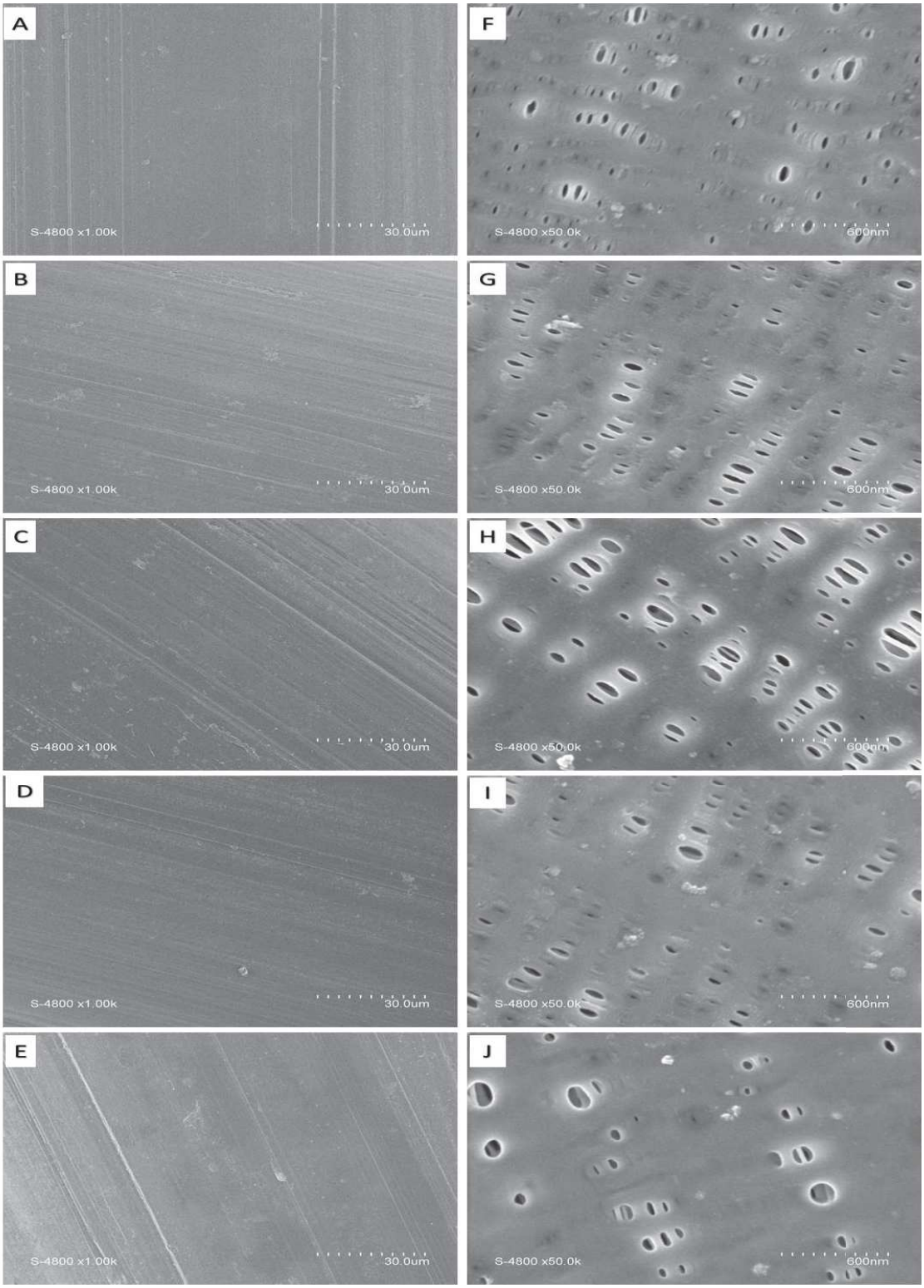

Figure 5.2 Scanning electron micrographs for (A) non-immersed PP fibers surface; surface of PP fibers immersed for 20 days in (B) [emim] [$MeSO_4$], (C) [emim] [DCA], (D) [emim] [$EtSO_4$] and (E)[emim][Ac]; (F) non-immersed PP fiber pores; pores of PP fibers immersed for 20 days in (G) [emim] [$MeSO_4$], (H) [emim] [DCA], (I) [emim] [$EtSO_4$] and (J)[emim][Ac].

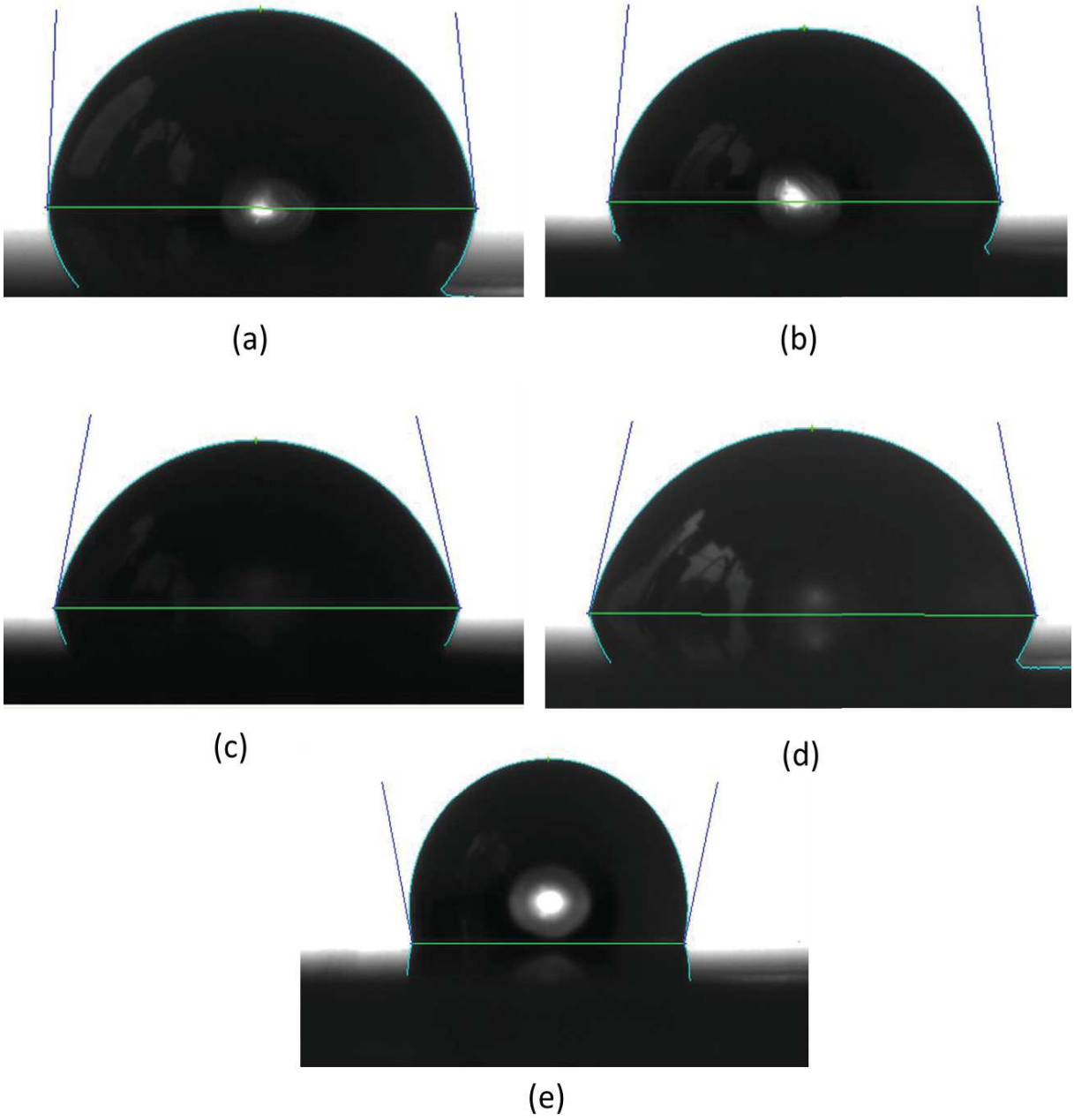

Figure 5.3 Contact angle of absorbents with PP membrane fiber (a) [emim] [$MeSO_4$], (b), [emim][DCA] (c) [emim] [$EtSO_4$], (d) [emim][Ac] and (e) Water.

LEP is another key parameter which is used to evaluate the wettability of porous membrane for liquid absorbents (Zhao et al., 2015a, 2015b). LEP defines the minimum pressure applied on the liquid to enter the membrane pores, which is estimated by Laplace-Young equation (Gabelman and Hwang, 1999; Kumar et al., 2002) given here below:

$$LEP = \Delta P = -\frac{4B\,\gamma\cos\beta}{d_{max}} \quad (5.1)$$

Where B represents pore geometry coefficient (B=1 for cylindrical pores; 0 < B < 1 for non-cylindrical pores), β is the contact angle between liquid absorbent and membrane and d_{max} is the maximum pore diameter of the membrane. According to Laplace-Young equation LEP is favored by small pore size and high surface tension. LEP of all ILs and water for membrane contactor used in this current study are presented in Table 5.2. In order to avoid wetting of the pores, transmembrane pressure for the current absorption process in membrane contactor was kept lower than the measured LEP.

Table 5.2 Contact angle and LEP of ILs and PP membrane contactor

Absorbent	**Contact Angle (deg)**		**LEP (Bar)**
	Before immersion	**After immersion**	
[emim][$MeSO_4$]	84.2	82.2	1.95
[emim][DCA]	82.9	81.0	2.19
[emim][$EtSO_4$]	71.1	71.0	5.70
[emim][Ac]	72.9	69.6	5.21
Water	101.9	-	5.65

5.2 CO_2 capture; single module absorption operation

5.2.1 CO_2 absorption in membrane contactor

CO_2 absorption experiments were carried out with four ILs coupled with PP membrane contactor according to the methodology described in chapter 3. Efficiency of the absorption process was evaluated at different gas flowrates and process temperatures using Equation 5.2 presented below.

$$Efficiency\ (\%) = \left(1 - \frac{C_{g-out}}{C_{g-in}}\right)100 \quad (5.2)$$

Figure 5.4 shows CO_2 removal efficiency based on the output gas phase, at different gas flowrates.

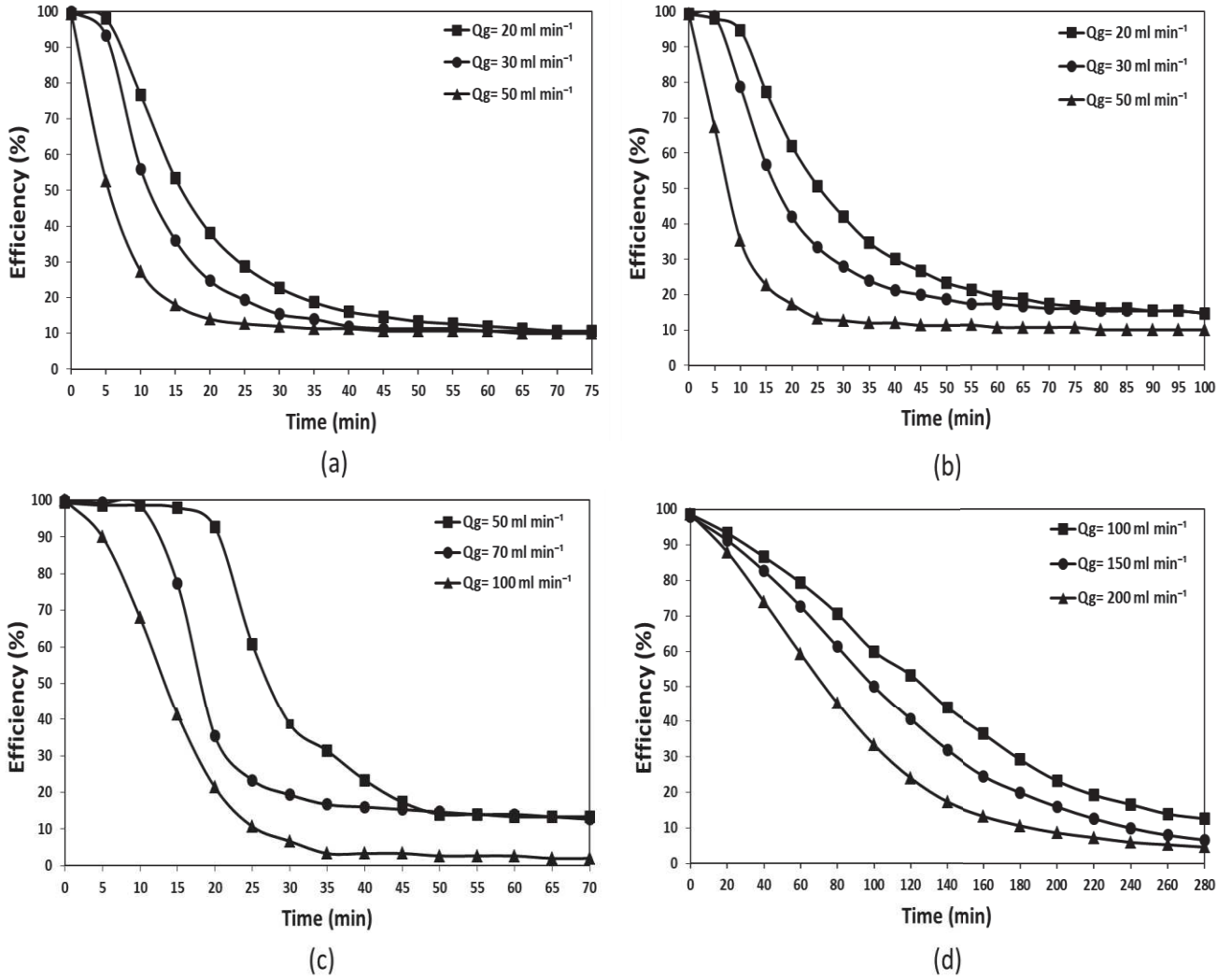

Figure 5.4 CO_2 removal efficiency against operation time for IL (a) [emim] [$MeSO_4$], (b), [emim][DCA] (c) [emim][$EtSO_4$] and (d) [emim][Ac] at T=288 K.

CO_2 removal efficiency is generally favored by lower gas flowrates. Initially the CO_2 concentration at the output gas phase increases very fast and slows down with time until reaching pseudo-steady-state. At pseudo-steady-state, the increase in CO_2 concentration becomes very slow and concentration can be considered constant with time. At lower gas flowrates the efficiency remains almost 100%, initially, as the IL can absorb more CO_2. An increase in gas flowrate reduces the CO_2 removal efficiency due to minimal residence time of gas inside the contactor (Yan et al., 2007; Yeon et al., 2005). Despite the reduction in efficiency with increase in gas flowrate, there is enhancement in the mass transfer due to greater average concentration of CO_2 on the gas side due to which the amount of CO_2 on the liquid side increases (Li and Chen, 2005; Zhang et al., 2006). Absorption with IL

[emim][$EtSO_4$] shows 98% efficiency even after 20 minutes and 15 minutes of recirculation at gas flowrate of 50 ml.min^{-1} and 70 ml.min^{-1}, respectively. Generally, ILs dissolve a certain amount of CO_2, which is mostly considered to be physisorption for RTILs (Gurau et al., 2011; Maginn, 2005). However, the initial faster absorption can be explained by the complex formation at gas liquid interface, which is more chemical in nature, as the IL has very lower CO_2 concentration during initial recirculation. The absorption becomes slower with time due to physical absorption in the bulk of the liquid and due to lower diffusivities of the ILs, until it reaches pseudo-steady-state. Gas flowrate has evident effect on the outlet concentration and removal efficiency of CO_2. For ILs [emim][$MeSO_4$] and [emim][DCA] after 10 minutes, a decrease in removal efficiency of 43 % and 58 %, respectively, was observed by using 50 ml.min^{-1} instead of 20 ml.min^{-1} of gas flowrate. For [emim][$EtSO_4$] after 10 minutes an efficiency drop of 28 % was recorded by increasing the gas flowrate from 50 ml.min^{-1} to 100 ml.min^{-1}. After 60 minutes of recirculation, the efficiency drop for [emim][Ac] was 20 % by applying 200 ml.min^{-1} instead of 100 ml.min^{-1} of gas flowrate. Apart from few exceptions, the pseudo-steady-state efficiency was not much affected by the gas flowrate. IL [emim][Ac] was observed to be far more efficient than other ILs, as even at the highest gas flowrate (200 ml.min^{-1}) it took 280 minutes to reach pseudo-steady-state. This phenomenon can also be confirmed from its very lower value of Henry constant. Despite being a RTIL, CO_2 absorption in IL [emim][Ac] is considered to be a chemisorption process (Gurau et al., 2011; Yokozeki et al., 2008). Gas flowrates were selected for ILs according to their performance. ILs operated at low gas flowrates were not able to withstand absorption for enough time at high flowrates, while those operated at high gas flowrates were too slow to reach pseudo-steady-state at low gas flowrates.

ILs used are thermally stable and there is no effect on the vapor pressure in the investigated range of current study. Temperature has two opposite effects on the absorption of CO_2 in ILs. It decreases viscosity of the IL thus enhances CO_2 diffusivity in ILs. But CO_2 solubility in RTILs is negatively affected by temperature. An increase in temperature reduces the CO_2 solubility and increases the Henry's law constant (Lei et al., 2014; Okoturo and VanderNoot, 2004). When temperature rises from 298 K to 313 K the values of Henry's law constant for IL [emim][DCA] and [emim][$EtSO_4$] increases from 74.3 Bar to 81.3 Bar and 45.7 Bar to 55.1 Bar, respectively. Figure 5.5 shows the evolution of efficiency and therefore of gas side outlet concentration of CO_2 at different temperatures. It is clear from the figure that increase in temperature has reduced the removal efficiency. However, the efficiency at pseudo-steady-

state remains nearly unaffected. When the temperature is enhanced from 288 K to 313 K and at 20 minutes of recirculation time, an efficiency drop of 12 %, 8 % and 31 % was observed for ILs [emim] [$MeSO_4$], [emim][DCA] and [emim] [$EtSO_4$], respectively. For [emim][Ac] when temperature was increased from 288 K to 323 K and after 80 minutes, a drop of 17 % in removal efficiency can be observed.

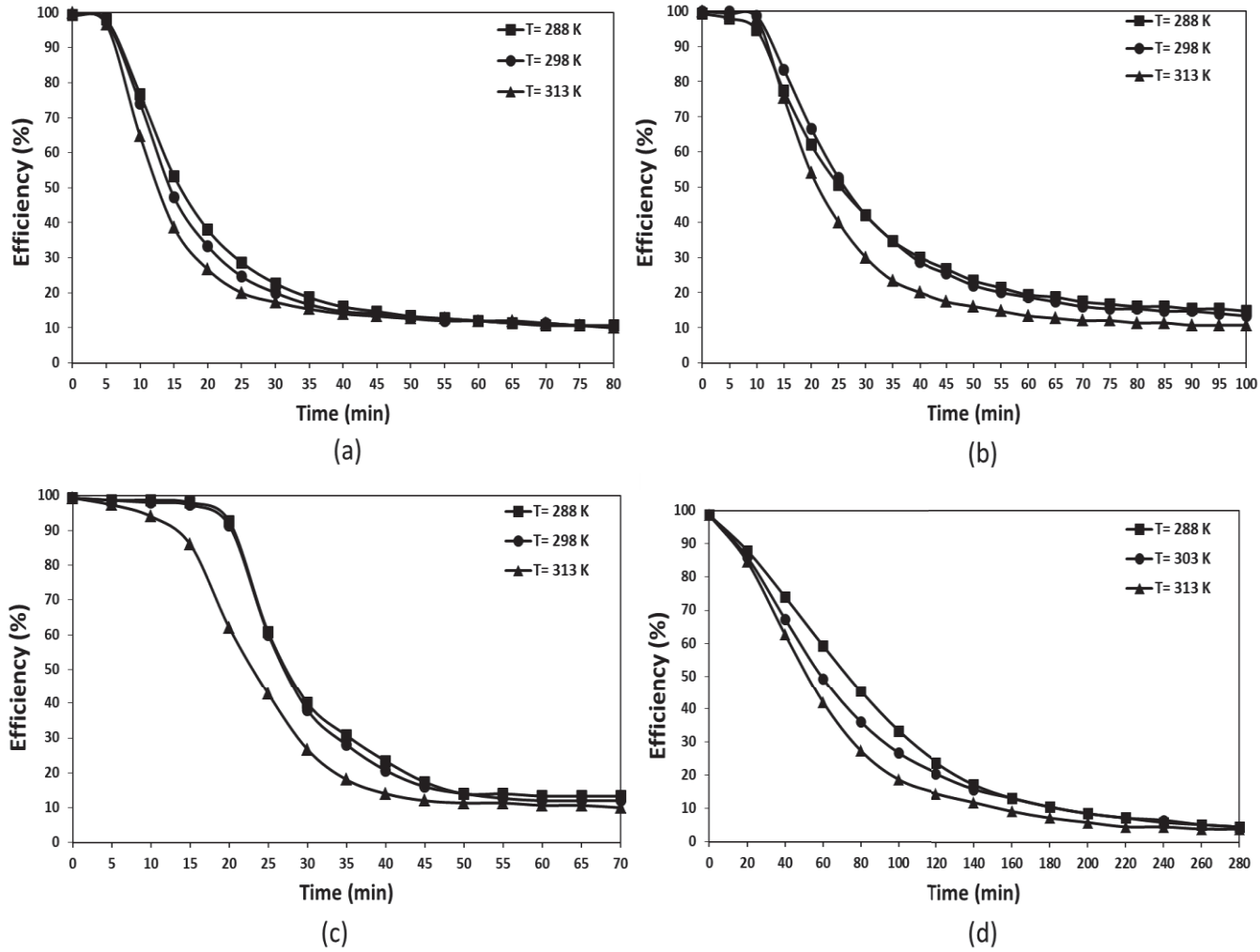

Figure 5.5 CO_2 removal efficiency against operation time for IL (a) [emim][$MeSO_4$] (Q_g=20 ml min^{-1}), (b) [emim][DCA] (Q_g=20 ml min^{-1}), (c) [emim][$EtSO_4$] (Q_g=50 ml min^{-1}) and (d) [emim] [Ac](Qg=100 ml min^{-1}).

5.2.2 Mass transfer kinetics

5.2.2.1 Mass transfer coefficient and CO_2 flux: Effect of gas flowrate, temperature and CO_2 loading

As discussed in previous section, increase in gas flowrate enhances mass transfer of CO_2 and its concentration on the liquid side. Both, mass transfer flux (mol m^{-2} s^{-1}) and experimental overall mass transfer coefficient (m s^{-1}) increase with gas flowrate enhancement. The results which are reported in Figure 5.6 show that for [emim][$MeSO_4$] and [emim] [DCA], the increase of gas flowrate from 20 ml min^{-1} to 50 ml min^{-1}, enhances the CO_2 flux and experimental mass transfer coefficient from 1.2 10^{-5} mol m^{-2} s^{-1} to 3.1 10^{-5} mol m^{-2} s^{-1} and 9.3 10^{-6} m s^{-1} to 2.3 10^{-5} m s^{-1}, respectively. In the case of IL [emim][$EtSO_4$] when gas flowrate is increased from 50 ml min^{-1} to 100 ml min^{-1}, it is observed an enhancement from 3.1 10^{-5} mol m^{-2} s^{-1} to 6.2 10^{-5} mol m^{-2} s^{-1} and 2.3 10^{-5} m s^{-1} to 4.6 10^{-5} m s^{-1}, respectively. For [emim][Ac] increasing gas flowrate from 100 ml min^{-1} to 200 ml min^{-1} results in an increase of CO_2 flux and experimental mass transfer coefficient from 6.2 10^{-5} mol m^{-2} s^{-1} to 1.2 10^{-4} mol m^{-2} s^{-1} and 4.6 10^{-5} m s^{-1} to 9.3 10^{-5} m s^{-1}, respectively. Liquid phase mass transfer coefficient remains unaffected by variations in gas flowrate.

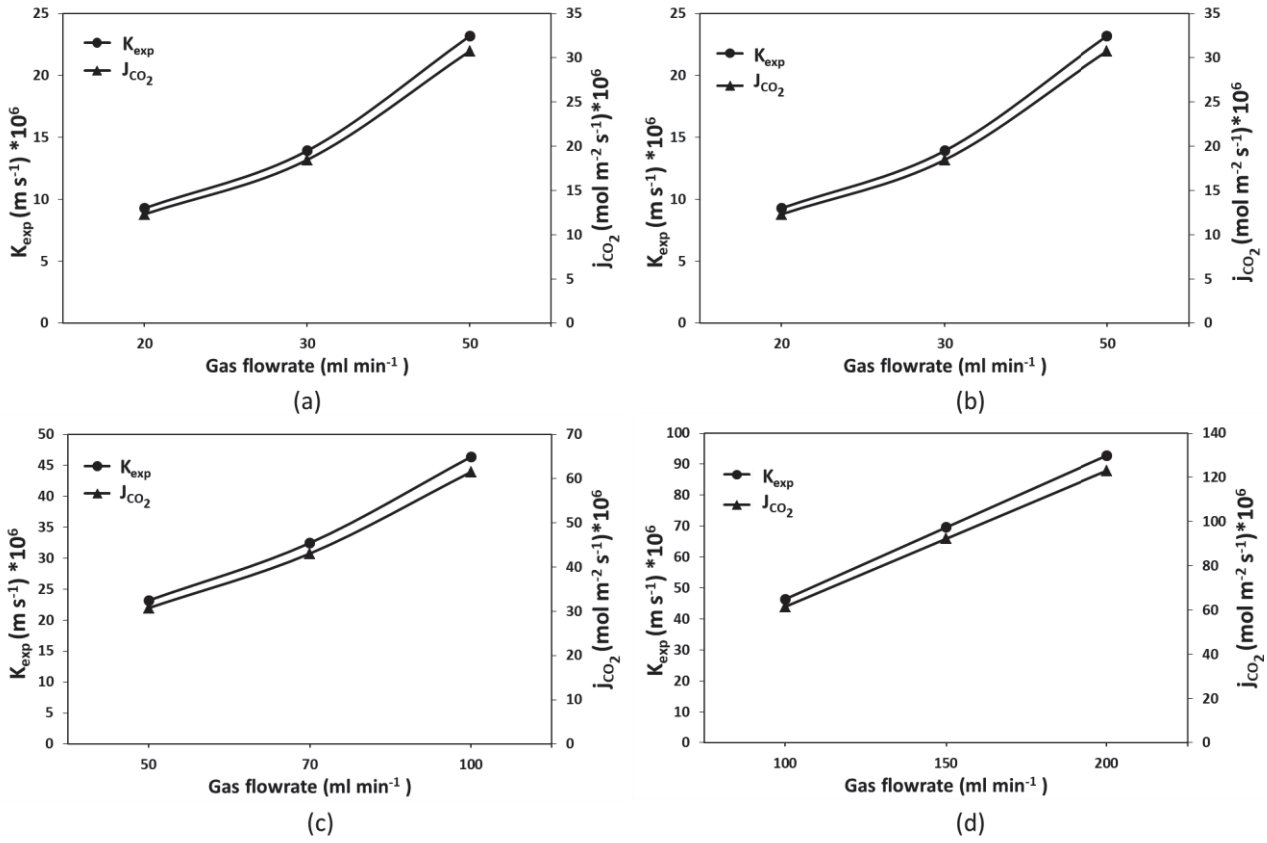

Figure 5.6 Effect of gas flowrate on CO_2 flux (j_{CO_2}) and experimental mass transfer coefficient (K_{exp}) for IL (a) [emim][$MeSO_4$], (b), [emim][DCA] (c) [emim][$EtSO_4$] and (d) [emim][Ac] at T=288 K.

As discussed previously, temperature affects both diffusion coefficient and Henry's law constant, both have opposite effects on mass transfer performance. To see the effect of temperature on mass transfer flux and experimental mass transfer coefficient; values were taken after few minutes of recirculation. The effects can be observed in Figure 5.7. Both mass transfer flux and experimental mass transfer coefficient decrease with temperature enhancement. However, the effect is much smaller compared to gas flowrate. Liquid side mass transfer coefficient is a function of diffusivity, Reynolds number and Schmidt number. Liquid side mass transfer coefficients show considerable amount of increase with increase in temperature as all the above-mentioned parameters are temperature dependent. For ILs [emim][$MeSO_4$], [emim] [DCA], [emim][$EtSO_4$] and [emim][Ac] if temperature is increased from 288 K to 313 K, liquid mass transfer coefficient increases from 2.3 10^{-6} m s^{-1} to 4.5 10^{-6} m s^{-1}, 1.7 10^{-6} m s^{-1} to 10.3 10^{-6} m s^{-1}, 2.1 10^{-6} m s^{-1} to 4.0 10^{-6} m s^{-1} and 1.4 10^{-6} m s^{-1} to 3.1 10^{-6} m s^{-1}, respectively.

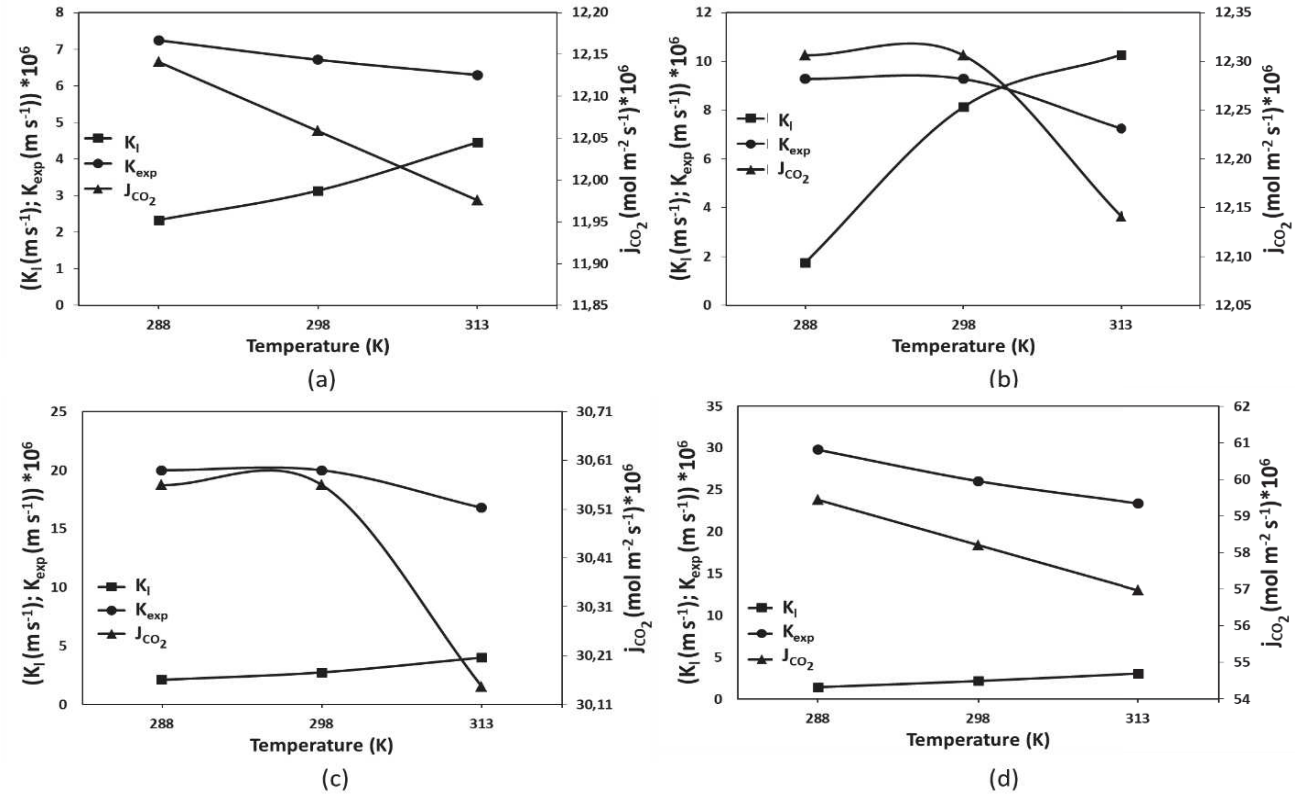

Figure 5.7 Effect of operation temperature on CO_2 flux (j_{CO_2}), experimental mass transfer coefficient (K_{exp}) and liquid mass transfer coefficient (K_l) for ILs (a) [emim][$MeSO_4$] (Q_g=20 ml min^{-1}), (b) [emim][DCA] (Q_g=20 ml min^{-1}), (c) [emim][$EtSO_4$] (Q_g=50 ml min^{-1}) and (d) [emim][Ac] (Q_g=100 ml min^{-1}).

CO_2 mass transfer flux and experimental mass transfer coefficients are continuously evolving with operation time as shown in Figure 5.8. These values decrease continuously but tend to reach a pseudo-steady-state where it becomes almost constant. It nearly takes 50-70 minutes for these values to be stable in case of [emim][$MeSO_4$], [emim][DCA] and [emim][$EtSO_4$] while for [emim][Ac] the pseudo-steady-state is not really reached at 280 minutes of experiment. The driving force for the mass transfer here is concentration gradient which continuously evolves with operation time due to accumulation of CO_2 on the liquid side. Both mass transfer flux and experimental mass transfer coefficient depend upon the logarithmic mean of the driving force. Logarithmic mean of the driving force continuously evolves due to the evolution of CO_2 concentration in the gas phase (C_g^*) in equilibrium with the corresponding CO_2 concentration in the liquid phase (C_l^*). The equilibrium at gas liquid interface was defined by Henry's law constant.

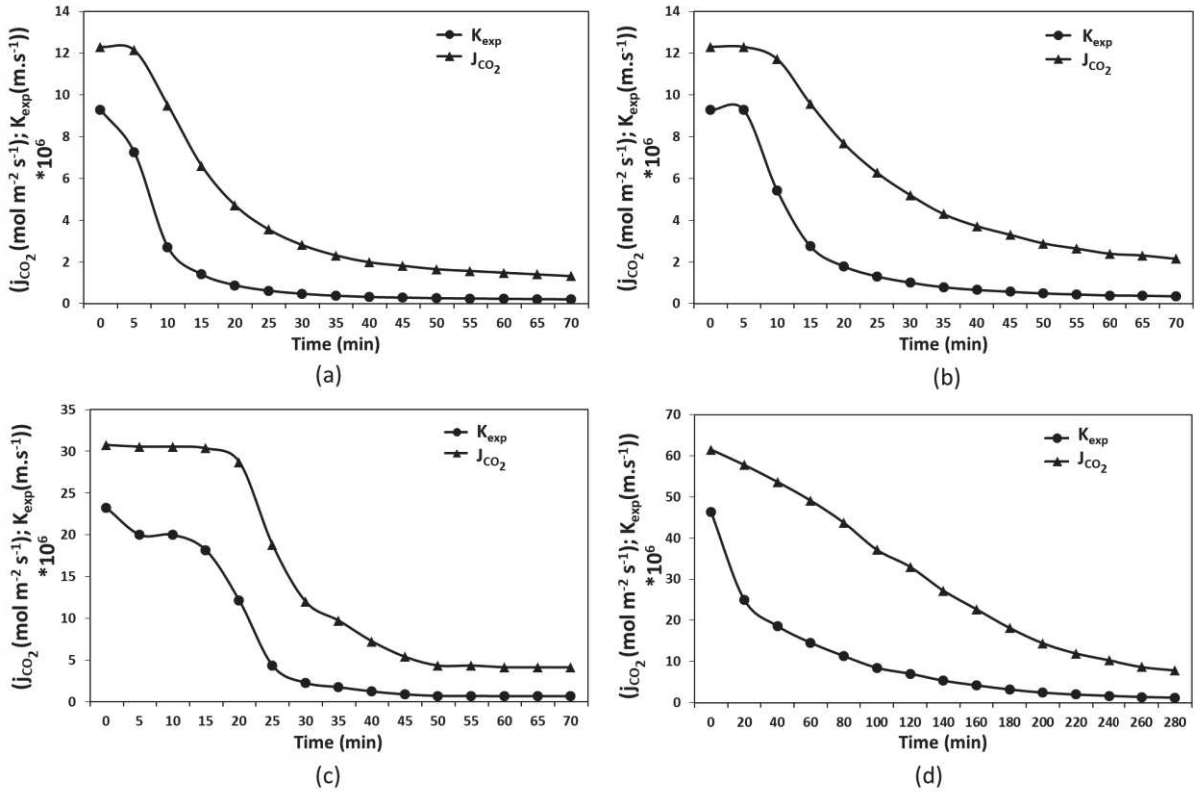

Figure 5.8 Variation of CO_2 flux (j_{CO_2}) and experimental mass transfer coefficient (K_{exp}) with operation time for four ILs (a) [emim][$MeSO_4$] (Q_g=20 ml min^{-1}), (b) [emim][DCA] (Q_g=20 ml min^{-1}), (c) [emim][$EtSO_4$] (Q_g=50 ml min^{-1}) and (d) [emim][Ac] (Q_g=100 ml min^{-1}) at T=288 K.

5.2.2.2 Enhancement factor and first order rate constant: Effect of CO_2 loading

During recirculation, ILs continuously absorbs CO_2, which accumulates on the IL which is recirculated in between shell side of the contactor and the tank. This accumulation slows down the gradient and then the mass transfer process and absorption kinetics. This phenomenon is explained here in terms of enhancement factor and first order rate constant. Enhancement factors and first order rate constants were calculated as explained in Section 4.1. In Figure 5.9 we can notice that absorption rate changes with time. Initially CO_2 loading (α_t) increases very rapidly but slows down with time as far as the number of recirculation loops increases. During the first ten minutes, [emim][$MeSO_4$], [emim][DCA] and [emim][$EtSO_4$] absorb respectively 56 %, 48 % and 48 % of the total absorption capacity CO_2, the rest of the CO_2 is absorbed during the last 70 minutes of the process. In case of [emim][Ac], 34 % of the total absorption capacity of CO_2 is done in the first 10 minutes, whereas the total absorption time was 280 minutes. The slow absorption rate of the ILs might be due to two reasons. Physical absorption in the bulk, which hinders the mass transfer due to high viscosity of ILs and low diffusivities and low driving force (concentration difference) due to high CO_2 loading in initial minutes. The enhancement factor is used to quantify the improvement of mass transfer due to the presence of chemical reaction. The results show strong dependency of the enhancement factor on CO_2 concentration in IL. In Figure 5.9 we can observe that the enhancement factor drops very rapidly in the first minutes of absorption and then slows down (almost reaches a negligible value) as absorption reaches pseudo-steady-state. The decrease in enhancement factor shows that increase in CO_2 loading is reducing the mass transfer enhancement due to chemical reaction. The enhancement factor for IL [emim] [Ac] is much higher than other ILs. Based on the enhancement factor the mass transfer enhancement of CO_2 in these ILs can be ranked as [emim] [Ac] >> [emim][$EtSO_4$] > [emim][$MeSO_4$] > [emim] [DCA]. First order rate constant is another parameter considered to predict the changes in the absorption behavior with increase in CO_2 concentration in ILs. The first order rate constant shows strong dependency on CO_2 concentration in ILs as it

decreases very rapidly in the first minutes of absorption. Based on the first order rate constant the initial fast absorption can be considered as interfacial chemical absorption in which the mass transfer happens only at the interface. After enough recirculation of the IL, CO_2 absorption at the interface becomes negligibly small and CO_2 diffuses through the bulk of the ILs. Based on the first order rate constant, ILs can be ranked as [emim] [Ac] > [emim][$EtSO_4$] > [emim][$MeSO_4$] > [emim] [DCA].

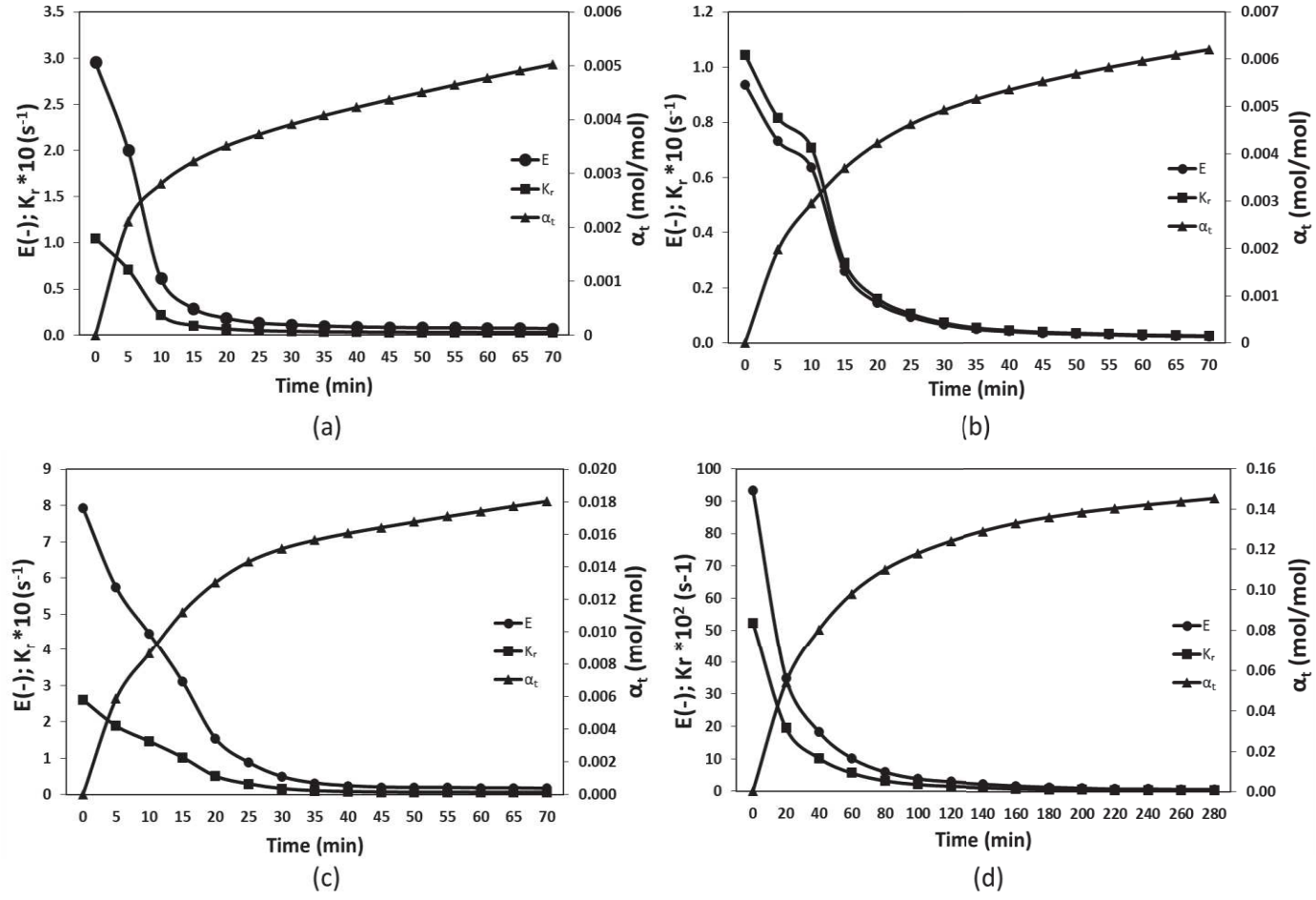

Figure 5.9 Evolution of enhancement factor (E), first order rate constant (K_r) and CO_2 loading (α_t) with operation time for IL (a) [emim] [$MeSO_4$], (b), [emim][DCA] (c) [emim][$EtSO_4$] and (d) [emim][Ac] at T=313 K.

Table 5.3 shows values of experimental mass transfer coefficient, CO_2 loading of the ILs and enhancement factors at initial time (t_i) and when the absorption reaches pseudo-steady-state (t_s). A smaller increment in temperature has considerably affected the CO_2 loadings. At initial times the experimental mass transfer coefficient seems to be unaffected with increase in temperature. However, after some recirculation this coefficient was reported to be lower at

high temperatures. There was a significant decrease in enhancement factor with increase in temperature.

Table 5.3 CO_2 loading, experimental mass transfer coefficient and enhancement factor

IL	Q_g (ml min^{-1})	Time	100 α_t (mol mol^{-1})	K_{exp} (m s^{-1}) 10^6	E (-)
		T=298 K			
[emim][$MeSO_4$]	20	t_i	-	9.28	5.57
		t_s	0.55	0.22	0.13
[emim][DCA]	20	t_i	-	9.27	1.64
		t_s	0.72	0.32	0.057
[emim][$EtSO_4$]	50	t_i	-	23.31	18.71
		t_s	2.11	0.59	0.47
[emim][Ac]	100	t_i	-	46.40	122.50
		t_s	16.70	0.44	1.99
		T=313 K			
[emim][$MeSO_4$]	20	t_i	-	9.28	2.96
		t_s	0.51	0.22	0.07
[emim][DCA]	20	t_i	-	9.27	0.94
		t_s	0.62	0.24	0.02
[emim][$EtSO_4$]	50	t_i	-	23.20	7.93
		t_s	1.80	0.48	0.17
[emim][Ac]	100	t_i	-	46.37	93.32
		t_s	14.50	0.37	0.76

5.3 CO_2 capture; coupled absorption/desorption vs single module absorption

5.3.1 CO_2 absorption/desorption in membrane contactor

The absorption performance of CO_2 in two different 1-ethyl-3-methyl imidazolium based ILs in single module absorption setup and coupled absorption/desorption setup are presented here in terms of efficiency and CO_2 loadings. The ILs studied for comparative analysis between single module absorption and coupled absorption/desorption were [emim][$MeSO_4$] and

[emim][DCA]. The CO_2 removal efficiency in the membrane absorber was found using Equation 5.2. Figure 5.10 below represents the CO_2 removal efficiencies of ILs [emim][$MeSO_4$] and [emim][DCA] in the membrane absorber against operation time. The efficiencies for both single module absorption and coupled absorption/desorption at various feed gas flowrates (of membrane absorber) are reported here. ILs were able to achieve nearly 100 % efficiency in the beginning of the operation. During recirculation of the single module absorption, IL absorbs CO_2 inside membrane absorber which leads to the accumulation of CO_2 in the liquid side and hence the efficiency decreases with the operation time. After enough recirculation the absorption process reaches pseudo-steady-state where the absorption rate becomes nearly constant (constant CO_2 removal efficiency). When coupled absorption/desorption is considered, the IL during a single cycle absorbs (passing from membrane absorber) and desorbs (passing from membrane stripper) CO_2. As can be seen from Figure 5.10 the coupled process retained a very high efficiency, even after 70 minutes of operation. For the [emim][$MeSO_4$] at 20 ml min^{-1} of feed gas flowrate retained pseudo-steady-state efficiencies were of 65 % for coupled absorption/desorption and 11 % for single module absorption. In the case of [emim][DCA] at 20 ml min^{-1} of feed gas flowrate pseudo-steady-state efficiencies were of 59 % and 17 % for coupled absorption/desorption and single module absorption, respectively.

Considering feed gas flowrate of 10 ml min^{-1} for coupled absorption/desorption process ILs [emim][$MeSO_4$] and [emim][DCA] shows 82 % and 66 % efficiency. The rest of 18 % and 34 % CO_2 remains absorbed and cannot be desorbed in a single cycle having the same operating conditions. The above-mentioned results explain the physical absorption nature of the RTILs [emim][$MeSO_4$] and [emim][DCA]. Retaining very high absorption efficiencies for coupled process with RT sweep desorption shows the easy capacity of CO_2 desorption with RTILs compared to that of conventional absorbents which require a huge amount of heat and energy to desorb CO_2.

Feed gas flowrate has shown significant effect on the CO_2 removal efficiencies. Increase in gas flowrate decreases the CO_2 removal efficiency, particularly for coupled process. Increase in gas flowrate has two significant effects; a decrease in the residence time of gas inside the membrane absorber and increase in mass transfer flux across the interface. This increase in mass transfer flux also causes high CO_2 loading, which again negatively affects the absorption performance of absorbents.

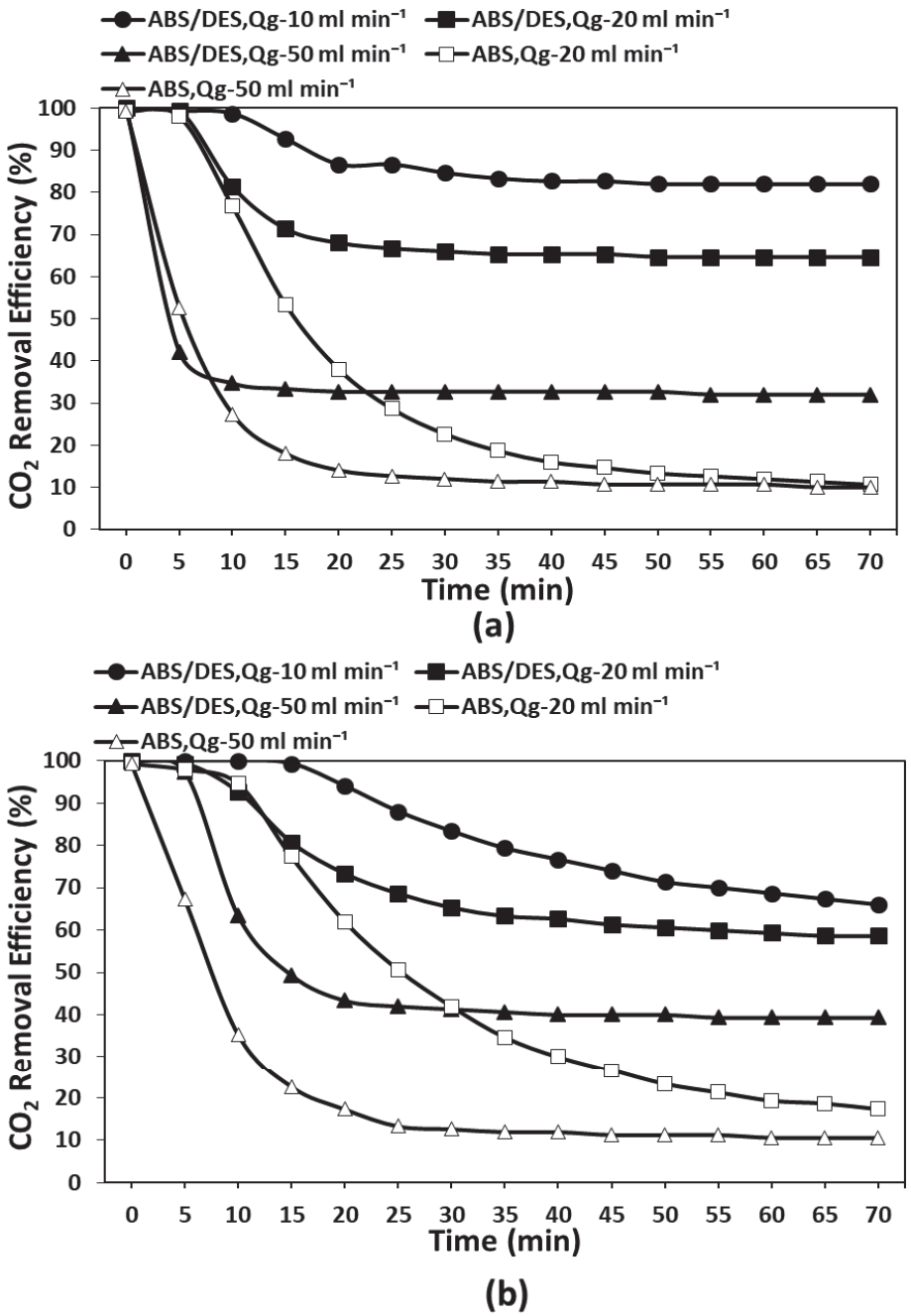

Figure 5.10 CO_2 removal efficiency of the membrane absorber for coupled absorption/desorption (ABS/DES) and single module absorption (ABS) at different gas flowrate against operation time for IL (a) [emim][$MeSO_4$] and (b) [emim] [DCA].

The increase in CO_2 loading with the operation time is presented in Figure 5.11. A huge difference can be observed between the loadings of single module absorption and coupled absorption/desorption. At feed gas flowrate of 20 ml min^{-1} after 70 minutes of recirculation, CO_2 loading reaches 1 10^{-3} mol mol^{-1} for coupled absorption/desorption and 5.6 10^{-3} mol mol-

^{1} for single module absorption, while using IL [emim][$MeSO_4$] as an absorbent. For IL [emim][DCA], at feed gas flowrate of 20 ml min^{-1} after 70 minutes of recirculation CO_2 loading reached 2.7 10^{-3} mol mol^{-1} for coupled absorption/desorption and 7.5 10^{-3} mol mol^{-1} for single module absorption. We can notice an initial faster increase in the CO_2 loading which later slows down with time. The initial faster loading can be attributed as result of interfacial absorption which later slows down when the absorption is transferred toward the bulk of the IL (low diffusion coefficients causes high mass transfer resistance). Initially, the CO_2 loading rate drops with time due to the accumulation of CO_2 on the liquid side until it reaches the pseudo-steady-state. At pseudo-steady-state the absorption rate and thus the CO_2 loading rate becomes nearly constant. After this stage, a constant amount of CO_2 is accumulated with further recirculation.

Maximal CO_2 loading (α_{max}) at pseudo-steady-state is presented in Figure 5.12. Effect of feed gas flowrate on the CO_2 can be observed from the figure. A higher feed gas flowrate increases the CO_2 loading. For [emim][$MeSO_4$], in case of single module absorption, increase in feed gas flowrate from 20 ml min^{-1} to 50 ml min^{-1} increases CO_2 loading from 5.8 10^{-3} mol mol^{-1} to 9 10^{-3} mol mol^{-1}. For coupled absorption/desorption an increase from 1 10^{-3} mol mol^{-1} to 1.8 10^{-3} mol mol^{-1} is observed by increasing feed gas flowrate from 20 ml min^{-1} to 50 ml min^{-1}. A very low CO_2 loading is retained during absorption desorption operation of RTILs. For [emim][$MeSO_4$] at pseudo-steady-state, 50 ml min^{-1} feed gas flowrate and coupled absorption/desorption operation keeps nearly a constant CO_2 loading of 1.8 10^{-3} mol mol^{-1} which for single module absorption is 9 10^{-3} mol mol^{-1}. For [emim][DCA] under the same operating conditions CO_2 loading of 4.8 10^{-3} mol mol^{-1} for coupled absorption/desorption and 9.4 10^{-3} mol mol^{-1} for single module absorption are observed. A huge difference between the CO_2 loadings of coupled absorption/desorption and single module absorption confirms the physical absorption nature and ease of CO_2 desorption of these RTILs. Moreover, the RT sweep desorption was much more efficient for [emim][$MeSO_4$] compared to [emim][DCA] as the later IL retained nearly double CO_2 loading at pseudo-steady-state.

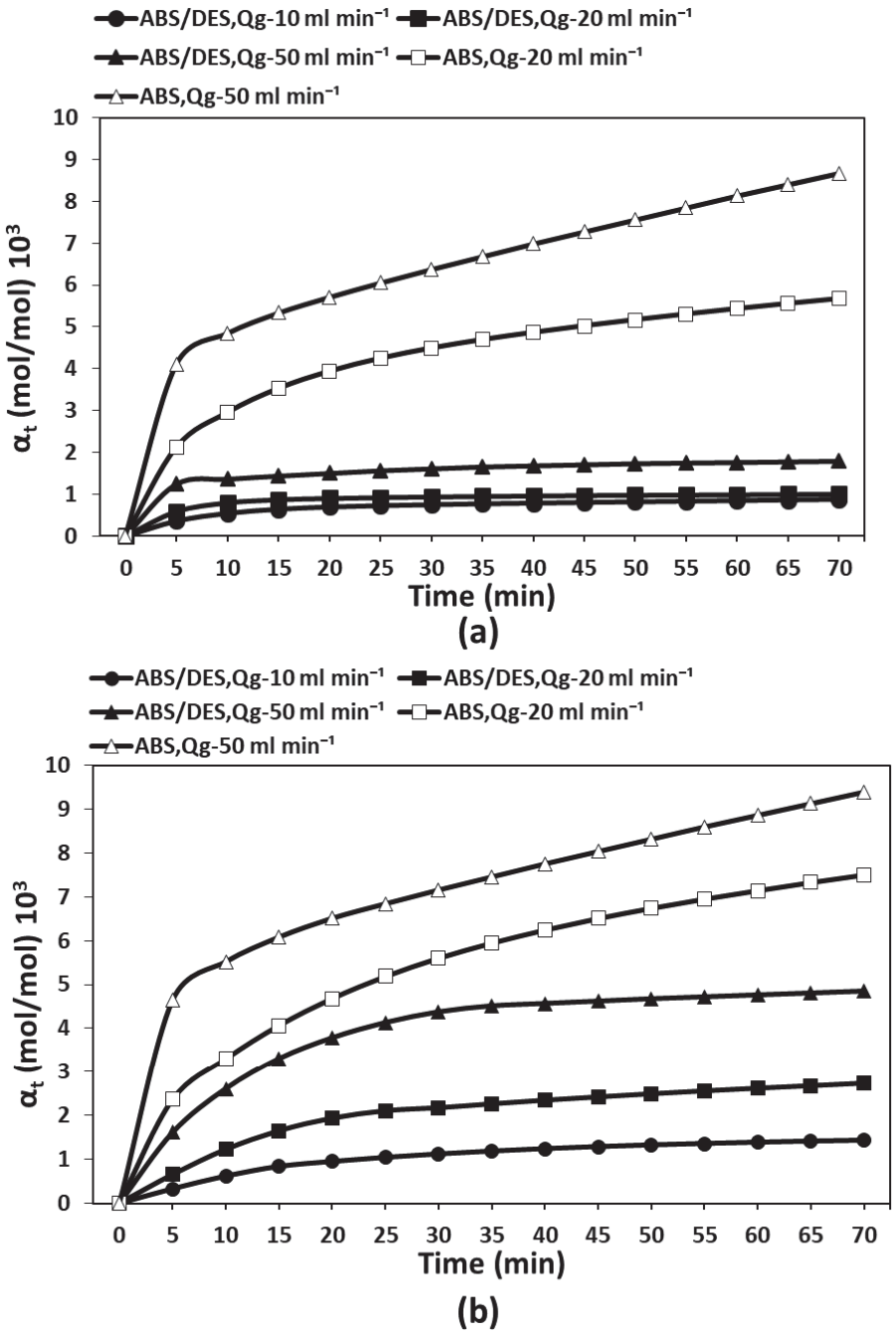

Figure 5.11 CO_2 loading α_t of the IL (a) [emim][$MeSO_4$] and (b) [emim][DCA] during coupled absorption/desorption (ABS/DES) and single module absorption (ABS) at different gas flowrates against operation time.

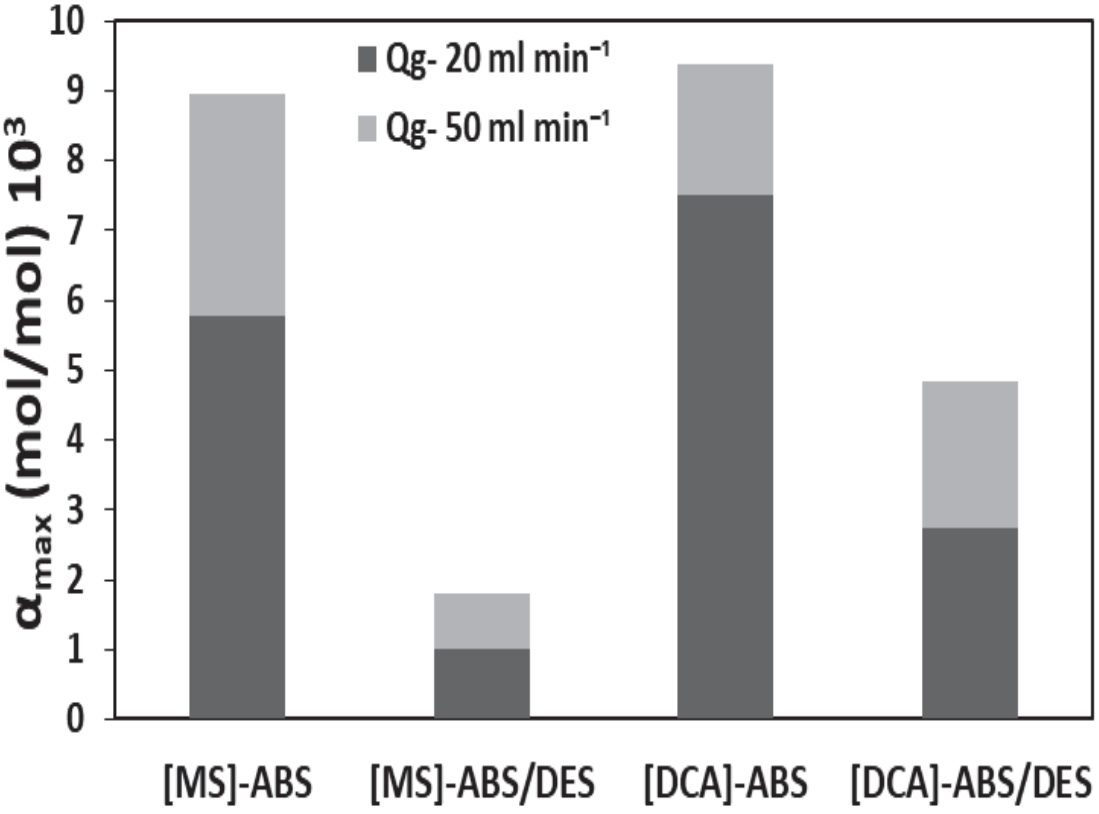

Figure 5.12 Maximal CO_2 loading, α_{max}, of the ILs [emim][$MeSO_4$] ([MS]) and [emim][DCA] ([DCA]) during coupled absorption/desorption (ABS/DES) and single module absorption (ABS) after 70 minutes of operation

As explained in the experimental section in the coupled process the IL in a single recirculation step absorbs CO_2 in the membrane absorber and desorbs it in the membrane stripper. The stripping efficiency of the RTILs in the membrane stripper is presented here. The CO_2 stripping efficiency can be calculated by the following equation:

$$Stripping\ efficiency\ (\%) = \left(1 - \frac{C_{l,out}}{C_{l,in}}\right) 100 \qquad (5.3)$$

Where $C_{l,in}$ and $C_{l,out}$ represents CO_2 concentrations of the IL at inlet and outlet of the membrane stripper.

Stripping efficiency of the CO_2 in the membrane stripper during coupled absorption/desorption operation against operation time is presented in Figure 5.13. The stripping gas flowrate was always kept constant at 100 ml min^{-1}. Feed gas flowrate in membrane absorber was varied from 20 ml min^{-1} to 50 ml min^{-1}. A considerable effect of feed

gas flowrate on the striping efficiency can be observed. A higher stripping efficiency is achieved at lower feed gas flowrate. This effect might be due to the lower CO_2 loading at lower feed gas flowrates which increases the stripping efficiency due to the presence of less amount of CO_2 to be desorbed. Another important phenomenon which can be observed from the Figure 5.13 below is the very low initial efficiency which increases with time and nearly reaches a constant value at pseudo-steady-state. Initially, [emim][$MeSO_4$] achieves a stripping efficiency of 18 % at 20 ml min^{-1} feed gas flowrate which increases up to 86 % at pseudo-steady-state. IL [emim][DCA] is able to achieve only 4 % initial efficiency at the same operating conditions and reaches 65 % at pseudo-steady-state. Initially the absorption behaves more like interfacial chemical in nature and the sweep gas stripping is not very efficient. The interfacial faster absorption is not effective at higher concentrations of CO_2 in the IL. Thus, the absorption later adopts the physical absorption nature and shifts to the bulk of the IL. Sweep gas stripping becomes much efficient for the physically absorbed CO_2 in the RTILs and nearly reaches 86 % for [emim][$MeSO_4$]. It can also be observed that stripping is much more efficient for IL [emim][$MeSO_4$] than for [emim][DCA]. IL [emim][$MeSO_4$] is also able to achieve very high stripping efficiency (from 18%-86%) compared to [emim][DCA] (from 4%-65 %).

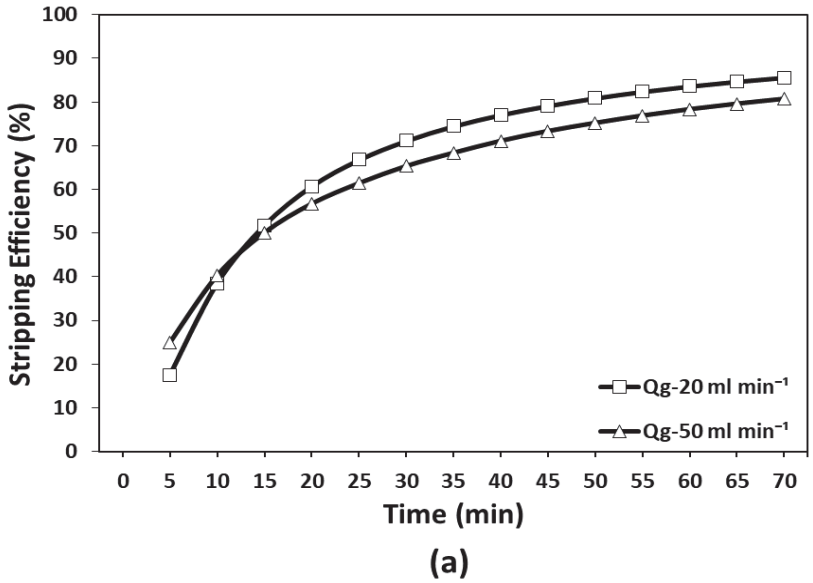

(a)

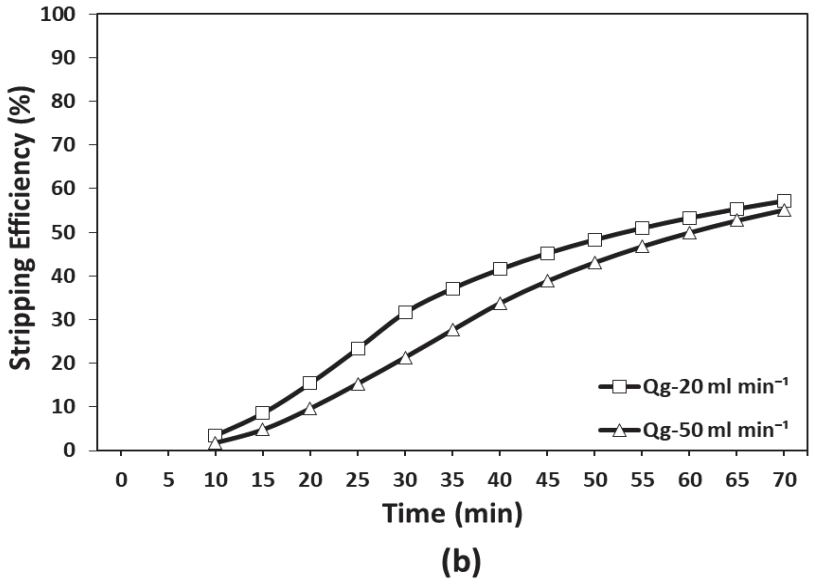

Figure 5.13 Stripping efficiency of the membrane stripper during coupled absorption/desorption against operation time for IL (a) [emim][$MeSO_4$] and (b) [emim] [DCA]; stripping gas flowrate, $Q_{N_2} = 100\ ml\ min^{-1}$

5.3.2 Mass transfer coefficient and enhancement factor

Experimental mass transfer coefficient at pseudo-steady-state was calculated for two different feed gas flowrates and presented in Figure 5.14. An increase in mass transfer coefficient was observed with increase in feed gas flowrate inside membrane absorber, in most cases except for [emim][$MeSO_4$] during coupled absorption/desorption operation where a minor decrease was observed with feed gas flowrate enhancement. The increase in mass transfer coefficient is primarily due to the increase in membrane flux with increase in feed gas flowrate. The exception for [emim][$MeSO_4$] might be due to the lower pseudo-steady-state efficiency of this IL at higher feed gas flowrates. Coupled absorption/desorption process retained a very high mass transfer coefficient compared to the single module absorption. At the feed gas flowrate of 20 ml min^{-1}, IL [emim][$MeSO_4$] showed an increase in mass transfer coefficient from 0.2 10^{-6} m s^{-1} to 1.9 10^{-6} m s^{-} for single module absorption and coupled absorption/desorption, respectively. For [emim][DCA] at the same conditions, the increase was from 0.3 10^{-6} m s^{-1} to 1.6 10^{-6} m s^{-1} for single module absorption and coupled absorption/desorption, respectively. The enhanced mass transfer for coupled absorption/desorption process is due to the lower CO_2 concentration of the ILs. The lower

mass transfer coefficients of single module absorption explain the increased mass transfer resistance due to the higher CO_2 concentration of the ILs.

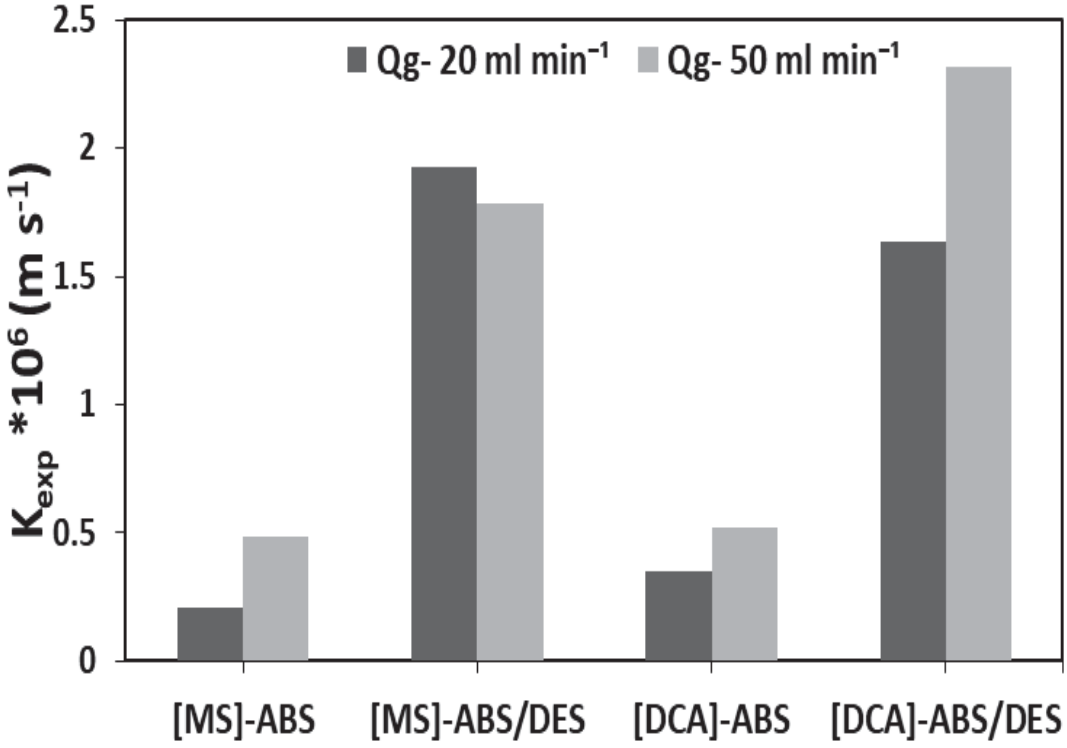

Figure 5.14 Experimental mass transfer coefficient, K_{exp}, for CO_2 absorption in ILs [emim][$MeSO_4$] ([MS]) and [emim][DCA] ([DCA]) during coupled absorption/desorption (ABS/DES) and single module absorption (ABS) at pseudo-steady-state

The enhancement factor represents the enhancement in mass transfer due to the presence of chemical reaction. Figure 5.15 presents a comparison of enhancement factor between coupled absorption/desorption and single module absorption at pseudo-steady-state. The enhancement factor nearly remained constant after achieving pseudo-steady-state. An increase in feed gas flowrate has positively affected the enhancement factor except for [emim][$MeSO_4$] during coupled absorption/desorption where the increase in gas flowrate has decreased the enhancement factor. At feed gas flowrate of 50 ml min^{-1}, enhancement factor of IL [emim][$MeSO_4$] for single module absorption was noted to be of 0.7 magnitude, nearly 4 time less than for coupled absorption/desorption which was noted to be 2.6. For IL [emim][DCA] under the same conditions, the single module absorption enhancement factor was noted to be 0.75, nearly 4.5 times less than for coupled absorption/desorption. The high

magnitude enhancement factor for coupled absorption/desorption and nearly four-time lower values at single module absorption, verifies the dependency of this factor on the CO_2 concentration in the IL. The coupled process retains the high magnitude of enhancement due to the continuous desorption of CO_2 in the membrane stripper.

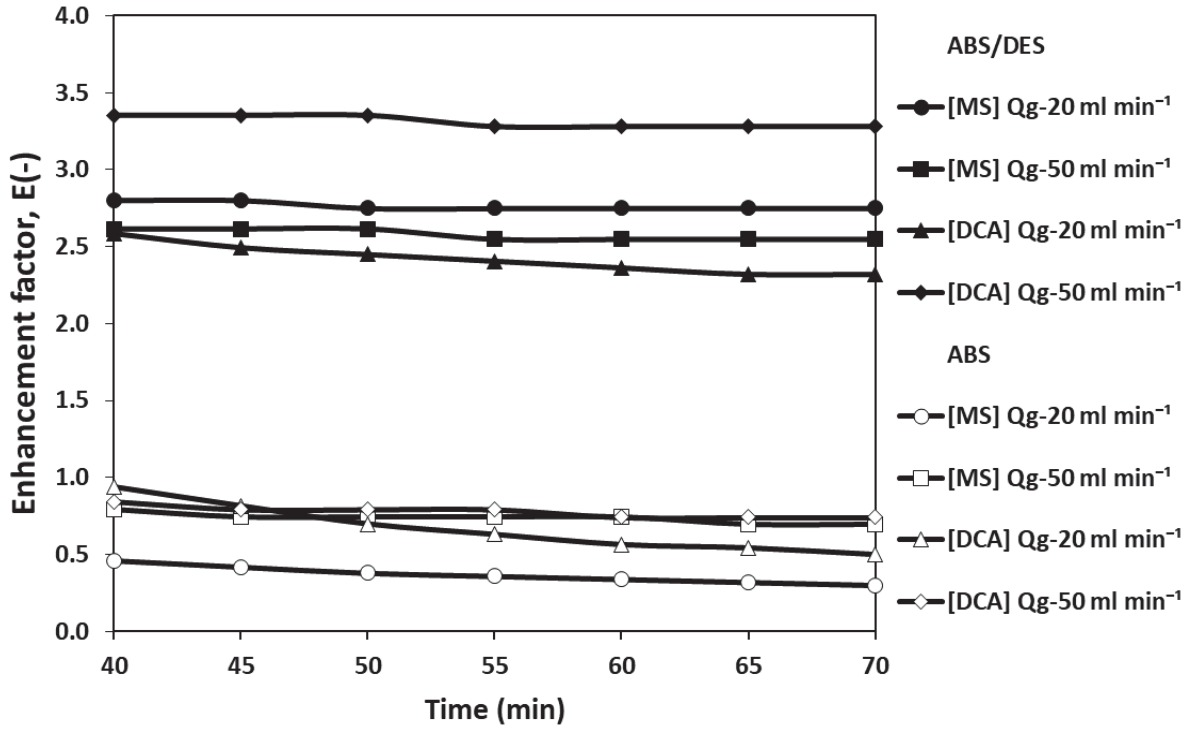

Figure 5.15 Enhancement factor, E, for CO_2 absorption in ILs [emim][$MeSO_4$] ([MS]) and [emim][DCA] ([DCA]) during coupled absorption/desorption (ABS/DES) and single module absorption (ABS) at pseudo-steady-state

5.4 Conclusion

This chapter presented the characterization of ILs, membranes and the experimental outcomes of the post-combustion carbon dioxide capture with RTILs in HFMC. All the RTILs showed very good feasibility for use as absorbent for CO_2 from CO_2/N_2 mixture, in a membrane contactor. Very good CO_2 absorption performance was observed for both single module setup and coupled absorption/desorption setup. Coupled absorption/desorption setup was very efficient compared to single module absorption setup and can be recommended for commercial scale continuous post-combustion carbon capture. This setup might be very suitable after further modifications and improvements, particularly modifications in the means of desorption inside the membrane stripper.

Chapter 6. Modeling and Simulation Under Isothermal Conditions

Isothermal modeling approach developed in Section 4.2.1 of Chapter 4 was implemented for the absorption of CO_2 in four different imidazolium based RTILs, 1-ethyl-3-methylimidazolium methyl sulfate [emim][$MeSO_4$], 1-ethyl-3-methylimidazolium dicyanamide [emim][DCA], 1-ethyl-3-methylimidazolium ethyl sulfate [emim][$EtSO_4$] and 1-ethyl-3-methylimidazolium acetate [emim][Ac]. The CO_2 absorption is based on the single module absorption and coupled absorption/desorption arrangements described in Section 3.5 of Chapter 3.

Simulations under isothermal conditions are presented in this chapter after the model was validated. The following publications from the authors correspond to this Chapter.

- Sohaib, Q., Gómez-Coma, L., Albo, J., Druon-Bocquet, S., Irabien, A., Sanchez-Marcano, J., 2019. Mathematical Modeling of CO_2 Absorption with Ionic Liquids in a Membrane Contactor, Study of Absorption Kinetics and Influence of Temperature. *J. Chem. Technol. Biotechnol.*
- Sohaib, Q., Gómez-Coma, L., Albo, J., Druon-Bocquet, S., Irabien, A., Sanchez-Marcano, J., 2020. CO_2 Capture in a Hollow Fiber Membrane Contactor Coupled with Ionic Liquid: Influence of Membrane Wetting and Process Parameters. *Sep. Purif. Technol.*
- Sohaib, Q., Vadillo, J.M., Gómez-Coma, L., Albo, J., Druon-Bocquet, S., Irabien, A., Sanchez-Marcano, J., 2020. Post-Combustion CO_2 Capture by Coupling [emim] Cation Based Ionic Liquids with a Membrane Contactor; Pseudo-Steady-State Approach. *Int J Greenh Gas Control.*
- Sohaib, Q., Vadillo, J.M., Gómez-Coma, L., Albo, J., Druon-Bocquet, S., Irabien, A., Sanchez-Marcano, J., 2020. CO_2 Capture with Room Temperature Ionic Liquids; Coupled Absorption/Desorption and Single Module Absorption in Membrane Contactor. *Chem. Eng. Sci.*

6.1 Model validation: Comparison of simulations with experimental data

As explained in the introduction of this chapter, isothermal model was validated with both experimental arrangements, single module absorption and coupled absorption/desorption.

For single module absorption (Chapter 3, section 3.5) experimental results of gas side outlet dimensionless concentration of CO_2 against recirculation time were plotted and compared with the simulation results (Figure 6.1). The experimental results were presented with standard error bars. The ionic liquid flowrate and CO_2 feed concentration were kept constant at 60 ml min^{-1} and 15 % by volume, respectively. Surface tension of the ILs in the present work (Ranges from 45 to 52.6 mN m^{-1}) is low compared to water (71.9 mN m^{-1}) which increases the risk of wetting. However, no wetting assumptions were adopted for the current process due to the use of fresh hydrophobic membranes (having small pore size of 0.04 μm) operated nearly at atmospheric pressure with thick absorbents having remarkably high value of viscosity (up to 288 mPa s for ILs used in this work). Moreover, a slight transmembrane pressure difference was applied, to ensure non-wetted conditions.

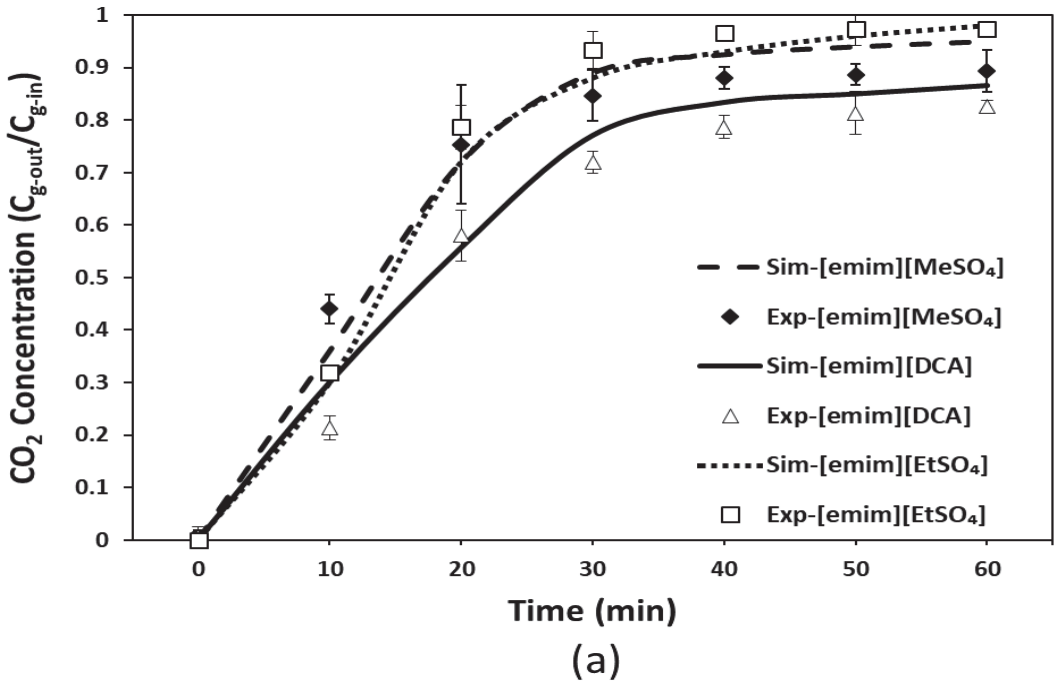

(a)

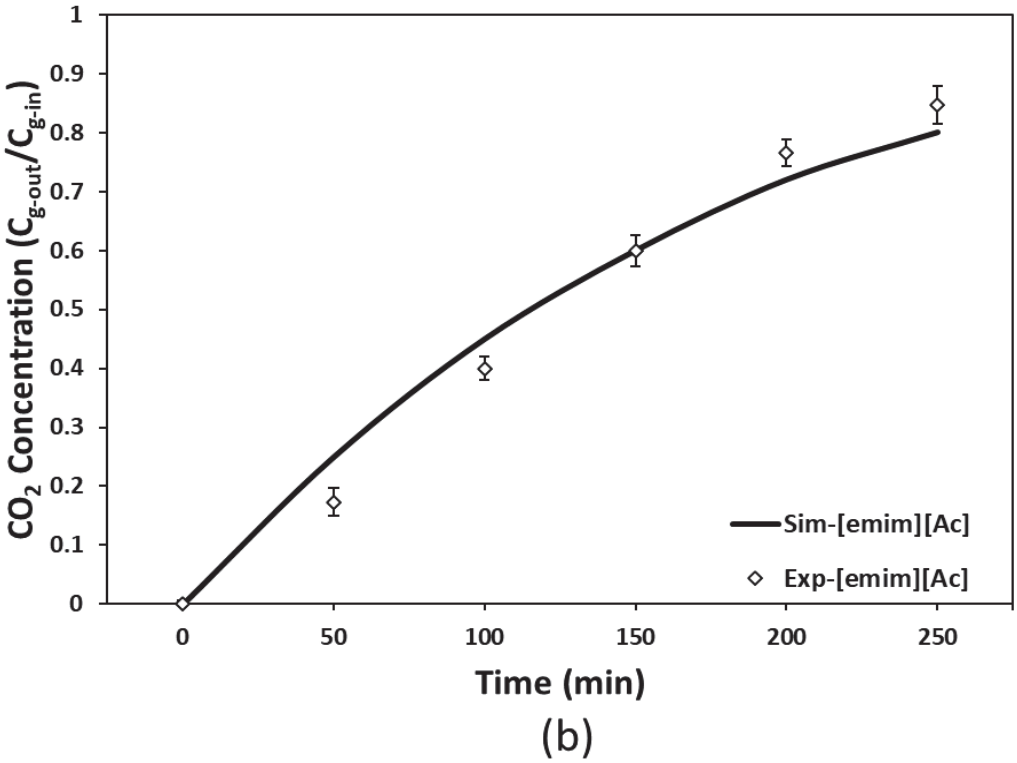

Figure 6.1 Single module absorption; comparison of simulation with experimental data under non-wetting assumption (a) [emim] [$MeSO_4$], [emim] [DCA] and [emim] [$EtSO_4$] at $Q_g = 50\ ml\ min^{-1}$ (b) [emim] [Ac] at $Q_g = 100\ ml\ min^{-1}$; $T = 288\ K$, $Q_{IL} = 60\ ml\ min^{-1}$, $CO_2\ concentartion = 15\ \%\ vo$.

Figure 6.1 shows a gradual increase in CO_2 outlet dimensionless concentration by increasing recirculation time, as the absorbent moves toward saturation with more recirculation and absorption. If we consider the experimental errors represented as bars on the figure there was a quite good agreement between experimental and simulation results. The pseudo-steady-state 2D dynamic model was able to closely predict the experimental data within a range of 2-5 % standard deviation.

The simulations obtained from the dynamic model developed for the coupled absorption/desorption were compared with the corresponding experimental data and presented here in Figure 6.2. IL was considered for countercurrent recirculation on the shell side of membrane absorber and membrane stripper. Gas mixture containing 15 % CO_2 (and N_2 rest to balance) was used as a feed to the lumen side of membrane absorber in open loop conditions. Pure N_2 passing from the lumen side of membrane stripper was used as sweep gas. Simulations of dimensionless concentration of CO_2 at the outlet of membrane absorber were plotted against operation time. Experimental data (dots in the Figure 6.2) are also

presented in the figure to compare it with simulated results. We can notice that even if the simulations resulted on overestimated values of CO_2 extracted respect to experimental data the shape of the curve of the evolution of this extraction is similar. If we consider the industrial origin of the fibers it is possible that inhomogeneities are present through the structure of membranes' length. Indeed, some partial wetting can be present at different location of fibers which might underestimate the comparison with simulations. In actual experiments, we observe an average of gas absorption through 2300 fibers length.

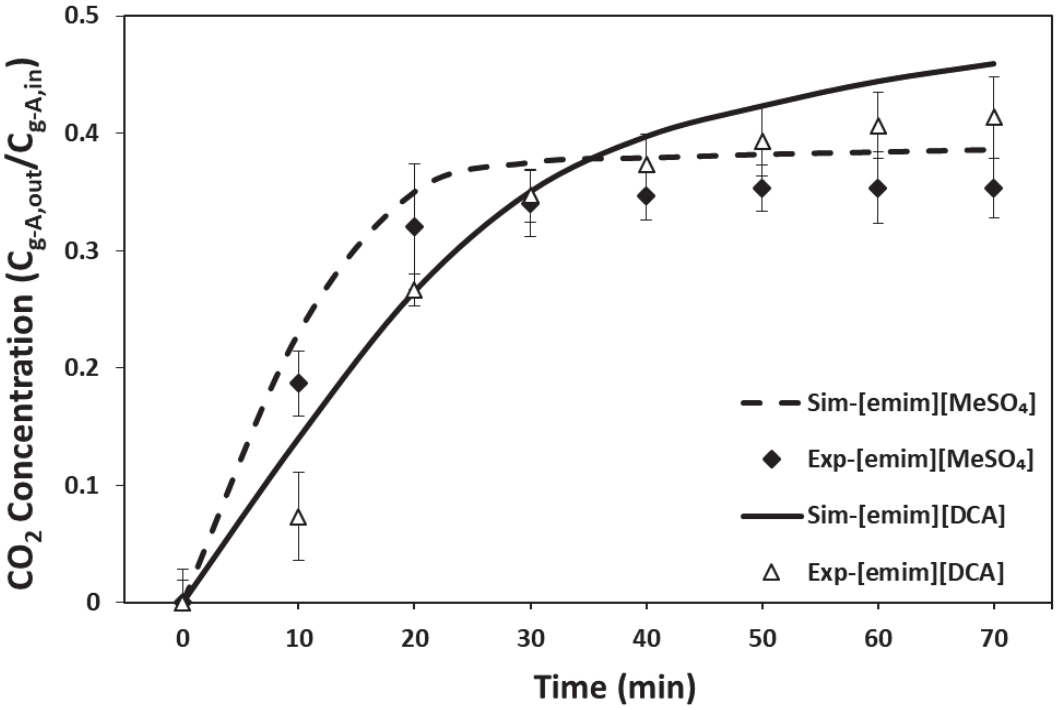

Figure 6.2 Coupled absorption/desorption; comparison of simulation with experimental results under non-wetting assumption; $Q_g = 20\ ml\ min^{-1}, T = 288\ K$, $Q_{IL} = 60\ ml\ min^{-1}$, $CO_2\ concentration = \ 15\ \%\ vol.$

Once the model is validated, it could be further used for other studies.

6.2 Single module absorption

The model developed for single module absorption is based on the experimental arrangements presented in Section 3.5 of Chapter 3. IL flows counter currently (in a closed loop) from the reservoir to the shell side of the membrane absorber (membrane stripper

disconnected) while gas flows through the lumen side of the membrane absorber. The modeling approach for the simulations presented here, is described in Section 4.2.1 of Chapter 4.

6.2.1 Concentration distribution of CO_2 under non-wetting mode

Figure 6.3 shows concentration distribution of CO_2 in tube, membrane, and shell of the contactor under no-wetting mode for IL [emim][$EtSO_4$]. Steady-state modeling approach was implemented. The gas mixture flows in the inner (tube) side from z=0, where its concentration is maximum (C_0), towards z=L. Absorbent is allowed to flow counter currently in the shell side, as it enters at z=L where CO_2 concentration is minimum and moves towards z=0 while absorbing CO_2 which diffuses from the walls of porous membrane. Concentration difference (driving force) causes to diffuse CO_2 through the walls of porous membrane from tube side towards shell side. Diffusion is the dominant mass transfer mechanism in radial direction due to the huge concentration difference while in axial direction convection is the dominant mechanism due to fluid flow. Figure 6.3 shows that CO_2 concentration decreases gradually as it moves forward in the contactor while it increases in the shell side when the absorbent moves forward in the shell of the contactor.

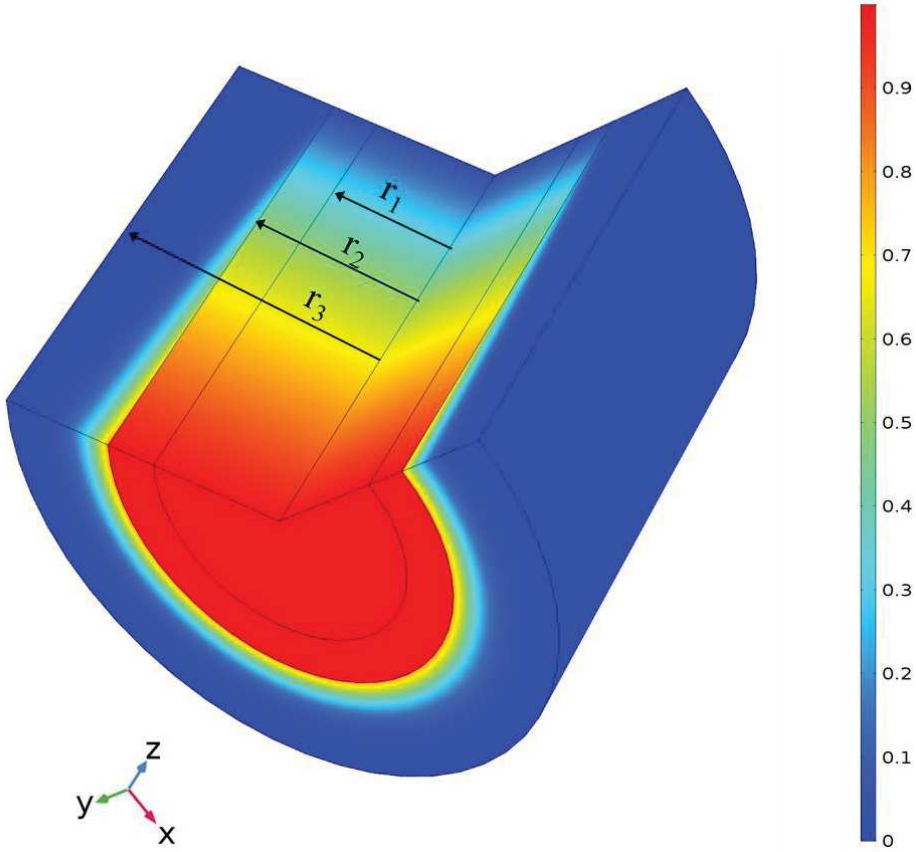

Figure 6.3 Overall dimensionless concentration profile of CO_2 (tube, membrane and shell) under non-wetting assumption for IL [emim][$EtSO_4$]; Steady-state modeling; $Q_{IL} = 50\ ml.min^{-1}$, $Q_g = 20\ ml.min^{-1}$, $\varphi_v =$ 15 %, $T = 291K$.

Pseudo-steady-state two-dimensional concentration distribution of CO_2 with IL [emim][$EtSO_4$] is presented in Figure 6.4. This figure shows that initially [emim][$EtSO_4$] can capture the whole amount of CO_2. After 40 minutes of absorption time the process reaches to pseudo-steady-state where the absorption is very low, and the rate is nearly constant.

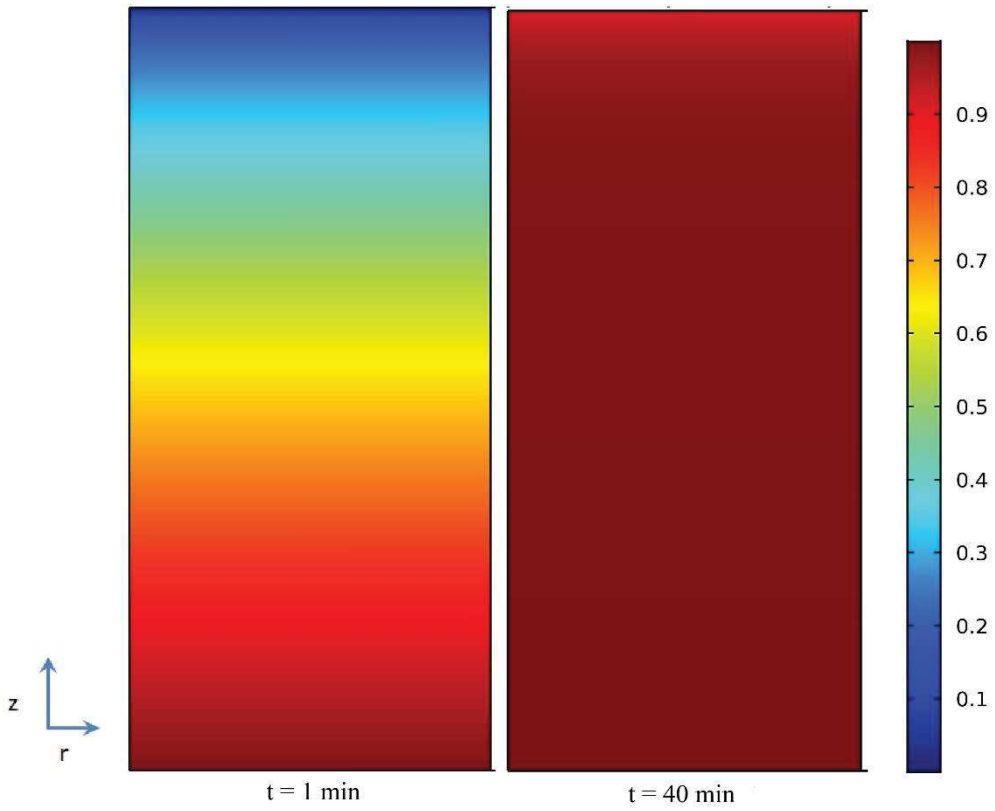

Figure 6.4 Dimensionless concentration profile of CO_2 in the tube for IL [emim][$EtSO_4$]; Pseudo-steady-state modeling; $Q_{IL} = 50\ ml.min^{-1}$, $Q_g = 70\ ml.min^{-1}$, $\varphi_v =$ 15 %, $T = 318\ K$.

6.2.2 Membrane wetting

Wetting is a major challenge in membrane contactor operations as it significantly increases the mass transfer resistance. Some studies predict that wetting can cause six times drop in CO_2 absorption and that 5 % wetting can cause up to 20% reduction in mass transfer coefficient (Mosadegh-Sedghi et al., 2014; Wang et al., 2005; Zhao et al., 2016).

Although the assumptions of non-wetted membrane seem to be validated following the agreements of simulation and experimental results presented in Figures 6.1 and 6.2, a partial wetting analysis was carried out to observe its effect on the efficiency, CO_2 flux and IL loading for long term operability. Indeed, long term operations and pressure variations can cause penetration of the liquid into the pores of porous membrane causing partial wetting of the membrane and leading to a huge drop in the CO_2 flux. Penetration of the viscous IL into the pores of the membrane can lead to a zero flux across the membrane if the wetting dominates the membrane. Therefore, five different membrane wetting conditions have been

investigated. Apart from non-wetted and fully wetted conditions, three partially wetted conditions have been considered: 5% wetting, 20% wetting and 50% wetting. X% wetting means that X% of the pore's length is filled with ionic liquid. These wetting conditions were investigated in a single module absorption with IL [emim][$EtSO_4$]. It is important to notice that these values are theoretical, as we explained above the actual amount and location of wetting can be much more complex considering the industrial origin of fibers.

Figure 6.5 presents concentration distribution of CO_2 in membrane under partial wetting and full wetting mode. Figure 6.5 (a), (b) and (c) represents membranes under 5%, 20% and half wetting conditions, respectively, while figure 6.5(d) represents full wetting mode. It can be observed that increase in membrane wetting causes a significant increase in CO_2 dimensionless concentration at outlet of contactor and reduces the separation efficiency. In partial wetting modes, a completely different concentration distribution can be observed in wetted and non-wetted portion of membrane due to the increase of the mass transfer resistance in the wetted portion. The fully wetted membrane presents an extremely low separation effectiveness therefore this condition will not be further considered, and focus will be put on non-wetted and partially wetted conditions.

Simulations of the normalized ($C_{g-A}/C_{g-A,max}$) radial concentration drop of CO_2 in the 20 % and 50% wetted portion of the membrane are shown in Figure 6.6, for [emim][$EtSO_4$]. C_{g-A} in the figure represents local CO_2 concentration inside the wetted portion of the membrane while $C_{g-A,max}$ is the maximum interfacial CO_2 concentration. Concentration drop presented here is only in the wetted portion of the membrane at axial length of L/2. This huge drop of concentration in the wetted portion starts near the gas filled portion of membrane moving towards the shell boundary from where the absorbent is penetrated. A significant drop of CO_2 concentration in the wetted portion of the membrane can be observed.

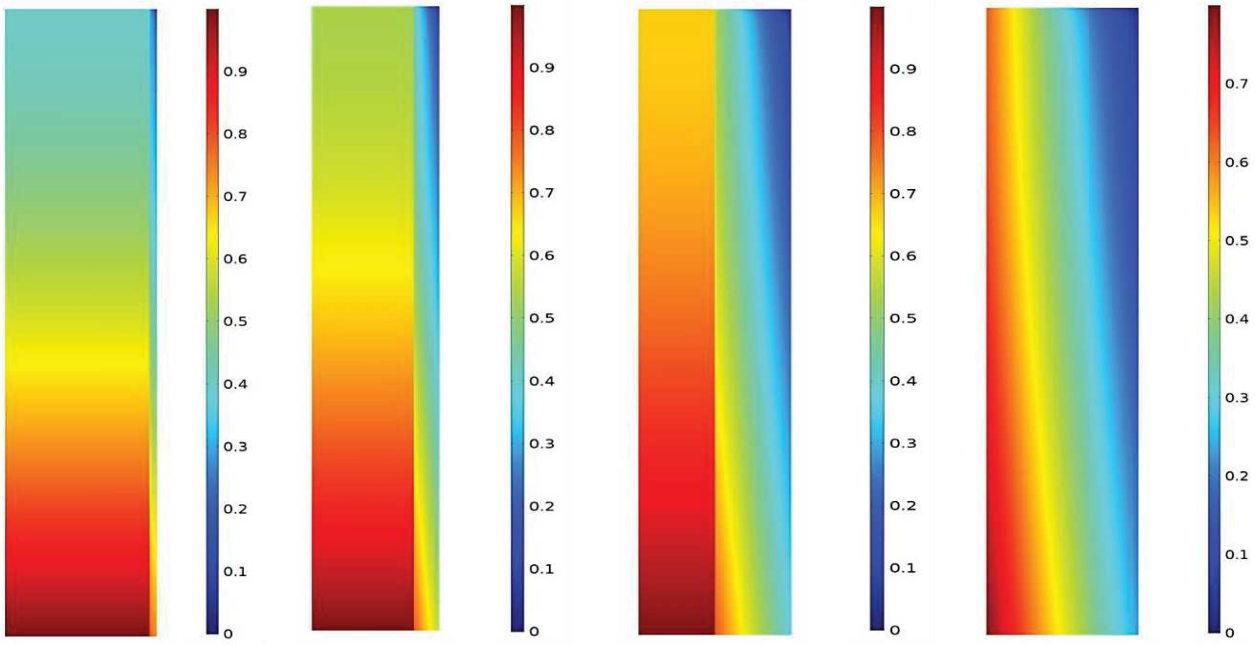

Figure 6.5 Dimensionless concentration distribution of CO_2 along porous membrane for IL [emim][$EtSO_4$]; (a) 5% wetting (b) 20% wetting (c) half wetting (d) full wetting; Steady-state modeling; $Q_{IL} = 50\ ml.min^{-1}$, $Q_g = 20\ ml.min^{-1}$, $\varphi_v =$ 15 %, $T = 291$.

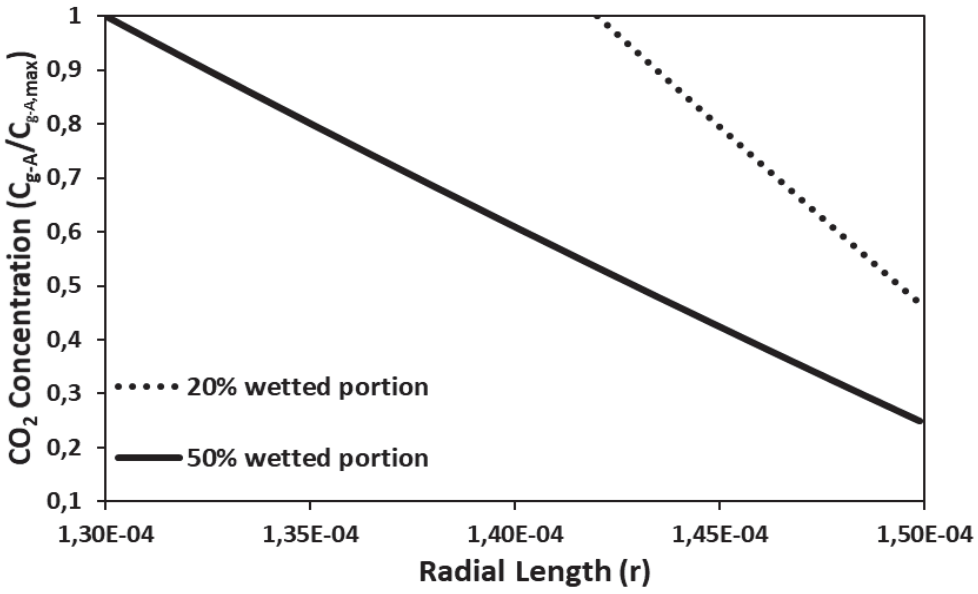

Figure 6.6 Radial concentration drop of CO_2 in wetted portion of membrane for IL [emim][$EtSO_4$]; Steady-state modeling; $Q_{IL} = 50\ ml.min^{-1}$, $Q_g = 20\ ml.min^{-1}$, $\varphi_v =$ 15 %, $T = 291$.

Figure 6.7 presents the drop in CO_2 absorption efficiency with increase in membrane wetting. The absorption efficiency was calculated according to equation 5.2 of chapter 5. A significant reduction in mass transfer can be seen due to membrane wetting. A 5% membrane wetting has caused almost 40 % reductions in the separation efficiency. A major drop in efficiency can be observed by wetting of a small portion of membrane. Efficiency of CO_2 separation drops from 97% to 20 % when conditions changes from non-wetting to full wetting mode.

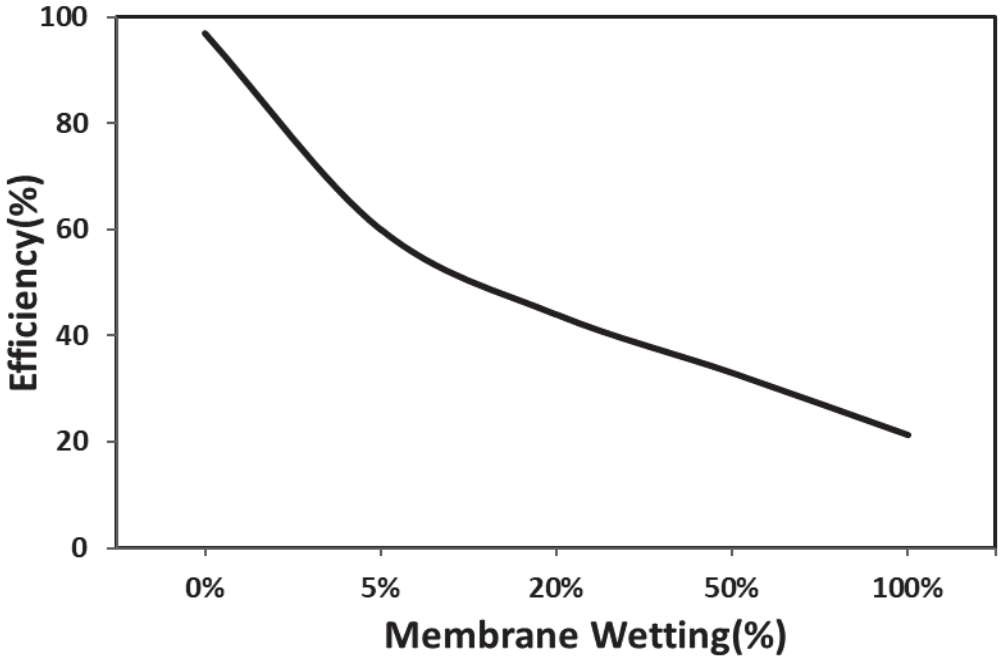

Figure 6.7 Effect of membrane wetting on separation efficiency of CO_2 for IL [emim][$EtSO_4$]; Steady-state modeling; $Q_{IL} = 50\ ml.min^{-1}$, $Q_g = 20\ ml.min^{-1}$, $\varphi_v = 15\ \%$, $T = 291$.

Figure 6.8 demonstrates the effect of partial wetting on the CO_2 flux and maximal IL loading (α_{max}) after 60 minutes of operation. It's very clear that the adverse effect of wetting is much stronger at the beginning as a drop of nearly one half of the flux was noted for 5 % wetting of the membrane. Moreover, the drop in the mass transfer flux affects α (maximal IL loading at 60 minutes of operation time) which decreases by 67 % when the membrane is 20 % wetted compared to non-wetted membrane.

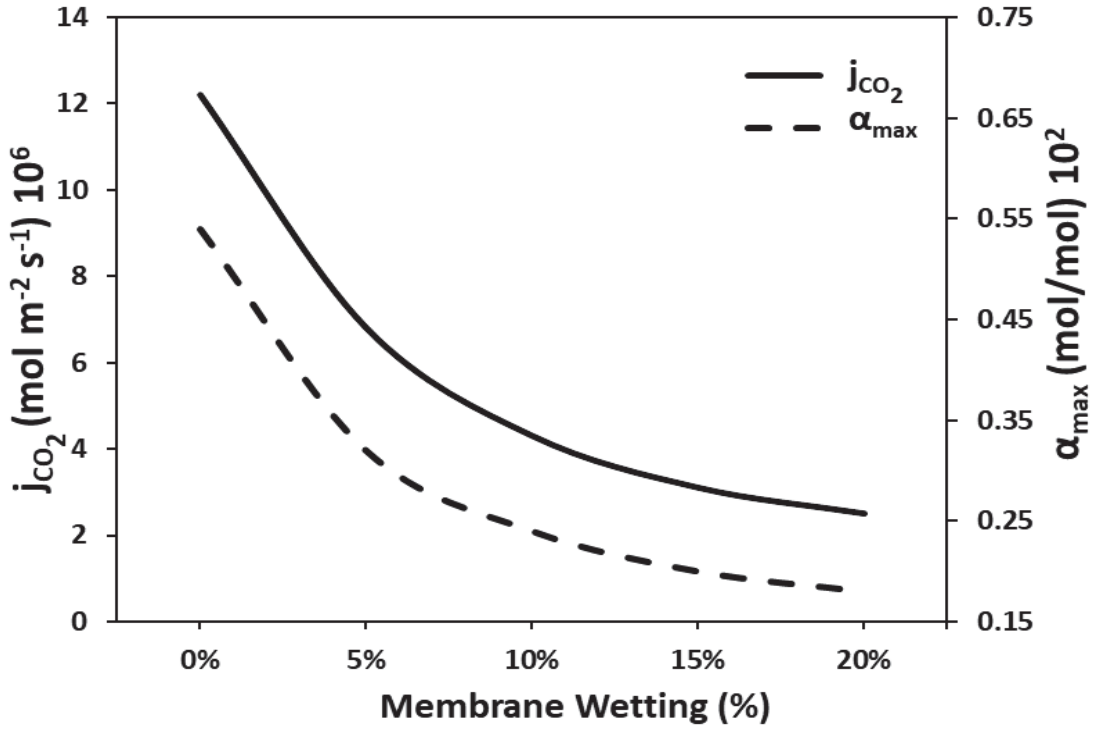

Figure 6.8 Effect of partial wetting of the membrane on CO_2 flux and IL loading for IL [emim] [$MeSO_4$]; pseudo-steady-state modeling; $Q_g = 20\ ml\ min^{-1}$; $Q_{IL} = 60\ ml\ min^{-1}$, $T = 288\ K$, $CO_2\ concentration = \ 15\ \%\ vol.$

Parametric and operational conditions analysis

6.2.2.1 Effect of membrane porosity and tortuosity

It is clear from Equation 4.46 that porosity has a significant effect on the mass transfer of CO_2. A higher porosity will reduce membrane mass transfer resistance and process will be more efficient (Asfand and Bourouis, 2015). In this study, the effect of membrane porosity on CO_2 removal efficiency was investigated and reported in Figure 6.9. IL [emim][$EtSO_4$] was considered for the current analysis. Porosity has also direct effect on tortuosity of the membrane. An increase in porosity decreases tortuosity which makes the process more efficient.

In non-wetting conditions increasing porosity from 0.1 to 0.5 increased efficiency by 53 %. In case of 20 % wetting an increase of 42 % was observed. From above results it can be clearly concluded that lower porosity has increased membrane mass transfer resistance. However, in terms of membrane manufacturing, there are some limitations on membrane porosity enhancement due to fabrication and mechanical strength problems.

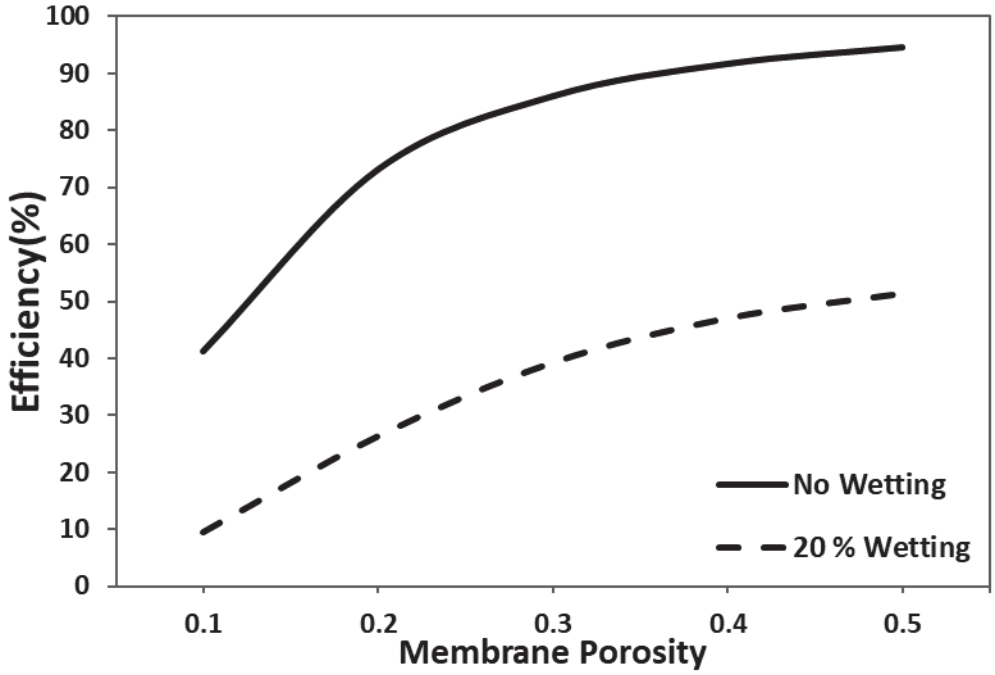

Figure 6.9 Effect of membrane porosity on the separation efficiency of CO_2 under non-wetted and partially wetted modes for IL [emim][$EtSO_4$]; Steady-state modeling; $Q_{IL} = 50\ ml.min^{-1}$, $Q_g = 20\ ml.min^{-1}$, $\varphi_v =$ 15 %, $T = 291$.

Both porosity and tortuosity are interdependent parameters. Tortuosity can be found using various correlations based on porosity. Here the tortuosity was calculated using the correlation developed by Iversen et al. (1997), as mentioned in Section 3.4 of Chapter 3. Tortuosity can directly affect the mass transfer resistance in porous membrane. Increase in tortuosity increases the mass transfer resistance in porous membrane (Asfand and Bourouis, 2015). Keeping a constant value of porosity (0.5), an increase in tortuosity significantly affected the removal efficiency (Figure 6.10). A decrease of about 20 % in removal efficiency was observed by changing tortuosity value from 1 to 7 in non-wetting mode. In case of 20 % wetting, the removal efficiency decreased by 22 %.

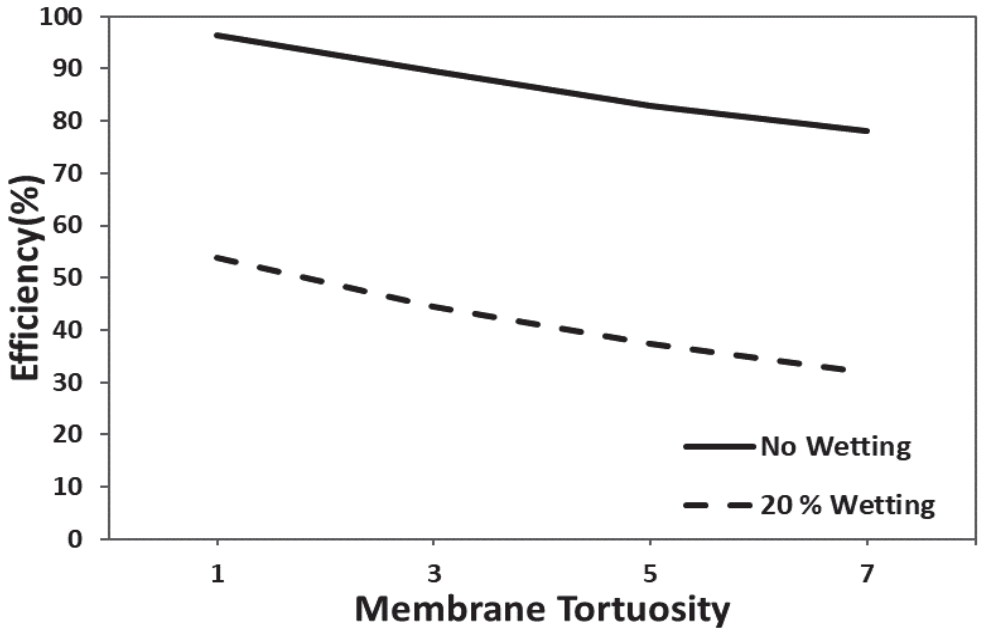

Figure 6.10 Effect of membrane tortuosity on the separation efficiency of CO_2 under non-wetted and partially wetted modes for IL [emim][$EtSO_4$]; Steady-state modeling; $Q_{IL} = 50\ ml.min^{-1}$, $Q_g = 20\ ml.min^{-1}$, $\varphi_v = 15\ \%$, $T = 291$.

6.2.2.2 Effect of fiber diameter and module length

In the current study gas flows inside the fibers. Increasing fiber inner diameter will increase gas volume. Number of fibers, gas and liquid velocities and other dimensions were kept constant. Increase in fiber inner diameter which in turn causes an increase in gas volume makes the process less efficient. As other dimensions and conditions were kept constant, there was more CO_2 available for the same amount of absorbent, which reduced separation efficiency. A smaller inner diameter will enhance the separation efficiency as shown in Figure 6.11. The effect of changing fiber diameter has been studied and confirmed by Dai et al. (2016). Fiber inner diameter was changed from 5 mm to 1mm which effectively enhanced separation efficiency. Azari et al. (2016) and Lu et al. (2014) reported opposite effects when absorbent was passed inside the fiber. Increasing the fiber diameter has enhanced CO_2 separation due to increase in mass transfer area.

A significant drop in removal efficiency was observed by increasing fiber inner diameter, for both non-wetted and partially wetted modes considering IL [emim][$EtSO_4$] as an absorbent

on the shell side. In no wetting conditions changing fiber inner diameter from 0.1 mm to 1 mm reduced efficiency by 33%. In case of 20 % wetting the efficiency is reduced by 47%.

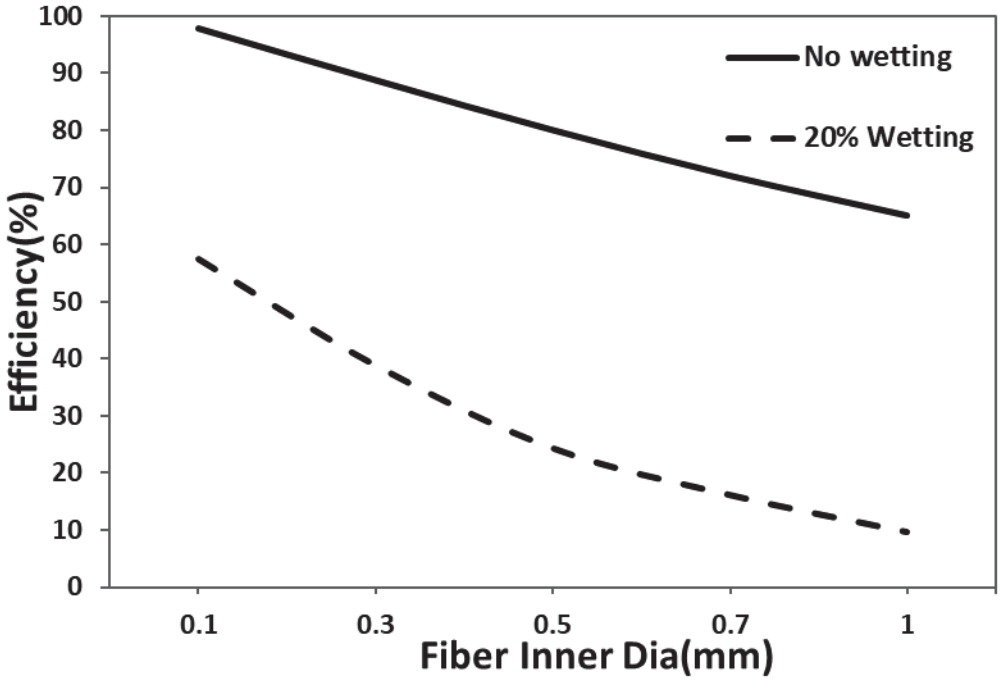

Figure 6.11 Effect of fiber inner diameter on the separation efficiency of CO_2 under non-wetted and partially wetted modes for IL [emim][$EtSO_4$]; Steady-state modeling; $Q_{IL} = 50\ ml.min^{-1}$, $Q_g = 20\ ml.min^{-1}$, $\varphi_v = 15\ \%$, $T = 291$.

Increase in membrane length causes an increase in mass transfer surface area and increase in absorbent residence time in module, which enhances the process efficiency. A significant increase in efficiency was observed with increase in module length, for both non-wetted and partially wetted conditions, during the simulations (Figure 6.12). Similar effects have been confirmed in other studies. Ahmad et al. (2015) reported that increasing module length enhances separation performance, while separating carbon dioxide from methane in HFMCs. Increasing fiber length will increase permeation which in turn will enhance absorption performance. In another study by Zhang et al. (2017), the fiber length was increased from 200 cm to 1000 cm which increased the CO_2 absorption efficiency in piperazine from 56% to 84 %. Wang et al. (2013) also reported the same effects in membrane stripping for CO_2 desorption from MEA. It was reported that long residence time in membrane contactor due to increased membrane length has resulted in better separation performances. An initial change

in module length causes more variation in removal efficiency. The variation in removal efficiency decreases with further change in module length.

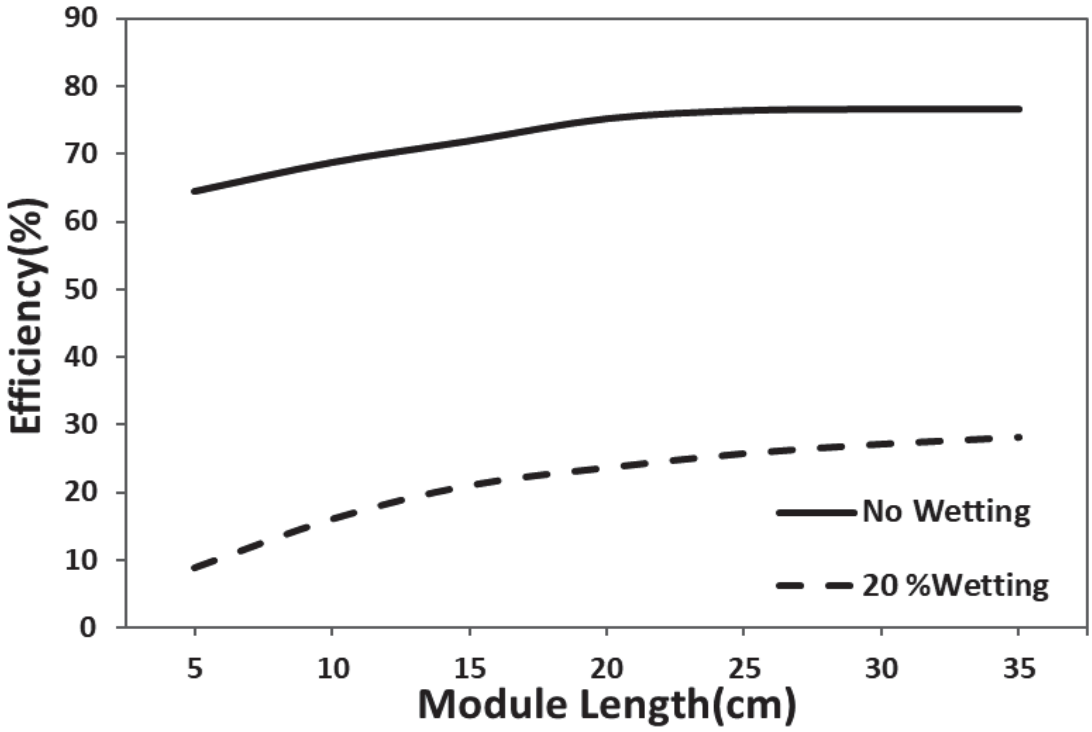

Figure 6.12 Effect of membrane module length on the separation efficiency of CO_2 under non-wetted and partially wetted modes for IL [emim][$EtSO_4$]; Steady-state modeling; $Q_{IL} = 50\ ml.min^{-1}$, $Q_g = 20\ ml.min^{-1}$, $\varphi_v = 15\ \%$, $T = 291$.

In this study, pressure drop in the membrane module is not considered. Increase in length may cause an increase in pressure drop due to high absorbent viscosity which in turn may cause membrane wetting. CO_2 concentration also drops progressively along membrane length which reduces driving force for separation (Dai et al., 2016c). Thus, an optimized value for membrane module length must be used for optimum separations.

6.2.2.3 Effect of gas and absorbent flowrate

Effect of gas flowrate on CO_2 removal performance ($C_{g\text{-}out}/C_{g\text{-}in}$) is shown in Figure 6.13 the removal of CO_2 is enhanced by decreasing the gas flowrate. Improving gas flowrate leads to minimal gas residence time in the tube, which leads to allow more CO_2 to pass from the

contactor without absorption. This decrease in CO_2 residence time considerably reduces the performance of the removal (Yan et al., 2007; Yeon et al., 2005). Although even if CO_2 absorption performance decreases with increase in gas flowrate, the amount of CO_2 absorbed in the liquid phase will increase. The CO_2 absorption productivity decreases as there is more CO_2 available at gas outlet which is not absorbed due to high gas flowrate. However, the CO_2 amount in the liquid phase increases because of the enhanced mass transfer (Li and Chen, 2005). This enhancement in mass transfer is due to the greater average concentration of CO_2 at gas side because of the higher gas flowrate (Zhang et al., 2006).

Figure 6.13 shows dimensionless concentration of CO_2 against radial dimensionless length at outlet of the tube considering IL [emim][$EtSO_4$] as an absorbent. It is evident from this figure that increasing gas flowrate has significantly decreased the removal productivity, for both non-wetted and partially wetted modes. Gas flowrate was varied from 10 ml min^{-1} to 130 ml min^{-1} while keeping a constant absorbent flowrate at 50 ml min^{-1}. CO_2 dimensionless concentration at the outlet of the tube was increased by 35 % and 38 % in non-wetting and partial wetting modes, respectively, by varying gas flowrate from 10 ml min^{-1} to 130 ml min^{-1}. Gas flowrate should be very carefully optimized as it directly affects the CO_2 transport and causes a high/low CO_2 flux across membrane.

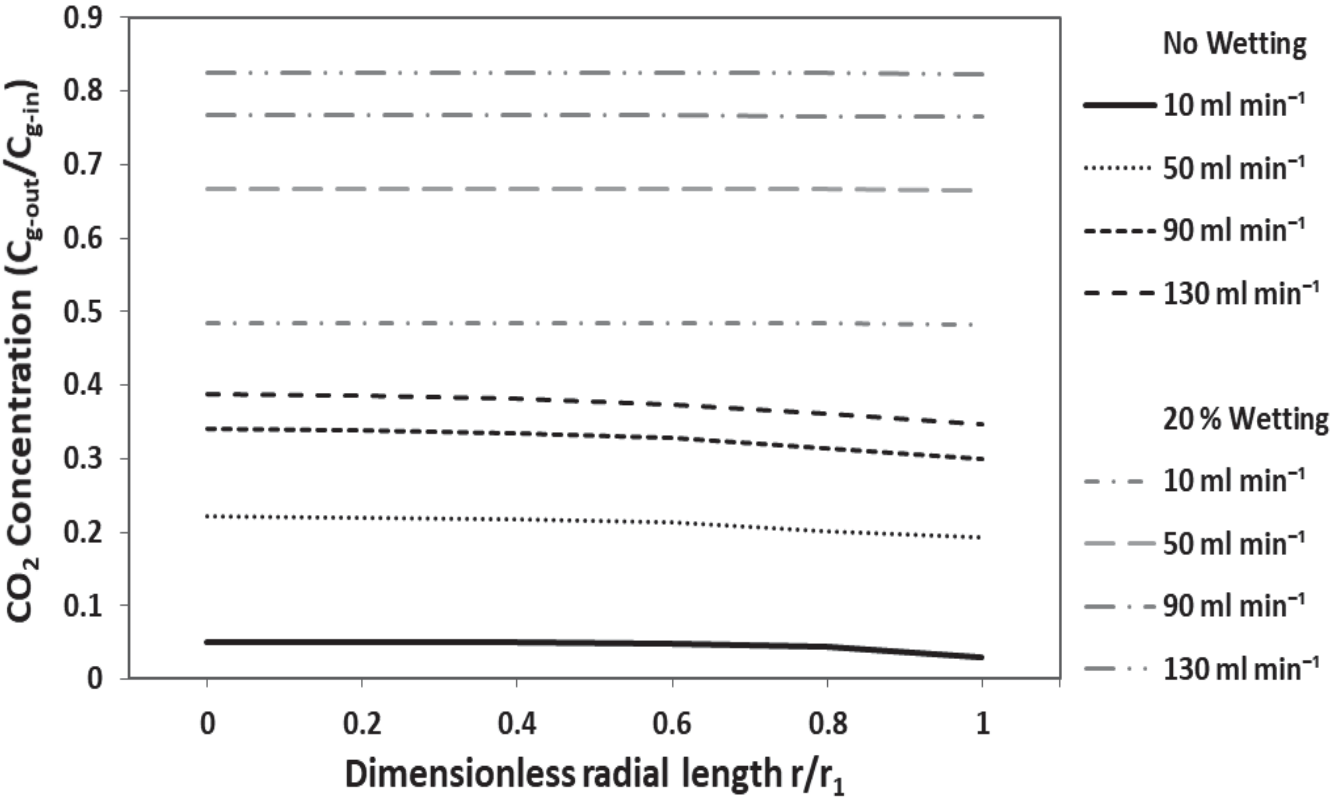

Figure 6.13 Effect of gas flowrate on separation performance of CO_2 under non-wetted and partially wetted modes for IL [emim][$EtSO_4$]; Steady-state modeling; $Q_{IL} = 50\ ml.min^{-1}$, $\varphi_v = 15\ \%, T = 291$.

Absorbent flowrate can affect the CO_2 removal productivity, as shown in Figure 6.14. An increase in absorbent flowrate increases the performance of CO_2 removal (Yan et al., 2007). A lower absorbent flowrate reduces the driving force for the CO_2 due to the lower concentration difference. Increasing absorbent flowrate allows more fresh absorbent to enter the system to absorb CO_2. It also increases the volume of absorbent for the same amount of CO_2 in gas phase. Increasing absorbent flowrate also reduces liquid boundary layer thickness which results in an increase in liquid mass transfer coefficient and diffusivity (Gong et al., 2006; Li and Chen, 2005; Mansourizadeh et al., 2010; Yan et al., 2007). CO_2 flux was increased by increasing water and NaOH flowrate in PVDF membrane contactor. Wang at al. (Wang et al., 2004) reported that increasing absorbent flowrate increases the CO_2 absorption flux because of the instantaneous absorption.

Absorbent flowrate was varied from 5 ml min^{-1} to 65 ml min^{-1} while gas flowrate was kept constant at 130 ml.min^{-1}. A higher gas flowrate was used to study the effect of absorbent flowrate on process performance. At lower gas flowrates, the performance was high enough which made it impossible to study the effect of higher absorbent flowrates. CO_2 dimensionless concentration at the outlet of the tube dropped by 12% and 16% for non-wetting and partial wetting modes, respectively, by increasing liquid flowrate from 5 ml min^{-1} to 65 ml min^{-1}.

Apart from the enhancement in the CO_2 removal productivity with increase in absorbent flowrate, several authors have reported the influence of absorbent flowrate on the membrane wetting (Mosadegh-Sedghi et al., 2014). A significant increase in pore wetting due to increase in absorbent flowrate has been reported. Boributh et al. (2012) observed an increase in the wetting ratio by a factor of approximately 8 while increasing the absorbent velocity from 0.1 m s^{-1} to 0.4 m s^{-1}. Other researchers have attributed this increase in wetting to the reduction in absorbent boundary resistance with absorbent flowrate enhancement (Zhang et al., 2008). Mavroudi et al. (2006), observed that total mass transfer resistance increased with time and became more significant at higher absorbent flowrates while working on the CO_2 absorption in a water-membrane contactor setup. This author has reported that this behavior

might be due to the possible increase in pressure with increase in absorbent flowrate, thus resulting in higher transmembrane pressure and increasing membrane pore wetting. An optimized value of absorbent flowrate is required to reduce the potential for wetting and to control both capital and operational cost for the process (Malek et al., 1997; Yan et al., 2007).

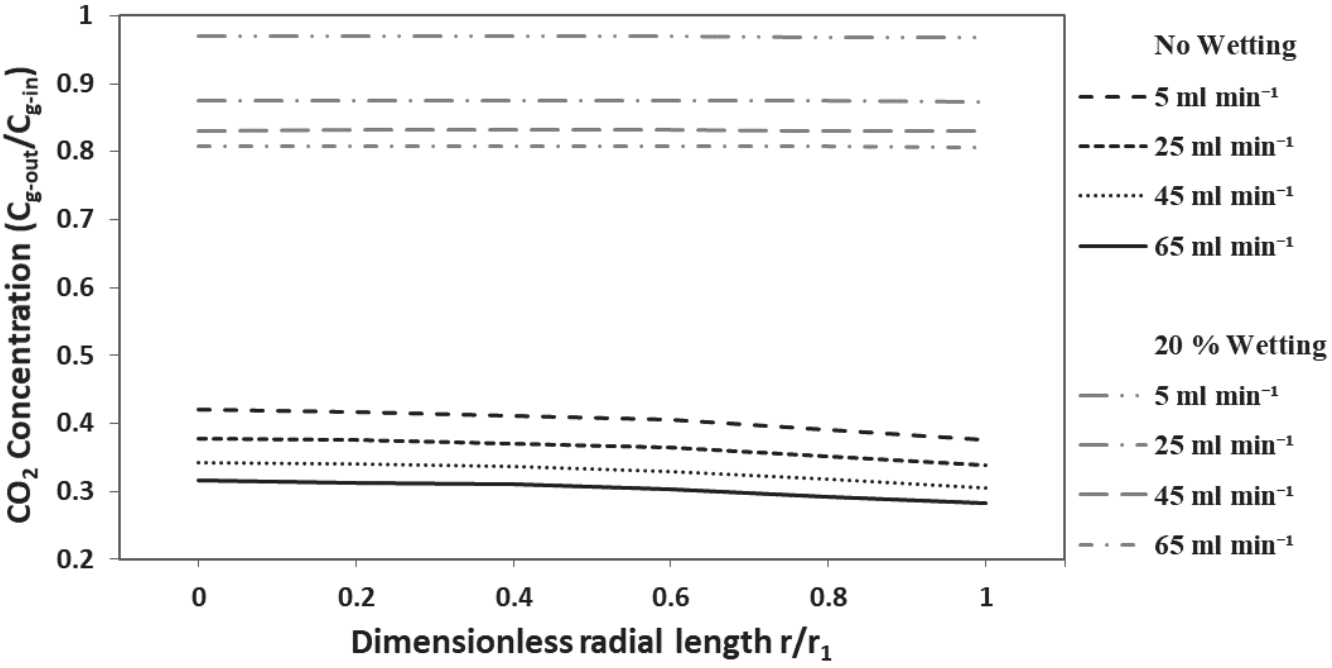

Figure 6.14 Effect of IL flowrate on separation performance of CO_2 under non-wetted and partially wetted modes for IL [emim][$EtSO_4$]; Steady-state modeling; $Q_g = 130\ ml.min^{-1}$, $\varphi_v = 15\ \%, T = 291$.

It can be observed that there is a minor decrease in concentration when moving towards the wall of the membrane (r_1), in no-wetting mode. It may be due to the reduction of CO_2 concentration near the membrane wall by the absorption. Moreover, in partial wetting conditions there is almost no drop in concentration because the driving force is decreased due to wetting and increased membrane mass transfer resistance.

A sensitivity analysis was carried out for IL [emim] [$MeSO_4$] in a closed loop which leads the process to reach a pseudo-steady-state due to continuous loading of CO_2 to the IL. At pseudo-steady-state the CO_2 loading becomes very slow and constant. Operating time (IL recirculation time) to reach pseudo-steady-state is dependent upon the operating conditions like gas and liquid flowrates. Figure 6.15 presents dependency of the operation time to reach pseudo-steady-state upon gas and liquid flowrates. The results clearly demonstrated the

dominancy of the gas flowrate over liquid flowrate. When the liquid flowrate was fixed at 40 ml min^{-1}, an increase in gas flowrate by 40 ml min^{-1} has decreased the operating time to reach pseudo-steady-state by 42 minutes. It clearly describes the improved mass transfer flux at higher gas flowrates which causes the IL to reach rapidly to the target loading value. A decrease of only 4 minutes in operating time was observed by increasing liquid flowrate by 40 ml min^{-1}, at a fixed gas flowrate of 50 ml min^{-1}.

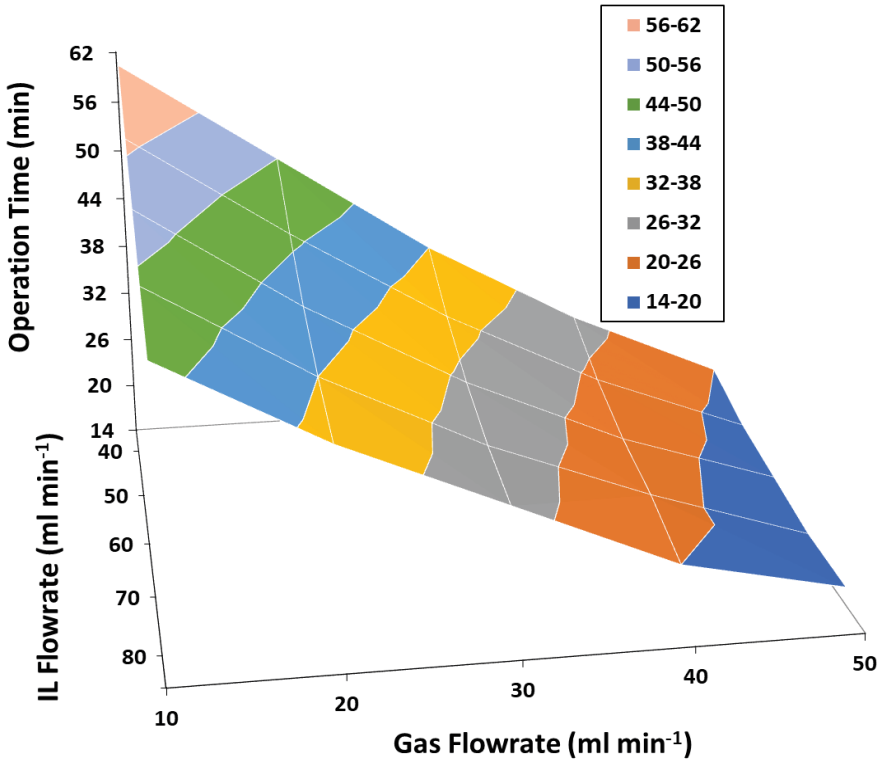

Figure 6.15 Dependency of the operating time over gas and liquid flowrates for IL [emim] [$MeSO_4$]; Pseudo-steady-state; $T = 288\ K$, $CO_2\ concentration = 15\ \%\ vol.$

6.3 Coupled absorption/desorption

The model developed for coupled absorption/desorption is based on the experimental arrangements presented in Section 3.5 of Chapter 3. IL recirculates counter currently (in a closed loop), at the same time through the shell side of both membrane absorber and membrane stripper, while feed and sweep gas flows through the lumen side of the membrane absorber and membrane stripper, respectively. The integrated (membrane absorption and stripping) modeling approach for the simulations presented here, is described in Section 4.2.1 of Chapter 4.

6.3.1 Parametric analysis

A parametric analysis was carried out for coupled absorption/desorption process to study and compare the effect of porosity of the membrane and sweeping gas flowrate on the gas side outlet CO_2 concentration of the membrane absorber. IL [emim][$MeSO_4$] was selected for this analysis. Obvious effects of sweeping gas flowrate on outlet CO_2 concentration of gas side can be observed from Figure 6.16. On the contrary, we can notice that porosity of membrane has no impact on the process. Considering membranes with 60 % of porosity, increase in sweeping gas flowrate from 50 ml min^{-1} to 200 ml min^{-1} results on a decreased of the normalized gas side outlet CO_2 concentration from 0.7 to 0.1. It represents an enhancement of productivity of the system of 60 %.

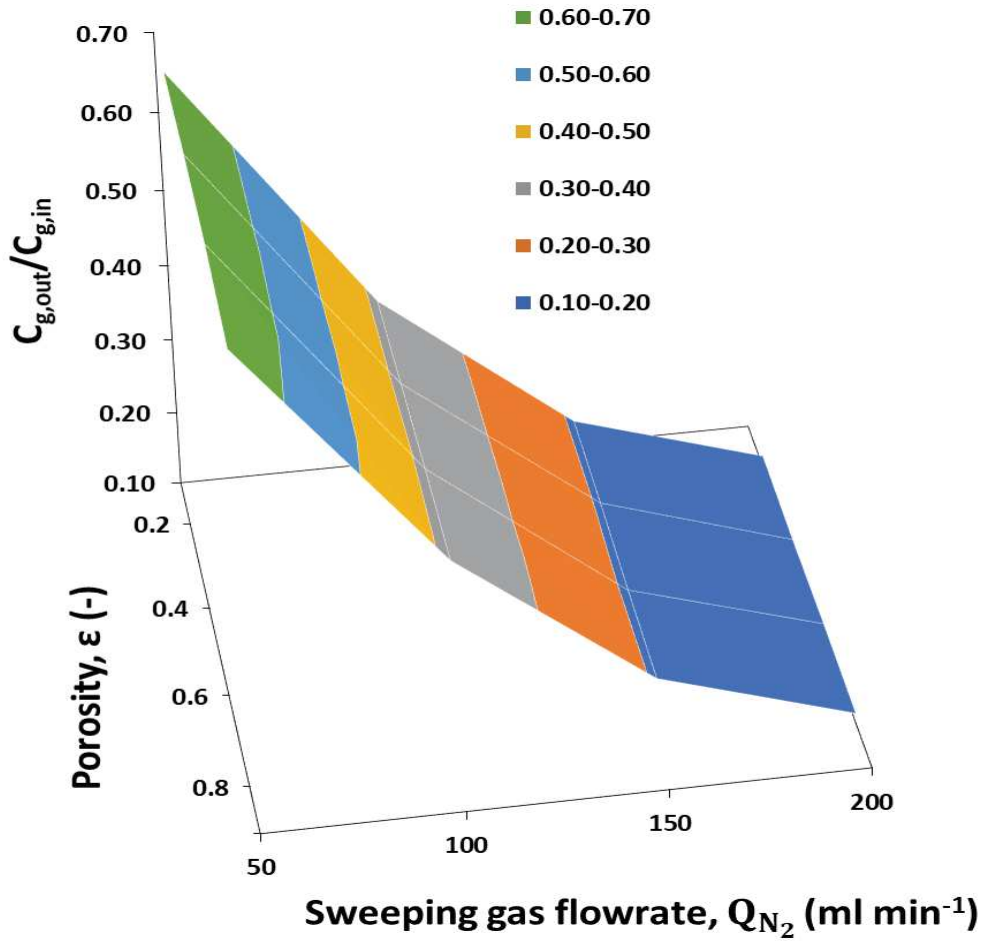

Figure 6.16 Effect of sweeping gas flowrate and porosity on the outlet concentration of CO_2 in the feed stream for IL [emim] [$MeSO_4$]; Pseudo-steady-state; $T = 288\ K$, $Q_{IL} = 60\ ml.min^{-1}$, $CO_2\ concentration = 15\ \%\ vol.$

6.3.2 Optimization; zero CO_2 outlet concentration

The analysis to achieve zero CO_2 concentration (100 % efficient stripping) was carried out to optimize the sweeping gas flowrate, porosity of the membrane and IL flowrate at the membrane stripper outlet in a single absorption desorption cycle. Simulations have been run with different values for these parameters to achieve the target of zero CO_2 concentration at the membrane stripper outlet. The results of simulation are presented in Figure 6.17. Increase in gas flowrate and membrane porosity and decrease in liquid flowrate were found favorable in achieving the target concentration. For 60 % porous membrane, 48 ml min^{-1} liquid flowrate must be maintained when 200 ml min^{-1} sweeping gas flowrate is passed from the membrane stripper. Reducing the sweeping gas flowrate to 50 ml min^{-1} needs a reduction of 30 ml min^{-1} in the liquid flowrate to maintain zero CO_2 concentration at the outlet. The gas side outlet concentration of the membrane stripper doesn't look much sensitive to membrane porosity. Sensitivity of the optimization can be ranked as $Q_{IL} > Q_{N_2} > \varepsilon$.

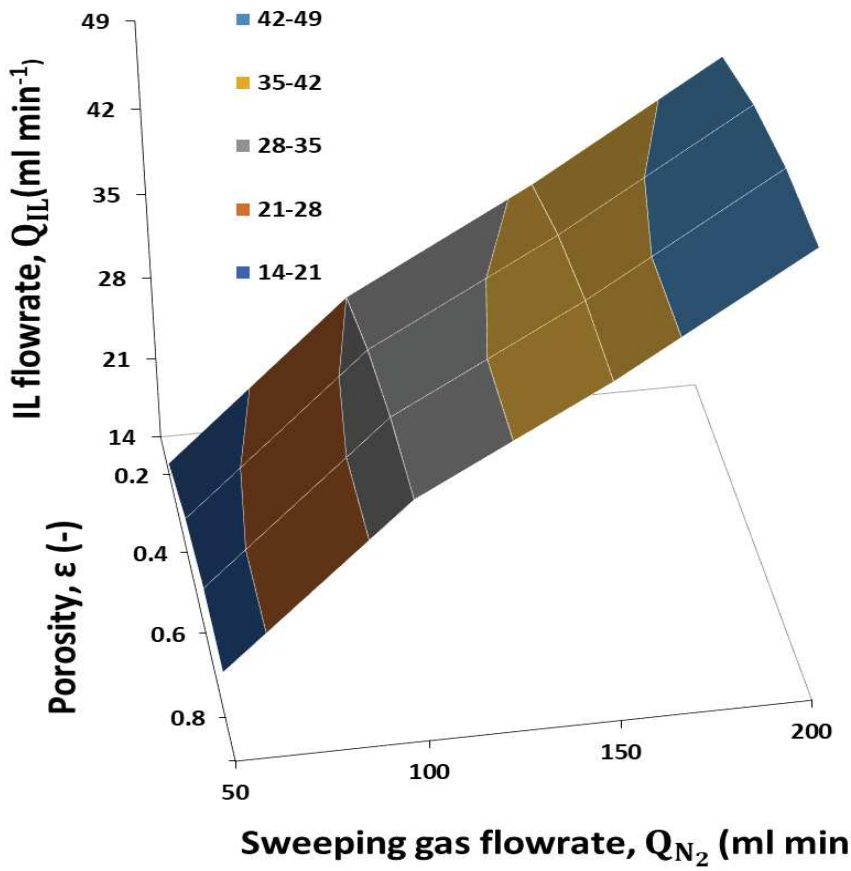

Figure 6.17 Optimizing sweeping gas flowrate, IL flowrate and membrane porosity for achieving zero concentration of CO_2 at the membrane stripper outlet, for IL [emim] [$MeSO_4$]; Pseudo-steady-state; $T = 288\ K$, $CO_2\ concentration = 15\ \%\ vol.$

6.4 Conclusion

This chapter presented simulations for the isothermal modeling approach developed in Section 4.2.1 of Chapter 4 for the absorption of CO_2 in four different imidazolium based RTILs, [emim][$MeSO_4$], [emim][DCA], [emim][$EtSO_4$] and [emim][Ac]. The models well replicated the experimental data of the single module absorption setup and coupled absorption/desorption setup. A detailed membrane pore wetting analysis revealed a significant reduction in mass transfer in case of membrane wetting. Module characteristics and operating conditions affected the absorption process. Effect of gas flowrate was more dominant than liquid flowrate. For coupled absorption/desorption setup, CO_2 concentration at gas side outlet was way more sensitive to sweeping gas flowrate than porosity. Moreover, the simulations for coupled absorption/desorption setup were optimized for continuous zero concentration of CO_2 at the membrane stripper outlet.

Chapter 7. Modeling and Simulation Under Non-Isothermal Conditions

Non-isothermal modeling approach developed in Section 4.2.2 of Chapter 4 was implemented for the absorption of CO_2 in four amino-based TSILs namely: tetramethylammonium glycinate $[N_{1111}][Gly]$, 1-ethyl-3-methylimidazolium glycinate [emim][Gly], 1-butyl-3-methylimidazolium glycinate [bmim][Gly] and 1-hexyl-3-methylimidazolium glycinate [hmim][Gly]. Properties of the aqueous amino acid ionic liquids are presented in Table 7.1 below. TSILs provide very high CO_2 solubility which can reach up to three times of the corresponding alkyl chain RTILs. These ILs are able to absorb CO_2 by both chemical and physical sorption, for which the CO_2 loading increases with an increase in pressure. Moreover, TSILs can absorb CO_2 at low partial pressures due to chemical reaction (Shiflett and Yokozeki, 2009). The main drawback of the amino acid-based ILs is their very high viscosity (> 200 mPa.s) which also reduces the diffusivity of CO_2 and slows down the absorption process (Feng et al., 2010; Jiang et al., 2002). As these ILs are highly soluble in water, using the aqueous solutions instead of pure ILs can reduce the viscosity to a very low value.

Table 7.1 Properties of the aqueous amino acid-based task specific ionic liquids

IL concentration (mole L^{-1})	ρ (g cm^{-3}) 303 K	μ (mPa s) 303 K	D_{CO_2} (cm^2 s^{-1}) 10^5 303 K	Ref.
$[N_{1111}][Gly]$				
0.3	1.0003	1.5	1.20	(Jing et al., 2012)
0.7	1.0068	1.6	1.11	(Jing et al., 2012)
1.0	1.0116	1.7	1.06	(Jing et al., 2012)
2.0	1.0278	2.6	0.72	(Jing et al., 2012)
[emim][Gly]				
0.5	1.0093	0.941	1.982	(Wu et al., 2015)
1.0	1.0231	1.176	1.658	(Wu et al., 2015)
1.5	1.0320	1.409	1.435	(Wu et al., 2015)
2.0	1.0379	1.778	1.191	(Wu et al., 2015)
[bmim][Gly]				
0.5	1.0090	0.994	1.896	(Wu et al., 2016)

1.0	1.0256	1.278	1.551	(Wu et al., 2016)
1.5	1.0341	1.850	1.154	(Wu et al., 2016)
2.0	1.0452	2.628	0.871	(Wu et al., 2016)
[hmim][Gly]				
0.5	1.0096	1.09	1.65	(Guo et al., 2013)
0.8	1.0178	1.36	1.32	(Guo et al., 2013)
1.0	1.0234	1.58	1.14	(Guo et al., 2013)
1.2	1.0284	1.86	0.97	(Guo et al., 2013)

A different (than isothermal model described in Section 4.2.1 of Chapter 4) modeling approach based on non-isothermal conditions was implemented for absorption of CO_2 in the aqueous solutions of amino acid based reactive ILs used as absorbents in the membrane contactor. In fact, for very reactive absorbents as considered for the current study, the process of absorption of CO_2 is non-isothermal as the energy of dissolution reaction is released and accumulated along the membrane contactor length.

To our knowledge these absorbents have never been applied for CO_2 absorption in HFMCs. Simulations under non-isothermal conditions are presented in this chapter after the model was validated. The following publication from the authors corresponds to this Chapter.

- Sohaib, Q., Muhammad, A., Younas, M., Rezakazemi, M., Druon-Bocquet, S., Sanchez-Marcano, J., 2020. Rigorous Non-Isothermal Modeling Approach for Mass and Energy Transport during CO_2 Absorption into Amino Acid Ionic Liquids in Hollow Fiber Membrane Contactors

7.1 Model validation; comparison between simulations and experimental data

As explained above the ILs used in the current study have never been implemented in the membrane contactor absorption operations. Indeed, to validate the model experimental data of CO_2 absorption in a membrane contactor absorption with IL monoethanolamine glycinate ([MEA][Gly]) carried out by (Lu et al. (2017) was considered. This IL is composed by the same anion of ILs considered for simulations. Moreover, it also presents almost comparable physicochemical properties. The model described in chapter 4, considers the same HFMC experimental setup of Lu et al. (2017). Characteristics of the membrane and operating conditions were also those used by these authors, they are reported in Table 7.2.

Table 7.2 Membrane characteristics and operating conditions

Parameter	**Value**	**unit**
Outer diameter of the tube (d_o)	$5.0\ 10^{-4}$	m
Membrane thickness (δ)	$1.0\ 10^{-4}$	m
Length of the contactor (L)	0.250	m
Number of fibers (N)	1200	-
Membrane pore diameter(d_p)	0.05	μm
Porosity (ε)	60	%
Packing factor (∅)	0.26	-
Feed gas flowrate, $Q_{g,}$	800	ml min^{-1}
Liquid flowrate, Q_{IL}	80-160	ml min^{-1}
Gas inlet pressure, $P_{g,in}$	1.08	Bar
Temperature, T	289	K
Absorbent Concentration, C_{IL}	0.5	mol L^{-1}

Simulations were carried out for the unloaded solvent $C_{l\text{-}in}$=0 at temperature T=289 K, gas side pressure P= 1.08 bar, IL concentration C_{IL}= 0.5 mol L^{-1} and gas flowrate Q_g= 800 ml min^{-1}. The liquid flowrate was varied from 80 to 160 ml min^{-1}, and the normalized CO_2 concentration at the gas side outlet was calculated and reported in Figure 7.1. The square dots represent the experimental data of the IL [MEA][Gly], while the lines represent simulations of the four ILs considered for this work. The results from this figure show that trends between the experimental data and simulations are identical. However, the values of separation performance of [MEA][Gly] are a bit lower than the simulated values for all other ILs except for the [hmim][Gly]. The difference in the separation performance is probably due to the different physicochemical properties and reactivity of the ILs considered for simulations. Indeed, we took the assumption that the model gives enough precision to be used in simulations with ILs studied here.

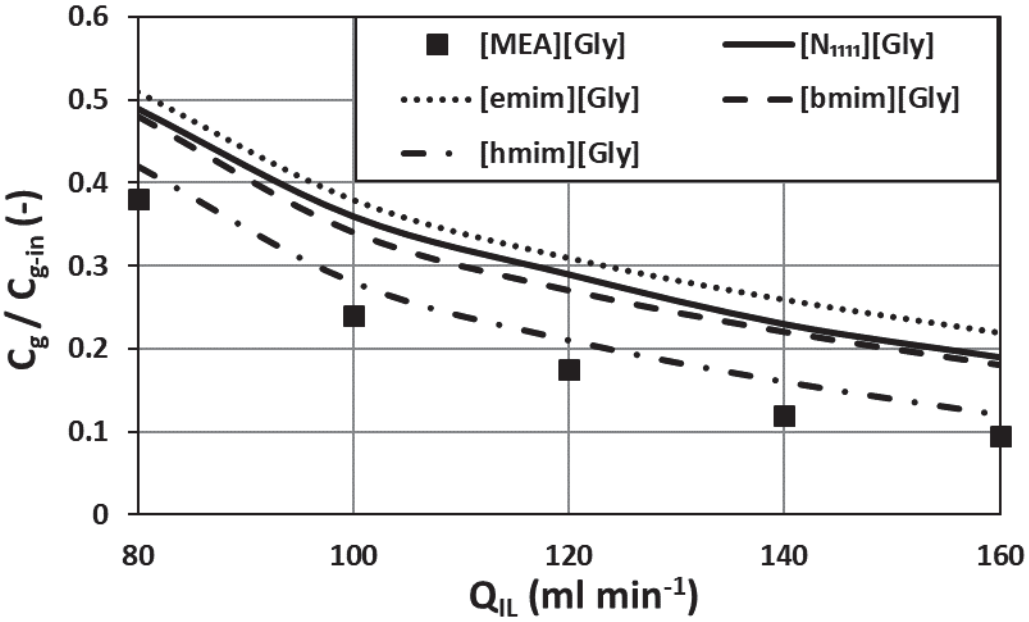

Figure 7.1 Comparison between the simulations (line) and experimental data (square dots); $Q_g = 800\ ml\ min^{-1}$, $C_{l-in} = 0\ mol\ L^{-1}$, $C_{IL-in} = 0.5\ mol\ L^{-1}$, $T_{l-in}, T_{g-in} = 289\ K$.

7.2 Axial interfacial profiles: CO_2 concentration, IL concentration, temperature distribution, reaction rate K_2 rise

This section presents the simulations of CO_2 concentration, IL concentration and variations of temperature and reaction rate constant over the interfacial boundary of the membrane. As mentioned in the preceding sections, the gas/liquid equilibrium over the interfacial boundary is defined by Henry's Law. Hatta numbers presented in Table 4.3 have confirmed the reaction for absorption specie and ILs to occur at the interface mostly. This number can define whether the reaction occurs in the bulk or the liquid film depending upon its value (Kierzkowska-Pawlak, 2012). The steady-state gradual evolution of axial concentration of CO_2 and IL is presented in Figure 7.2. Unloaded absorbent was introduced to the tube side at z=0 while the gas mixture having 15 % CO_2 and N_2 (rest to balance) was passed counter currently from the shell side of the membrane contactor. The absorbents were considered at chemical equilibrium having homogenous concentration at the inlet of the contactor. A gradual decrease in CO_2 concentration of both gas phase and absorbents can be observed toward the respective outlets due to absorption at the interface. At the inlet of the gas side, a faster drop in the concentration of CO_2 can be observed demonstrating the effect of CO_2 concentration on the absorption process. The gradual decrease in the concentration of

absorbent along with the fiber length shows the enrichment of the absorbent with CO_2. Similar trend of absorption can be seen for all ILs. ILs $[N_{1111}][Gly]$ and [bmim][Gly] have nearly the same concentration profiles. IL [hmim][Gly] can be regarded as the most efficient one while [emim][Gly] as the least efficient one among all ILs.

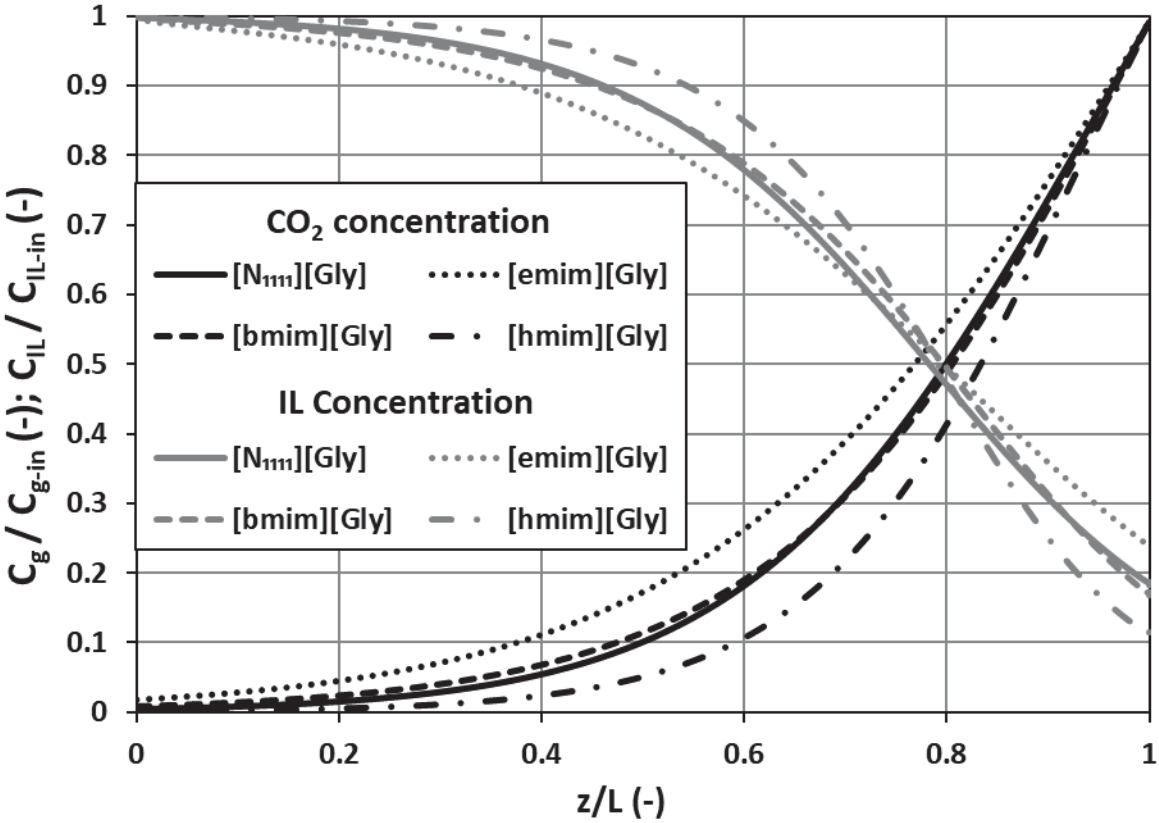

Figure 7.2 Normalized axial concentration distribution of absorption specie (CO_2) and absorbents over mass transfer interface; $Q_{IL} = 20\ ml\ min^{-1}$, $Q_g = 60\ ml\ min^{-1}$, $C_{l-in} = 0\ mol\ L^{-1}$, $C_{IL-in} = 1\ mol\ L^{-1}$, $T_{l-in}, T_{g-in} = 298\ K$.

Figure 7.3 shows the axial temperature profile of the liquid phase for the four ILs having inlet temperature of 298 K. The temperature was considered as recorded near the interface. As mentioned in the assumptions (Section 4.2.2 of Chapter 4) the gas mixture was considered to be dry which helps avoiding the condensation of water vapors near the liquid inlet. The pressure was kept higher to avoid the evaporation of water in the lateral sections near the liquid outlet. The temperature rise ranges from 10 to 25 K depending upon the reactivity of the IL. The radial temperature gradient was almost negligible due to the excellent heat transfer within and between the domains. A variation of temperature can be observed along

the fiber's length. Temperature reaches a maximum value of 317, 310, 312 and 325 K for ILs $[N_{1111}][Gly]$, [emim][Gly], [bmim][Gly] and [hmim][Gly], respectively. A high magnitude of temperature gradient can be observed in the section after half contactor length of the fiber (z/L=0.5-z/L=1).

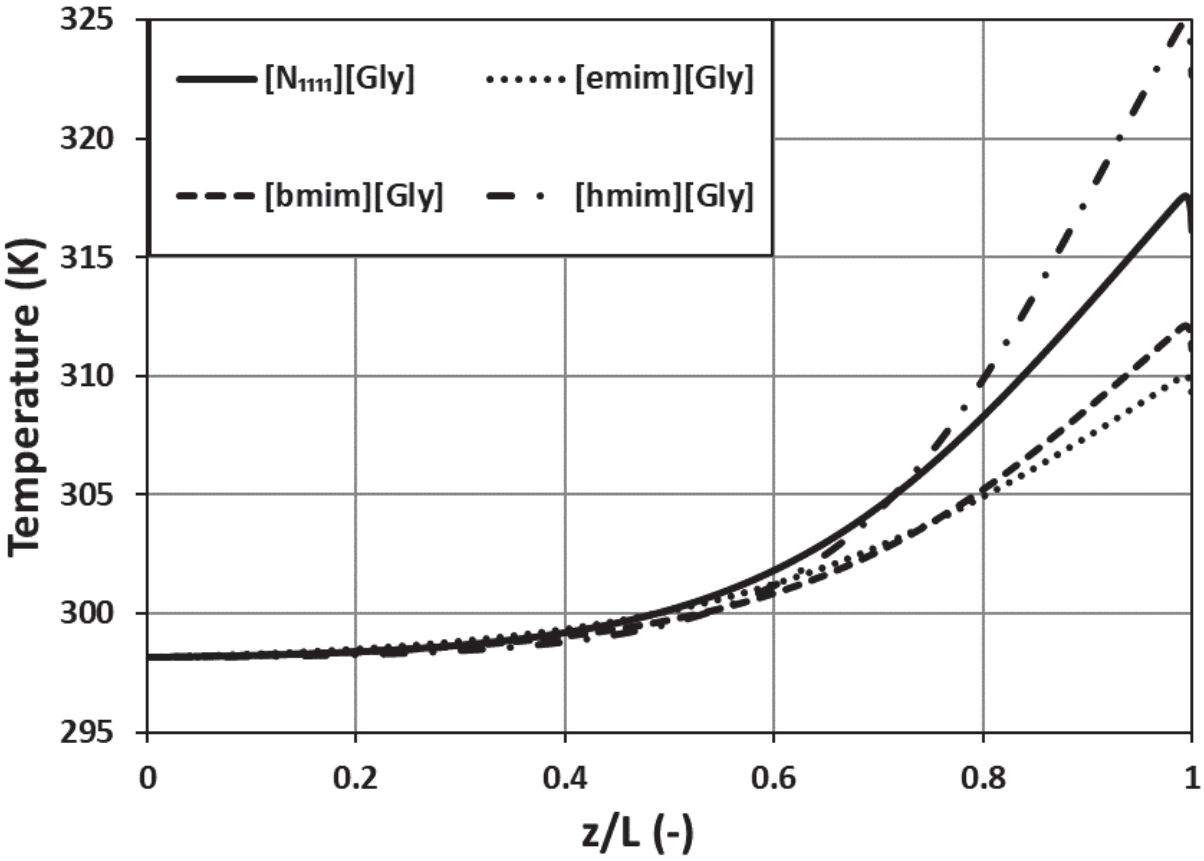

Figure 7.3 Temperature profile of the liquid phase over mass transfer interface; $Q_{IL} = 20\ ml\ min^{-1}$, $Q_g = 60\ ml\ min^{-1}$, $C_{l-in} = 0\ mol\ L^{-1}$, $C_{IL-in} = 1\ mol\ L^{-1}$, $T_{l-in}, T_{g-in} = 298\ K$.

Reaction rate constant (K_2) is a function of temperature. K_2 values and their dependency upon temperature are listed in Table 4.3. These values were recorded near the interfacial boundary at the inlet temperature of 298 K. There is a gradual evolution of K_2 along the fiber length as K_2 is a function of temperature, which is presented in Figure 7.4. In order to understand and observe the trend and compare the values between different ILs, the K_2 values were normalized by the maximum value at the corresponding axial boundary. Correspondence in the trends (Figures 7.3 and 7.4) of K_2 and temperature variation along fiber length can be evidently observed. K_2 for the IL [hmim][Gly] seems to have strong dependency on

temperature compared to other three ILs. A very slight change in the K_2 can be observed for IL [emim][Gly].

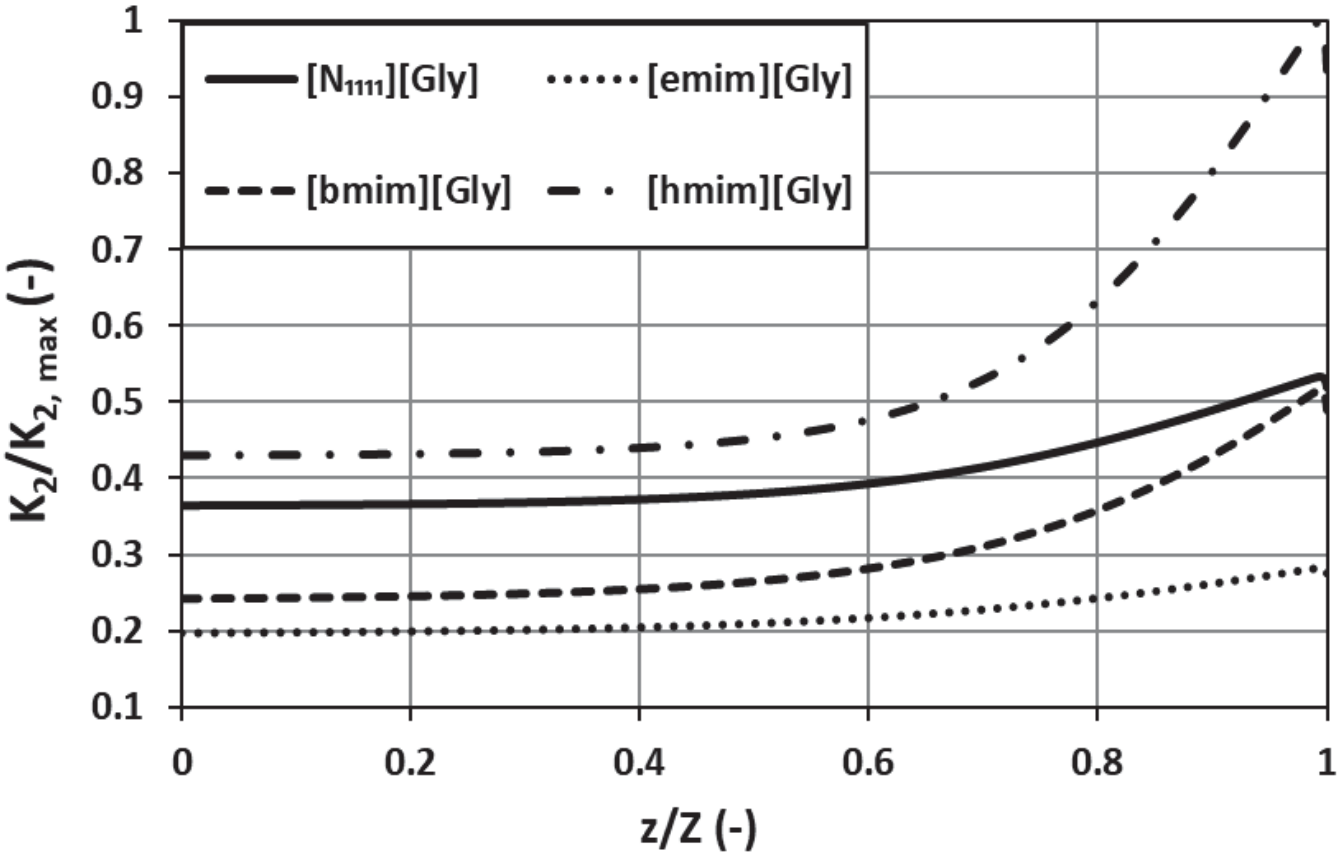

Figure 7.4 Normalized axial reaction rate constant distribution over mass transfer interface; $Q_{IL} = 20\ ml\ min^{-1}$, $Q_g = 60\ ml\ min^{-1}$, $C_{l-in} = 0\ mol\ L^{-1}$, $C_{IL-in} = 1\ mol\ L^{-1}$, $T_{l-in}, T_{g-in} = 298\ K$.

7.3 Ionic Liquids performance; comparative analysis

Concentration of the IL has a strong influence on the separation performance of the four ILs. On one hand, increase in IL concentration decreases both diffusivity and solubility of CO_2 in the IL, on the other hand it increases the reaction rate (Feng et al., 2010; Zhou et al., 2012). The decrease in solubility is in accord with salting out effect (Weisenberger and Schumpe, 1996). The overall effect can be observed in Figure 7.5, which shows that generally the efficiency is enhanced by an increase in IL concentration. The lower CO_2 concentration represents higher separation performance. For IL $[N_{1111}][Gly]$ the efficiency increases by 23 % for increasing IL concentration from 0.3 to 2.0 mol L^{-1}. For [emim][Gly] an efficiency

increases of 18 % was observed for increasing IL concentration 0.5 to 1.5 mol L^{-1}. Further increase in IL concentration led to decreased efficiency. This phenomenon can be linked with the strong dependence of the membrane contactor absorption process on the physicochemical (viscosity, density and diffusion coefficient) properties of the absorbent. Similarly, for [bmim][Gly] an efficiency increase of 18 % was observed for increasing IL concentration from 0.5 to 2.0 mol L^{-1} while for [hmim][Gly] the increase was 13 % for an increase in IL concentration from 0.5 to 1.2 mol L^{-1}. A comparative analysis of the performance of four ILs was carried out at IL concentration of 1 mol L^{-1}. IL [hmim][Gly] was found with the highest efficiency of 85 % among all ILs. While comparing the ILs at 2 mol L^{-1} the efficiencies were 83, 75 and 75 % for [bmim][Gly], [emim][Gly] and [N_{1111}][Gly], respectively. An increase in the CO_2 solubilities have been reported with an increase in the alkyl chain of the imidazolium cation (Baltus et al., 2004; Chen et al., 2006). However, the effect of the alkyl chain cation was found to be minor compared to anions (Supasitmongkol and Styring, 2010). This effect seems to be validated regarding the separation efficiencies of imidazolium cation based ILs reported above.

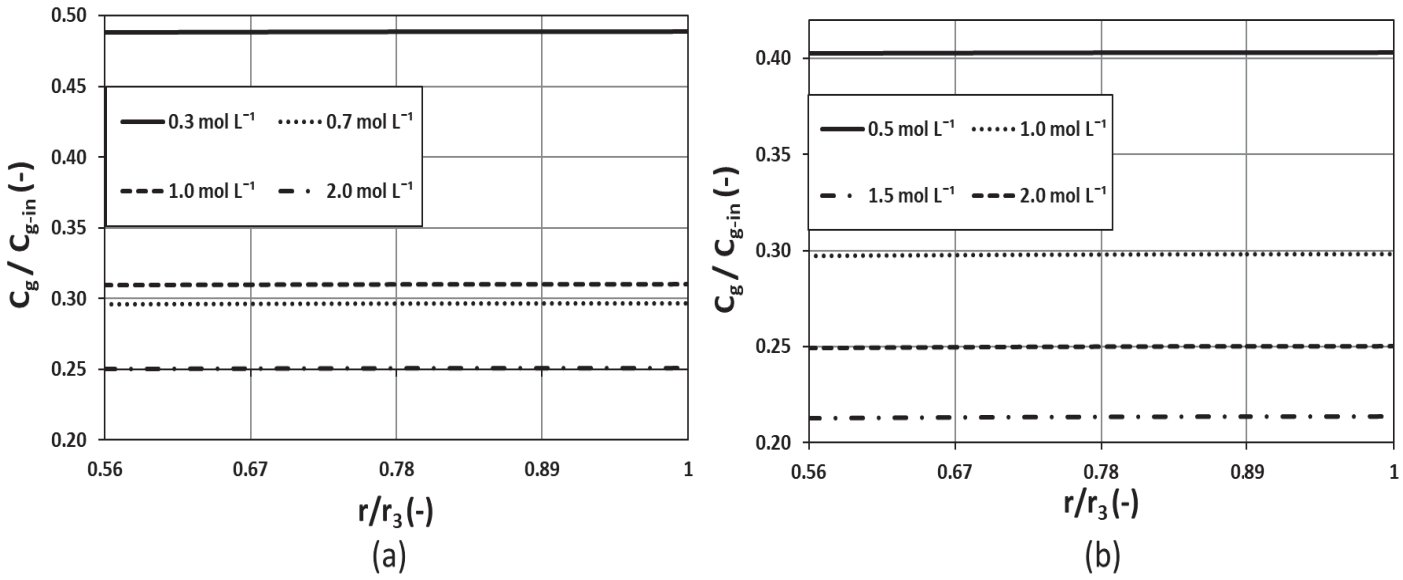

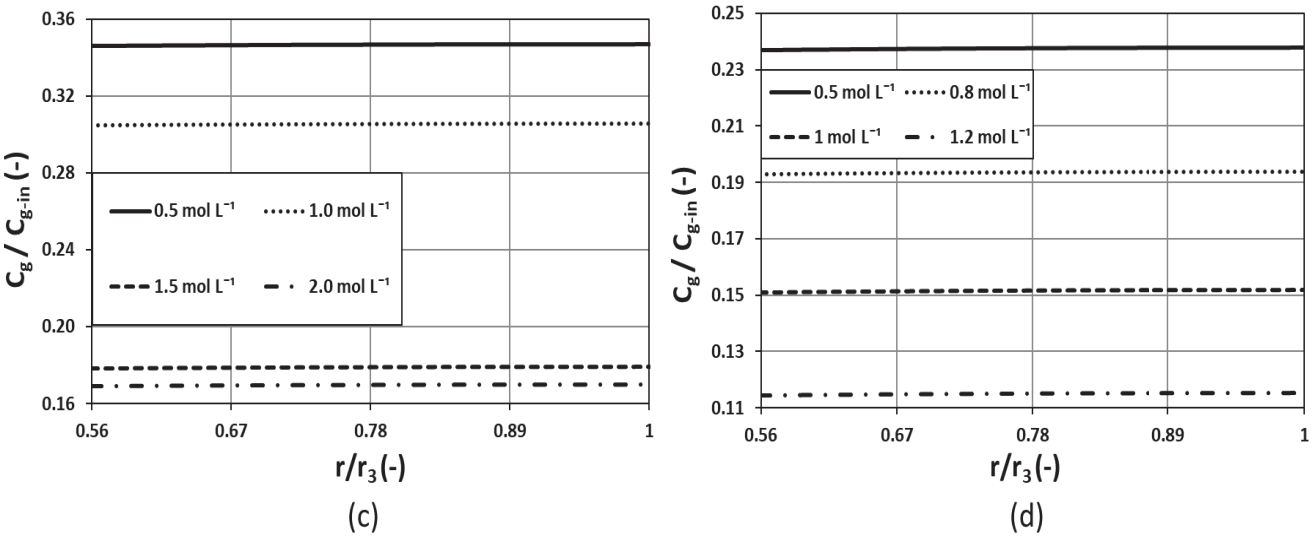

Figure 7.5 Normalized radial profiles of gas phase CO_2 concentrations for different concentration of ionic liquids (a) $[N_{1111}][Gly]$, (b) [emim][Gly], (c) [bmim][Gly] and (d) [hmim][Gly]; $Q_{IL} = 20\ ml\ min^{-1}$, $Q_g = 60\ ml\ min^{-1}$, $C_{l-in} = 0\ mol\ L^{-1}$, $T_{l-in}, T_{g-in} = 298\ K$

Temperature can affect both physisorption and chemisorption of the CO_2 in ILs. Normally in the case of the absorption process with a chemical reaction, the temperature can affect the physical solubility, diffusivity, and reaction rate. Physical solubility of CO_2 in the ILs decreases with increase in temperature (Lei et al., 2014; Okoturo and VanderNoot, 2004). Diffusivity of the CO_2 in ILs and gaseous mixture has proportionality with the temperature. An increase in temperature increases the diffusivity of CO_2 due to a decrease in viscosity of the ILs. Similar results have been reported elsewhere in the literature (Guo et al., 2013; Jing et al., 2012). Feng et al. (2010) have reported that an increase in temperature increases the reaction rate of the glycine based ILs. The overall effect of temperature on the absorption performance are reported in Figure 7.6.

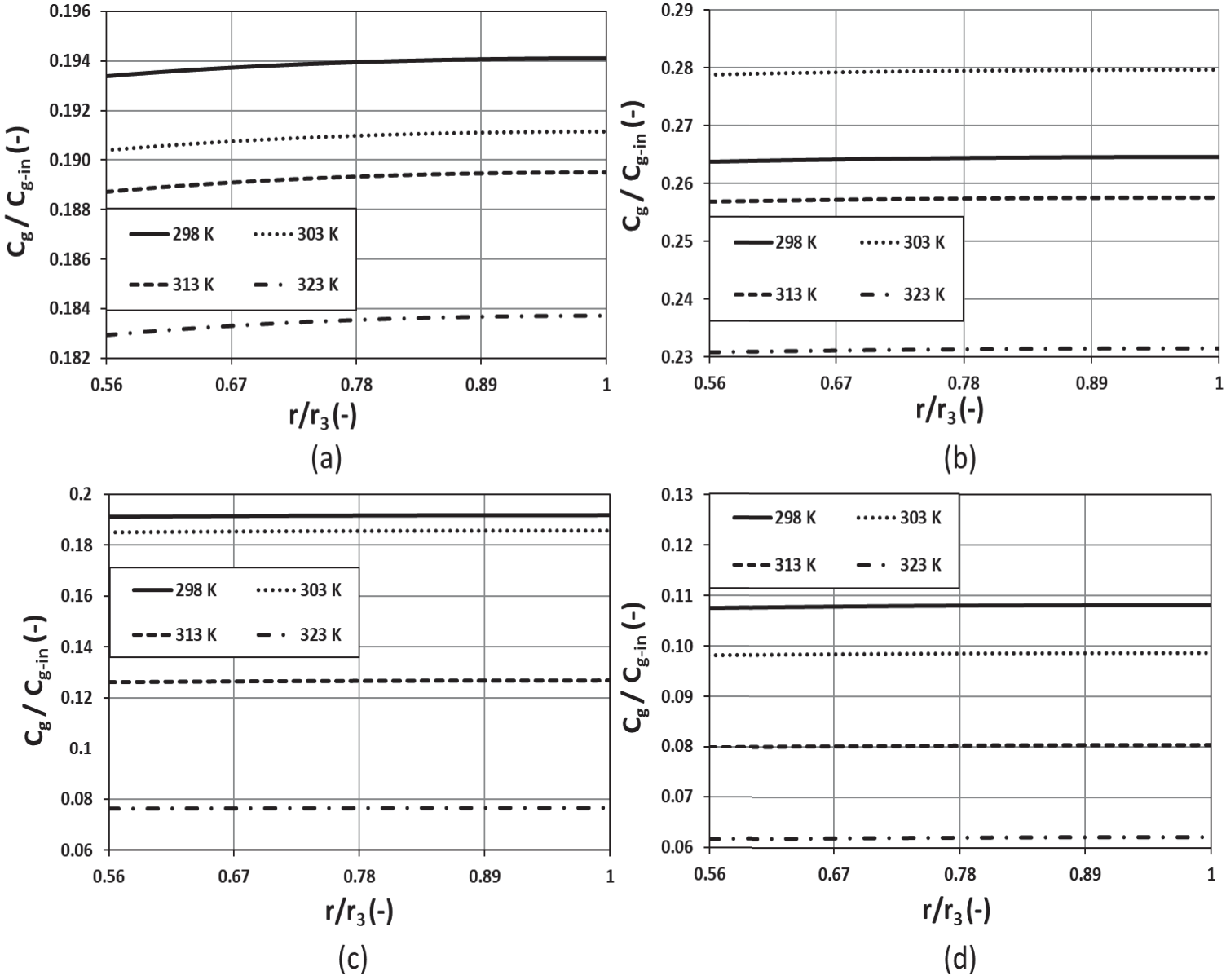

Figure 7.6 Normalized radial profiles of gas phase CO_2 concentrations at different process temperatures for ionic liquids (a) $[N_{1111}][Gly]$, (b) [emim][Gly], (c) [bmim][Gly] and (d) [hmim][Gly]; $Q_{IL} = 20\ ml\ min^{-1}$, $Q_g = 60\ ml\ min^{-1}$, $C_{l-in} = 0\ mol\ L^{-1}$, $C_{IL-in} = 1\ mol\ L^{-1}$

An increase can be observed in the separation performance with increase in temperature. However, the increase is less compared to that observed for IL concentration. An increase in temperature from 298 to 323 K has increased the efficiency by nearly 1, 3, 11 and 5 % for ILs $[N_{1111}][Gly]$, [emim][Gly], [bmim][Gly] and [hmim][Gly], respectively. Effect of

temperature on the separation performance of IL [N_{1111}][Gly] was almost negligible. Strong influence of temperature can be observed for IL [bmim][Gly].

The enhancement in the separation efficiency with an increase in IL concentration (higher reaction rates) and temperature (higher reaction rates and diffusivities) also shows the dominance of the chemisorption over the physisorption in the current membrane contactor absorption process. It is noteworthy here that the process was steady-state and the IL entering the contactor was always unloaded.

7.4 Boundary flux across the gas/liquid interface

Figure 7.7 shows the local boundary flux of CO_2 across the mass transfer interface for the four ILs at different concentrations and countercurrent flow configurations. Considering no wetting conditions for this study, the mass transfer interface (gas/liquid contact) resides on the boundary between membrane and tube, while the membrane is filled with gas. For all ILs, the local flux profiles pass through a maximum value near the end of the fiber length of z/L=1. The local CO_2 flux increases with a slow rate starting from z/L=0. However, the rate increases as the profile moves toward the end of the fiber's length: z/L=1. The effect of IL concentration on the CO_2 boundary flux is obvious from Figure 7.7. The trend of the boundary flux can be divided in two parts, before and after the middle of the contactor's length. Near the CO_2 inlet (z/L=1) boundary flux is higher for high IL concentration, and then decreases with the contactor's length. The effect of IL concentration is almost negligible near the middle of the length. Moving towards the CO_2 exit (z/L=0) from middle of the contactor the boundary flux of the lower IL concentration becomes dominant. Due to the high concentration of CO_2 near the inlet, there is a high driving force which leads to high values of flux. The CO_2 concentration is very low in the section before the half contactor's length due to the high absorption near the inlet. Therefore, there is a low driving force and low flux. Among all of the ILs, the [hmim][Gly] has shown the highest interfacial boundary flux. As the high IL concentration means low diffusivity and low solubility, yet again the dominance of chemisorption over physisorption was observed for the current absorption process, due to higher boundary flux at higher concentrations.

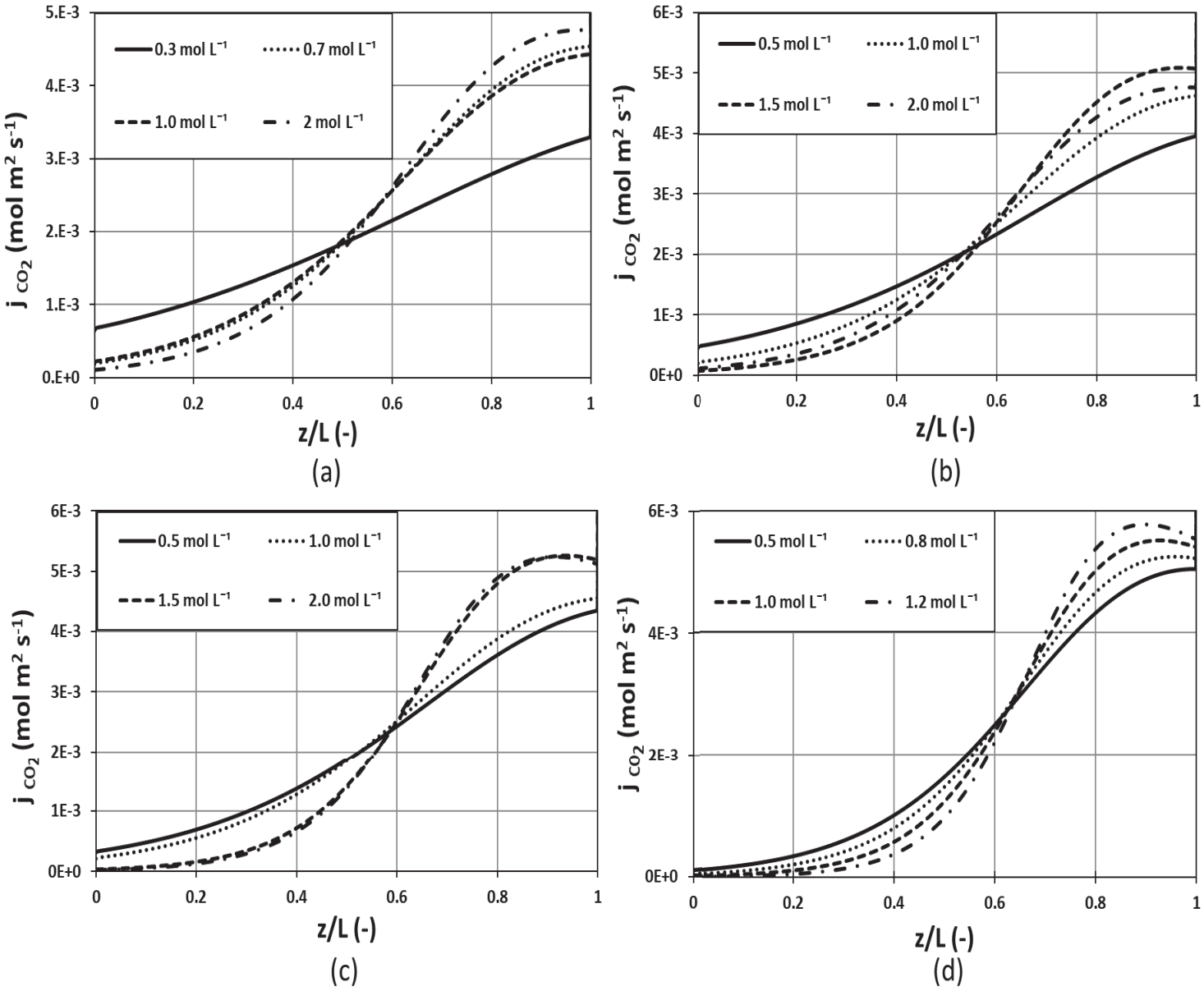

Figure 7.7 Axial profiles of the CO_2 boundary flux across the mass transfer interface for different concentrations of the ionic liquids (a) [N_{1111}][Gly], (b) [emim][Gly], (c) [bmim][Gly] and (d) [hmim][Gly]; $Q_{IL} = 20\ ml\ min^{-1}$, $Q_g = 60\ ml\ min^{-1}$, $C_{l-in} = 0\ mol\ L^{-1}$, $T_{l-in}, T_{g-in} = 298\ K$.

The effect of temperature on the boundary flux is presented in Figure 7.8. No evident effect can be observed except for ILs [bmim][Gly] and [hmim][Gly]. Stronger influence of the temperature on the CO_2 boundary flux can be observed for IL [bmim][Gly] while the effect is almost negligible for [N_{1111}][Gly]. Similar effects were observed for the temperature influence on the separation efficiency and reported above in Section 7.3. The trend is almost

identical to the previous one reported for ILs concentration. In the first half of the contactor, length boundary flux is high for low process temperatures while in the 2nd half contactor it is high for the high process temperatures.

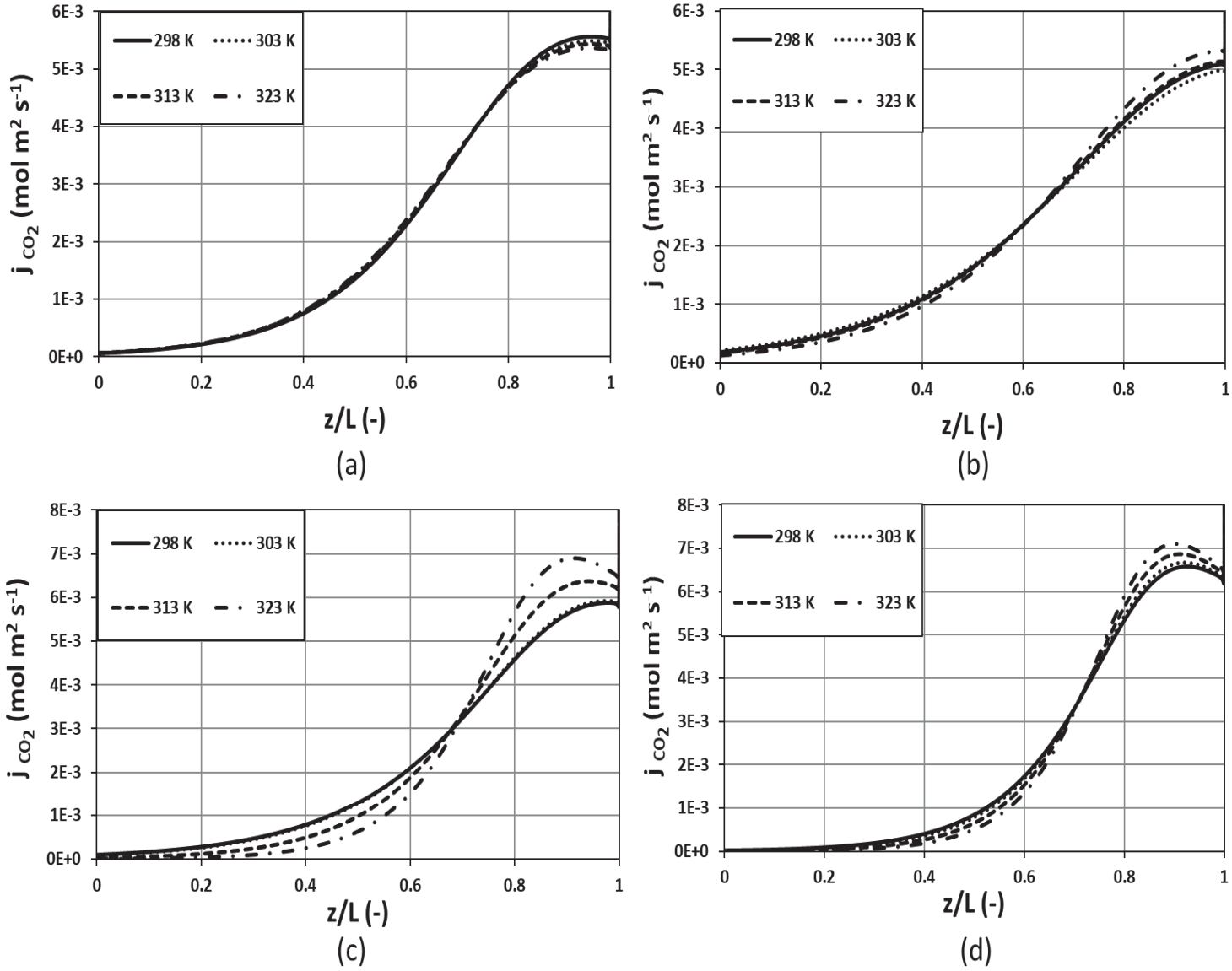

Figure 7.8 Axial profiles of the CO_2 boundary flux across the mass transfer interface at different process temperatures for the ionic liquids (a) [N_{1111}][Gly], (b) [emim][Gly], (c) [bmim][Gly] and (d) [hmim][Gly]; $Q_{IL} = 20\ ml\ min^{-1}$, $Q_g = 60\ ml\ min^{-1}$, $C_{l-in} = 0\ mol\ L^{-1}$, $C_{IL-in} = 1\ mol\ L^{-1}$.

7.5 Reaction rate across the gas/liquid interface

Axial profiles of the reaction rate of CO_2 for the four ILs are presented in Figure 7.9.

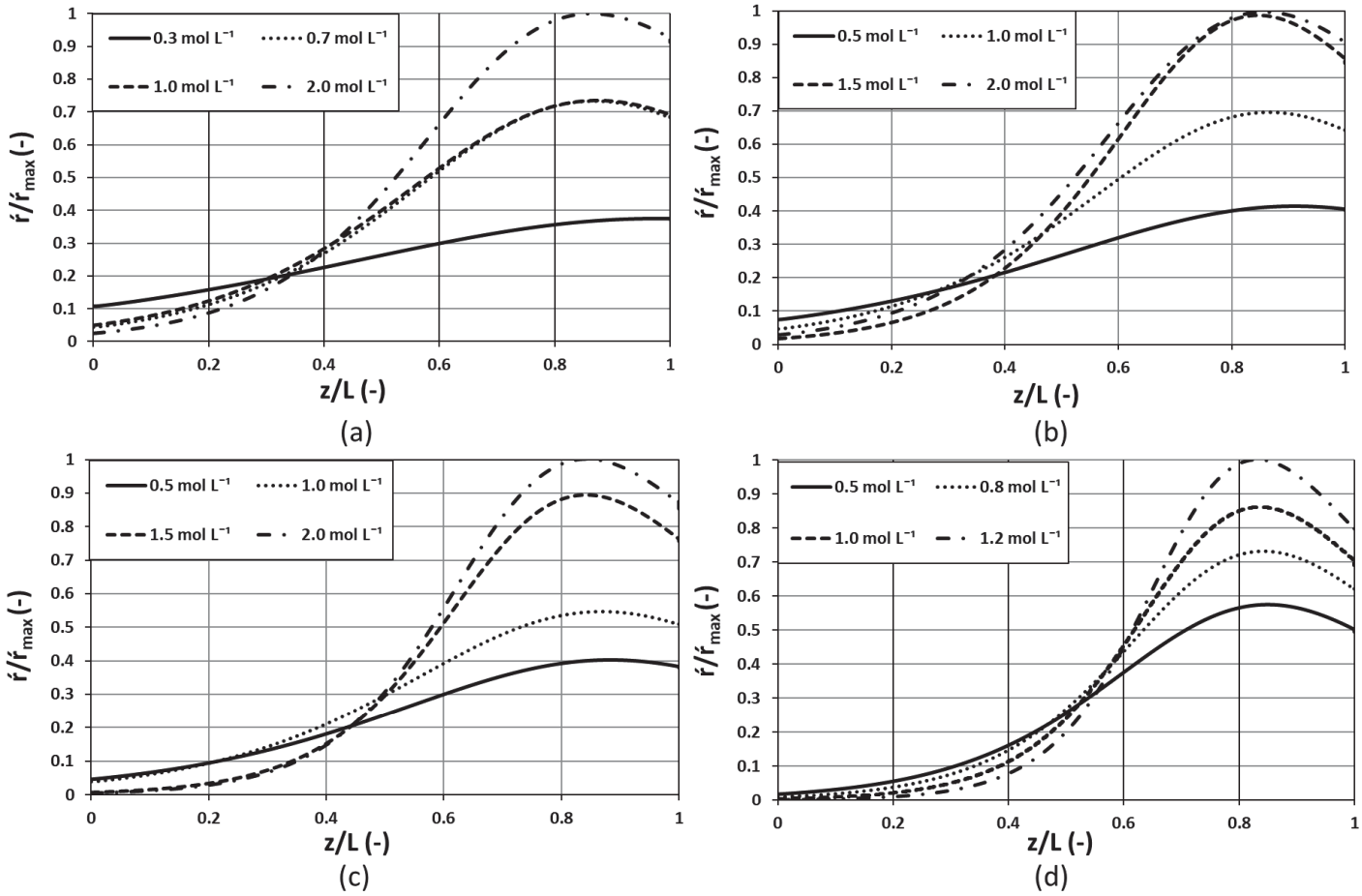

Figure 7.9 Axial profiles of the reaction rate across the mass transfer interface for different concentrations of the ionic liquids (a) [N_{1111}][Gly], (b) [emim][Gly], (c) [bmim][Gly] and (d) [hmim][Gly]; $Q_{IL} = 20\ ml\ min^{-1}$, $Q_g = 60\ ml\ min^{-1}$, $C_{l-in} = 0\ mol\ L^{-1}$, $T_{l-in}, T_{g-in} = 298\ K$.

As discussed in the preceding sections (Section 4.2.2.3 of Chapter 4, Section 7.3 and 7.4 of Chapter 7), due to the high values of Hatta number, dominancy of chemisorption over physisorption and consideration of unloaded solvent at the inlet the absorption can be considered to happen mostly near the interface. Thus, the axial profile of the reaction rate presented here was calculated over the interfacial boundary. In order to better observe the trends, the values were normalized with the maximal value over the corresponding axial length. The very strong influence of the IL concentration on the reaction rate can be observed. Starting near the contactor length of z/L=0, the reaction rate is a little higher for low IL concentrations than for high IL concentrations. Moving along the contactor length the reaction rate becomes very high for the high IL concentrations. The low reaction rates for the

high ILs concentration near the liquid inlet (z/L=0) are due to the very low concentration of CO_2 at the gas outlet (z/L=0). In the case of high IL concentrations, the CO_2 is absorbed very quickly at the gas side inlet (z/L=1). The maximal values of the reaction rate for all ILs were recorded near the contactor length at z/L=0.8. Hoff et al. (2004) and Hoff and Svendsen (2014) reported that the complex formation after the reaction affects the overall absorption process. However, due to unloaded solvent and steady-state conditions, the reaction mostly occurs near the interface and the effect can be neglected on the overall absorption. However, very high liquid flowrates were used in their studies, which create radial concentration gradients.

Variation of the reaction rate along with the fiber length cannot only be justified by the variation in the CO_2 and IL concentrations. It can be seen from Figure 7.3 of the temperature profile that there is a gradual increase in the temperature along the fiber's length which affects the reaction rate along the fiber. It can also be observed from Figure 7.4, that reaction rate constant gradually increases along the fiber length. The overall effect of temperature on the reaction rate is presented in Figure 7.10. The effect is lower compared to that reported for IL concentration. On the overall, the reaction rate is enhanced with high temperatures. The reaction rate of the IL [bmim][Gly] seems to be highly affected with temperature while the effect is very low for IL $[N_{1111}][Gly]$.

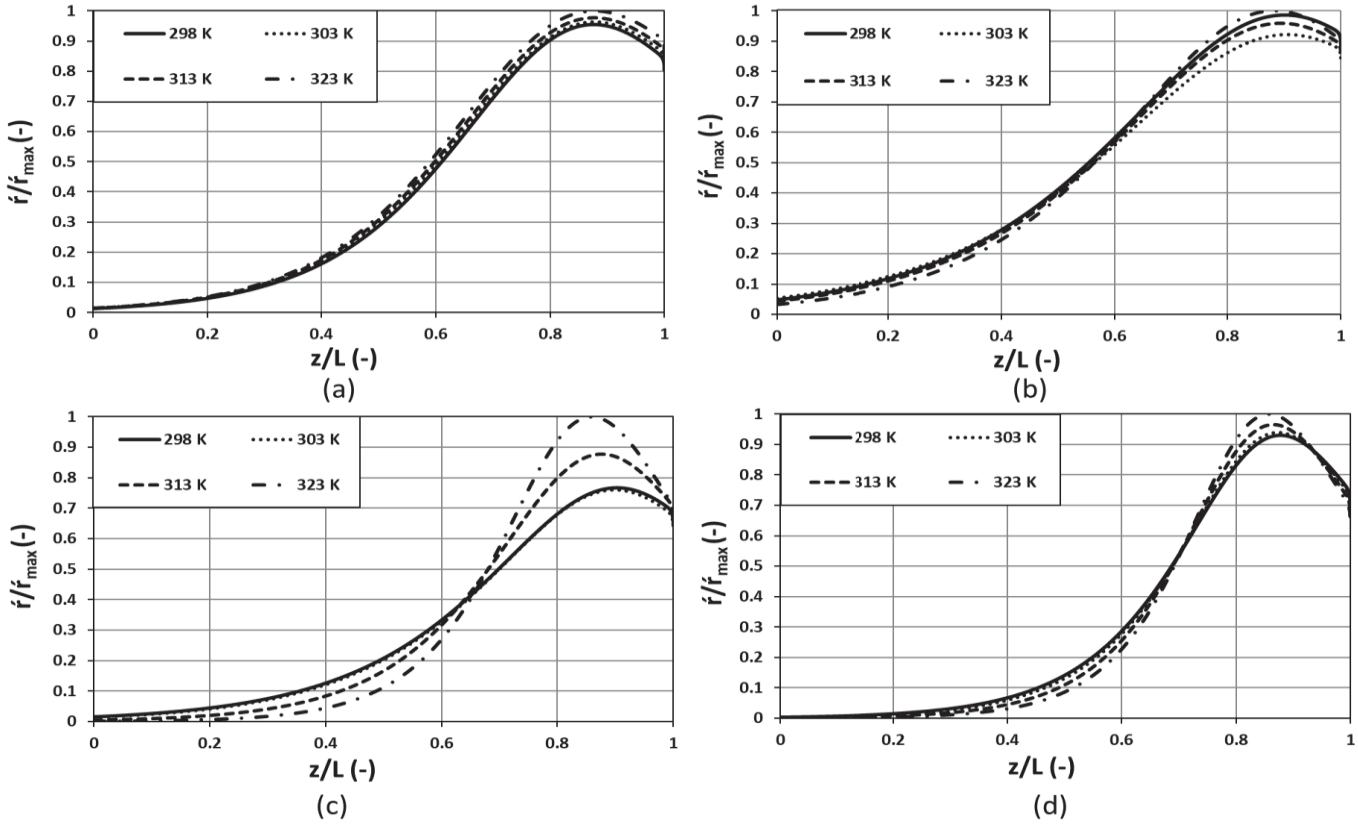

Figure 7.10 Axial profiles of the reaction rate across the mass transfer interface at different process temperatures for the ionic liquids (a) [N_{1111}][Gly], (b) [emim][Gly], (c) [bmim][Gly] and (d) [hmim][Gly]; $Q_{IL} = 20\ ml\ min^{-1}$, $Q_g = 60\ ml\ min^{-1}$, $C_{l-in} = 0\ mol\ L^{-1}$, $C_{IL-in} = 1\ mol\ L^{-1}$.

7.6 Conclusion

This chapter presented simulations for the non-isothermal modeling approach developed in Section 4.2.2 of Chapter 4, for the absorption of CO_2 in four amino-based TSILs namely: [N_{1111}][Gly], [emim][Gly], [bmim][Gly] and [hmim][Gly]. Simulations from the model were compared with the available experimental data for another amino acid-based IL monoethanolamine glycinate [MEA][Gly]. Aqueous AAILs used for CO_2 absorption in HFMCs showed superior performance due to their reactive nature compared to RTILs. Significant increase in temperature was observed along the fiber length due to the release of energy of dissolution of CO_2 in reactive AAILs, which makes the process non-isothermal in nature. The rise in temperature and increase in CO_2 concentration has generally favored the absorption performance.

Conclusions and Outlook

This thesis aimed to develop an experimental and modeling approach for CO_2 absorption in a hollow fiber membrane contactor with four different imidazolium-based RTILs, and four task specific AAILs. The imidazolium based RTILs considered for this work were [emim][$MeSO_4$], [emim][DCA], [emim][$EtSO_4$] and [emim][Ac] while the AAILs considered were [N_{1111}][Gly], [emim][Gly], [bmim][Gly] and [hmim][Gly]. The main concern of the present work was to study the feasibility of coupling RTILs and AAILs with HFMCs for post-combustion CO_2 capture, in experiments as well as modeling and simulations.

For this purpose, single module and dual module coupled absorption/desorption membrane gas separation units were developed, for post combustion CO_2 capture. Solubility of CO_2 in RTILs at gas/liquid equilibrium was measured by isochoric pressure drop principle using a custom-built equilibrium solubility measurements apparatus. ILs and membrane fibers were characterized by measuring thermal stability of the ILs, surface tension of the ILs, surface morphologies and porous structure analysis of the fibers, contact angle measurements and finally, measuring LEP or breakthrough pressure. The study was further extended by developing robust and rigorous dynamic modeling approaches for isothermal (absorption with RTILs) and non-isothermal (absorption with AAILs) absorptions of CO_2 in HFMCs with ILs. Wetting analysis, parametric analysis, sensitivity and optimization studies were performed by steady-state and pseudo-steady-state models.

The experimentally found solubility of CO_2 in the four RTILs can be ranked as [emim][Ac] > [emim][$EtSO_4$] > [emim][$MeSO_4$] > [emim] [DCA]. Diffusivity was predominantly affected by viscosity of the RTILs and was found in the order of [emim][DCA] > [emim][$MeSO_4$] > [emim][$EtSO_4$] > [emim][Ac]. Solubility and diffusivity are the most important parameters for CO_2 absorption in the current setup for which the above-mentioned order of ranking is opposite. However, the overall effect of both parameters can only be observed from the overall absorption performance. All the RTILs were found thermally stable for the current experiments in the temperature range of 288-323 K. No noticeable effects of RTILs on surface and porous structure of PP membranes were observed, during 20 days of immersion of fibers in the RTILs. Contact angles of the RTILs with PP membrane fiber were in the

range of 72 ^{O}-85 ^{O}, which were affected by a drop of only 1^{O}-2^{O} in contact angles measured after 40 days of immersion of fiber in RTILs.

Single module absorption setup in which only one membrane module was used as absorber, could absorb CO_2 at a very high rate which slowed down gradually due to gradual accumulation of CO_2 in the absorbent with operation time. The CO_2 loading rate of the RTILs also slowed down with time. The absorption rate and hence the separation performance decreased with time until it reached pseudo-steady-state. At pseudo-steady-state, the absorption rate became very slow and was nearly constant. The absorption with RTILs was more affected by feed gas flowrate rather than process temperature. An increase in gas flowrate and decrease in process temperature could increase the overall performance as it enhanced the overall mass transfer coefficient and CO_2 flux. Coupled absorption/desorption in which one membrane module was used as membrane absorber and the 2nd one was used as membrane stripper/desorber simultaneously within the same cycle, could maintain a very high and long-term CO_2 absorption rate compared to single module absorption. Single step absorption and desorption allowed the absorbent to keep very low CO_2 loading and thus providing long-term high performance. Membrane stripper was able to achieve nearly 90 % efficiency in a single step after absorption in membrane absorber, which confirmed the very physical absorption nature, ease of regeneration, energy saving nature and feasibility of the RTILs in the current setup. The pseudo-steady-state CO_2 separation efficiency difference between coupled absorption/desorption and single module absorption was as high as 55 %. At very low feed gas flowrate of 10 ml min^{-1} the coupled arrangements were able to maintain pseudo-steady-state efficiency of up to 82 %.

Simulations of the isothermal modeling approach, which was developed for steady-state and pseudo-steady-state absorption of CO_2 in RTILs, was in a very strong agreement with experimental data from both single module absorption and coupled absorption/desorption. A detailed analysis of the partial and full wetting of the membrane confirmed the significance of membrane wetting in the mass transfer across the membrane. Nearly one half of the CO_2 flux was dropped by simulating a 5 % partially wetted membrane. A fully wetted membrane could drop the CO_2 flux to nearly zero, hindering the mass transfer. Parameters that could influence the CO_2 separation including membrane porosity, membrane tortuosity, fiber diameter and fiber length were analyzed. Although increase in gas flowrate reduced the gas side CO_2 separation efficiency, however, the mass transfer and CO_2 flux increased with increase in both gas and liquid flowrates. A sensitivity analysis for the operation time during pseudo-

steady-state confirmed that the process was much more sensitive to variations in gas flowrate than liquid flowrate. For coupled absorption/desorption, sweeping gas flowrate, IL flowrate and membrane porosity were optimized for achieving zero concentration of CO_2 at the membrane stripper outlet. Sensitivity of the optimized parameters could be ranked as IL flowrate > sweep gas flowrate > membrane porosity. Simulations of the non-isothermal modeling approach, which was developed for steady-state absorption of CO_2 in highly reactive AAILs, was studied and compared with experimental data from literature with a different absorbent given the fact that no experiment with AAILS previously existed, giving enough precision for further simulations. Simulations with the reactive AAILs reported significant temperature variations along the contactor length due to reaction between solute and absorbent, for which the heat of absorption accumulated along the length of the contactor. Other temperature dependent parameters were influenced due to this variation including diffusivity of CO_2, solubility of CO_2, rate constant and reaction rate. Although the effect of process temperature on the CO_2 separation performance was significant enough, however, a stronger influence was recorded due to concentration of the ILs. Dominancy of the chemisorption could be observed with very effective mass transfer near the gas/liquid interface. Diffusion of reaction products could affect the process, but it was neglected however, as the reaction only occurred over and/or near the gas/liquid interface.

Post-combustion CO_2 capture with HFMC has been well investigated before and our understandings of the process and process improvements are progressing rapidly. However, there are some aspects that need to be addressed to make this process more feasible.

Selection of appropriate absorbents to be used with HFMCs is very critical because of the various problems caused by conventional absorbents. Although IL are proven to be feasible and better absorbents for CO_2 capture, however there are some challenges that still need to be resolved including high viscosities of the ILs and manufacturing cost. Both challenges can be resolved by either mixing a ratio of water and/or tailoring the structures of anions and/or cations of the ILs, while keeping in mind the CO_2 solubility, which is the most important parameter. Many researchers are already working on exploring and resolving these issues to make ILs more feasible for post-combustion CO_2 capture with HFMCs. The two types of ILs, namely RTILs and TSILs have different impact on the absorption process. RTILs can provide a moderate CO_2 absorption capacity but can be regenerated very easily. Thus, RTILs can be very energy efficient and cost effective which makes them very feasible for long term continuous post-combustion CO_2 absorption operations. TSILs can provide very high

absorption capacity, however the regeneration is not very easy due to the reactive nature of the absorbents and can be expensive. For hydrophobic membrane contactors, high surface tension ILs are favorable to avoid pore wetting. Moreover, some ILs can be corrosive for different type of fibers and are not feasible for long term operations. Therefore, careful selection of the ILs for HFMC based post-combustion CO_2 capture is very critical.

Although single module absorption has been extensively investigated and used for post-combustion CO_2 capture, coupled absorption/desorption however, provided far more better absorption performance than single module absorption. Coupled absorption/desorption operation along with RTILs (with the advantage of very easy regeneration) might be very suitable for commercial scale continuous post-combustion carbon capture. With little more modifications, the process can be optimized to achieve 100 % separation efficiency in a single cycle. The optimization study has been performed in this work for three parameters, which can be further extended for other parameters. Few other modifications and process improvements are essential to make it more applied and feasible, particularly modifications in the means of desorption inside the membrane stripper. More effective desorption techniques could be implemented such as, vacuum desorption or vacuum with a little increase in temperature. Coupled process could also be implemented for TSILs, but with very effective simultaneous desorption step. The feasibility can be investigated further. Specific economic analysis was not performed, in this work. It is further recommended for future works to address economics of the coupled process, while considering the optimized process framework.

The 2-D isothermal and non-isothermal models developed in this work can be used for different absorbents. Although the models correctly predict the experimental data, however, to improve the predictive capacity of the model, very accurate estimation of the various parameters and physicochemical properties are required. For example, during wetting analysis, the wetting ratios considered were simple approximations (homogenous wetting along the membrane pore, only a portion of the pore length is filled with liquids). The actual amount and location of wetting can be much more complex considering the industrial origin of fibers. Similarly, the gas diffusion through different domains have been calculated using theoretical correlations. Although the correlations used here, have been verified and compared with experimental data in various literature studies, however, there could be a difference between the actual values and the calculated ones, especially for the ILs that have not been verified before. Coupled absorption/desorption could be a very feasible option to be

used on industrial scale. Therefore, model predictions are recommended by using large scale parameters and operating conditions from the industrial environment. This could be performed along with the optimization of the process and cost analysis for the continuous coupled absorption/desorption loop. These investigations can be performed using process simulators.

Bibliography

3M™ Liqui-Cel™ EXF 1X5.5 Series Membrane Contactor [WWW Document], 2020. URL https://www.3m.com/3M/en_US/company-us/all-3m-products/~/3M-Liqui-Cel-MM-Series-Membrane-Contactor/?N=5002385+3290342764+3290344668&preselect=8710655+8758377+8759203&rt=rud (accessed 3.13.20).

Aghaie, M., Rezaei, N., Zendehboudi, S., 2018. A systematic review on CO 2 capture with ionic liquids: Current status and future prospects. Renew. Sustain. Energy Rev. https://doi.org/10.1016/j.rser.2018.07.004

Ahmad, F., Lau, K.K., Lock, S.S.M., Rafiq, S., Khan, A.U., Lee, M., 2015. Hollow fiber membrane model for gas separation: Process simulation, experimental validation and module characteristics study. J. Ind. Eng. Chem. 21, 1246–1257. https://doi.org/10.1016/j.jiec.2014.05.041

Ahmad, N.A., Leo, C.P., Ahmad, A.L., Nur Izwanne, M., 2019. Swelling reduction of polyvinylidenefluoride hollow fiber membrane incorporated with silicoaluminophosphate-34 zeotype filler for membrane gas absorption. Sep. Purif. Technol. https://doi.org/10.1016/j.seppur.2018.12.015

Aki, S.N.V.K., Mellein, B.R., Saurer, E.M., Brennecke, J.F., 2004. High-pressure phase behavior of carbon dioxide with imidazolium-based ionic liquids. J. Phys. Chem. B. https://doi.org/10.1021/jp046895+

Albo, J., Irabien, A., 2012. Non-dispersive absorption of CO 2 in parallel and cross-flow membrane modules using EMISE. J. Chem. Technol. Biotechnol. 87, 1502–1507. https://doi.org/10.1002/jctb.3790

Albo, J., Luis, P., Irabien, A., 2011. Absorption of coal combustion fl ue gases in ionic liquids using different membrane contactors. Desalin. Water Treat. 27, 54–49. https://doi.org/10.5004/dwt.2011.2050

Albo, J., Luis, P., Irabien, A., 2010. Carbon Dioxide Capture from Flue Gases Using a Cross-Flow Membrane Contactor and the Ionic Liquid 1-Ethyl-3-methylimidazolium Ethylsulfate. Ind. Eng. Chem. Res. 49, 11045–11051. https://doi.org/10.1021/ie1014266

Almeida, H.F.D., Teles, A.R.R., Lopes-Da-Silva, J.A., Freire, M.G., Coutinho, J.A.P., 2012. Influence of the anion on the surface tension of 1-ethyl-3- methylimidazolium-based ionic liquids. J. Chem. Thermodyn. 54, 49–54. https://doi.org/10.1016/j.jct.2012.03.008

Anthony, J.L., Anderson, J.L., Maginn, E.J., Brennecke, J.F., 2005. Anion Effects on Gas Solubility in Ionic Liquids. J. Phys. Chem. B. https://doi.org/10.1021/jp046404l

Anthony, J.L., Maginn, E.J., Brennecke, J.F., 2002a. Solubilities and thermodynamic properties of gases in the ionic liquid 1-n-butyl-3-methylimidazolium

hexafluorophosphate. J. Phys. Chem. B. https://doi.org/10.1021/jp020631a

Anthony, J.L., Maginn, E.J., Brennecke, J.F., 2002b. Solubilities and Thermodynamic Properties of Gases in the Ionic Liquid 1- n -Butyl-3-methylimidazolium Hexafluorophosphate. J. Phys. Chem. B 106, 7315–7320. https://doi.org/10.1021/jp020631a

Aresta, M. (Ed.), 2003. Carbon Dioxide Recovery and Utilization. Springer Netherlands, Dordrecht. https://doi.org/10.1007/978-94-017-0245-4

Asfand, F., Bourouis, M., 2015. A review of membrane contactors applied in absorption refrigeration systems. Renew. Sustain. Energy Rev. 45, 173–191. https://doi.org/10.1016/j.rser.2015.01.054

Azari, A., Ali, M., Sanaeepur, H., 2016. International Journal of Greenhouse Gas Control CFD study of CO 2 separation in an HFMC : Under non-wetted and partially-wetted conditions 49, 81–93.

Baltus, R.E., Culbertson, B.H., Dai, S., Luo, H., DePaoli, D.W., 2004. Low-Pressure Solubility of Carbon Dioxide in Room-Temperature Ionic Liquids Measured with a Quartz Crystal Microbalance. J. Phys. Chem. B. https://doi.org/10.1021/jp036051a

Barker, T., 2007. Climate Change 2007 : An Assessment of the Intergovernmental Panel on Climate Change, An Assessment of the Intergovernmental Panel on Climat Change. https://doi.org/10.1256/004316502320517344

Barrett, 1966. Gas Absorption on a Sieve Plate, Ph.D. Thesis. University of Cambridge.

Barton, A.F.M., 1991. Handbook of Solubility Parameters and Other Cohesion Parameters, in: Handbook of Solubility Parameters and Other Cohesion Parameters.

Biolin Scientific [WWW Document], 2020. URL https://www.biolinscientific.com/measurements/surface-tension (accessed 3.13.20).

Bird, R.B., Stewart, W.E., Lightfoot, E.N., 2002. Transport Phenomena, Transport Phenomena. https://doi.org/10.1016/j.ijhydene.2006.08.059

Blanchard, L.A., Gu, Z., Brennecke, J.F., 2001. High-pressure phase behavior of ionic liquid/CO2 systems. J. Phys. Chem. B. https://doi.org/10.1021/jp003309d

Blath, J., Christ, M., Deubler, N., Hirth, T., Schiestel, T., 2011. Gas solubilities in room temperature ionic liquids - Correlation between RTiL-molar mass and Henry's law constant. Chem. Eng. J. https://doi.org/10.1016/j.cej.2011.05.084

Blath, J., Deubler, N., Hirth, T., Schiestel, T., 2012. Chemisorption of carbon dioxide in imidazolium based ionic liquids with carboxylic anions. Chem. Eng. J. 181–182, 152–158. https://doi.org/10.1016/j.cej.2011.11.042

Boributh, S., Rongwong, W., Assabumrungrat, S., Laosiripojana, N., Jiraratananon, R., 2012. Mathematical modeling and cascade design of hollow fiber membrane contactor for CO 2 absorption by monoethanolamine. J. Memb. Sci.

https://doi.org/10.1016/j.memsci.2012.01.048

Cadena, C., Anthony, J.L., Shah, J.K., Morrow, T.I., Brennecke, J.F., Maginn, E.J., 2004. Why is CO2 so Soluble in Imidazolium-Based Ionic Liquids? J. Am. Chem. Soc. https://doi.org/10.1021/ja039615x

Camper, D., Becker, C., Koval, C., Noble, R., 2005. Low pressure hydrocarbon solubility in room temperature ionic liquids containing imidazolium rings interpreted using regular solution theory. Ind. Eng. Chem. Res. https://doi.org/10.1021/ie049312r

Caplow, M., 1968. Kinetics of Carbamate Formation and Breakdown. J. Am. Chem. Soc. https://doi.org/10.1021/ja01026a041

Carvalho, P.J., Regueira, T., Fernández, J., Lugo, L., Safarov, J., Hassel, E., Coutinho, J.A.P., 2014. High pressure density and solubility for the CO2 + 1-ethyl-3-methylimidazolium ethylsulfate system. J. Supercrit. Fluids. https://doi.org/10.1016/j.supflu.2014.01.011

Chabanon, E., Bounaceur, R., Castel, C., Rode, S., Roizard, D., Favre, E., 2015. Pushing the limits of intensified CO2 post-combustion capture by gas-liquid absorption through a membrane contactor. Chem. Eng. Process. Process Intensif. https://doi.org/10.1016/j.cep.2015.03.002

Chabanon, E., Roizard, D., Favre, E., 2013. Modeling strategies of membrane contactors for post-combustion carbon capture: A critical comparative study. Chem. Eng. Sci. 87, 393–407. https://doi.org/10.1016/j.ces.2012.09.011

Chabanon, E., Roizard, D., Favre, E., 2011. Membrane contactors for postcombustion carbon dioxide capture: A comparative study of wetting resistance on long time scales. Ind. Eng. Chem. Res. https://doi.org/10.1021/ie200704h

Chau, J., Jie, X., Sirkar, K.K., 2016. Polyamidoamine-facilitated poly(ethylene glycol)/ionic liquid based pressure swing membrane absorption process for CO2 removal from shifted syngas. Chem. Eng. J. https://doi.org/10.1016/j.cej.2015.09.120

Chau, J., Obuskovic, G., Jie, X., Sirkar, K.K., 2014. Pressure swing membrane absorption process for shifted syngas separation: Modeling vs. experiments for pure ionic liquid. J. Memb. Sci. 453, 61–70. https://doi.org/10.1016/j.memsci.2013.10.038

Chen, Y., Zhang, S., Yuan, X., Zhang, Y., Zhang, X., Dai, W., Mori, R., 2006. Solubility of CO2 in imidazolium-based tetrafluoroborate ionic liquids. Thermochim. Acta. https://doi.org/10.1016/j.tca.2005.11.023

Constantinou, A., Barrass, S., Gavriilidis, A., 2014. CO2 absorption in polytetrafluoroethylene membrane microstructured contactor using aqueous solutions of amines. Ind. Eng. Chem. Res. https://doi.org/10.1021/ie403444t

Costa, A.J.L., Esperanca, M.S.S., Marrucho, I.M., Rebelo, L.P.N., 2011. Densities and Viscosities of 1-Ethyl-3-methylimidazolium n -Alkyl Sulfates. J. Chem. Eng. Data 56, 3433–3441.

Cuéllar-Franca, R.M., Azapagic, A., 2015. Carbon capture, storage and utilisation technologies: A critical analysis and comparison of their life cycle environmental impacts. J. CO2 Util. https://doi.org/10.1016/j.jcou.2014.12.001

D'Alessandro, D.M., Smit, B., Long, J.R., 2010. Carbon dioxide capture: Prospects for new materials. Angew. Chemie - Int. Ed. https://doi.org/10.1002/anie.201000431

Dai, Z., Ansaloni, L., Deng, L., 2016a. Precombustion CO $_2$ Capture in Polymeric Hollow Fiber Membrane Contactors Using Ionic Liquids: Porous Membrane versus Nonporous Composite Membrane. Ind. Eng. Chem. Res. 55, 5983–5992. https://doi.org/10.1021/acs.iecr.6b01247

Dai, Z., Deng, L., 2016. Membrane absorption using ionic liquid for pre-combustion CO2 capture at elevated pressure and temperature. Int. J. Greenh. Gas Control 54, 59–69. https://doi.org/10.1016/j.ijggc.2016.09.001

Dai, Z., Noble, R.D., Gin, D.L., Zhang, X., Deng, L., 2016b. Combination of ionic liquids with membrane technology: A new approach for CO2separation. J. Memb. Sci. 497, 1–20. https://doi.org/10.1016/j.memsci.2015.08.060

Dai, Z., Usman, M., Hillestad, M., Deng, L., 2016c. Modeling of a tubular membrane contactor for pre-combustion CO 2 capture using ionic liquids: Influence of the membrane configuration, absorbent properties and operation parameters. Green Energy Environ. 1, 266–275. https://doi.org/10.1016/j.gee.2016.11.006

Danckwerts, 1970. Gas–Liquid Reactions. McGraw-Hill, New York.

deMontigny, D., Tontiwachwuthikul, P., Chakma, A., 2006. Using polypropylene and polytetrafluoroethylene membranes in a membrane contactor for CO2 absorption. J. Memb. Sci. https://doi.org/10.1016/j.memsci.2005.10.024

Dindore, V.Y., Brilman, D.W.F., Geuzebroek, R.H., Versteeg, G.F., 2004. Membrane-solvent selection for CO2 removal using membrane gas-liquid contactors. Sep. Purif. Technol. https://doi.org/10.1016/j.seppur.2004.01.014

Dindore, V.Y., Brilman, D.W.F., Versteeg, G.F., 2005. Hollow fiber membrane contactor as a gas-liquid model contactor. Chem. Eng. Sci. https://doi.org/10.1016/j.ces.2004.07.129

Dindore, V.Y., Versteeg, G.F., 2005. Gas-liquid mass transfer in a cross-flow hollow fiber module: Analytical model and experimental validation. Int. J. Heat Mass Transf. https://doi.org/10.1016/j.ijheatmasstransfer.2005.03.002

Farla, J.C.M., Hendriks, C.A., Blok, K., 1995. Carbon dioxide recovery from industrial processes. Energy Convers. Manag. https://doi.org/10.1016/0196-8904(95)00131-V

Fazaeli, R., Razavi, S.M.R., Sattari Najafabadi, M., Torkaman, R., Hemmati, A., 2015. Computational simulation of CO $_2$ removal from gas mixtures by chemical absorbents in porous membranes. RSC Adv. 5, 36787–36797. https://doi.org/10.1039/C5RA02001H

Feng, Z., Cheng-Gang, F., You-Ting, W., Yuan-Tao, W., Ai-Min, L., Zhi-Bing, Z., 2010.

Absorption of CO2 in the aqueous solutions of functionalized ionic liquids and MDEA. Chem. Eng. J. https://doi.org/10.1016/j.cej.2010.04.013

Feron, P.H.M., 2010. Exploring the potential for improvement of the energy performance of coal fired power plants with post-combustion capture of carbon dioxide. Int. J. Greenh. Gas Control. https://doi.org/10.1016/j.ijggc.2009.10.018

Figueroa, J.D., Fout, T., Plasynski, S., McIlvried, H., Srivastava, R.D., 2008. Advances in CO2 capture technology-The U.S. Department of Energy's Carbon Sequestration Program. Int. J. Greenh. Gas Control. https://doi.org/10.1016/S1750-5836(07)00094-1

Fröba, A.P., Kremer, H., Leipertz, A., 2008. Density, Refractive Index, Interfacial Tension, and Viscosity of Ionic Liquids [EMIM][EtSO $_4$], [EMIM][NTf $_2$], [EMIM][N(CN) $_2$], and [OMA][NTf $_2$] in Dependence on Temperature at Atmospheric Pressure. J. Phys. Chem. B 112, 12420–12430. https://doi.org/10.1021/jp804319a

Fuller, E.N., Schettler, P.D., Giddings, J.C., 1966. A new method for prediction of binary gas-phase diffusion coefficients. Ind. Eng. Chem. 58, 18–27. https://doi.org/10.1021/ie50677a007

Gabelman, A., Hwang, S.-T., 1999. Hollow fiber membrane contactors. J. Memb. Sci. 159, 61–106. https://doi.org/10.1016/S0376-7388(99)00040-X

Ghandi, K., 2014. A Review of Ionic Liquids, Their Limits and Applications. Green Sustain. Chem. https://doi.org/10.4236/gsc.2014.41008

Gómez-Coma, L., Garea, A., Irabien, A., 2014a. Non-dispersive absorption of CO2in [emim][EtSO4] and [emim][Ac]: Temperature influence. Sep. Purif. Technol. 132, 120–125. https://doi.org/10.1016/j.seppur.2014.05.012

Gómez-Coma, L., Garea, A., Irabien, A., 2014b. Non-dispersive absorption of CO2 in [emim][EtSO4] and [emim][Ac]: Temperature influence. Sep. Purif. Technol. 132, 120–125. https://doi.org/10.1016/j.seppur.2014.05.012

Gómez-Coma, L., Garea, A., Irabien, Á., 2017. Hybrid Solvent ([emim][Ac]+water) to Improve the CO2Capture Efficiency in a PVDF Hollow Fiber Contactor. ACS Sustain. Chem. Eng. 5, 734–743. https://doi.org/10.1021/acssuschemeng.6b02074

Gómez, E., González, B., Calvar, N., Tojo, E., Domínguez, Á., 2006. Physical Properties of Pure 1-Ethyl-3-methylimidazolium Ethylsulfate and Its Binary Mixtures with Ethanol and Water at Several Temperatures. J. Chem. Eng. Data 51, 2096–2102. https://doi.org/10.1021/je060228n

Gong, Y., Wang, Z., Wang, S., 2006. Experiments and simulation of CO2removal by mixed amines in a hollow fiber membrane module. Chem. Eng. Process. Process Intensif. 45, 652–660. https://doi.org/10.1016/j.cep.2006.01.009

Guo, H., Zhou, Z., Jing, G., 2013. Kinetics of carbon dioxide absorption into aqueous [Hmim][Gly] solution. Int. J. Greenh. Gas Control. https://doi.org/10.1016/j.ijggc.2013.03.024

Gurau, G., Rodríguez, H., Kelley, S.P., Janiczek, P., Kalb, R.S., Rogers, R.D., 2011. Demonstration of chemisorption of carbon dioxide in 1,3-dialkylimidazolium acetate ionic liquids. Angew. Chemie - Int. Ed. 50, 12024–12026. https://doi.org/10.1002/anie.201105198

Happel, J., 1959. Viscous flow relative to arrays of cylinders. AIChE J. 5, 174–177. https://doi.org/10.1002/aic.690050211

Hoff, K.A., Juliussen, O., Falk-Pedersen, O., Svendsen, H.F., 2004. Modeling and experimental study of carbon dioxide absorption in aqueous alkanolamine solutions using a membrane contactor. Ind. Eng. Chem. Res. https://doi.org/10.1021/ie034325a

Hoff, K.A., Svendsen, H.F., 2014. Membrane contactors for CO2 absorption - Application, modeling and mass transfer effects. Chem. Eng. Sci. https://doi.org/10.1016/j.ces.2014.05.001

Huang, K., Peng, H.L., 2017. Solubilities of Carbon Dioxide in 1-Ethyl-3-methylimidazolium Thiocyanate, 1-Ethyl-3-methylimidazolium Dicyanamide, and 1-Ethyl-3-methylimidazolium Tricyanomethanide at (298.2 to 373.2) K and (0 to 300.0) kPa. J. Chem. Eng. Data. https://doi.org/10.1021/acs.jced.7b00476

Iliuta, I., Bougie, F., Iliuta, M.C., 2015. CO2 removal by single and mixed amines in a hollow-fiber membrane module-investigation of contactor performance. AIChE J. https://doi.org/10.1002/aic.14678

Intergovernmental Panel on Climate Change, 2014. Climate Change 2014 Mitigation of Climate Change, Climate Change 2014 Mitigation of Climate Change. https://doi.org/10.1017/cbo9781107415416

International Energy Agency (IEA), 2019. Energy and the Sustainable Development Goals, in: World Energy Outlook 2019. IEA Publications, pp. 79–128.

International Energy Agency (IEA), 2013. Technology Roadmap Carbon capture and storage - 2013 edition, IEA, PARIS. https://doi.org/https://www.iea.org/reports/technology-roadmap-carbon-capture-and-storage-2013

IPCC, 2005. IPCC special report on carbon dioxide capture and storage. Prepared by working group III of the Intergovernmental Panel on Climate Change, in: IPCC Special Report on Carbon Dioxide Capture and Storage. https://doi.org/10.1002/anie.201000431

Iversen, S.B., Bhatia, V.K., Dam-Johansen, K., Jonsson, G., 1997. Characterization of microporous membranes for use in membrane contactors. J. Memb. Sci. https://doi.org/10.1016/S0376-7388(97)00026-4

Jalili, A.H., Mehdizadeh, A., Shokouhi, M., Ahmadi, A.N., Hosseini-Jenab, M., Fateminassab, F., 2010. Solubility and diffusion of CO2and H2S in the ionic liquid 1-ethyl-3-methylimidazolium ethylsulfate. J. Chem. Thermodyn. 42, 1298–1303. https://doi.org/10.1016/j.jct.2010.05.008

Jiang, Y.Y., Wang, G.N., Zhou, Z., Wu, Y.T., Geng, J., Zhang, Z.B., 2002.

Tetraalkylammonium amino acids as functionalized ionic liquids of low viscosity. Chem. Commun. 8, 505–507. https://doi.org/10.1039/b713648j

Jie, X., Chau, J., Obuskovic, G., Sirkar, K.K., 2013. Preliminary studies of CO2 removal from precombustion syngas through pressure swing membrane absorption process with ionic liquid as absorbent. Ind. Eng. Chem. Res. 52, 8783–8799. https://doi.org/10.1021/ie302122s

Jing, G., Zhou, L., Zhou, Z., 2012. Characterization and kinetics of carbon dioxide absorption into aqueous tetramethylammonium glycinate solution. Chem. Eng. J. https://doi.org/10.1016/j.cej.2011.11.007

Johnson, K.E., 2007. What's an ionic liquid? Electrochem. Soc. Interface.

Kazarian, S.G., Briscoe, B.J., Welton, T., 2000. Combining ionic liquids and supercritical fluids: In situ ATR-IR study of CO2 dissolved in two ionic liquids at high pressures. Chem. Commun. https://doi.org/10.1039/b005514j

Khaisri, S., deMontigny, D., Tontiwachwuthikul, P., Jiraratananon, R., 2010. A mathematical model for gas absorption membrane contactors that studies the effect of partially wetted membranes. J. Memb. Sci. https://doi.org/10.1016/j.memsci.2009.10.028

Khoo, H.H., Bu, J., Wong, R.L., Kuan, S.Y., Sharratt, P.N., 2011. Carbon capture and utilization: Preliminary life cycle CO2, energy, and cost results of potential mineral carbonation, in: Energy Procedia. https://doi.org/10.1016/j.egypro.2011.02.145

Kiani, A., Bhave, R.R., Sirkar, K.K., 1984. Solvent extraction with immobilized interfaces in a microporous hydrophobic membrane. J. Memb. Sci. https://doi.org/10.1016/S0376-7388(00)81328-9

Kierzkowska-Pawlak, H., 2012. Determination of kinetics in gas-liquid reaction systems. An overview. Ecol. Chem. Eng. S. https://doi.org/10.2478/v10216-011-0014-y

Klomfar, J., Součková, M., Pátek, J., 2011. Temperature dependence of the surface tension and density at 0.1 MPa for 1-ethyl- and 1-butyl-3-methylimidazolium dicyanamide. J. Chem. Eng. Data. https://doi.org/10.1021/je200502j

Kohl, A.L., Nielsen, R.B., 1997. Gas purification 5th ed. Houst. Gulf Publ. Co. https://doi.org/10.1016/B978-088415220-0/50009-4

Kothandaraman, A., 2010. Carbon Dioxide Capture by Chemical Absorption : A Solvent Comparison Study. Carbon N. Y.

Krishnamurthy, S., Rao, V.R., Guntuka, S., Sharratt, P., Haghpanah, R., Rajendran, A., Amanullah, M., Karimi, I.A., Farooq, S., 2014. CO2 capture from dry flue gas by vacuum swing adsorption: A pilot plant study. AIChE J. https://doi.org/10.1002/aic.14435

Kumar, P.S., Hogendoorn, J.A., Feron, P.H.M., Versteeg, G.F., 2002. New absorption liquids for the removal of CO2 from dilute gas streams using membrane contactors. Chem. Eng.

Sci. https://doi.org/10.1016/S0009-2509(02)00041-6

Kumar, P.S., Hogendoorn, J.A., Versteeg, G.F., Feron, P.H.M., 2003. Kinetics of the reaction of CO2 with aqueous potassium salt of taurine and glycine. AIChE J. https://doi.org/10.1002/aic.690490118

Kuramochi, T., Ramírez, A., Turkenburg, W., Faaij, A., 2012. Comparative assessment of CO2 capture technologies for carbon-intensive industrial processes. Prog. Energy Combust. Sci. https://doi.org/10.1016/j.pecs.2011.05.001

Larriba, M., Navarro, P., García, J., Rodríguez, F., 2013. Liquid-liquid extraction of toluene from heptane using [emim][DCA], [bmim][DCA], and [emim][TCM] ionic liquids. Ind. Eng. Chem. Res. 52, 2714–2720. https://doi.org/10.1021/ie303357s

Lei, Z., Dai, C., Chen, B., 2014. Gas solubility in ionic liquids. Chem. Rev. 114, 1289–1326. https://doi.org/10.1021/cr300497a

Li, J., Dai, Z., Usman, M., Qi, Z., Deng, L., 2016. CO2/H2 separation by amino-acid ionic liquids with polyethylene glycol as co-solvent. Int. J. Greenh. Gas Control. https://doi.org/10.1016/j.ijggc.2015.12.027

Li, J.L., Chen, B.H., 2005. Review of CO2absorption using chemical solvents in hollow fiber membrane contactors. Sep. Purif. Technol. 41, 109–122. https://doi.org/10.1016/j.seppur.2004.09.008

Lin, S.H., Tung, K.L., Chen, W.J., Chang, H.W., 2009. Absorption of carbon dioxide by mixed piperazine-alkanolamine absorbent in a plasma-modified polypropylene hollow fiber contactor. J. Memb. Sci. https://doi.org/10.1016/j.memsci.2009.01.039

Lu, J., Wang, L., Sun, X., Li, J., Liu, X., 2005. Absorption of CO2 into aqueous solutions of methyldiethanolamine and activated methyldiethanolamine from a gas mixture in a hollow fiber contactor. Ind. Eng. Chem. Res. https://doi.org/10.1021/ie058023f

Lu, J.G., Ge, H., Chen, Y., Ren, R.T., Xu, Y., Zhao, Y.X., Zhao, X., Qian, H., 2017. CO2capture using a functional protic ionic liquid by membrane absorption. J. Energy Inst. 90, 933–940. https://doi.org/10.1016/j.joei.2016.08.001

Lu, J.G., Hua, A.C., Xu, Z.W., Li, J.T., Liu, S.Y., Wang, Z.L., Zhao, Y.L., Pan, C., 2013. CO2capture by membrane absorption coupling process: Experiments and coupling process evaluation. J. Memb. Sci. 431, 9–18. https://doi.org/10.1016/j.memsci.2012.12.039

Lu, J.G., Lu, C.T., Chen, Y., Gao, L., Zhao, X., Zhang, H., Xu, Z.W., 2014. CO2capture by membrane absorption coupling process: Application of ionic liquids. Appl. Energy 115, 573–581. https://doi.org/10.1016/j.apenergy.2013.10.045

Lu, J.G., Lu, Z.Y., Chen, Y., Wang, J.T., Gao, L., Gao, X., Tang, Y.Q., Liu, D.G., 2015. CO<inf>2</inf> absorption into aqueous blends of ionic liquid and amine in a membrane contactor. Sep. Purif. Technol. 150, 278–285. https://doi.org/10.1016/j.seppur.2015.07.010

Luis, P., Garea, A., Irabien, A., 2009. Zero solvent emission process for sulfur dioxide recovery using a membrane contactor and ionic liquids. J. Memb. Sci. 330, 80–89. https://doi.org/10.1016/j.memsci.2008.12.046

Lv, Y., Yu, X., Tu, S.T., Yan, J., Dahlquist, E., 2010. Wetting of polypropylene hollow fiber membrane contactors. J. Memb. Sci. https://doi.org/10.1016/j.memsci.2010.06.067

Ma, Q., 1998. NASA GISS: Science Briefs: Greenhouse Gases: Refining the Role of Carbon Dioxide [WWW Document]. NASA Goddard Inst. Sp. Stud.

Maginn, E.J., 2005. Design and evaluation of ionic liquids as novel CO2 absorbents, 2005. Univ. Norte Dame Notre Dame. https://doi.org/10.2172/859167

Malek, A., Li, K., Teo, W.K., 1997. Modeling of Microporous Hollow Fiber Membrane Modules Operated under Partially Wetted Conditions. Ind. Eng. Chem. Res. 36, 784–793. https://doi.org/10.1021/ie960529y

Mansourizadeh, A., Ismail, A.F., 2009. Hollow fiber gas-liquid membrane contactors for acid gas capture: A review. J. Hazard. Mater. https://doi.org/10.1016/j.jhazmat.2009.06.026

Mansourizadeh, A., Ismail, A.F., Matsuura, T., 2010. Effect of operating conditions on the physical and chemical CO2 absorption through the PVDF hollow fiber membrane contactor. J. Memb. Sci. 353, 192–200. https://doi.org/10.1016/j.memsci.2010.02.054

Maring, B.J., Webley, P.A., 2013. A new simplified pressure/vacuum swing adsorption model for rapid adsorbent screening for CO2 capture applications. Int. J. Greenh. Gas Control. https://doi.org/10.1016/j.ijggc.2013.01.009

Markewitz, P., Kuckshinrichs, W., Leitner, W., Linssen, J., Zapp, P., Bongartz, R., Schreiber, A., Müller, T.E., 2012. Worldwide innovations in the development of carbon capture technologies and the utilization of CO2. Energy Environ. Sci. https://doi.org/10.1039/c2ee03403d

Mavroudi, M., Kaldis, S.P., Sakellaropoulos, G.P., 2006. A study of mass transfer resistance in membrane gas-liquid contacting processes. J. Memb. Sci. https://doi.org/10.1016/j.memsci.2005.07.025

Mejía, I., Stanley, K., Canales, R., Brennecke, J.F., 2013. On the high-pressure solubilities of carbon dioxide in several ionic liquids. J. Chem. Eng. Data 58, 2642–2653. https://doi.org/10.1021/je400542b

Moganty, S.S., Baltus, R.E., 2010. Diffusivity of Carbon Dioxide in Room-Temperature Ionic Liquids. Ind. Eng. Chem. Res. 49, 9370–9376. https://doi.org/10.1021/ie101260j

Morgan, D., Ferguson, L., Scovazzo, P., 2005. Diffusivities of gases in room-temperature ionic Liquids: Data and correlations obtained using a lag-time technique. Ind. Eng. Chem. Res. 44, 4815–4823. https://doi.org/10.1021/ie048825v

Mosadegh-Sedghi, S., Brisson, J., Rodrigue, D., Iliuta, M.C., 2012. Morphological, chemical and thermal stability of microporous LDPE hollow fiber membranes in contact with

single and mixed amine based CO 2 absorbents. Sep. Purif. Technol. https://doi.org/10.1016/j.seppur.2012.05.025

Mosadegh-Sedghi, S., Rodrigue, D., Brisson, J., Iliuta, M.C., 2014. Wetting phenomenon in membrane contactors - Causes and prevention. J. Memb. Sci. https://doi.org/10.1016/j.memsci.2013.09.055

Moya, C., Palomar, J., Gonzalez-Miquel, M., Bedia, J., Rodriguez, F., 2014. Diffusion Coefficients of CO2 in Ionic Liquids Estimated by Gravimetry. Ind. Eng. Chem. Res. 53, 13782–13789. https://doi.org/10.1021/ie501925d

Muhammad, A., Younas, M., Rezakazemi, M., 2017. Quasi-dynamic modeling of dispersion-free extraction of aroma compounds using hollow fiber membrane contactor. Chem. Eng. Res. Des. 127, 52–61. https://doi.org/10.1016/j.cherd.2017.09.007

Nazet, A., Sokolov, S., Sonnleitner, T., Makino, T., Kanakubo, M., Buchner, R., 2015. Densities, Viscosities, and Conductivities of the Imidazolium Ionic Liquids [Emim][Ac], [Emim][FAP], [Bmim][BETI], [Bmim][FSI], [Hmim][TFSI], and [Omim][TFSI]. J. Chem. Eng. Data 60, 2400–2411. https://doi.org/10.1021/acs.jced.5b00285

Neftel, A., Moor, E., Oeschger, H., Stauffer, B., 1985. Evidence from polar ice cores for the increase in atmospheric CO 2 in the past two centuries. Nature. https://doi.org/10.1038/315045a0

Odeh, N.A., Cockerill, T.T., 2008. Life cycle GHG assessment of fossil fuel power plants with carbon capture and storage. Energy Policy. https://doi.org/10.1016/j.enpol.2007.09.026

Ohno, H., Fukumoto, K., 2007. Amino acid ionic liquids. Acc. Chem. Res. https://doi.org/10.1021/ar700053z

Okoturo, O.O., VanderNoot, T.J., 2004. Temperature dependence of viscosity for room temperature ionic liquids. J. Electroanal. Chem. 568, 167–181. https://doi.org/10.1016/j.jelechem.2003.12.050

Ortiz, A., Gorri, D., Irabien, Á., Ortiz, I., 2010. Separation of propylene/propane mixtures using Ag+-RTIL solutions. Evaluation and comparison of the performance of gas-liquid contactors. J. Memb. Sci. 360, 130–141. https://doi.org/10.1016/j.memsci.2010.05.013

Papatryfon, X.L., Heliopoulos, N.S., Molchan, I.S., Zubeir, L.F., Bezemer, N.D., Arfanis, M.K., Kontos, A.G., Likodimos, V., Iliev, B., Romanos, G.E., Falaras, P., Stamatakis, K., Beltsios, K.G., Kroon, M.C., Thompson, G.E., Klöckner, J., Schubert, T.J.S., 2014. CO2 capture efficiency, corrosion properties, and ecotoxicity evaluation of amine solutions involving newly synthesized ionic liquids. Ind. Eng. Chem. Res. https://doi.org/10.1021/ie501897d

Pehnt, M., Henkel, J., 2009. Life cycle assessment of carbon dioxide capture and storage from lignite power plants. Int. J. Greenh. Gas Control. https://doi.org/10.1016/j.ijggc.2008.07.001

Perry, H.R., 2007. Perry's Chemical Engineering Handbook, 8th Edn ed, McGraw-Hill.

Qi, Z., Cussler, E.L., 1985a. Microporous hollow fibers for gas absorption. J. Memb. Sci. https://doi.org/10.1016/s0376-7388(00)83150-6

Qi, Z., Cussler, E.L., 1985b. Microporous hollow fibers for gas absorption. II. Mass transfer across the membrane. J. Memb. Sci. https://doi.org/10.1016/S0376-7388(00)83150-6

Quijada-Maldonado, E., Van Der Boogaart, S., Lijbers, J.H., Meindersma, G.W., De Haan, A.B., 2012. Experimental densities, dynamic viscosities and surface tensions of the ionic liquids series 1-ethyl-3-methylimidazolium acetate and dicyanamide and their binary and ternary mixtures with water and ethanol at T = (298.15 to 343.15 K). J. Chem. Thermodyn. 51, 51–58. https://doi.org/10.1016/j.jct.2012.02.027

Ramdin, M., De Loos, T.W., Vlugt, T.J.H., 2012. State-of-the-art of CO \n 2 capture with ionic liquids. Ind. Eng. Chem. Res. 51, 8149–8177. https://doi.org/10.1021/ie3003705

Rangwala, H.A., 1996. Absorption of carbon dioxide into aqueous solutions using hollow fiber membrane contactors. J. Memb. Sci. https://doi.org/10.1016/0376-7388(95)00293-6

Razavi, S.M.R., Razavi, S.M.J., Miri, T., Shirazian, S., 2013. CFD simulation of CO2 capture from gas mixtures in nanoporous membranes by solution of 2-amino-2-methyl-1-propanol and piperazine. Int. J. Greenh. Gas Control. https://doi.org/10.1016/j.ijggc.2013.02.011

Ren, S., Hou, Y., Wu, W., Tian, S., Liu, W., 2012. CO 2 capture from flue gas at high temperatures by new ionic liquids with high capacity. RSC Adv. https://doi.org/10.1039/c2ra00996j

Riemer, P.W.F., Ormerod, W.G., 1995. International perspectives and the results of carbon dioxide capture disposal and utilisation studies. Energy Convers. Manag. https://doi.org/10.1016/0196-8904(95)00128-Z

Ritchie, H., Roser, M., 2020. CO_2 and Greenhouse Gas Emissions [WWW Document]. Our World Data. URL https://ourworldindata.org/co2-and-other-greenhouse-gas-emissions#licence (accessed 5.16.20).

Rochelle, G.T., 2009. Amine Scrubbing for CO2 Capture. Science (80-.). https://doi.org/10.1126/science.1176731

Saidi, M., 2017. Mathematical modeling of CO2absorption into novel reactive DEAB solution in hollow fiber membrane contactors; kinetic and mass transfer investigation. J. Memb. Sci. 524, 186–196. https://doi.org/10.1016/j.memsci.2016.11.028

Sander, R., 2015. Compilation of Henry's law constants (version 4.0) for water as solvent. Atmos. Chem. Phys. 15, 4399–4981. https://doi.org/10.5194/acp-15-4399-2015

Sands, P., 1992. The United Nations Framework Convention on Climate Change. Rev. Eur.

Community Int. Environ. Law. https://doi.org/10.1111/j.1467-9388.1992.tb00046.x

Santos, C.S., Baldelli, S., 2009. Alkyl Chain Interaction at the Surface of Room Temperature Ionic Liquids: Systematic Variation of Alkyl Chain Length ($R = C_1 - C_4, C_8$) in both Cation and Anion of [RMIM][$R - OSO_3$] by Sum Frequency G. J. Phys. Chem. B 113, 923–933. https://doi.org/10.1021/jp807924g

Schmidt, H., Stephan, M., Safarov, J., Kul, I., Nocke, J., Abdulagatov, I.M., Hassel, E., 2012. Experimental study of the density and viscosity of 1-ethyl-3- methylimidazolium ethyl sulfate. J. Chem. Thermodyn. 47, 68–75. https://doi.org/10.1016/j.jct.2011.09.027

Schumpe, A., 1993. The estimation of gas solubilities in salt solutions. Chem. Eng. Sci. https://doi.org/10.1016/0009-2509(93)80291-W

Seibert, A.F., Py, X., Mshewa, M., Fair, J.R., 1993. Hydraulics and mass transfer efficiency of a commercial-scale membrane extractor, in: Separation Science and Technology. https://doi.org/10.1080/01496399308019494

Shen, S., Kentish, S.E., Stevens, G.W., 2010. Shell-side mass-transfer performance in hollow-fiber membrane contactors. Solvent Extr. Ion Exch. https://doi.org/10.1080/07366299.2010.515176

Shiflett, M.B., Yokozeki, A., 2009. Phase behavior of carbon dioxide in ionic liquids: [emim][acetate], [emim][trifluoroacetate], and [emim][acetate] + [emim][trifluoroacetate] mixtures. J. Chem. Eng. Data 54, 108–114. https://doi.org/10.1021/je800701j

Singh, B., Strømman, A.H., Hertwich, E.G., 2011. Comparative life cycle environmental assessment of CCS technologies. Int. J. Greenh. Gas Control. https://doi.org/10.1016/j.ijggc.2011.03.012

Soriano, A.N., Doma, B.T., Li, M.H., 2009. Carbon dioxide solubility in some ionic liquids at moderate pressures. J. Taiwan Inst. Chem. Eng. 40, 387–393. https://doi.org/10.1016/j.jtice.2008.12.002

Styring, P., Jansen, D., de Coninck, H., Reith, H., Armstrong, K., 2011. Carbon Capture and Utilisation in the green economy, Centre for Low Carbon Futures.

Sung, S., Suh, M.P., 2014. Highly efficient carbon dioxide capture with a porous organic polymer impregnated with polyethylenimine. J. Mater. Chem. A. https://doi.org/10.1039/c4ta02861a

Supasitmongkol, S., Styring, P., 2010. High CO2 solubility in ionic liquids and a tetraalkylammonium-based poly(ionic liquid). Energy Environ. Sci. 3, 1961. https://doi.org/10.1039/c0ee00293c

UNIDO; IEA, 2011. Carbon Capture and Storage in Industrial Applications - Technology Roadmap [WWW Document]. IEA.

Vataščin, E., Dohnal, V., 2017. Thermodynamic properties of aqueous solutions of [EMIM]

thiocyanate and [EMIM] dicyanamide. J. Chem. Thermodyn. https://doi.org/10.1016/j.jct.2016.12.008

Versteeg, G.F., van Swaal, W.P.M., 1988. Solubility and Diffusivity of Acid Gases (CO2, N2O) in Aqueous Alkanolamine Solutions. J. Chem. Eng. Data. https://doi.org/10.1021/je00051a011

Villeneuve, K., Albarracin Zaidiza, D., Roizard, D., Rode, S., 2018. Modeling and simulation of CO2 capture in aqueous ammonia with hollow fiber composite membrane contactors using a selective dense layer. Chem. Eng. Sci. https://doi.org/10.1016/j.ces.2018.06.016

Wang, C., Guo, Y., Zhu, X., Cui, G., Li, H., Dai, S., 2012. Highly efficient CO 2 capture by tunable alkanolamine-based ionic liquids with multidentate cation coordination. Chem. Commun. https://doi.org/10.1039/c2cc32365f

Wang, C., Luo, H., Jiang, D.E., Li, H., Dai, S., 2010. Carbon dioxide capture by superbase-derived protic ionic liquids. Angew. Chemie - Int. Ed. https://doi.org/10.1002/anie.201002641

Wang, G., Hou, W., Xiao, F., Geng, J., Wu, Y., Zhang, Z., 2011. Low viscosity triethylbutylammonium acetate as a task-specific ionic liquid for reversible CO2 absorption. J. Chem. Eng. Data 56, 1125–1133. https://doi.org/10.1021/je101014q

Wang, R., Li, D.F., Liang, D.T., 2004. Modeling of CO2 capture by three typical amine solutions in hollow fiber membrane contactors. Chem. Eng. Process. Process Intensif. 43, 849–856. https://doi.org/10.1016/S0255-2701(03)00105-3

Wang, R., Zhang, H.Y., Feron, P.H.M., Liang, D.T., 2005. Influence of membrane wetting on CO2 capture in microporous hollow fiber membrane contactors. Sep. Purif. Technol. 46, 33–40. https://doi.org/10.1016/j.seppur.2005.04.007

Wang, Z., Fang, M., Yan, S., Yu, H., Wei, C.C., Luo, Z., 2013a. Optimization of blended amines for CO2 absorption in a hollow-fiber membrane contactor. Ind. Eng. Chem. Res. https://doi.org/10.1021/ie401676t

Wang, Z., Fang, M., Yu, H., Ma, Q., Luo, Z., 2013b. Modeling of CO 2 Stripping in a Hollow Fiber Membrane Contactor for CO 2 Capture. Energy & Fuels 27, 6887–6898. https://doi.org/10.1021/ef401488c

Weisenberger, S., Schumpe, A., 1996. Estimation of Gas Solubilities in Salt Solutions at Temperatures from 273 K to 363 K. AIChE J. https://doi.org/10.1002/aic.690420130

Wu, Z., Huang, Z., Zhang, Y., Qin, Y.H., Ma, J., Luo, Y., 2016. Kinetics analysis and regeneration performance of 1-butyl-3-methylimidazolium glycinate solutions for CO 2 capture. Chem. Eng. J. https://doi.org/10.1016/j.cej.2016.03.030

Wu, Z., Zhang, Y., Lei, W., Yu, P., Luo, Y., 2015. Kinetics of CO 2 absorption into aqueous 1-ethyl-3-methylimidazolium glycinate solution. Chem. Eng. J. https://doi.org/10.1016/j.cej.2014.11.133

Yan, S., Fang, M., Zhang, W., Zhong, W., Luo, Z., Cen, K., 2008. Comparative analysis of CO2 separation from flue gas by membrane gas absorption technology and chemical absorption technology in China. Energy Convers. Manag. https://doi.org/10.1016/j.enconman.2008.05.027

Yan, S. ping, Fang, M.X., Zhang, W.F., Wang, S.Y., Xu, Z.K., Luo, Z.Y., Cen, K.F., 2007. Experimental study on the separation of CO2from flue gas using hollow fiber membrane contactors without wetting. Fuel Process. Technol. 88, 501–511. https://doi.org/10.1016/j.fuproc.2006.12.007

Yan, X., Anguille, S., Bendahan, M., Moulin, P., 2019. Ionic liquids combined with membrane separation processes: A review. Sep. Purif. Technol. https://doi.org/10.1016/j.seppur.2019.03.103

Yang, H., Xu, Z., Fan, M., Gupta, R., Slimane, R.B., Bland, A.E., Wright, I., 2008. Progress in carbon dioxide separation and capture: A review. J. Environ. Sci. https://doi.org/10.1016/S1001-0742(08)60002-9

Yeon, S.H., Lee, K.S., Sea, B., Park, Y.I., Lee, K.H., 2005. Application of pilot-scale membrane contactor hybrid system for removal of carbon dioxide from flue gas. J. Memb. Sci. 257, 156–160. https://doi.org/10.1016/j.memsci.2004.08.037

Yim, J.H., Ha, S.J., Lim, J.S., 2018. Measurement and Correlation of CO2Solubility in 1-Ethyl-3-methylimidazolium ([EMIM]) Cation-Based Ionic Liquids: [EMIM][Ac], [EMIM][Cl], and [EMIM][MeSO4]. J. Chem. Eng. Data 63, 508–518. https://doi.org/10.1021/acs.jced.7b00532

Ying, H., Baltus, R.E., 2007. Experimental measurement of the solubility and diffusivity of CO 2 in room-temperature ionic liquids using a transient thin-liquid-film method. Ind. Eng. Chem. Res. https://doi.org/10.1021/ie070501u

Yokozeki, A., Shiflett Mark, B., Junk Christopher, P., Grieco Liane, M., Foo, T., 2008. Physical and chemical absorptions of carbon dioxide in room-temperature ionic liquids. J. Phys. Chem. B 112, 16654–16663.

Yu, C.H., Huang, C.H., Tan, C.S., 2012. A review of CO2 capture by absorption and adsorption. Aerosol Air Qual. Res. https://doi.org/10.4209/aaqr.2012.05.0132

Zhang, H.Y., Wang, R., Liang, D.T., Tay, J.H., 2008. Theoretical and experimental studies of membrane wetting in the membrane gas-liquid contacting process for CO2 absorption. J. Memb. Sci. https://doi.org/10.1016/j.memsci.2007.09.050

Zhang, H.Y., Wang, R., Liang, D.T., Tay, J.H., 2006. Modeling and experimental study of CO2absorption in a hollow fiber membrane contactor. J. Memb. Sci. 279, 301–310. https://doi.org/10.1016/j.memsci.2005.12.017

Zhang, Xiangping, Zhang, Xiaochun, Dong, H., Zhao, Z., Zhang, S., Huang, Y., 2012. Carbon capture with ionic liquids: overview and progress. Energy Environ. Sci. 5, 6668. https://doi.org/10.1039/c2ee21152a

Zhang, Z., Chen, F., Rezakazemi, M., 2017. Chemical Engineering Research and Design Modeling of a CO 2 -piperazine-membrane 1, 375–384.

Zhao, S., Cao, C., Wardhaugh, L., Feron, P.H.M., 2015a. Membrane evaporation of amine solution for energy saving in post-combustion carbon capture: Performance evaluation. J. Memb. Sci. https://doi.org/10.1016/j.memsci.2014.09.029

Zhao, S., Feron, P.H.M., Cao, C., Wardhaugh, L., Yan, S., Gray, S., 2015b. Membrane evaporation of amine solution for energy saving in post-combustion carbon capture: Wetting and condensation. Sep. Purif. Technol. https://doi.org/10.1016/j.seppur.2015.03.015

Zhao, S., Feron, P.H.M., Deng, L., Favre, E., Chabanon, E., Yan, S., Hou, J., Chen, V., Qi, H., 2016. Status and progress of membrane contactors in post-combustion carbon capture: A state-of-the-art review of new developments. J. Memb. Sci. 511, 180–206. https://doi.org/10.1016/j.memsci.2016.03.051

Zhou, Z., Jing, G., Zhou, L., 2012. Characterization and absorption of carbon dioxide into aqueous solution of amino acid ionic liquid [N1111][Gly] and 2-amino-2-methyl-1-propanol. Chem. Eng. J. 204–205, 235–243. https://doi.org/10.1016/j.cej.2012.07.108

Zubeir, L.F., Romanos, G.E., Weggemans, W.M.A., Iliev, B., Schubert, T.J.S., Kroon, M.C., 2015. Solubility and Diffusivity of CO<inf>2</inf> in the Ionic Liquid 1-Butyl-3-methylimidazolium Tricyanomethanide within a Large Pressure Range (0.01 MPa to 10 MPa). J. Chem. Eng. Data 60, 1544–1562. https://doi.org/10.1021/je500765m

Abstract

Post-combustion CO_2 capture in a hollow fiber membrane contactor (HFMC), using imidazolium-based room temperature ionic liquids (RTILs) and amino acid ionic liquids (AAILs) as absorbents, was studied through an experimental and modeling approach. Equilibrium solubility of CO_2 in RTILs was measured by isochoric pressure drop. Pore wetting was analyzed by measuring surface tension of the RTILs, contact angle and liquid entry pressure (LEP). The experimental work of CO_2 capture from a gas mixture was carried out with a laboratory scale unit using a single HFMC for absorption or two coupled HFMCs one for absorption and a second for desorption working simultaneously. Furthermore, robust and rigorous dynamic modeling approaches were developed for isothermal (with RTILs) and non-isothermal (with AAILs) absorption. Both isothermal and non-isothermal models were validated with experimental data and were used to simulate a large range of operating conditions. Initial high values of CO_2 absorption rate and experimental mass transfer coefficients decreased with operation time and reached a nearly constant value at pseudo-steady-state. Before reaching pseudo-steady-state, the separation efficiency of coupled process was higher when compared with the absorption with a single module.

Keywords: Post-Combustion CO_2 Capture, Membrane Contactor, Ionic Liquid, CO_2 Solubility, Modeling and Simulation.

Résumé

Des contacteurs membranaires à fibres creuses (HFMC) ont été utilisés pour la capture du CO_2 des courants gazeux. Pour ce faire, des liquides ioniques à température ambiante (RTIL) et des liquides ioniques d'acides aminés (AAIL) à base d'imidazolium ont été utilisés comme absorbants, avec une double approche expérimentale et de modélisation. La solubilité du CO_2 à l'équilibre dans les RTIL a été mesurée par la chute de pression isochronique. Le mouillage des pores a été analysé avec la mesure de la tension superficielle des RTIL, l'angle de contact et la pression d'intrusion (LEP). Le travail expérimental de capture du CO_2 à partir d'un mélange gazeux a été réalisé avec une unité à l'échelle de laboratoire en utilisant soit un HFMC pour l'absorption simple soit deux HFMC couplés, travaillant simultanément un en absorption et le second en désorption. En outre, une approche de modélisation en régime dynamique robuste et rigoureuse a été développée pour l'absorption isotherme (avec des RTIL) et non isotherme (avec des AAIL), les modèles développés ont étés validés avec les résultats expérimentaux et utilisés pour simuler un large éventail des conditions opératoires. Le flux d'absorption du CO_2 et les coefficients de transfert de masse expérimentaux, initialement très élevés, décroisent avec le temps atteignant une valeur presque constante arrivant à un état pseudo-stationnaire. Avant d'atteindre l'état pseudo-stationnaire, le rendement de séparation du procédé couplé s'est montré plus efficace que l'absorption avec un module unique.

Mots-clés: Capture de CO_2 Post-combustion, Contacteur à Membrane, Liquide Ionique, Solubilité au CO_2, Modélisation et Simulation.